STRUCTURAL ANALYSIS, PARAGENESIS, AND GEOCHRONOLOGY OF THE ARROW URANIUM DEPOSIT, WESTERN ATHABASCA BASIN, SASKATCHEWAN, CANADA: IMPLICATIONS FOR THE DEVELOPMENT OF THE PATTERSON LAKE CORRIDOR

A Thesis Submitted to the College of

Graduate and Postdoctoral Studies

In Partial Fulfillment of the Requirements

For the Degree of Master of Science

In the Department of Geological Sciences

University of Saskatchewan

Saskatoon

By

SEAN HILLACRE

PERMISSION TO USE

In presenting this thesis/dissertation in partial fulfillment of the requirements for a Postgraduate degree from the University of Saskatchewan, I agree that the Libraries of this University may make it freely available for inspection. I further agree that permission for copying of this thesis/dissertation in any manner, in whole or in part, for scholarly purposes may be granted by the professor or professors who supervised my thesis/dissertation work or, in their absence, by the Head of the Department or the Dean of the College in which my thesis work was done. It is understood that any copying or publication or use of this thesis/dissertation or parts thereof for financial gain shall not be allowed without my written permission. It is also understood that due recognition shall be given to me and to the University of Saskatchewan in any scholarly use which may be made of any material in my thesis/dissertation.

DISCLAIMER

Reference in this thesis/dissertation to any specific commercial products, process, or service by trade name, trademark, manufacturer, or otherwise, does not constitute or imply its endorsement, recommendation, or favoring by the University of Saskatchewan. The views and opinions of the author expressed herein do not state or reflect those of the University of Saskatchewan, and shall not be used for advertising or product endorsement purposes.

Requests for permission to copy or to make other uses of materials in this thesis/dissertation in whole or part should be addressed to:

Head of the Department of Geological Sciences
114 Science Place
University of Saskatchewan
Saskatoon, Saskatchewan S7N 5E2
Canada

OR

Dean
College of Graduate and Postdoctoral Studies
University of Saskatchewan
116 Thorvaldson Building, 110 Science Place
Saskatoon, Saskatchewan S7N 5C9
Canada

Abstract

The Athabasca Basin in northern Saskatchewan hosts the world's highest-grade uranium deposits, which are commonly spatially associated with structural zones that have undergone episodes of brittle reactivation, alteration, and polyphase fluid movement. The most recent significant discoveries of uranium mineralization in the Athabasca Basin have been associated with a series of geophysical conductors along a NE-SW-trending structural zone, termed the Patterson Lake corridor, in the southwestern portion of the Basin. The Arrow Deposit, which is along this trend and hosted exclusively in the basement rocks below the Athabasca Supergroup sandstones, has an indicated mineral resource of 179.5 Mlbs U_3O_8 at a grade of 6.88% U_3O_8, and is the largest undeveloped uranium resource in the Basin. The present study examines the relationships between the ductile framework and brittle reactivation of deep-seated structures, mineral paragenesis, and radiogenic and stable isotope analyses of uranium mineralization at the Arrow Deposit. Hand sample examination, structural analysis from oriented drill core, thin section microscopy, and electron microprobe analysis has been used to generate a detailed paragenesis of the Arrow Deposit, which was used to select mineralized samples for isotopic analysis that were categorized based on cross-cutting relationships, textures, and chemical composition. Paragenetic information was integrated with structural analysis utilizing over 18,000 measurements of foliation, fractures, veins, shears, mylonites, breccias, cataclasites, fault gouges, and plunge and trend of slickenstriae and ductile lineations. Through this study, the structural system at Arrow has been interpreted as a partitioned, sinistral strike-slip dominated, brittle-ductile fault system of complex Riedel-style geometry. The Arrow system developed along sub-vertical, NE-SW-trending heterogeneous high strain zones (named the A1 through A5 shears) along the limb of a regional-scale fold, and further evolved through episodic reactivation events creating small-scale brittle fault linkages oblique to, and connecting the main fault zone, allowing for migration of fluids, alteration of host rocks, and precipitation of uranium. Uranium mineralization at Arrow occurs as botryoidal, cubic, vein, semi-massive, and massive uraninite (UO_2), as well as younger alteration phases including uranium-silicates (e.g. coffinite) and uranyl oxy-hydroxide minerals (e.g. uranophane). Regression of the concentrations of substituting elements including Fe, Si, and Ca give an average chemical age of initial uraninite crystallization of approximately 1,425 Ma. In-situ secondary ionization mass spectrometry (SIMS) U-Pb ages obtained in this study (~700, ~1,200, and ~1,300 Ma) are comparable with those obtained from the Shea Creek area and reveal

numerous episodes of uranium mineralization, remobilization, and alteration associated with multi-stage deformation during the Proterozoic. The geochronological data on uranium mineralization and post-mineralization alteration and resetting events broadly correspond to major orogenic events that have affected the North American shield. The oldest uraninites (~1,300 to 1,425 Ma) are botryoidal, cubic, and semi-massive occurrences commonly replacing clay minerals and micas. Younger (~1,200 and ~700 Ma) uraninites occur as cubic crystals, semi-massive and massive lenses, and form the matrix of breccias. The youngest uraniferous minerals are the products of alteration and/or remobilization of uraninite through subsequent fluid-flow events. This study demonstrates that the U–Pb isotope systematics of uranium-rich minerals from the Arrow Deposit have been affected by paleo-fluid-flow events that were controlled by regional and global-scale tectonic events. The precision and high spatial resolution of the SIMS method allowed for measurement of $\delta^{18}O$ values from ~10 μm spots on uraninites from the Arrow Deposit. The range of $\delta^{18}O$ values (-34.5 to -15.2 ‰) are low, and comparable to those obtained from other unconformity-type deposits in the Basin such as Cigar Lake and Shea Creek. The low $\delta^{18}O$ values indicate that the uraninite likely underwent recrystallization via interaction with late, relatively low temperature Athabasca fluids with $\delta^{18}O$ values in the range of -20 to -16 ‰. The other discoveries along the Patterson Lake corridor (Triple R, Cannon, Bow, Harpoon, Spitfire) have not been studied in detail, and so this study of the structural context of the Arrow Deposit is important as it emphasizes that protracted reactivation of deep-seated NE-SW-trending structures and their subsidiaries was a fundamental control on uranium mineralization in the SW Athabasca Basin. Continued studies integrating mineral paragenesis, geochemistry, and structural geology with geochronological context will aid in understanding the evolution of uranium deposits within the recently established southwestern Athabasca Basin uranium camp.

ACKNOWLEDGEMENTS

This project benefitted from the support and guidance of many people. I extend my utmost gratitude to my supervisor, Dr. Kevin Ansdell for his invaluable guidance and motivation throughout the course of completing this thesis. I acknowledge the Natural Sciences and Engineering Research Council (NSERC) for providing financial support through an NSERC-NexGen Energy Ltd. Collaborative Research and Development Grant to Dr. Kevin Ansdell. A special thanks to the Society of Economic Geologists Canada Foundation and Barrick Gold Corporation for choosing me as one of the 2017 Barrick scholars, and providing additional funding through awarding me a Graduate Student Fellowship. Thanks to Tom Bonli at the University of Saskatchewan for assistance with the SEM-EMPA analyses, and Dr. Mostafa Fayek and Ryan Sharpe at the University of Manitoba for exceptional guidance with the SIMS analyses. Thanks to Robert Millar and Angela Cooper at Saskatchewan Research Council (SRC) for thin section preparation and providing laboratory space for mineralized sample sorting and preparation.

My sincere thanks are extended to NexGen Energy Limited for accommodating and funding this project, providing employment, logistical support, and access to information and equipment that was essential to this research. Special thanks to Brian McEwan for his thought-provoking criticism and steadfast support during the course of this project. Many late-night conversations and enlightening discussions with Brian in the field helped to greatly improve the manuscript and research outcomes. A special thanks also goes out to all my past and present technical staff colleagues at NexGen for insightful discussion and support over the course of this project.

DEDICATION

For my soulmate, Caitlin Glew, my mother, Patti, my father, David, my brother, Paul, and of course, Dr. Moose Hunter. You all picked me up when I was down, gave me confidence when I was overwhelmed, and always maintained a tireless belief in my abilities. “Confidence is key”. Without your support, understanding, encouragement, and love, I would not be where I am today. Thank you.

TABLE OF CONTENTS

page

LIST OF TABLES

Table Number Page Number

LIST OF FIGURES

Figure Number Page Number

LIST OF APPENDICES

Appendix Number Page Number

CHAPTER 1

INTRODUCTION

Canada has remained a leading producer of uranium for years, accounting for about 22% of global uranium production with approximately 15% of Canada's electricity coming from nuclear power generated by 19 operational reactors (World Nuclear Association, 2018). Canada's uranium is used exclusively for the generation of electricity at nuclear power plants, and 100% of the uranium production in Canada comes from Saskatchewan mines (Saskatchewan Mining Association, 2017). The Proterozoic Athabasca Basin is the primary location of uranium deposits and mines in Saskatchewan. Unconformity-related uranium deposits in the Basin are unsurpassed as the highest-grade uranium deposits in the world, some of which are one hundred times the world average grade (World Nuclear Association, 2018). Although there have been past-producing mines in the western Basin (i.e. Cluff Lake), the vast majority of uranium exploration and mining activity over the last 50+ years has been focussed in the eastern portion of the Basin (i.e. McArthur River, Cigar Lake, Key Lake, Rabbit Lake; Fig. 1.1 and 1.2).

Although fewer in abundance, a number of significant deposits and prospects have been discovered in the western portion of the Basin, including the Kianna deposit on the Shea Creek property south of Cluff Lake, and Maybelle River in the far west (Fig. 1.2). Since 2012, exploration projects led by a number of companies along the Patterson Lake corridor in the southwestern Basin has led to the discovery of the significant high-grade Arrow and Triple R deposits, as well as the Bow, South Arrow, Cannon, Harpoon, and Spitfire discoveries (Fig. 1.3). The Arrow uranium deposit is the flagship discovery on NexGen Energy's Rook I property and is the largest undeveloped uranium resource in the basin. The twenty-first hole ever drilled by NexGen at the Rook I property, AR-14-001, intersected high-grade uranium at the on-land Arrow target in 2014. AR-14-001 encountered multiple structural zones containing uranium mineralization, and at the time of drilling, no other holes existed within a 4 km radius. The Arrow Deposit is located within the Rook I property at the southwestern margin of the Athabasca Basin approximately 75 km south of the past-producing Cluff Lake uranium deposits (Fig. 1.2). Since the discovery of Rabbit Lake by Gulf Minerals Ltd. in 1968 (Sibbald, 1985), unconformity-related uranium deposits in the eastern portion of the Athabasca Basin, such as the Cigar Lake, Eagle Point, and McArthur River deposits, have been well studied (e.g. Hoeve & Sibbald 1978; Hoeve et al., 1980; Sibbald, 1985;

Fayek & Kyser 1993; Kotzer & Kyser, 1995; Quirt, 1999; Fayek et al., 2002a; Jefferson et al., 2007; Alexandre et al., 2009; Mercadier et al., 2010; Cloutier et al., 2011). Unconformity-related uranium deposits conventionally host pods of mineralization just above, below, or along the unconformable contact between Athabasca Supergroup sandstones and the underlying crystalline basement rock and are typically associated with structures that cut the unconformity. Akin to the Eagle Point uranium deposit in the eastern Basin, Arrow is a structurally-controlled deposit, hosted entirely by crystalline basement rocks below the Athabasca Supergroup sedimentary rocks. The mineralized area of Arrow is currently defined as 308 m wide by 895 m in strike length, with mineralization starting at 110 m from surface and extending to 980 m. The Arrow Deposit has an indicated mineral resource estimate of 179.5 million pounds (Mlbs) U_3O_8 contained within 1.18 million tonnes (Mt) grading 6.88% U_3O_8 including a high-grade core of 164.9 Mlbs U_3O_8 contained within 0.40 Mt grading 18.84% U_3O_8 and an inferred mineral resource estimate of 122.1 Mlbs U_3O_8 contained within 4.25 Mt grading 1.30% U_3O_8 (Mathisen and Ross, 2017).

1.1 The Patterson Lake Corridor, Southwestern Athabasca Basin

The most recent significant discoveries of uranium mineralization in the Athabasca Basin have been associated with a series of deep-seated conductors which comprise the NE-SW-trending geophysical feature termed the Patterson Lake corridor (Fig. 1.3). These discoveries include NexGen's Arrow Deposit (179.5 Mlbs @ 6.88% U_3O_8 indicated; Mathisen and Ross, 2017) and Fission Uranium Corp.'s Triple R deposit (87.76 Mlbs @ 1.82% U_3O_8 indicated; Fission Uranium Corp., 2018), and the South Arrow, Bow, Cannon, Harpoon (NexGen), and Spitfire (Purepoint/Cameco/Orano) discoveries (Fig. 1.3). The Patterson Lake corridor is one of many prominent NE-SW trending conductive features in the SW Athabasca Basin and is a crustal-scale structural zone extending over 50 km in strike. Through the present study, the corridor has been found to be dominated by heterogeneous high-strain, with rocks showing evidence for deformation events under both ductile and brittle regimes. The highly deformed and altered rocks along the Patterson Lake corridor are likely related to reactivation of the corridor and other major structural corridors in the region during the Taltson-Thelon (ca. 2.0 - 1.9 billion years (Ga) ago; Fig. 1.1) and Hudsonian (ca. 1.9 - 1.8 Ga) orogenies (e.g. Card et al., 2007; Card et al., 2014).

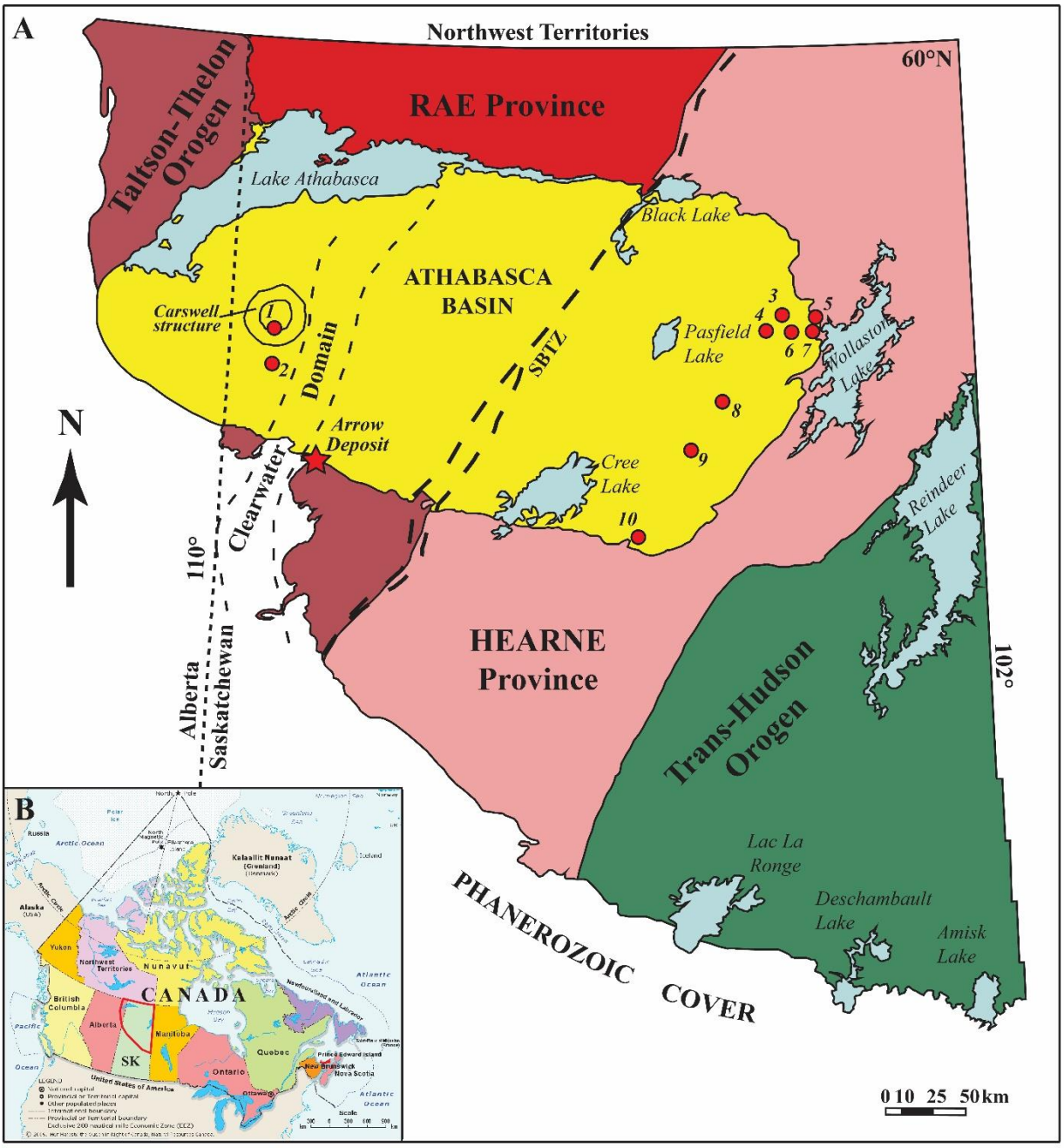

Fig. 1.1. A) Simplified map of northern Saskatchewan and Alberta illustrating the main constituents of the Precambrian Shield, the Taltson-Thelon and Trans-Hudson orogens, the Clearwater domain, the Snowbird Tectonic Zone (SBTZ), Carswell structure, and the location of the Arrow Deposit and other major unconformity-related uranium deposits in the Athabasca Basin: 1) Cluff Lake, 2) Shea Creek (Kianna), 3) Dawn Lake, 4) Midwest, 5) Collins Bay, 6) McClean Lake and Sue, 7) Rabbit Lake, 8) Cigar Lake, 9) McArthur River, 10) Key Lake (Modified from Sheahan et al., 2016). B) Map of Canada showing the location of Fig. 1.1A (red polygon) in Saskatchewan (SK) and Alberta (After Card et al., 2014).

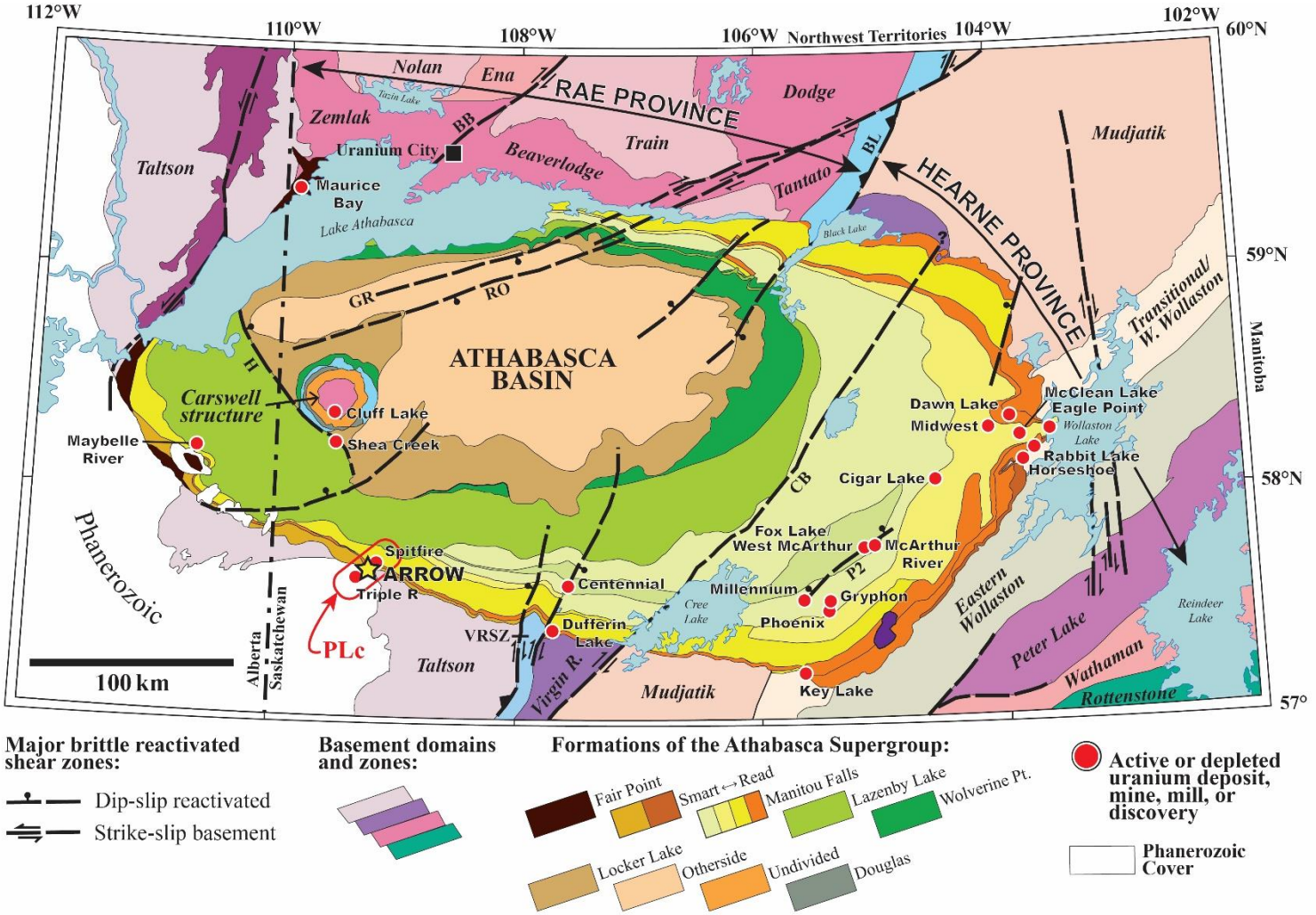

Fig. 1.2. Geologic setting of Athabasca Basin unconformity-related uranium deposits. The Arrow Deposit (yellow star) lies along the Patterson Lake corridor (PLc) in the SW Basin. Major uranium deposits, mines, or prospects are highlighted, as well as major brittle reactivated shear zones: BB = Black Bay, BL = Black Lake, CB = Cable Bay, GR = Grease River, H = Harrison, RO = Robillard, VRSZ = Virgin River shear zone. (Modified from Jefferson et al., 2007).

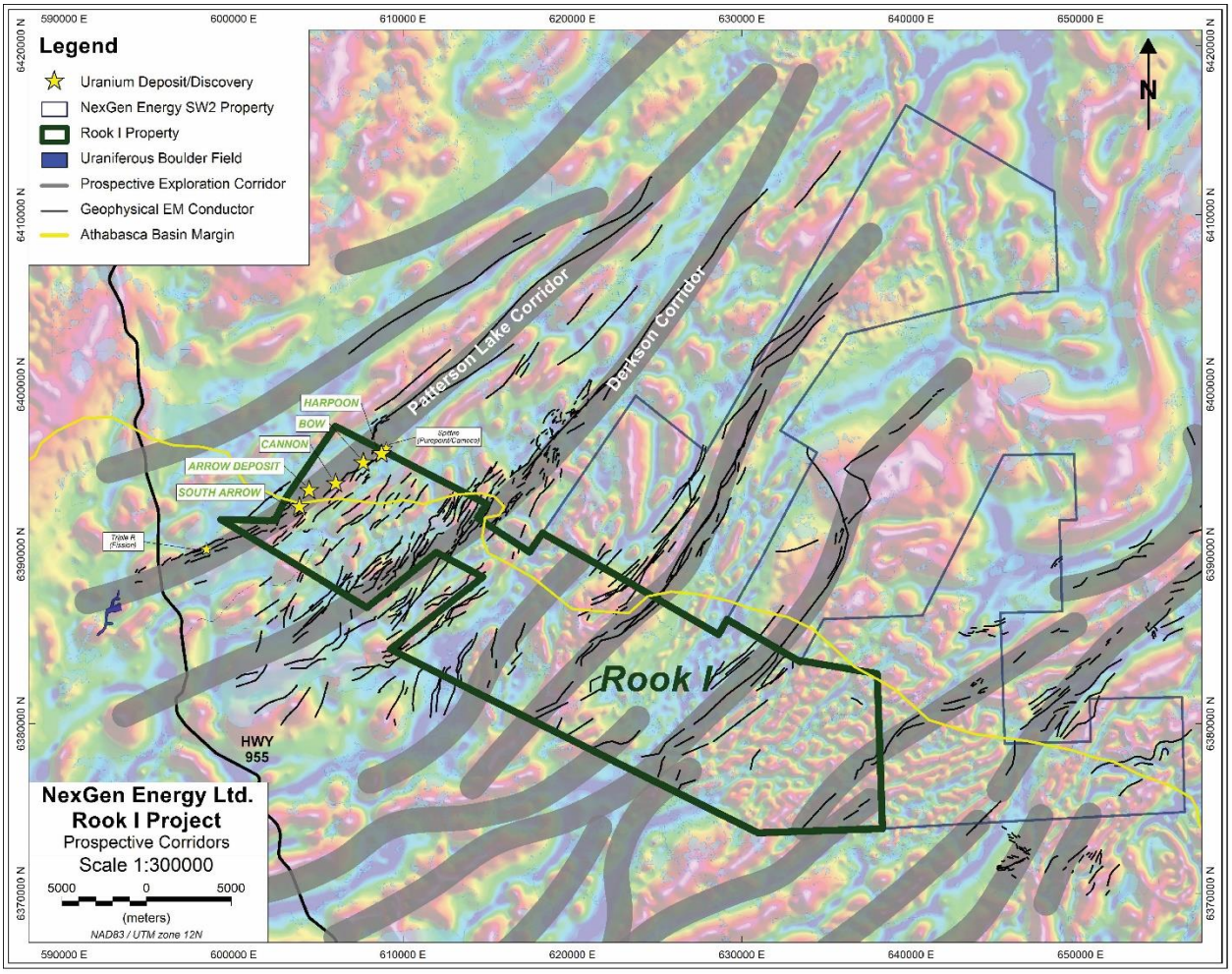

Fig. 1.3. Magnetic tilt geophysical map of NexGen Energy's Rook I property, highlighting local geophysical EM conductors and corresponding prospective corridors. The Arrow Deposit lies along the Patterson Lake corridor, northeast along strike from the South Arrow uranium discovery and the Triple R deposit, and southwest along strike from the Harpoon, Bow, Cannon, and Spitfire uranium discoveries.

1.2 Overview of the Genesis of Unconformity-Related Uranium Deposits in the Athabasca Basin

A vast literature on unconformity-related uranium deposits exists today, composed of numerous studies focused on paragenesis, geophysics, alteration mineralogy, stable isotope geochemistry, and less so structural analysis, in order to develop genetic models for these types of deposits. Unconformity-type uranium deposits derive their nomenclature from their spatial association with a nonconformity between Archean to Paleoproterozoic meta-igneous and/or metasedimentary basement rocks and overlying Paleoproterozoic to Mesoproterozoic sedimentary

rocks filling intracratonic basins such as the Athabasca Basin (Kyser and Cuney, 2008). Overall, three end-member styles of mineralization have been described, based on the host rock and proximity to the unconformity: 1) Sandstone-hosted mineralization perched above the unconformity such as at Cigar Lake, McClean Lake, and Maybelle River; 2) Mineralization right at the unconformity, hosted primarily in sandstones but also in the basement rocks, such as McArthur River, Midwest, and Key Lake; and 3) Basement-hosted fracture-controlled or vein mineralization below the unconformity, such as Arrow, Eagle Point, and Cluff Lake. Each of these models are characterized by different alteration patterns, metal contents, and mineralization signatures which have been related to the prevailing flow patterns of the mineralizing fluid. Jefferson et al. (2007) categorized sandstone/unconformity-hosted and basement-hosted uranium deposits into egress and ingress style, as described below.

The ingress model suggests that uraniferous oxidized basinal brines are introduced into the basement rocks through Athabasca Supergroup-cutting faults, where an oxidation-reduction reaction with the basement rock or a reduced fluid in the basement results in the precipitation of uranium minerals (Jefferson et al., 2007). In the egress model, reduced basement-sourced fluids are channelled upward along faults to the basin where they meet and reduce uraniferous oxidized basinal brines, inducing uranium mineral precipitation at or above the unconformity (Jefferson et al., 2007). As far as the reductant goes, graphite dissolution (Alexandre et al., 2005; Jefferson et al., 2007) or ferrous iron liberated from mafic or sulphide minerals in the basement (Quirt, 1989; Derome et al., 2003) are most commonly favored as the responsible sources for the reduction of the oxidized uraniferous fluids.

Other distinguishing features between the ingress and egress genetic models are alteration mineralogy and extent, and metal endowment of the ore (i.e. mono- vs. polymetallic). The discrete interaction between the in-fluxing mineralizing fluid and the faulted basement rocks in the ingress model results in a spatially confined alteration halo around the basement-hosted deposits, making them relatively inconspicuous compared to extensive egress-style alteration halos and geochemical signatures. The host rock alteration in ingress-style deposits is typified by chloritization (clinochlore) of mafic minerals, pervasive clay alteration (illitization or sericitization) of feldspars, sillimanite, cordierite, and subsequent chloritization (sudoite) of minerals including illite (Jefferson et al., 2007). The ore body in the basement-hosted ingress-style deposit model is

described in the literature as monometallic (simple), lacking the suite of base metals and others associated with sandstone-hosted egress-style deposits. Egress-style deposits are described as having widespread alteration halos, due to the much higher permeability and porosity of the overlying sedimentary rocks compared to the basement rock, thus allowing for relatively unchecked flow of the mineralizing fluid. Egress-style alteration halos are, in general, composed of pervasive illite and/or sudoite replacement of diagenetic dickite, quartz dissolution and/or silicification, local chlorite (clinochlore) proximal to the unconformity, and a hematite-illite-chloritic clay cap immediately surrounding the deposit (Jefferson et al., 2007). The ore bodies in the egress sandstone- or unconformity-hosted deposit model are described as polymetallic (complex), and may contain anomalous concentrations of Ni, Zn, Co, Pb, Mo, and Cu sulphides and arsenides, as well as Au or platinum group elements in addition to uranium (Jefferson et al., 2007).

Various stable isotope, mineralogical, and in situ microanalytical studies have been utilized in attempts to construct metallogenetic models and characterize the fluids associated with uranium mineralization and determine their source (e.g. Kotzer and Kyser, 1995; Fayek and Kyser, 1997; Quirt, 1999; Alexandre et al., 2009; Cloutier et al., 2009; Mercadier et al., 2011). The hypotheses resulting from this body of works has been a point of contention among researchers and industry workers for years. Interpretations of the data have resulted in different schools of thought regarding the number of fluid sources involved in the mineralization process, including those derived from the basin (i.e. ingress), the basement (i.e. egress), or a combination of both (i.e. bi-directional flow). Regardless of the source, a key factor in the formation of these deposits is the ability of an oxidized U^{6+}-bearing fluid to be reduced and thus precipitate the insoluble U^{4+} as uranium minerals. In general, researchers have recognized that unconformity-type uranium deposits appear to be associated with up to three fluid signatures: 1) $CaCl_2$-rich brine; 2) NaCl-rich brine; and 3) low-salinity NaCl-dominant fluid (Kotzer and Kyser, 1995; Derome et al., 2003; 2005; Mercadier et al., 2010; 2011).

Furthermore, detailed petrographic and geochemical work has been completed on mineralization-associated clay mineral species in order to obtain information on alteration mineral paragenesis, and to utilize clay minerals as a proxy for uranium exploration. Such studies have indicated that illite and chlorite have an intimate association to mineralization events (e.g. Quirt,

1986), while dickite and kaolinite are interpreted to be associated with basin diagenesis and late alteration in the basement rocks. Clay crystallinity and geothermometric studies have indicated syn-ore clay mineral crystallization temperatures in the range of 140°C to 230°C (e.g. Kotzer and Kyser, 1995; Quirt, 1999; Alexandre et al., 2009). Analyses of fluid inclusions corroborates these formation temperatures, suggesting a minimal basin thickness of approximately five kilometers at the time of uranium mineralization (e.g. Derome et al., 2003; 2005). However, a more recent interpretation by Chi et al. (2018), based on stratigraphic and fluid inclusions, suggests that the thickness of the sediments above the unconformity were significantly less.

Copious geochronological studies have been completed and described both the relative and absolute timing of ore-forming events at numerous unconformity-related deposits including, but not limited to, Cigar Lake (e.g. Fayek et al., 2002a), McArthur River (e.g. Alexandre et al., 2007), Rabbit Lake and Dawn Lake (e.g. Alexandre et al., 2005), Eagle Point (Cloutier et al., 2011), and Shea Creek (Sheahan et al., 2016). A variety of isotopic systems have been employed to draw a connection between the relative timing determined by paragenetic studies and absolute ages of ore-forming and fluid flow events. The proposed absolute ages of unconformity-related uranium deposits in the Basin show a wide range in ages from approximately 700 to 1,600 Ma (e.g. Fayek et al., 2002a; Alexandre and Kyser, 2005), and have dominantly been obtained through U-Pb of uraninite and Ar^{40}/Ar^{39} or K-Ar of phyllosilicate alteration minerals associated with mineralization (e.g. Alexandre and Kyser, 2003). Recent studies of unconformity-related uranium deposits in Saskatchewan, such as the Cigar Lake deposit, have demonstrated the value of using a combination of SIMS techniques in conjunction with electron microprobe analyses to study the chronology of complex uranium-rich minerals (e.g. Fayek et al. 2000a; 2002a). These and other studies demonstrate that the U–Pb isotope systematics of uranium-rich and alteration minerals in many Athabasca Basin uranium deposits have been affected by paleo-fluid-flow events that were likely brought on by regional and global-scale tectonic events (Kotzer and Kyser, 1995; Kyser, 2000; Kyser et al., 2000).

Despite the disparity and issues with various aspects of the genesis of unconformity-related uranium deposits, it is generally agreed upon by researchers and industry geologists that these types of deposits are first and foremost structurally controlled. The majority of uranium deposits in the eastern Athabasca Basin are situated along a massive structural trend marking the transition

zone between the Mudjatik and Wollaston domains (Fig. 1.2; Jefferson et al., 2007). Although fewer in number than geochemical or geochronological studies, structural studies of Athabasca Basin uranium deposits have shown that nearly all of them are directly associated with graphitic brittle-ductile or brittle-reactivated shear zones and faults, regardless of genetic model or proximity to the unconformity (e.g. Cloutier et al., 2011, Dieng et al., 2013). These studies are valuable, as they commonly integrate the structural geology with paragenetic, geochemical, and geochronological data. However, in some cases the structural details are overlooked, and only a broad structural context is provided through general characterization of the faults or shear zones as dextral or sinistral, reverse or normal, etc. Sufficient detailing of the structural component of these deposits through structural analysis should be undertaken, as the structure is a strong common denominator in the genesis all of these deposits, regardless of location within the Basin. As with other areas of the Basin, no structural studies have been completed on the Patterson Lake corridor to date, and so this is the first.

The consensus among academic and industry workers alike is that at least one brittle-reactivated or reused shear/fault zone, one or more uraniferous brines/waters, and a source of reduction of that/those fluid(s) are all required for the formation of an unconformity-related uranium deposit. Establishing the timing relationships between fault zone activity, uranium mineralization/remobilization, and regional thermo-tectonic and perturbation events is a critical step in understanding uranium deposits such as Arrow, which are hosted within the highly deformed and metamorphosed Paleoproterozoic terranes that make up the basement rocks to the southwestern Athabasca Basin. The southwestern Athabasca Basin has been the focus of intense exploration activity in the last few years; however, the characteristics and setting of uranium mineralization in the area are only beginning to be understood.

The key goal of this study is to integrate multiple geoscience disciplines to create a cohesive and comprehensive geological analysis of the Arrow deposit. By marrying structural geology, mineralogy, geochemistry, and geochronology, a compelling story about the formation and evolution of the Arrow Deposit and the Patterson Lake corridor has manifested. The present research and other studies that have recently begun (e.g. Card, 2017) provide further implications for uranium exploration vectoring in the southwestern Athabasca Basin. The key component of this study is to objectively describe and characterize the effects and control deep-seated structures,

metasomatism, and hydrothermal alteration appear to have on these types of deposits, building on what is understood about uranium deposits in other parts of the Basin. This study is the first and only comprehensive analysis of the structural and hydrothermal-metasomatic history and paragenetic relationships of the largest known uranium deposit along the Patterson Lake corridor. The current study is also the first attempt to relate absolute ages of uranium mineralization to paragenesis and structural evolution in this area. This will help to constrain the evolution of the Arrow Deposit and provide implications for other uranium occurrences along the Patterson Lake corridor. Overall, this study will yield constraints on the origin of basement-hosted unconformity-related uranium deposits across the Athabasca Basin.

The thesis is presently being prepared for submission as two papers to refereed international journals; the first will focus on the structural analysis and paragenesis of the Arrow Deposit. In addition, this and related research has been presented at numerous conferences, and the references for the abstracts and/or posters for these conferences are in listed in Appendix C and D.

CHAPTER 2

GEOLOGICAL SETTING

2.1 Regional Geology

The Rook I property is situated in the Western Churchill Structural Province of the Canadian Shield (Fig. 2.1A and B), which is divided into the Rae province to the west and the Hearne province to the east, separated by the Snowbird Tectonic Zone (SBTZ). Historically, the basement rocks south of the Athabasca Basin and west of the Virgin River shear zone (VRSZ), where the Rook I property lies, have been termed the Western Granulite Domain (Lewry and Sibbald, 1977) and the Lloyd Domain (e.g. Card, 2009) and considered to be Archean in age. However, recent mapping, geochronology, and geophysical analysis in the Lloyd Domain (e.g. Card et al., 2012; 2014) suggest that the rocks, and their metamorphic and structural history, are correlative with the 2,460 to 1,985 million years (Ma) old rocks present within the Paleoproterozoic Taltson Magmatic Zone in Alberta, and that these rocks extend below the southwest Athabasca Basin (Fig. 2.1A and B). This package of Taltson-aged rocks and plutons terminate against the MacDonald Fault along the eastern shore of Great Slave Lake in the Northwest Territories (Fig. 2.1B) and re-emerge south of the SW Athabasca Basin, extending to the east where they are truncated by the VRSZ (Fig. 2.1A; Hoffman 1988; Ashton et al., 2009; Card et al., 2014).

The VRSZ is a NE-SW trending segment of the SBTZ south of the Athabasca Basin, and divides the rocks of the Taltson and Virgin River Domains through a 5 to 7 km-wide zone of mylonitic rocks at Careen Lake (Card, 2002) and a 5 to 7 km-wide zone of heterogeneous mylonitization to the northeast (Card and Bosman, 2007). Rocks of the Taltson Domain lie within the hanging wall of the VRSZ and are dominated by NNE- to ENE-striking, sub-vertical oriented granulite-facies (M_1) intermediate orthogneisses, namely a ‘quartz dioritic suite’ (Card, 2009). Lewry and Sibbald (1977) originally described the Domain as being composed of orthogneisses of dominantly granodioritic composition, while Scott (1985) later described the same rocks as ‘felsic granulites’. Scott (1985) also interpreted narrow bands of granulite-facies supracrustal rocks termed the Careen Lake Group to both overlie and be intruded by (Card, 2002) rocks of the felsic granulite unit. The assortment of intermediate intrusive rocks termed the ‘quartz diorite suite’ is

considered to be the equivalent of the felsic granulite unit (Card and Bosman, 2007). A sample of the Taltson Domain quartz diorite from Lloyd Lake, southeast of the Rook I property, was dated by Card et al. (2014) using U-Pb SHRIMP analysis on zircon and yielded an interpreted crystallization age of 2,459 ± 14 Ma, with a Concordia age of 1,899 ± 26 Ma, interpreted as a metamorphic overprint coincident with M_2 amphibolite-facies metamorphism.

Historically, Taltson Domain rocks have been interpreted to be intercalated with gneissic charnockitic granites and Paleoproterozoic-aged metasedimentary psammitic gneiss and pelitic diatexite of the Careen Lake Group (Card, 2009; Fig. 2.2). However more recent studies (e.g. Card et al., 2018) suggest that many of these metasedimentary rocks described in outcrop are of metasomatic origin, and that true metasedimentary rocks may only comprise a few percent of the Taltson Domain. Late intrusive leucogranite to granite, pegmatitic granite, and quartz diorite units have been observed cutting the all aforementioned units in outcrop at both Lloyd and Fournier Lake (Card, 2009). The Taltson Domain also hosts a younger, 2,110 Ma ± 16 Ma, NE-elongated gabbro-anorthosite intrusion termed the Clearwater anorthosite complex, covering approximately 375 km^2 (Fig. 2.1; Hulbert, 1988; Crocker et al., 1993; Card et al., 2014). The Taltson orthogneisses were also intruded by younger Hudson granites (Peterson et al., 2002) between ca. 1.85 to 1.82 Ga (Bickford et al., 1994; Stern et al., 2003).

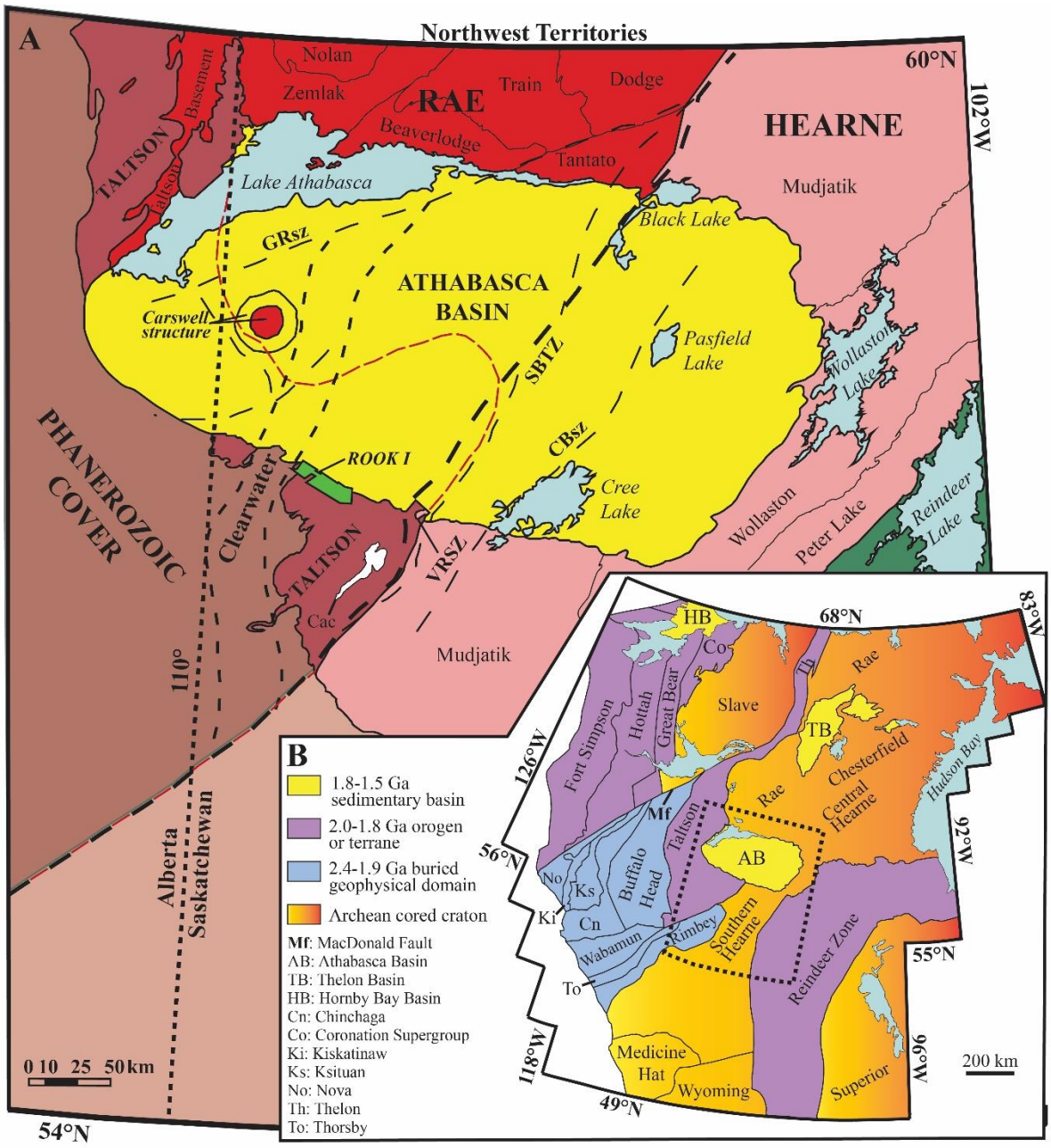

Fig. 2.1. A) Lithostructural domains of northern Saskatchewan and Alberta illustrating major components of the Churchill Structrural Province of the Precambrian Shield (Taltson, Rae, Hearne, Reindeer Zone) and overlying Phanerozoic cover. Note the location of the Rook I property and Clearwater anorthosite complex (Cac) within the Taltson Domain, and with respect to the Clearwater Domain, the Snowbird Tectonic Zone (SBTZ), the Virgin River Shear Zone (VRSZ), the Grease River Shear Zone (GRsz), and the Cable Bay Shear Zone (CBsz). Lithotectonic boundaries are extrapolated beneath the Basin and Phanerozoic cover (red dashed lines) and the Clearwater Domain is generalized and projected to surface. B) Cratonic map of western Laurentia showing Saskatchewan (dashed box) in context of continent-scale tectonics (Modified from Card et al., 2014).

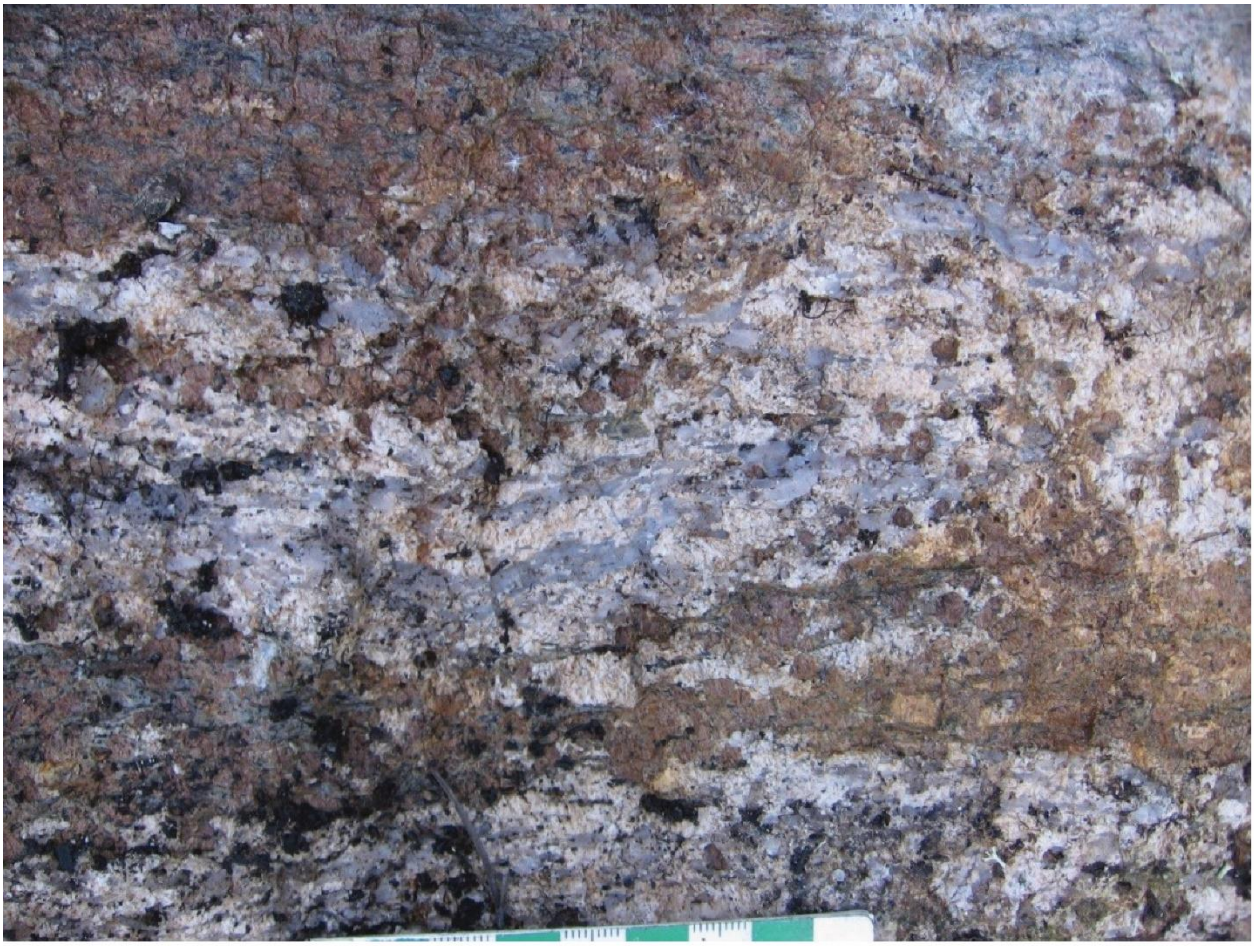

Fig. 2.2. Outcrop at Lloyd Lake within the Taltson Domain, previously mapped by Card (2009) as Careen Lake Group pelitic diatexite, however the metasedimentary origin of this rock type is now being called into question through re-examination of field photographs and drill core examination (e.g. Card and Noll, 2016; Card et al., 2017).

The Clearwater Domain lies immediately west of the Rook I property (Fig. 2.1A), identifiable as a massive NNE trending aeromagnetic high feature that truncates the western boundary and overprints magnetic trends of the Taltson Domain in Saskatchewan. The Clearwater magnetic high is underlain by multi-phase Clearwater granites, which contain large xenoliths of older granitic gneiss (Card, 2002). The Clearwater Domain is interpreted as a structurally bound zone of weakly deformed K-feldspar-rich porphyritic granite and granitoid gneiss (Fig. 2.3), based on studies of exposures in the Clearwater River gorge and limited drill core (Sibbald, 1974; Card, 2002; Jefferson et al., 2007). Card (2002) has suggested that the mingling between the different phases of the granite and between the granite and xenoliths led to the crystallization of significant magnetite, thus resulting in the anomalously high magnetic signature. Geochronology work done

on the Clearwater Domain by Stern et al. (2003) has provided a U-Pb zircon crystallization age for the porphyritic granites of 1,843 Ma, indicating they are contemporaneous with the intrusion of Hudson granites ca. 1.85 to 1.82 Ga into the orthogneisses of the Taltson Domain (Bickford et al., 1994; Stern et al., 2003). However, the gneissic granitoid rocks of the Clearwater yielded an imprecise U-Pb zircon age of ca. 2,529 Ma (Stern et al., 2003). The felsic intrusive rocks of the Clearwater Domain have shown anomalous uranium concentrations in drill core and thus may represent a possible source of uranium for the deposits in the area, analogous to uraniferous granitic/pegmatitic rocks in the eastern Basin being a plausible proto-ore source (e.g. Jeanneret et al., 2017 and references therein).

Fig. 2.3. Drill core photo of K-feldspar-rich, gneissic granitoid rock from the Clearwater Domain (From Card et al. 2018).

As aforementioned, the basement rocks under the southwestern Athabasca Basin were subjected to a protracted metamorphic and deformational history, involving multiple thermotectonic events. Taltson Domain rocks underwent a high-grade metamorphic event of undefined age (M_0) prior to the emplacement of the Clearwater anorthosite complex ca. 2,110 Ma (Card et al., 2014). Subsequently, a high-temperature metamorphic event (M_1) Paleoproterozoic in age, ca. 1.94 to 1.93 Ga (Stern et al., 2003; Card et al., 2018), reached upper amphibolite- to granulite-facies conditions in most parts of the Taltson Domain in Saskatchewan contemporaneous

with the Taltson-Thelon orogeny and was accompanied by rarely observed intrafolial, isoclinal F_2 folding and formation of a regional S_1 gneissosity (Fig. 2.4; Card et al., 2007; 2014). Characterizing the bulk of the domain is a gently northeast-dipping S_1 foliation (Card et al., 2008; 2014), with a composite gneissic S_1-S_2 foliation defined by preferred orientation of pyroxene, biotite, and hornblende, supporting that it was imparted during M_1 metamorphism under granulite-facies. This transposition foliation represents the dominant regional gneissosity of the Taltson Domain (Fig. 2.4). The presence of a garnet-clinopyroxene assemblage and a lack of hornblende in the least-altered rocks suggest that these anhydrous granulites would have formed at temperatures above 850°C and at pressures below approximately 5-7 kbar (Card et al., 2014). The composite S_1-S_2 foliation has been subsequently folded and transposed into NE to ENE-striking F_3 folds (Fig. 2.4), which have also deformed primary igneous layering within the Clearwater anorthosite complex (Card, 2009). The refolding of F_2 folds by F_3 folds resulted in an early Type 2 fold interference pattern (Fig. 2.4), which is overprinted by a Type 1 fold interference pattern created by refolding of F_3 by northwest-striking F_4 cross folds with axial surfaces near orthogonal to those of F_3 (Section 4.1; Card et al., 2008). Transposition with the F_3-axial planar foliation results in a steeply dipping transposition foliation, which is intensified proximal to, and within high strain corridors such as the VRSZ. D_3 deformation was generally weak in the central Taltson Domain but, where more intense within high strain zones, it is accompanied by a significant amphibolite-facies metamorphic (M_2) overprint (Card, 2009). The second-phase of metamorphism (M_2) is interpreted to be synchronous with D_3 deformation during Snowbird related deformation, ca. 1.92 to 1.90 Ga (Stern et al., 2003; Card et al., 2014), resulting in amphibolite-facies retrogression indicated by replacement of granulite-facies assemblages in the country rocks (i.e. orthopyroxene by biotite and magnetite in the quartz diorite suite (Card, 2009), and amphibole after pyroxene (Card et al., 2014)). Furthermore, a lack of partial melt component (Card et al., 2014) corroborates that M_2 metamorphism occurred under amphibolite-facies conditions below 650-700°C (e.g. Bucher and Frey, 1994). A third major thermotectonic event records mid-greenschist facies metamorphism (M_3) coincident with the Trans-Hudson orogeny.

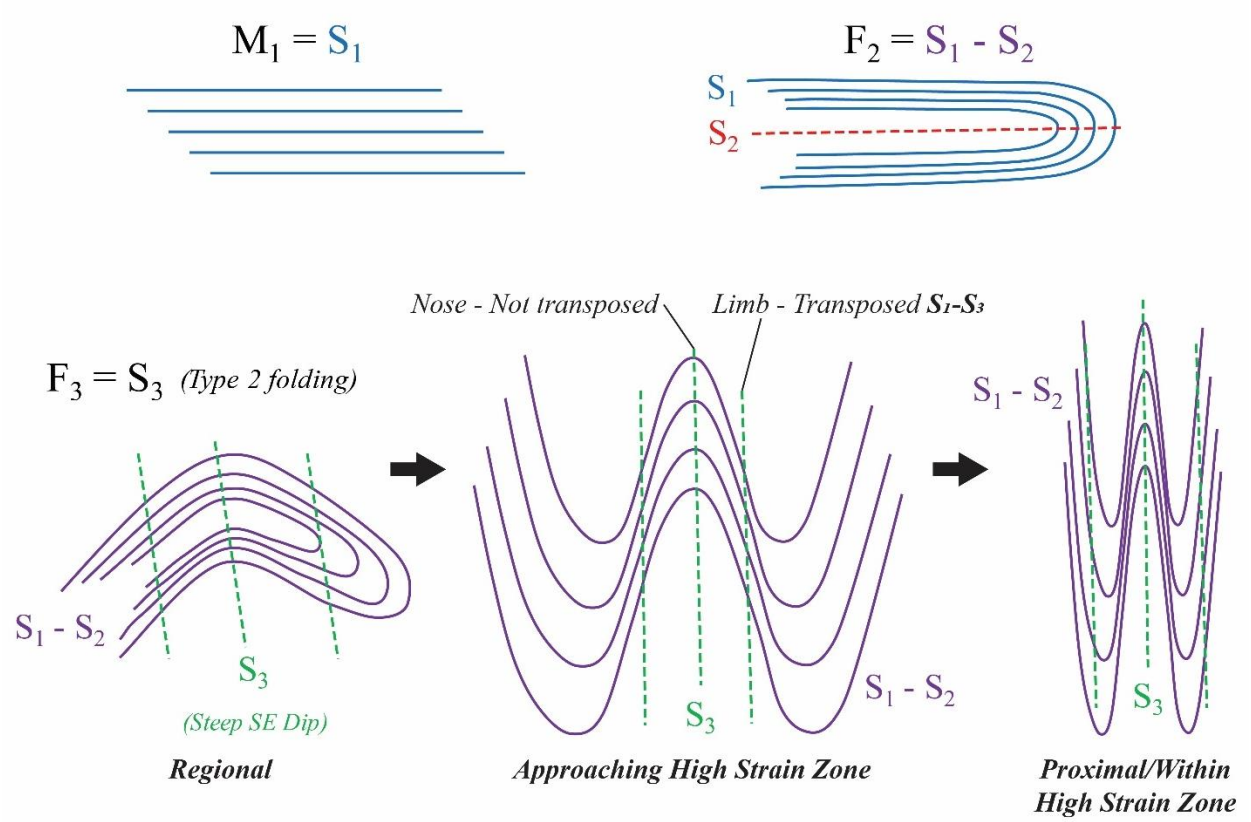

Fig. 2.4. Schematic diagram illustrating the development of S_1 through S_3 foliation generations and transposition foliations in the Taltson Domain. Nomenclature after Card et al., 2008.

The VRSZ contains outcrop evidence for multiple displacement episodes under ductile, brittle-ductile, and brittle conditions. Brittle reactivation of the VRSZ along the Dufferin Lake Fault is interpreted to have played a role in the formation of uranium deposits at the base of the Athabasca Basin along this trend (Card et al., 2007; Reid et al., 2014). West from the Virgin River shear zone, lineaments trending in a number of orientations, including northeast, northwest, and west, likely represent late, brittle-ductile and brittle fault zones with unknown displacements (Card et al., 2014). Brittle-ductile to brittle shear zones and faults are abundant across the Saskatchewan Shield rocks, and most commonly develop along the limbs of tight folds where pure shear is most pervasive during shortening and in shear zones. Shear zone development linked to F_3 folding is widespread in the Cable Bay straight belt, and analogous structures are common in the Lloyd fold domain (Section 4.1; Card, 2009). Many of these are related to reactivation of major shear zones in the region during the long-lived metamorphic and deformation history spanning from the Taltson-Thelon to Hudsonian orogenic events ca. 1.94 to <1.84 Ga (Hoffman, 1988; Card et al.,

2014). Exhumation of these granulite facies rocks thus occurred over a period of at least 140 million years. A recent study along the Wollaston-Mudjatik transition zone in the eastern Basin by Jeanneret et al. (2017) suggests that trans-Hudsonian pegmatites are the main proto-ore of the Athabasca unconformity-related uranium deposits. Their geochronological work suggests that uranium-enriched batches of melt produced through a ca. 1,840 to 1,813 Ma M_1-D_1 tectono-metamorphic event were transferred to upper crustal levels via these deep-seated, crustal-scale shear zones, and eventually differentiated to form uranium-rich pegmatites between 1,813 and 1,770 Ma (Jeanneret et al., 2017). Furthermore, monazite and zircon grains they collected from retrogressed migmatites recorded a younger event at ca. 1,720 Ma, which they interpret as the terminal cooling event down to approximately 300-400°C responsible for partial retrogression of the metamorphic assemblages. These new geochronological constraints provide implications for the timing of the onset of Athabasca sedimentation, such that the maximum age of the Athabasca Supergroup rocks should be 1,710 Ma old or younger (Jeanneret et al., 2017).

The present-day Athabasca Basin ("the Basin") is an erosional remnant, which covers most of northern Saskatchewan and extends into northern Alberta, of a large Paleoproterozoic-Mesoproterozoic sedimentary basin, (Fig. 1.2 and 2.1; Ramaekers et al., 2007). The present-day Basin measures approximately 425 km east-west by 225 km north-south, and at the centre, the Athabasca Supergroup sandstones have a maximum depth of approximately 1,500 m thick (Ramaekers, 1979d; Ramaekers, 1980; Tremblay, 1982). The Basin consists of a series of unmetamorphosed siliciclastic sedimentary rocks, predominantly sandstone, of the Athabasca Supergroup (Fig. 2.5; Bosman and Ramaekers, 2015). They were deposited during the period of ca. 1,710 to 1,500 Ma (Ramaekers et al., 2007; Jeanneret et al., 2017). Below the Athabasca basal unconformity within the crystalline basement rocks, the rocks exhibit a bleached zone (white zone), red hematite-stained zone (red zone), mixed hematite- and chlorite-altered zone (red-green zone), and a chlorite zone (green zone) where mafic and feldspathic minerals have been altered to chlorite. This has been interpreted to represent a paleoregolith and/or paleoweathering profile that has been overprinted by diagenetic and/or hydrothermal fluids (McDonald, 1980; Adlakha et al., 2014). Any combination of these repeating alteration zones may be present below the Athabasca sandstones.

The southwest portion of the Athabasca Supergroup is overlain by flat lying Phanerozoic stratigraphy of the Western Canada Sedimentary Basin, including carbonate-rich rocks of the Lower to Middle Devonian Elk Point Group, Lower Cretaceous Manville Group sandstones and mudstones, moderately lithified diamictites, and Quaternary unconsolidated sediments (Fig. 2.5; Bosman, 2017). South of the Basin where Athabasca sandstone cover becomes thin, paleo-valley fill and debris flow sandstones of the Devonian La Loche/Contact Rapids formation (Alberta) or Meadow Lake (Saskatchewan) formation unconformably overlie the basement rocks. The Devonian rocks exhibit variability in their composition and texture, consisting of older Athabasca sandstone and basement clasts hosted within either a finer green clay-sand matrix or a coarser pebbly brown matrix. The Cretaceous Manville Group is divided, from lower to upper, into the McMurray, Clearwater, and Grand Rapids formations (Alberta) or the Cantaur and Pense formations (Saskatchewan), composed of green-grey to black, very fine- to medium-grained sandstones interbedded with fissile mudstones, and fine- to coarse-grained, cross-bedded beige sandstone with minimal mudstone (Bosman, 2017; Bosman et al., 2018). Pleistocene glacial tills blanket the entire northern Saskatchewan region, with local exposed minor outcrops. Extensive moraines, drumlin fields, outwash plains, and large sinuous eskers characterize the present-day topography. The glacial tills are derived from both crystalline basement rocks as well as relatively soft Athabasca sandstones. In general, the thickness of the glacial tills increases towards the southwest (Campbell, 2007).

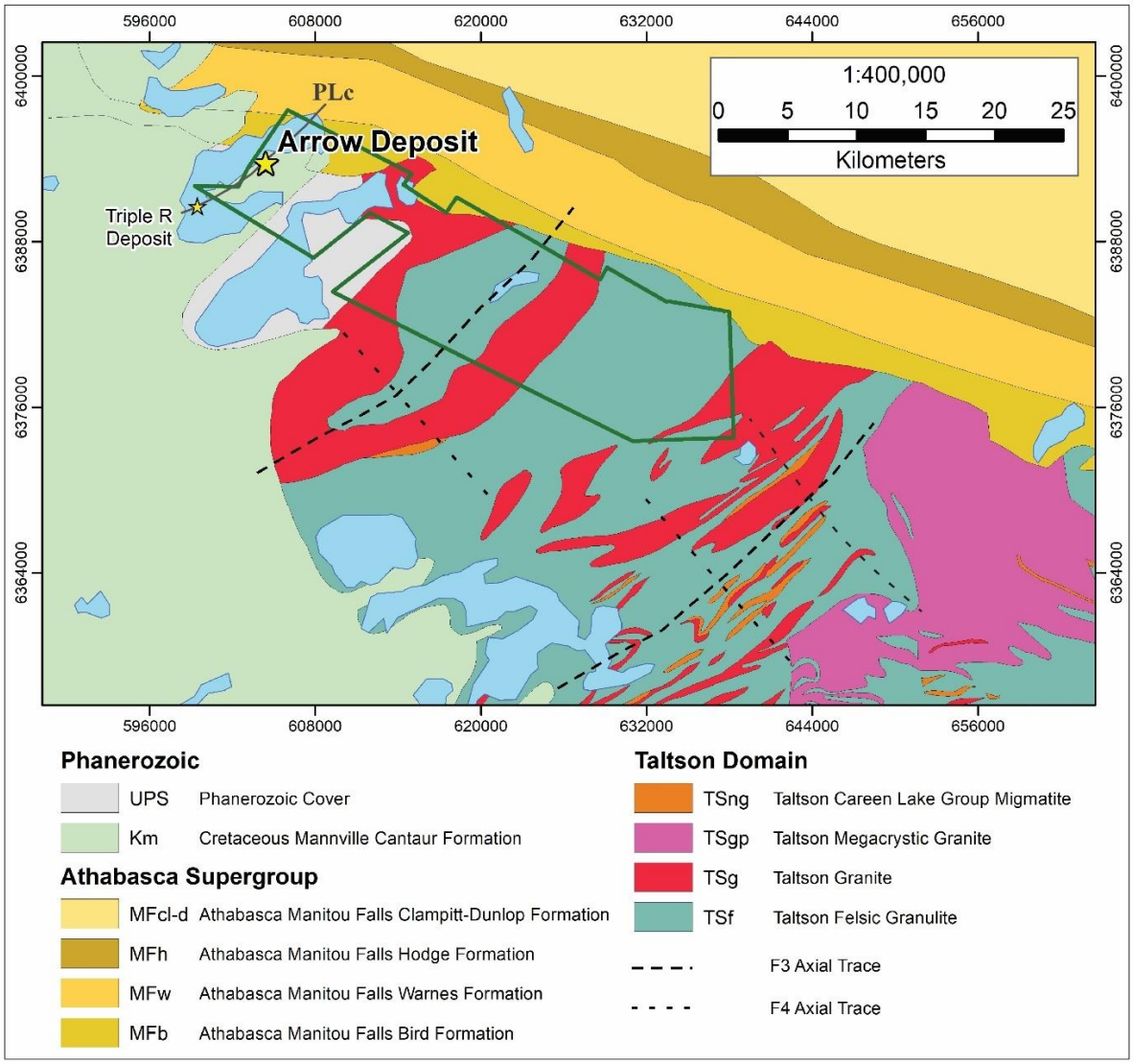

Fig. 2.5. Geological map showing Taltson Domain basement geology and generalized fold axial traces, as well as the overlying Athabasca Supergroup and Phanerozoic sedimentary geology of the southwestern Athabasca Basin region. The Rook I Property Area is outlined in dark green, showing the location of the Arrow Deposit, north along strike of the Patterson Lake corridor (PLc) from the Triple R uranium deposit. Bedrock geology 250k and sedimentary geology layers obtained from Saskatchewan GeoAtlas (2018-10-18).

2.2 Patterson Lake Corridor and Arrow Deposit Geology

The Arrow Deposit is hosted within Paleoproterozoic basement rocks of the Taltson Domain, characteristic of other portions of the southwest Rae Province in Saskatchewan (e.g. Card, 2017). The crystalline basement rocks, in which the Patterson Lake corridor is rooted, comprises a spectrum of variably altered mafic to ultramafic, intermediate, and local alkaline rock types. Fresh examples of any of these rock types are extremely rare, as they are overprinted by protracted deformation and metasomatism. The most abundant basement lithologies consist of gneissic, metasomatized feldspar-rich granitoid rocks and dioritic (Fig. 2.6A) to quartz dioritic (Fig. 2.6B) and quartz monzodioritic gneiss (Fig. 2.6C and D), with lesser granodioritic (Fig. 2.6E) and tonalitic gneiss (Card et al., 2018). Minor rock types encountered along the Patterson Lake corridor include weakly foliated or schistose ultrabasic rocks (Fig. 2.7A), mafic-rich gabbro (Fig. 2.7B) and amphibolite, porphyroblastic feldspar-rich syenite (Fig. 2.7C), migmatite, and relatively young mafic and alkaline dyke rocks including alkaline clinopyroxenite (Fig. 2.7E). Distinct white-blue to purple colored quartz is ubiquitous throughout all metamorphic rock types in the Patterson Lake corridor. The intermediate orthogneisses appear to be most affected, exhibiting pervasive silicification resulting in zones of rock with up to 80% modal abundance quartz. Although there is evidence for multiple phases of silicification along the Patterson Lake corridor, the earliest and most widespread event is syn- to post-peak metamorphism pervasive white to blue quartz flooding. In many cases the remnant gneissic foliation is still recognizable and is defined by pitted, argillized feldspar grains. Some ductile deformational events post-date the silicification, as the quartz-flooded rocks are locally sheared and silicification textures are often transposed to foliations. The nature and origin of the pervasive blue quartz within the Patterson Lake corridor is discussed in detail in Section 5.1.

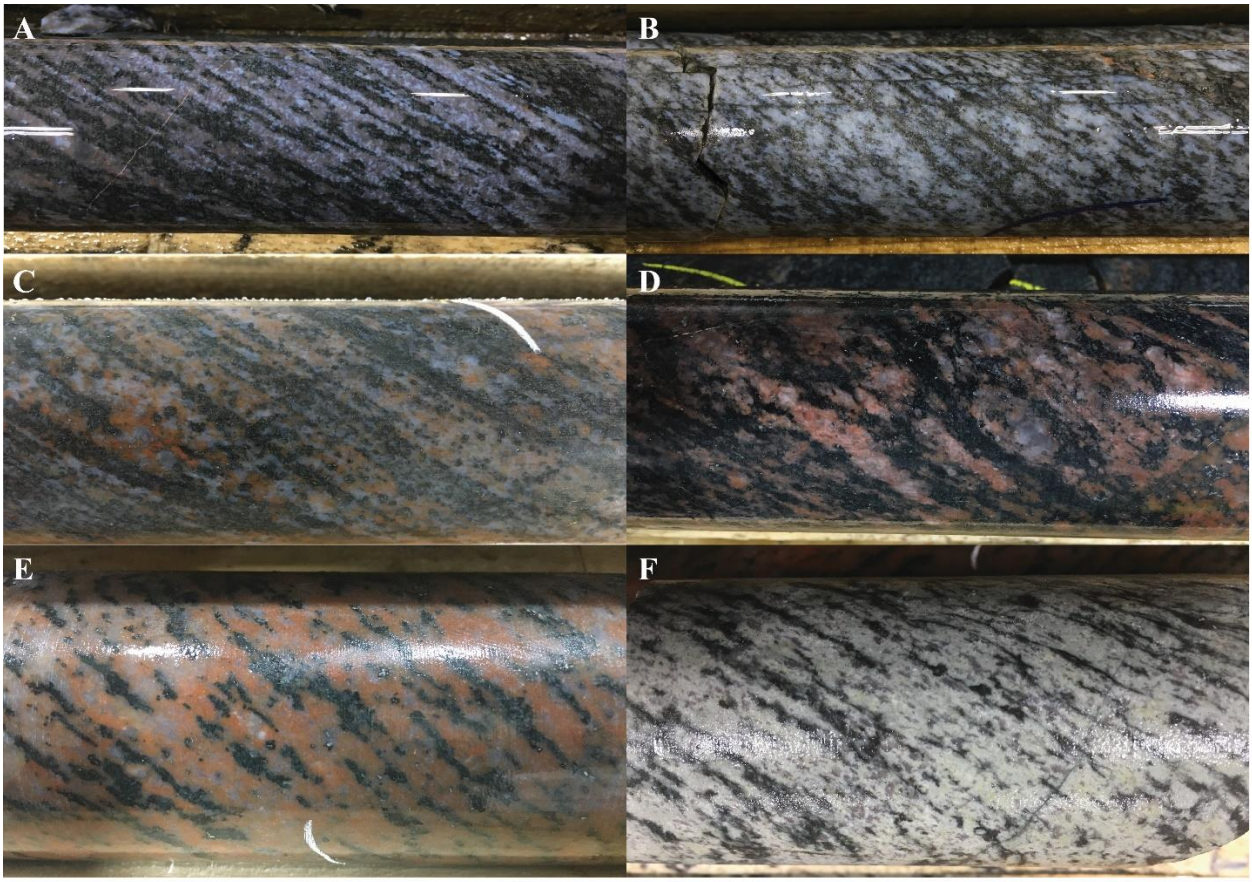

Fig. 2.6. A) Dioritic gneiss exhibiting trace to weak chloritization (AR-18-215c1, 637.7 m). B) Quartz dioritic gneiss with weak chloritization (AR-18-215c1, 629.2 m). C) Quartz monzodioritic gneiss with trace chloritization of pyroxene (AR-18-214c1, 463.5 m). D) Relatively unaltered quartz monzonitic gneiss (AR-18-215c1, 647.0 m). E) Granodioritic to monzo-granitic gneiss exhibiting weak chloritization (AR-18-216c1, 198.2 m). F) Albitized and weakly clay-altered granodioritic to monzo-granitic gneiss, proximal to Fig. 10E (AR-18-216c1, 199.8 m).

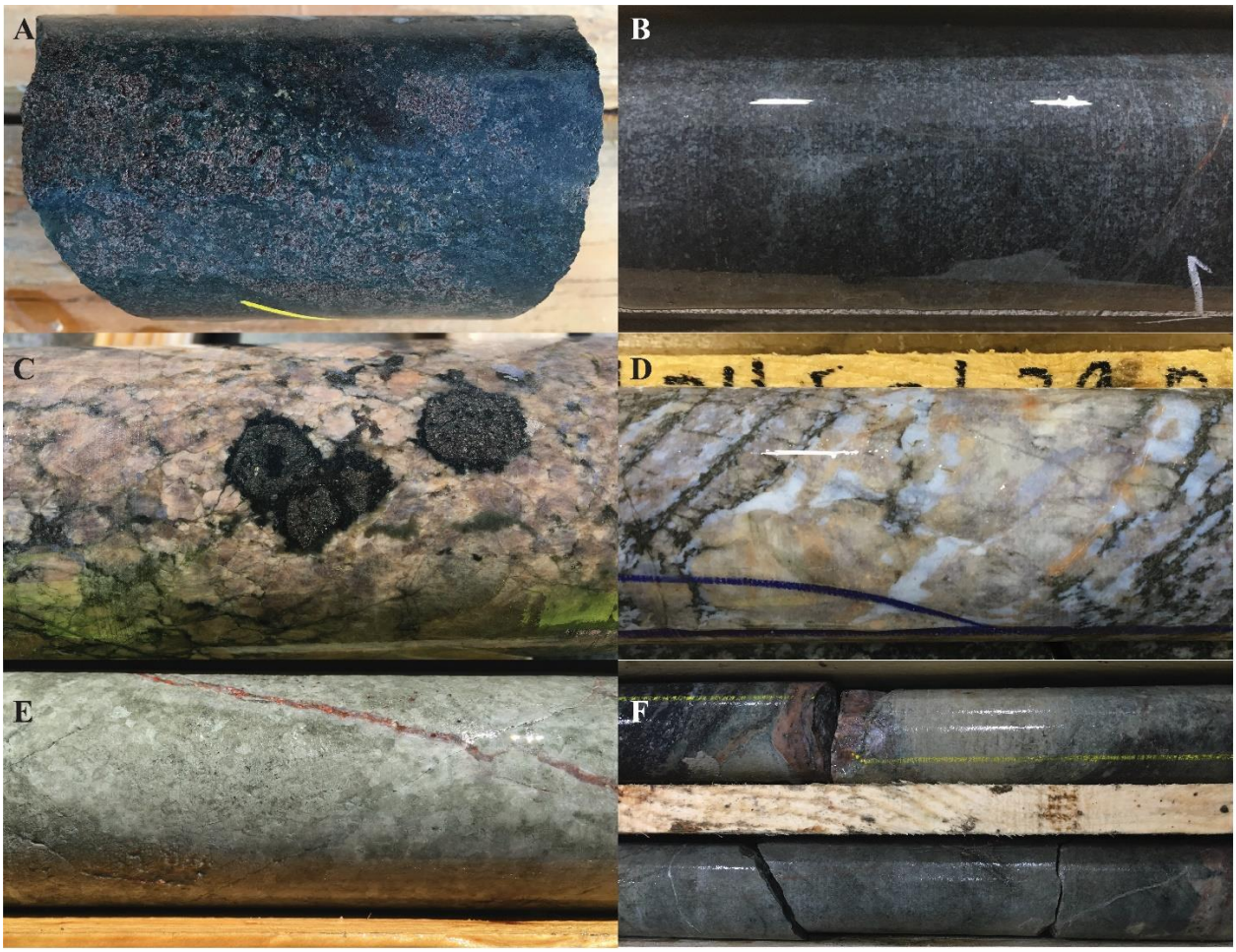

Fig. 2.7. A) Moderately chloritized, garnetiferous ultrabasic rock with weak schistosity (AR-18-210c3, 515.2 m). B) Trace to weakly chloritized, massive, fine- to medium-grained gabbro (AR-18-216c1, 174.2 m). C) Coarse-grained syenitic rock with biotite masses replacing perthitic K-feldspar. Subhedral to euhedral garnet porphyroblasts are overgrowing secondary biotite masses (HP-16-018, depth not recorded). D) Very coarse-grained syenitic dyke rock with secondary blue quartz, partially transposed to gneissosity of host rock (AR-18-215c1, 634.7 m). E) Massive, medium-grained green-white clinopyroxenite associated with hematite veinlets related to fenitic alteration (HP-16-020, 245.5 m). F) Pastel green-beige fenitic alteration of wall rock proximal to alkaline intrusive rock (AR-18-215c1, 132.3 m).

Alkaline intrusive rocks have been identified in drill core along the Patterson Lake corridor to the northeast of the Arrow Deposit, including calcite-rich, xenolith-bearing carbonatite-like rocks (Card, 2017), and medium- to coarse-grained, white-green clinopyroxenite (diopsidite; Card et al., 2018; Fig. 2.7E). Most of these rocks postdate regional metamorphism and are typically associated with alkalic metasomatism of wall rocks, resulting in haloes of fenitic alteration (Fig. 2.7F). The contact aureole-like nature of the fenitic alteration and spatial association of the dyke rocks with discrete high-strain zones indicates a clear link to these structures, suggesting that the

alkaline magma flowed along these conduits reusing them as the path of least resistance. The alkaline clinopyroxenite rocks observed to date in Rook I drill core are white-green in color and dominated by relatively coarse-grained crystalline clinopyroxene exhibiting well-developed planar striations and cleavage in hand specimen (Fig. 2.7E). Pastel green-beige and red-orange fenitic alteration aureoles are associated with the carbonatite (Card, 2017) and clinopyroxenite dyke rocks, resulting from in-situ metasomatic carbonation and/or sodium and potassium (alkali) metasomatism of the host rock by magmatic volatiles during the alkaline intrusive event (e.g. Currie et al., 1971; Kresten, 1988; Azer et al., 2008; Fig. 2.7F). Fenitization in granitoid rocks is characterized initially by hematite veinlets (Fig. 2.7E) and increased ordering of K-feldspar towards maximum microcline followed by conversion of plagioclase to albite plus calcite (Currie and Ferguson, 1971).

In the vicinity of the Arrow Deposit (Fig. 2.8), the dominant basement lithologies encountered are variably silicified porphyroblastic quartz-feldspar-garnet-biotite (+/- graphite) gneiss (Fig. 2.9 and 2.10) and intermediate orthogneisses (Fig. 2.6A through F) consisting of quartz monzodioritic to quartz dioritic gneiss with subordinate tonalitic, granodioritic, and granitic gneiss. Minor rock types include mafic-rich amphibolite and pyroxenite, ultrabasic and syenitic dykes, migmatite, and local porphyroblastic feldspar- and quartz-rich in situ anatectic pegmatites (Card et al., 2016; Fig. 2.7 and 2.8). The main fabrics and contacts of crystalline basement rocks in the Arrow Deposit area are all steeply dipping, with a northeast-southwesterly strike. The mineralized area of the Arrow Deposit, projected to surface in Figure 10, is defined as 280 m wide by 875 m in strike, with mineralization extending from 110 m below surface to 980 m depth. The dominant host rock of the Arrow Deposit is porphyroblastic, weakly to moderately gneissic and/or augen textured, pervasively quartz-flooded quartz-feldspar-garnet-biotite ± graphite gneiss, which has historically been called “semi-pelitic gneiss” (Fig. 2.8).

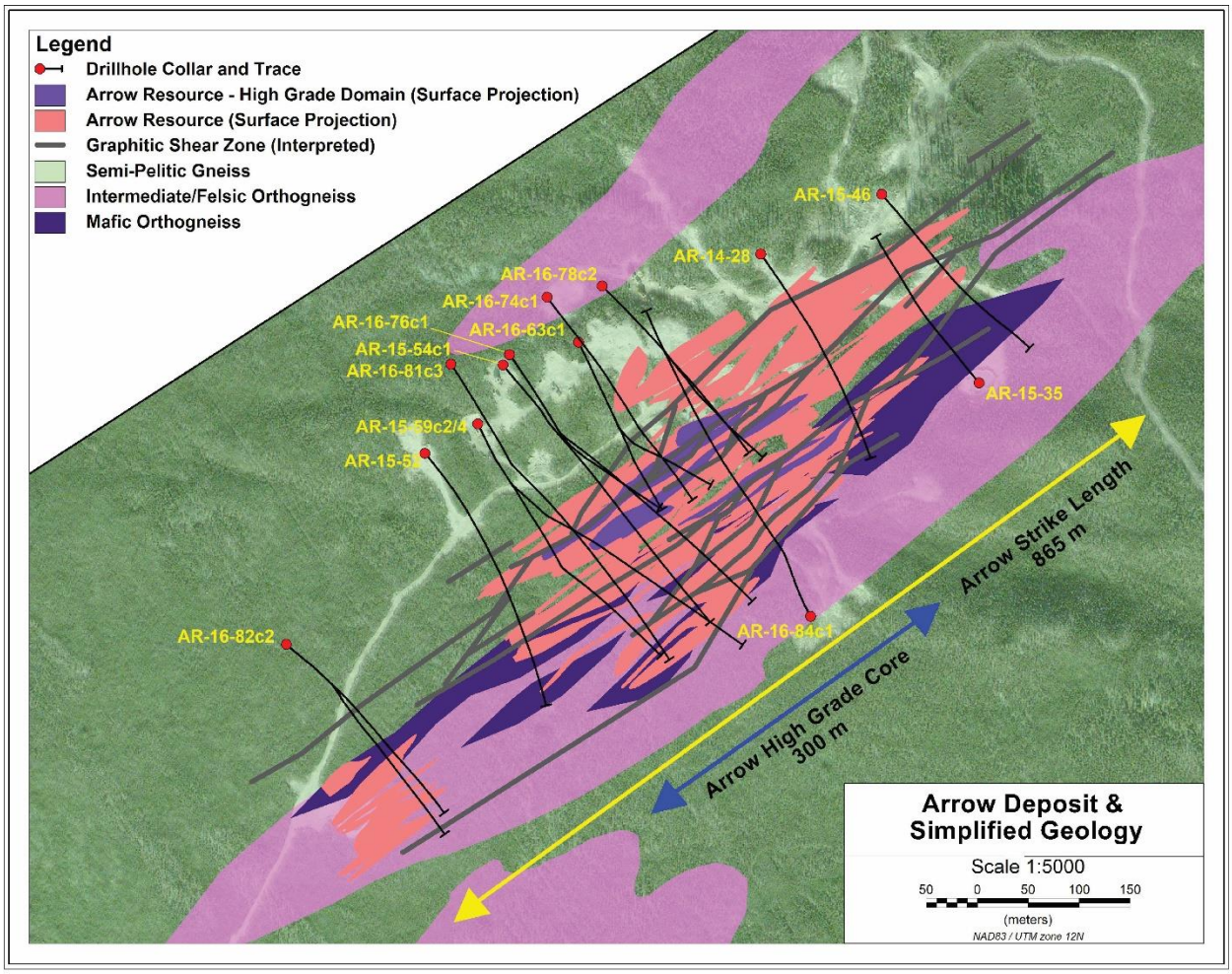

Fig. 2.8. Arrow plan map showing simplified basement geology projected to the unconformity surface, interpreted graphitic structures, and drill hole collars and traces for 18 representative holes selected for components of this study. Resource outline from Mathisen and Ross 2017.

The dominant host rock ("semi-pelitic gneiss") consists of approximately 30-80% blue quartz, 15-20% potassium feldspar, commonly replaced by white mica, 10-30% garnet, commonly replaced by chlorite, 1-10% graphite, and 1-5% biotite (Fig. 2.9 and 2.10). Accessory minerals include sillimanite, tourmaline, and rutile/anatase (Fig. 2.10). The rock type is extensive within the Arrow zone, hosting over 50% of the deposit (Fig. 2.8), and exhibits a wide range of alteration styles and intensities (Section 5.0). The origin of this rock has been a recent topic of study, with both metasedimentary and metasomatic origins being proposed. Historically, the rock has been proposed to be of metasedimentary origin as the mineral assemblage is similar to that observed in metapelites (i.e. presence of garnet, graphite, sillimanite). Based on more recent studies (e.g. Card, 2017; 2018; Onstad et al., 2017) and work detailed in this study, more comprehensive observation

of the paragenetic and textural relationships (Section 5.0) suggest a metasomatic origin through alteration and overprinting of a feldspathic igneous protolith (i.e. the metapelite mineral assemblage was not in equilibrium, evidenced by crosscutting and grain boundary relationships). Such relationships include red-purple garnet porphyroblasts, possibly of almandine ($Fe^{2+}_3Al_2(SiO_4)_3$) to pyrope ($Mg_3Al_2(SiO_4)_3$) composition, clearly overgrowing primary feldspar grains or secondary prismatic sillimanite (e.g. Fig. 2.9A and 2.10B, respectively), and graphite, which is strongly controlled by structure and overgrows other minerals (Fig. 2.11). This rock type, which comprises the dominant uranium ore host rock at the Arrow Deposit, is referred to as "semi-pelitic" gneiss in Figure 2.8 and 2.9 to maintain consistency with previous technical reports on the geology of the area. However, the best interpretation is that the rocks that host the Arrow Deposit are dominated by orthogneisses.

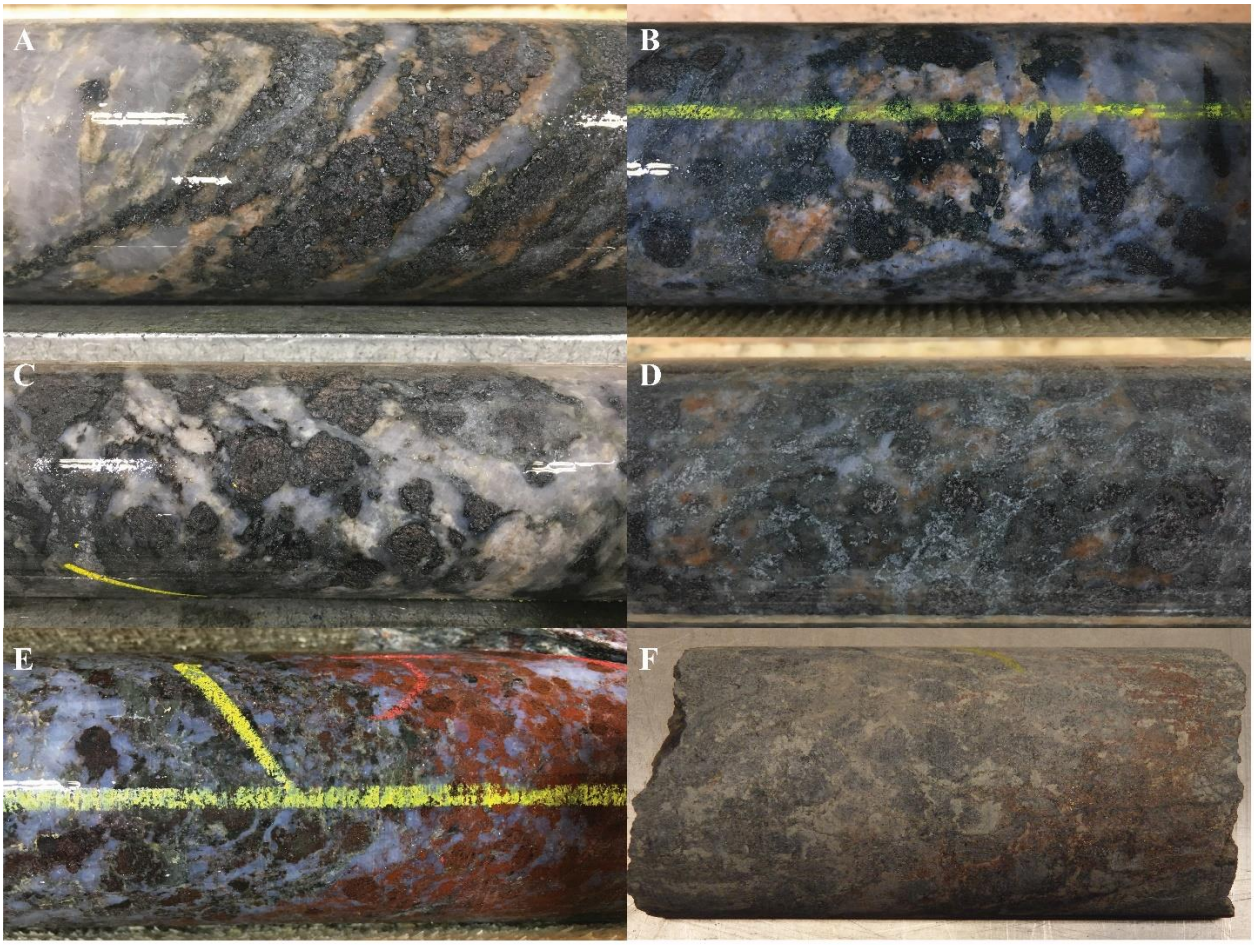

Fig. 2.9. A) Silicified "semi-pelitic gneiss" with chlorite-rimmed garnets preferentially growing over K-feldspar-rich bands (AR-18-213c1, 507.0 m). B) Porphyroblastic "semi-pelitic gneiss" exhibiting weak chloritization of garnets and trace albitization of K-feldspar (GAR-18-008, 580.9 m). C) Weakly albitized "semi-pelitic gneiss" with pink-purple, chlorite-rimmed garnet porphyroblasts (AR-18-213c1, 608.3 m). D) Weakly sericite- and chlorite-altered "semi-pelitic gneiss" with local relict K-feldspar visible (AR-18-213c1, 457.5 m) E) Moderately chloritized and hematized "semi-pelitic gneiss" typical of the "red-green zone" of the paleoweathering profile (GAR-18-012, 209.1 m). F) Strongly sericite- and chlorite-altered "semi-pelitic gneiss" lacking silicification proximal to the A2 shear, hosting U mineralization and associated hematite alteration (AR-15-059c2, 506.8 m).

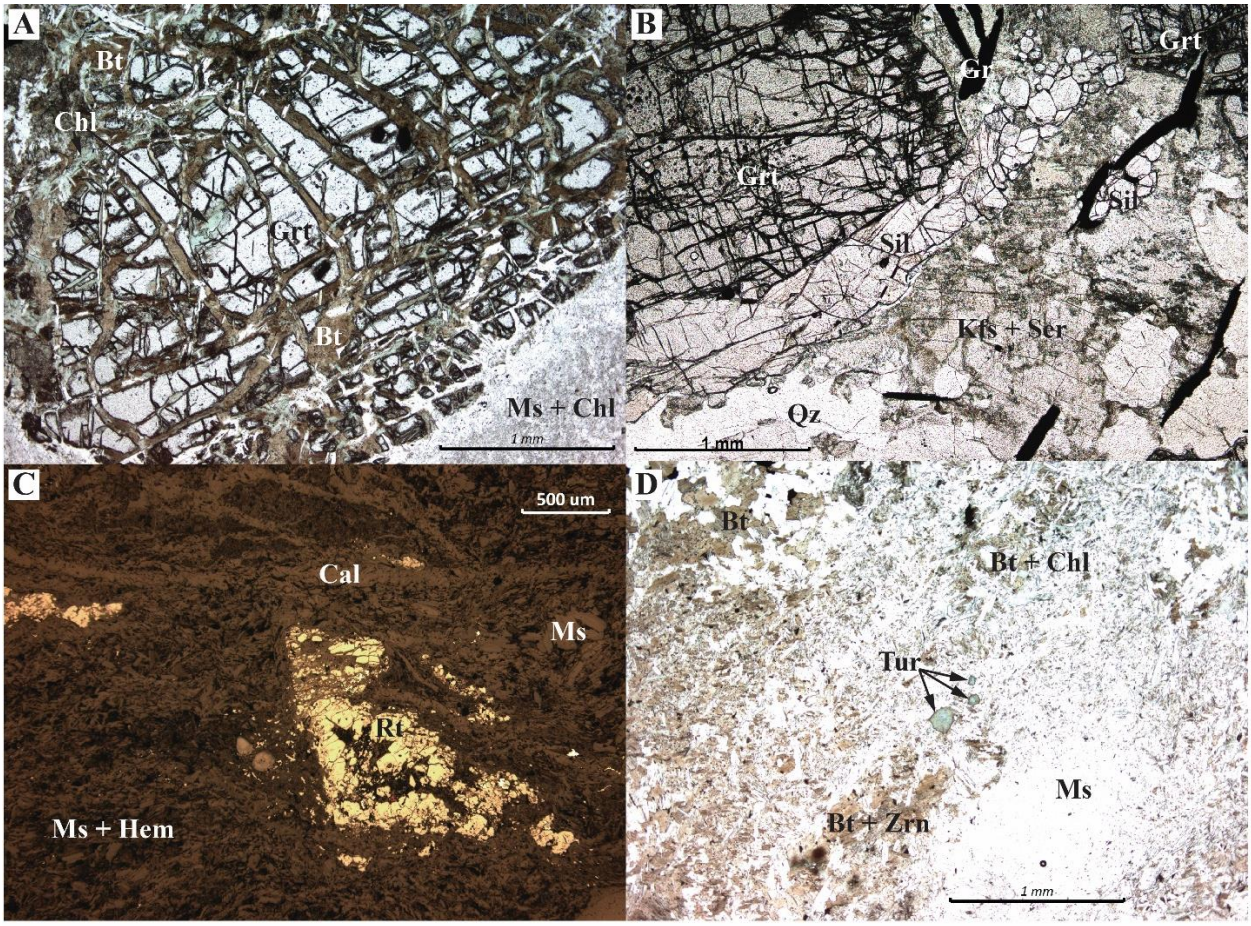

Fig. 2.10. Photomicrographs of thin sections cut from variably altered semi-pelitic gneiss. A) Plane-polarized light (PPL) image of a relatively unaltered garnet porphyroblast (Grt) in a matrix of fine-grained muscovite (Ms) and chlorite (Chl), with biotite (Bt) altering to chlorite along fractures (AR-16-084c1, 385.1 m). B) PPL image of sericite-altered K-feldspar (Kfs + Ser) and prismatic sillimanite (Sil) overgrown by garnet porphyroblasts (Grt). Late disseminated graphite (Gr) is observed crosscutting and draped around other minerals (AR-17-167c2, 680.0 m). C) Reflected light (RL) image of a strongly deformed, relict rutile crystal (Rt) within a matrix of muscovite and hematite (Ms + Hem) proximal to A2 mineralization. A late calcite vein (Cal) crosscuts the rock in the upper portion of the image (AR-15-059c2, 531.1 m). D) Blue-green tourmaline crystals (Tur) in a matrix of fine-grained muscovite (Ms) and biotite containing micrometer-scale zircons (Bt + Zrn). Biotite is altered to chlorite (Chl) locally. (AR-15-059c4, 798.45 m).

NE-SW striking, relatively quartz-poor, low- to medium-grade mylonites and phyllonites (termed the A1 to A5 Shears within the Arrow zone; Fig. 2.11A through C; Section 4.2) correlate with interpreted geophysical electromagnetic conductors across the property and locally host uranium mineralization within the Arrow Deposit (Fig. 1.3 and 2.8). They exhibit variable deformational textures and a range of mineralogical composition, consisting of variable proportions of chlorite, biotite, white mica, graphite, sulphides, and deformed quartz (Fig. 2.11; Section 4.2). Based on drill core observations and structural analysis, these high strain zones

display a dominant strike-slip component with a minor dip-slip component. The deformational and hydrothermal-metasomatic evolution of these structures is discussed in detail in Sections 4.1 and 4.2.

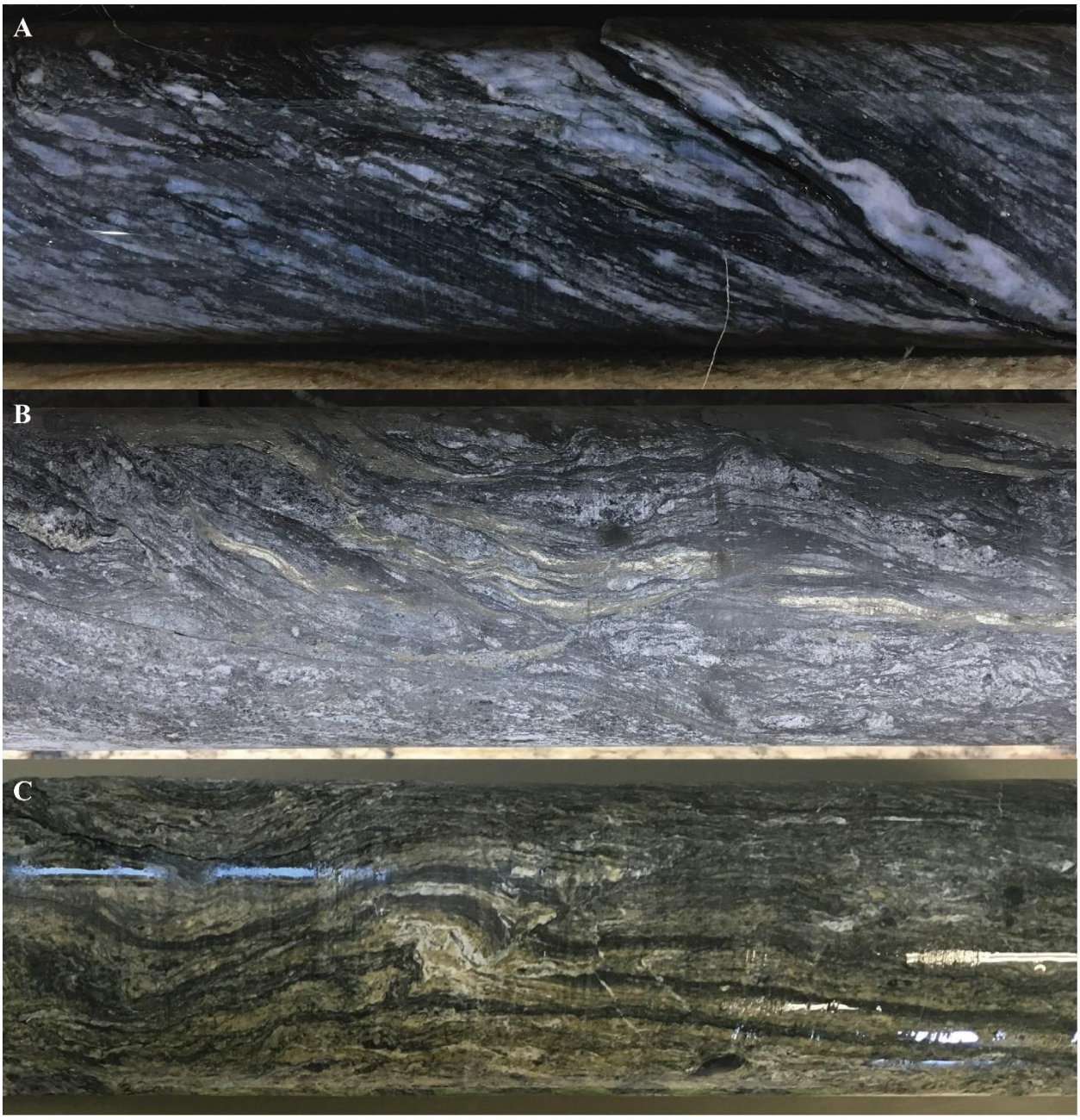

Fig. 2.11. A) Chloritic-graphitic medium-grade mylonite with ribboned quartz and weak C-S fabric (AR-18-216c1, 351.0 m). B) Low-grade mylonite with paragenetically late graphite and even younger iron sulfides mimicking and crosscutting anastomosing primary shear fabrics (AR-18-210c3, 805.6 m). C) Highly altered chloritic-sericitic-graphitic phyllonite exhibiting crenulated and curtain folded shear fabrics. Curtain fold axis is sub-parallel to the stretching lineation and perpendicular to core axis (AR-17-115c1, 682.3 m).

The crystalline basement rocks that host the Arrow Deposit are unconformably overlain by flat-lying Athabasca Supergroup sandstones. The Athabasca sandstones are planar- and cross-bedded, poorly sorted, medium- to coarse-grained, quartz arenite to conglomeratic sedimentary layers of the Read and Bird Formations of the Manitou Falls Group (Fig. 2.12A through C; Bosman and Ramaekers, 2015) and exhibit a variety of alteration features such as bleaching, de-silicification and complete friability, silicification, and clay alterations. The alteration profiles in the Athabasca Supergroup in the Patterson Lake area are similar to alteration halos above and around uranium deposits in the eastern Basin, however generally not as intense or widespread due to the depth of mineralization relative to the unconformity. Directly above the Arrow Deposit however, alteration in the sandstones increases with proximity to the upwards propagation of structures into the overlying Athabasca Supergroup.

The Athabasca Supergroup sandstones are overlain by a series of Phanerozoic and Quaternary rock types and deposits of variable thickness. Where Athabasca sandstone cover is thin towards the southern edge of the Rook I property, basement rocks are unconformably overlain by Devonian (Fig. 2.12D) or Cretaceous sedimentary rocks.

The Devonian sequences are made up of two distinct units. The most basal Devonian rocks are of the La Loche Formation, consisting of regolithic, poorly sorted breccia with clasts of older Athabasca sandstone and/or basement rock, and fine to coarse grained, white to medium brown-grey arkosic sandstone and conglomeratic sandstones (Norris, 1963; Bosman et al., 2018). The La Loche Formation grades into the Contact Rapids Formation (AB), equivalent to the Meadow Lake Formation (SK), which consists of poorly-sorted, green to red, fine- to coarse-grained sandstones with carbonate cement (Bosman et al., 2018; Fig. 2.12D and E).

Cantuar Formation rocks of the Cretaceous Mannville Group have also been encountered. They consist of green-grey to black, very fine- to medium-grained sandstone interbedded with fissile mudstones, and fine- to coarse-grained, cross-bedded beige sandstone with minimal mudstone (Bosman, 2018; Fig. 2.12F through H). The latter is commonly saturated with bitumen and often contains centimetre- to decimeter-scale coal beds (Fig. 2.12F).

The distribution of the Cretaceous strata in the area is widespread, however the Devonian sequences appear to be somewhat restricted to areas overlying the known uranium deposits in the area (i.e. Arrow, Triple R) suggesting that underlying structural controls affected deposition well into the Phanerozoic (Bosman, 2017). Furthermore, elevated uranium concentrations and clay alteration within the Phanerozoic stratigraphy may indicate the presence of late mobile uranium in the Patterson Lake area, thus allowing for the potential for lower-grade sandstone-hosted deposits (Bosman, 2017).

The geological sequence of the Patterson Lake corridor is capped with Pleistocene glacial tills. The glacial tills are typically 20 m to 50 m thick. Northeast to east-northeast trending drumlins are common, as are outwash plains and hummocky terrain. Glacial striations on exposed outcrops in the Rook I area also indicate a general ice direction movement to the southwest (Sykes and Schwab, 2014a; Sykes et al., 2014b).

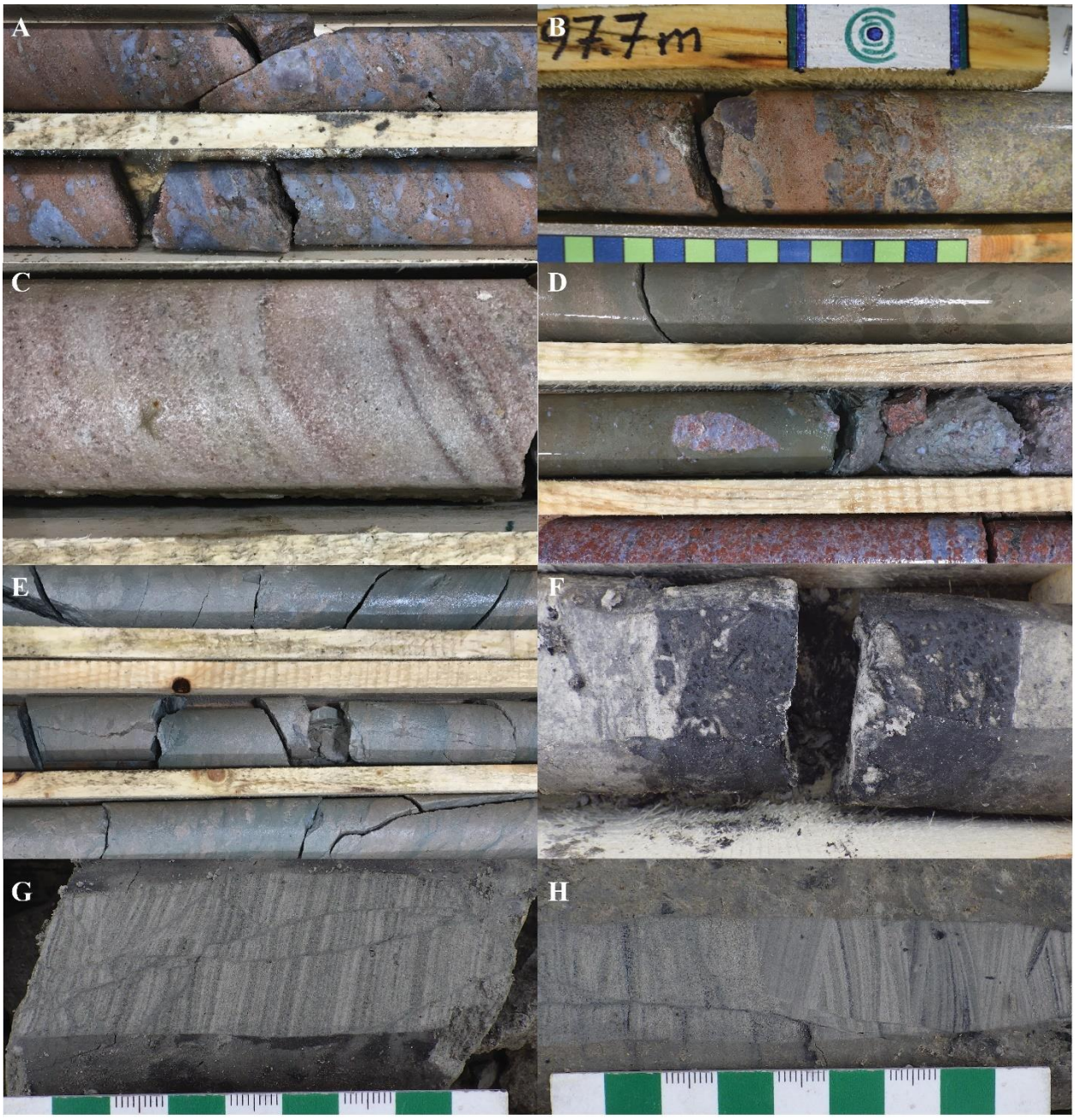

Fig. 2.12. A) NQ (47.6 mm diameter) drill core photo of planar-bedded Athabasca Supergroup sandstone hosting abundant basement clasts of blue quartz (AR-18-216c1, 103.0 m). B) Conglomeratic unconformity between Athabasca Supergroup sandstone and Taltson basement rock (NQ, AR-18-212c1, 97.7 m). C) Cross-bedded, weakly bleached quartz arenite sandstone of the Athabasca Supergroup (NQ, AR-18-216c1, 90.3 m). D) Unconformable contact between Devonian Meadow Lake Formation sandstone and Taltson basement rock (NQ, AR-18-211c1, 102.5 m). E) Poorly sorted, green-brown sandstone of the Devonian Meadow Lake Formation (NQ, AR-18-211c1, 96.3 to 100.95 m). F) HQ (63.5 mm diameter) drill core photo of a coal seam in Cantuar Formation sandstone (GAR-18-010, 28.5 m). G) Planar, interbedded Cretaceous Cantuar Formation sandstones and mudstones with normal micro-faults (GAR-18-010, 30.1 m). H) Cross-bedded Cantuar Formation sandstones and mudstones with normal micro-faults (HQ, GAR-18-010, 33.1 m).

CHAPTER 3

MATERIALS AND METHODS

3.1 Structural Data: Oriented diamond Drill Core Measurements

The methodology for structural analysis includes interpretations of individual structural measurements obtained from 139 oriented diamond drill holes completed during drill programs up to the end of 2016. Structural measurements include alpha and beta angles of planar structures including foliations, fractures, veins, shears, mylonites, breccias, cataclasites, and fault gouges, as well as gamma angles of linear structures including slickenslides and ductile lineations. Figure 3.1 illustrates the measurement of alpha (α), beta (β), and gamma (γ) angles from oriented drill core. The working data set is composed of more than 18,000 measurements in total, with measurements taken from sections comprising a minimum of two consecutive three-meter lengths of oriented drill core (Fig. 3.2) that have undergone beta rotation correction and confidence level assignment for quality assurance and quality control (QAQC). True orientations are then determined via Geo Calculator 4.9.7 and stereographically assessed with DIPS v.06. Drill hole orientation sampling bias is accounted for through the application of the Terzaghi weighting method, involving the application of a correction factor to each feature with subsequent stereographical analysis on the weighted dataset (Terzaghi, 1965). All measurements of planar features have undergone Terzaghi weighting to account for sampling bias, adding another layer of QAQC.

An average of one foliation measurement per three-meter run, and at least one brittle structural measurement per three-meter run were taken, with more structures measured in areas of importance (i.e. fault zones, high strain zones), and fewer structures measured in structurally quiescent areas. For quality control, the working data set was composed of measurements taken from a minimum of two consecutive 3-meter-long drill core "runs" that were oriented with a bottom-of-hole reference line, and an allowable range of ± 30° beta rotation from either reference line (Fig. 3.2). For quality assurance, the beta rotation criterion was put in place to ensure data used in this study was as reliable as possible without bias or mistakes introduced by human error during the orientation process at the drill site and/or data collection by field geologists. Any oriented structural data that did not comply with the QAQC stipulations were disregarded for use in this study. All 139 drill holes included in the working structural dataset were created as borehole

traverses in RocScience DIPS software. DIPS v.06 allows for easy application of Terzaghi weighting to oriented structural data and can eliminate the need to convert alpha and beta measurements to strike and dip prior to stereographic projection. The Terzaghi method involves application of a correction factor to each feature and subsequent stereographical analysis on the weighted dataset (Terzaghi, 1965). The result is a 'cleaner' stereonet, with ideally a more representative picture of structural trends through 'noise' reduction and accounting for drill hole bias.

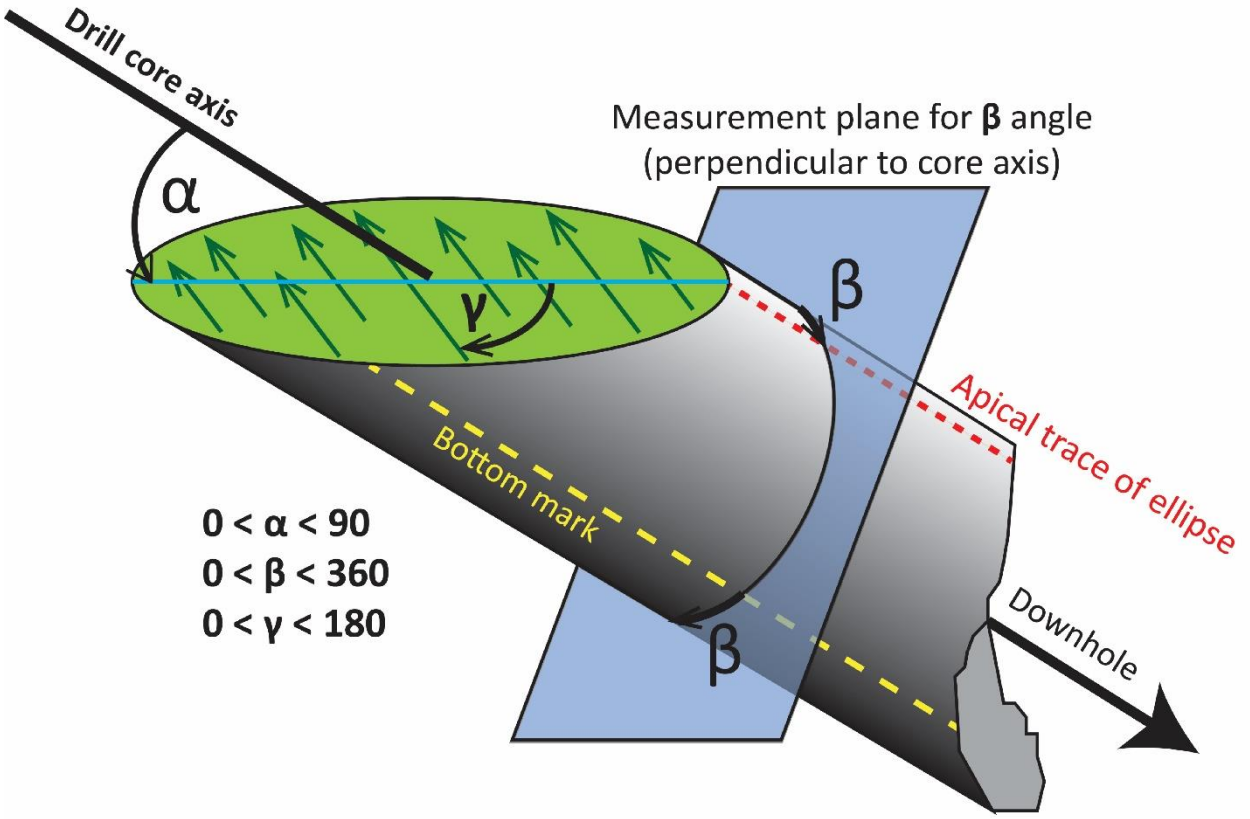

Fig. 3.1. Schematic diagram illustrating the geometry of alpha, beta, and gamma angles measured with respect to the drill core axis, bottom-of-hole orientation mark (yellow), and the apical trace (red) of the fracture plane ellipse long axis (blue). Gamma angle of lineations (dark green) is measured clockwise from the ellipse long axis on the "downhole" fracture surface (light green), and counter clockwise on the "uphole" fracture surface (After HCA, 2007).

Fig. 3.2. Oriented drill core showing orientation lines (blue and yellow) from four consecutive 3-meter runs in drill hole AR-16-078c2. From 270 to 273 m (ß rotation = 350°), from 273 to 276 m (ß rotation = 20°), and from 276 to 279 m (ß rotation = 340°). Measurements taken from consecutive runs were used for this study.

3.2 Mineralogical and Geochemical Data: Hand Sample, Thin Section, and Scanning Electron Microscope (SEM) and Electron Microprobe Analysis (EMPA)

Approximately 400 samples of unaltered, altered, and mineralized rocks were collected from 18 representative drill holes that intersect the deposit (Fig. 2.8). A combination of hand sample examination, thin section microscopy, and electron microprobe analysis has been used to generate a detailed paragenesis of the Arrow Deposit. A suite of over 50 polished and un-polished thin sections were cut from Arrow drill core and examined using transmitted and reflected light petrography. Crosscutting relationships and structural fabrics were observed in both hand sample and thin section, serving to integrate the mineralogical and structural evolution of the Deposit.

Polished thin sections were examined using transmitted and reflected light optical microscopy prior to electron microscopy in order to choose the most suitable mineralized samples for backscattered electron (BSE) and electron microprobe analysis (EMPA). Analyses on uraniferous phases was performed on a JEOL 8600 Superprobe electron microprobe analyzer,

housed at the Electron Microscopy Laboratory in the Department of Geological Sciences, University of Saskatchewan. Polished thin section samples were cleaned with deionized. water in an ultra-sonic bath and swabbed with methanol. A 150-200 angstrom coating of carbon, using a JEOL JEE vacuum carbon evaporator, was applied to each side of the samples prior to inletting into the microprobe. All analyses were performed at 20 kV and 50 nA. UO_2, ThO_2, PbO, SiO_2, TiO_2, Al_2O_3, Cr_2O_3, Fe_2O_3, Y_2O_3, Tb_2O_3, MnO, CuO, CaO, V_2O_5, P_2O_5, and K_2O components of uraniferous minerals were analyzed (Table 1 and 2). Calibration standards and count times used for each element in EMPA are provided in Appendix B.

Photomicrographs, BSE images, and select hand sample images in this paper are labelled with mineral abbreviations in compliance with those set forth by Whitney and Evans (2010). Mineral abbreviations will be explained in their first appearance in the paper, with only the abbreviation used in subsequent figures. A complete list of all mineral abbreviations used in this paper is provided for reference in Appendix A. Depth measurements in hand sample and photomicrographs represent core lengths from the drill collar regardless of the orientation of the drill hole and are not elevations. Radioactivity measurements in all figures and captions were made with Radiation Solutions RS-120 and RS-125 handheld scintillometers and are reported in counts per second (cps).

3.3 Chemical age determination via electron microprobe analyses

Electron microprobe analysis of uranium (U), thorium (Th), and lead (Pb) content in stable, naturally occurring minerals can indicate their age of formation or equilibration (Bowles 1990; 2015). Minerals most suitable for this dating method contain little or no "common" Pb; meaning that when dated the Pb contained within the mineral is primarily radiogenic. The chemical ages are therefore calculated based on the assumption that the total Pb content in the samples is of radiogenic origin and results only from the decay of U and Th, and that the minerals have not lost or acquired Pb since initial crystallization (Bowles 1990; 2015). Pb can however, be lost or gained through natural processes such as metamictization, or through contamination during sample preparation (i.e. use of lead laps). In old uraninites (>1,000 Ma; Bowles, 2015) a considerable amount of Pb will have been produced due to the mineral's high U content (up to 90 wt% U; Alexandre et al., 2005), thus creating the possibility for substantial Pb loss over time, and therefore low apparent ages. Pb may be lost through metamictization, a process in which Pb becomes mobile

through degradation of the mineral's crystal structure by the release of alpha particles from the decay of U and Th (Holland et al., 1955). The susceptibility of the U-Th-radiogenic Pb isotope system is therefore related to the extent of radiation damage due to the alpha-emission process, making this an important consideration in geochronology (Woodhead et al., 1991). This process occurs more rapidly in minerals with higher U and Th content, such as uraninite, and therefore must be considered on a case-by-case basis. In calculation of chemical ages, Pb loss is evident in three ways described by Bowles (2015): 1) the calculated chemical age is younger than the isotopic age, 2) a plot of PbO vs. UO_2 or ThO_2 fitted to a straight line through a least squares method exhibits a negative intercept on the PbO axis, or 3) Pb-bearing secondary minerals have formed rims or mantles around the original U-mineral. Additionally, Pb that is not contained within the crystal structure of the mineral to be analyzed may also be lost under the effects of the electron beam of the microprobe (Jercinovic et al., 2005). Through comparison with ages derived from isotopic measurements, Bowles (1990; 2015) has shown the results of the chemical age method to be valid.

^{238}U is the most abundant isotope of uranium, accounting for 99.27% of present-day uranium and decays to ^{206}Pb with a half-life of 4,468 Ma. Only 0.7204% of present-day uranium occurs as the ^{235}U isotope, which decays to produce ^{207}Pb with a half-life of 703.8 Ma (Bowles, 2015). Since the natural atomic proportions of U isotopes are known, for calculation of chemical ages, the quantity of ^{238}U can be taken as 0.992739 x the measured U, and the amount of ^{235}U as 0.007204 x the measured U (Bowles, 1990; 2015). Th occurs as a single isotope, ^{232}Th, which decays to produce ^{208}Pb through a much longer half-life of 14,008 Ma (Bowles, 2015). The amount of radiogenic Pb produced by any one of these radioactive isotopes can be described mathematically using known decay constants and the measured atomic proportions of the isotope in question. Bowles (2015) describes the amount of Pb produced by each ^{238}U and ^{232}Th in the following three equations:

$$Pb = {}^{238}U\,(e^{\lambda U238\,t} - 1) \qquad [1]$$

Equation 1 can then be rearranged to solve for time since formation, *t*, as:

$$t = ln((^{206}Pb/^{238}U) + 1) / \lambda_{U238} \qquad [2]$$

Where the relative amounts of U and Pb are given in their atomic proportions. An equivalent equation can be written for the age, t, using analysis of the single isotope of Th:

$t = ln((Pb/Th) + 1) / \lambda_{Th}$ [3]

In reality, the situation is more complicated when both U isotopes as well as Th are present, and thus the total amount of radiogenic Pb produced by the decay of U and Th is given by Bowles (2015) as:

$Pb = {}^{238}U\ (e^{\lambda U238\ t} - 1) + {}^{235}U\ (e^{\lambda U235\ t} - 1) + Th\ (e^{\lambda Th\ t} - 1)$ [4]

Where Pb is the sum of the Pb produced from each source.

In equations (1) through (4), λ_x represent the decay constants (in years) for each isotope as given by Jaffey et al. (1971):

$\lambda_{U238} = 1.55125 \times 10^{-10}$

$\lambda_{U235} = 9.8485 \times 10^{-10}$

$\lambda_{Th} = 4.9475 \times 10^{-11}$

Equation 2 can be simplified for use with microprobe data, and may be recast as:

$t = ln(1.104Pb/U + 1) / \lambda_{U238}$ [5]

Where the constant 1.104 accounts for the relative abundances of 238U and 235U and those of 206Pb and 207Pb. Equation 5 also allows for the proportions of U and Pb to be expressed as their weight percentage, rather than atomic proportion.

Other workers have fitted empirical formulae to the radioactive decay of U and Th to calculate chemical ages. Ranchin (1968) produced the formula:

$t = Pb*7550 / (U + 0.36Th)$ [6]

Where the proportions of U, Pb, and Th are given in weight percentage, and the age in Ma.

Cameron-Schiman (1978) produced an equation in similar form:

$t = Pb*10^{10} / (1.612U + 4.95Th)$ [7]

Where the proportions of U, Pb, and Th are expressed as their atomic percentage, and the age in years.

In any case, if the amounts of U, Th, and Pb are measured by microprobe analysis, the only unknown is time since formation, *t*, and thus a chemical age can be calculated using any one of these methods. In the present paper, chemical U-Pb ages for the uranium mineralization at Arrow were calculated using data on the U, Th, and Pb content of uranium minerals obtained from the electron microprobe using all three methods set out by Ranchin (1968), Cameron-Schiman (1978), and Bowles (1990; 2015), in order to compare the different methods individually, and to isotopic ages obtained through SIMS.

Various chemical ages derived from the composition of a single uraninite grain reflect variable alteration by subsequent fluids to form other uranium minerals (e.g. uranyl minerals and coffinite), which results in a decrease in the chemical Pb age and an increase in "foreign" elements other than uranium. As alteration is expected to result in a decrease in radiogenic Pb contents, the initial crystallization age of the uraninite may be estimated by extrapolating the chemical ages to the age when the concentrations of the substituting elements (e.g. Ca, Fe, and Si) were negligible (e.g. Alexandre and Kyser, 2005).

3.4 In Situ Secondary Ionization Mass Spectrometry (SIMS)

3.4.1 Selection of standard material and preparation of samples

Prior to Secondary Ion Mass Spectrometry (SIMS) analysis, the polished thin sections were cleaned with ethanol and polished with a 1-micron diamond-cleaning compound to remove the carbon coating that was used for the EMPA analyses. Each section was subsequently cleaned using soap, then immersed in a dilute soap solution in an ultrasonic cleaner. The sections were immersed three more times in the ultrasonic cleaner, first using tap water, then purified water, and finally ethanol. Once cleaning was complete, the sections were sputtered-coated with a thin layer of gold to provide a conductive surface. Isotopic ratios of radiogenic and stable isotopes were obtained from uranium-bearing minerals including uraninite and coffinite.

3.4.2 Instrumental mass fractionation (IMF)

During measurement, a mass-dependent bias, referred to as instrumental mass fractionation (IMF), is introduced. It typically favors the light isotope. The observed IMF results from a variety of processes, including secondary atom ionization (sputtering) and extraction (Sigmund, 1969; Shroeer et al., 1973; Yu & Lang, 1986), secondary ion transmission (Shimizu & Hart, 1982), and detection (Lyon et al., 1994; Riciputi et al., 1998). Sputtering and ionization, which depend strongly on sample characteristics (i.e., chemical composition), are the greatest contributors to variability in IMF. Therefore, accurate isotopic analysis by SIMS requires calibration using a mineral standard that is compositionally similar to the mineral under analysis to correct for IMF, in this case, uraninite. Ion-microprobe results from the standard are compared to its accepted isotopic composition in order to calculate a correction factor that is applied to the data obtained during the same analytical session (Holliger, 1988).

Uraninite grains vary considerably in their chemical composition and commonly exhibit chemical zoning at the micrometer-scale, thus posing complications when choosing a suitable standard reference material. It is impractical to find standards that match the wide range in chemical compositions of these minerals, and therefore a mass-bias model that accounts for variation in IMF with chemical composition for the minerals of interest is necessary. These models are developed using a suite of standards with chemical compositions that cover the range of compositions of the minerals from which a working calibration curve is developed (Fayek et al., 2002b). In addition, the relative ion-yields of two elements and their isotopes, such as U and Pb, may vary as function of chemical composition, producing incorrect measurements of elemental and isotopic ratios. For example, the $^{206}Pb/^{238}U$ ratio measured by SIMS may deviate significantly from their "true" $^{206}Pb/^{238}U$ value because Pb ionizes more readily than U. In addition, the $^{206}Pb/^{238}U$ ratio also may vary as a function of chemical composition of the sample because other elements present (e.g., Si, Ca, Fe etc.) may enhance the ion-yield of Pb^+ or U^+. Therefore, an ion-yield normalizing coefficient (α_{SIMS}) that accounts for variation in relative ion-yields with chemical composition for the mineral of interest is necessary (Holliger, 1991; Fayek et al., 2002b).

The standard and minerals of interest were analyzed during the same analytical session. The value of the standard was used to correct for IMF using the equation:

$\alpha_{SIMS} = R_{SIMS} / R_{STD}$ [8]

where R is the measured isotopic ratio (e.g., $^{207}Pb/^{235}U$ or $^{18}O/^{16}O$), SIMS denotes the samples, and STD denotes the standard.

The normalizing coefficient (α) was applied to the measured ratios from the minerals to obtain "true" isotopic ratios:

$R_{true} = R_{SIMS} / \alpha$ [9]

where R is the measured isotopic ratio.

3.4.3 Radiogenic isotopes

The SIMS analytical protocol for U-Pb measurements in uranium minerals using the CAMECA 7f ion microprobe is as follows. A ~10 nA primary ion beam of O^-, accelerated at 12.5 kV, was focused to a ~30 μm spot using a 30.1 μm entrance slit in the primary column. The sample accelerating voltage was +6.95 kV, with electrostatic analyzer in the secondary column set to accept +7.00 kV. The entrance and exit slits were narrowed to obtain flat-top peaks at a mass resolving power of about 1300. Ions were detected with an ETP 133H electron multiplier coupled with an ion-counting system with an overall deadtime of 30 ns. The following species were detected sequentially by switching the magnetic field: $^{204}Pb^+$, $^{206}Pb^+$, $^{207}Pb^+$, $^{208}Pb^+$, $^{235}U^+$, and $^{238}U^+$. A 50-volt energy offset suppressed hydride isobaric interferences. A typical analysis lasted ~8 minutes, comprising 30 cycles of analysis. Negligible common Pb ($^{204}Pb^+$) was detected.

Ratios corrected for mass bias (Equation 9) were used to calculate U-Pb isotopic ages using the ISOPLOT program (Ludwig, 1993). Pb-Pb ratios were used to iteratively calculate ages of uraninite using the following equation:

$^{207}Pb/^{206}Pb = {}^{235}U/^{238}U * e^{\lambda 2t} - 1 / e^{\lambda 1t} - 1$ [10]

where $^{207}Pb/^{206}Pb$ is the ratio measured by SIMS and corrected for mass bias, $^{235}U/^{238}U$ is 1/137.88, λ_2 and λ_1 are the decay constants for ^{235}U ($9.8485E^{-10}$ y^{-1}) and ^{238}U ($1.55125E^{-10}$ y^{-1}) and t is time in years.

3.4.4 Stable isotopes

Oxygen-isotope compositions of uraninite was also measured using the CAMECA 7f ion microprobe. A ~1 nA primary beam of Cs^+ was accelerated at 10kV and focused to a ~10 μm spot using a 230 μm entrance slit in the primary column. The sample accelerating voltage was +8.7 kV, with electrostatic analyzer in the secondary column set to accept -9.00 kV. The entrance and exit slits were narrowed to obtain flat-top peaks at a mass resolving power of about 350. An offset of 300-volts was used to eliminate molecular ion interferences. Ions were detected with an ETP 133H electron multiplier coupled with an ion-counting system using an overall deadtime of 30 ns. Two isotopes of oxygen, $^{16}O^-$ and $^{18}O^-$, were detected by switching the magnetic field. Analyses comprised 70 cycles and lasted ~10 minutes.

All stable-isotope data are presented in the δ-notation relative to the appropriate standard. Both hydrogen and oxygen are reported relative to Vienna Standard Mean Ocean Water (V-SMOW) in units of per mil (‰) and are calculated using the following equation:

$$\delta^2D \text{ or } \delta^{18}O\ (‰) = (R_{sample} / R_{V\text{-}SMOW} - 1) * 10^3 \qquad [11]$$

where R_{sample} is the ratio of the abundance of the heavy to the light isotope of the sample that has been normalized to obtain “true” isotopic ratios (see equation 9) and $R_{V\text{-}SMOW}$ is the ratio of the abundance of the heavy to the light isotope of the standard.

CHAPTER 4

STRUCTURAL ANALYSIS

4.1 Regional and Deposit-Scale Ductile Structural Framework

Within the Taltson Domain west of the VRSZ and Careen Lake, towards the Rook I property, lies the Lloyd fold domain described by Card et al. (2008). The Lloyd fold domain underwent multiple metamorphic and deformational episodes ca. 1.9 to 1.8 Ga (Card et al., 2008), resulting in multiple foliations (S_1 to S_3), fold generations (F_2, F_3, and F_4) and deep-seated shear zones. Intrafolial F_2 folds with near horizontal axial surfaces have only rarely been observed in the Taltson Domain, and F_3 refolding resulted in an early Type 2 fold interference pattern (e.g. Fig. 2.4). The most prominent fold generation, F_3, consists of open to close, north-northeast– to northeast-striking folds with sub-vertical axial planes dipping either northwest or southeast (Card et al., 2008). The composite S_1-S_2 foliation was deformed by the NNE- to NE-trending F_3 fold generation, producing a regional undulation in the pre-existing composite S_1-S_2 foliation. A well-developed axial S_3 foliation accompanies the F_3 folds, observed to dip steeply to the southeast of the Rook I property (Card, 2009). On highly strained F_3 fold limbs, S_1-S_2 and S_3 foliations are problematic to distinguish as the S_1-S_2 foliation is often transposed sub-parallel to S_3 (e.g. Card, 2009; this study), especially within or proximal to shear zones (e.g. VRSZ). Although extremely subtle, the earlier S_1-S_2 foliations may still be observed however in "low-strain" windows, within the hinge or nose domain of the F_3 folds (e.g. Fig. 2.4). An S_1-S_3 intersection lineation, co-linear with the F_3 fold axes, is widespread and indicates that the F_3 folds plunge dominantly to the northeast, and plunge southwest only rarely, likely due to northwest-striking F_4 cross folds near orthogonal to F_3 (Card et al., 2008). F_4 folds consist of north-northwest– to northwest-striking folds with sub-vertical axial surfaces orthogonal to F_3, resulting in a dominant Type 1 fold interference pattern observed across the Taltson (e.g. Card 2009). Arrow is a structurally controlled uranium deposit, hosted within a NE-SW-striking brittle-ductile deformation zone approximately 250 meters wide, over one kilometer in strike-length, and more than one kilometer in depth extent, which cuts Paleoproterozoic granulite facies rocks of the Taltson domain. Wall rocks contain a locally pervasive S_1-S_2 fabric that pre-dates the uranium mineralization of the Arrow deformation zone (Section 2.1). The early S_1-S_2, gently SE dipping gneissic foliation of the Taltson domain was locally folded by map-scale F_3 folds and is observed to be transposed sub-parallel to S_3

foliations, especially proximal to, and within high strain zones, which preferentially developed along highly strained F_3 fold limbs (e.g. Fig. 2.4; Card, 2009).

The oldest identifiable ductile fabric at Arrow, S_1-S_2 composite foliation, is transposed sub-parallel to an S_3 fabric contemporaneous with D_3 deformation across the Taltson Domain ca. 1.9 Ga, manifested through the Arrow zone as a sub-vertical and anastomosing, steeply SE dipping 'S_1-S_3' transposition foliation (e.g. Fig 2.4). Taltson S_1-S_2 foliations were transposed during deformation events along the Patterson Lake corridor, creating the steeply dipping, F_3 axial planar foliations observed through the Arrow zone (Fig. 4.1). Variability in the dip direction of the S_1-S_3 fabric increases through the core of the deposit, shifting locally to the NE and thus creating the mirrored pole distribution of Arrow foliation measurements in Figure 4.1. Along strike of the Arrow Deposit, foliation dip angles shallow out, dipping moderately to the SE at the Harpoon (NE along strike) and South Arrow (SW along strike) uranium showings (Fig. 4.1), illustrating a higher degree of structural disturbance and thus transposition at Arrow. Oblique axial-planar brittle fracturing or crenulations are observable within drill core-scale F_3 folding and local high strain folds, however in most cases axial planar foliation in these folds cannot be distinguished from the main foliation (Fig. 4.2). The composite foliation observed at Arrow contains a sub-horizontal object lineation related to deformation, present dominantly as a stretching lineation parallel to the longest axis (X) of the finite strain ellipsoid related to high strain along the Arrow shear zones (Section 4.3).

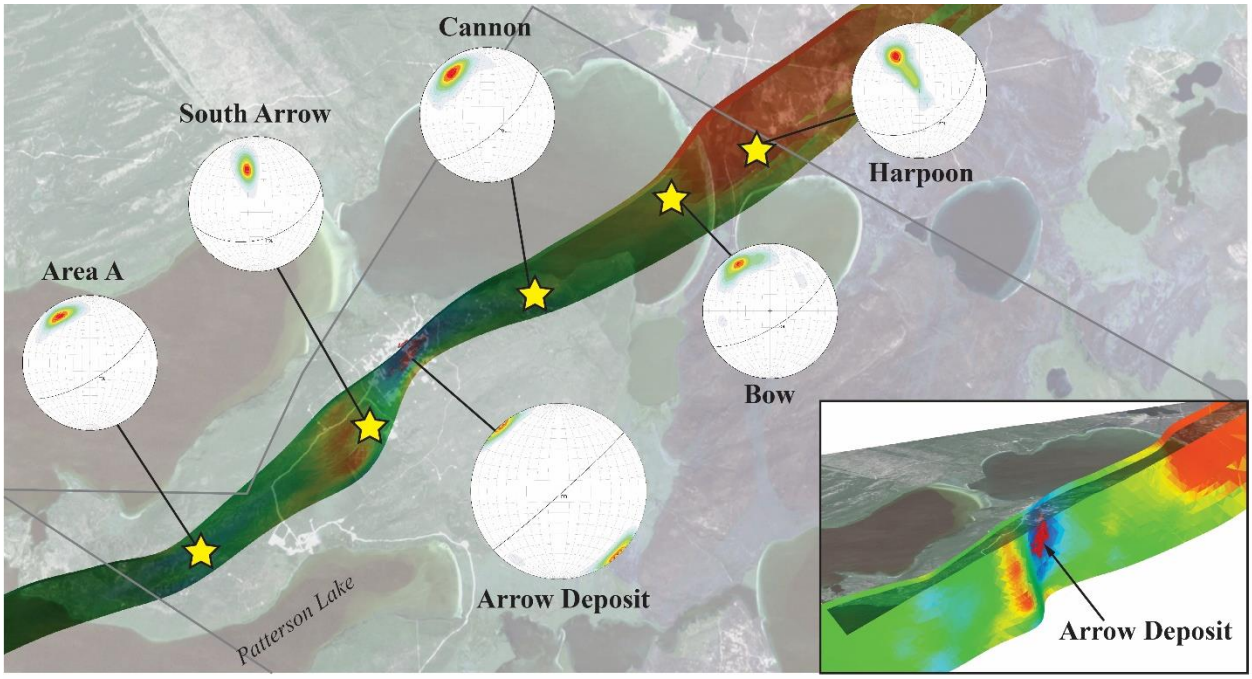

Fig. 4.1. 3D structural model of the Patterson Lake corridor constructed using EM geophysical data and oriented drill core data from the Arrow Deposit, and South Arrow, Harpoon, Bow, Cannon, and Area A uranium showings. Variability in dip along the corridor is marked by warm colors (shallow dip) and cool colors (steep dip). The geometry of the corridor illustrates the steepening of regional S_1-S_2 foliation at Arrow due to transposition with S_3 foliation during deformation. Inset is a sliced perspective view looking NW. The Rook I property boundary is outlined in grey. Mean dip and dip direction: Area A (*N = 617*) = 71°/148°; South Arrow (*N = 1,882*) = 46°/164°; Arrow Deposit (*N = 3,513*) = 87°/138°; Cannon (*N = 425*) = 68°/138°; Bow (*N = 354*)= 71°/148°; Harpoon (*N = 546*) = 45°/147°.

The early ductile framework set up during crustal scale orogenic events <1.94 Ga and related metamorphism was a key factor in the genesis of the Arrow Deposit. In the formation of a deep-seated structural system such as the Patterson Lake corridor, the regional ductile structural framework can act as a limiting or accommodating factor for subsequent brittle reactivation, fluid movement, and metal deposition. Regional F_3 and F_4 folds of the Lloyd fold domain described by Card et al. (2008) have been mapped throughout the Taltson Domain (Fig. 2.5; Card, 2009) and are interpreted to be pervasive through the study area, providing the groundwork for formation of the Patterson Lake corridor structural system and the Arrow Deposit. Because re-folding and fold interference patterns create variability in fold geometry, this can play a role in the spatial formation of zones of dilation (fluid accommodating) and zones of compression (fluid limiting). Despite local variability, stretching lineations (Fig. 4.3 and 4.4) are a useful tool in fold analysis as they preferentially form co-linear to fold axes (i.e. in curtain or sheath folds which are common in shear zones, especially mylonites; e.g. Cobbold and Quinquis, 1980). Object lineations are defined as

comprising elements that have volume, subdivided into aggregate or grain lineations (Passchier and Trouw, 2005). The term stretching lineation has genetic implications, as it refers to aggregates or single crystals which have been deformed by stretching. Since elongate crystals can also form normal to the stretching direction through boudinage or vein formation, care should be taken to distinguish true stretching lineations which represent the strain X-axis (Passchier and Trouw, 2005). When these types of lineations form in ductile shear zones with approximately simple shear, they also represent the 'direction of tectonic transport' (Passchier, 1998).

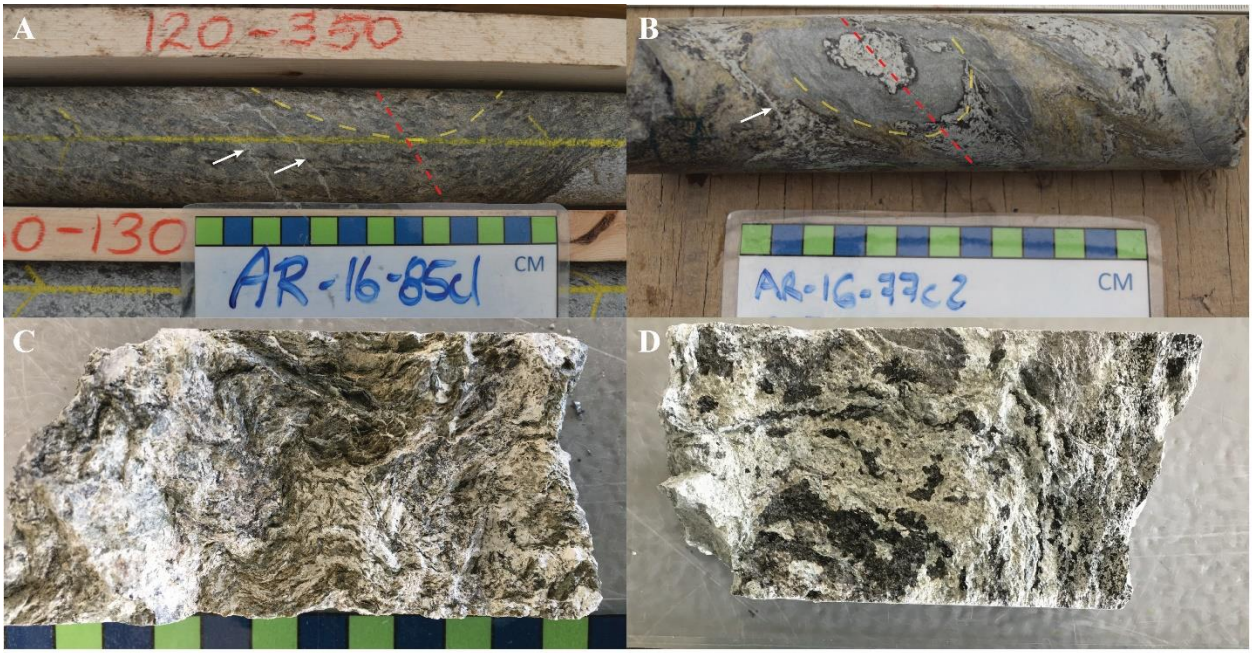

Fig. 4.2. A) NQ drill core photo of fold axial planar fractures (white arrows) crosscutting the limb of an asymmetric open fold. Axial plane shown in red; fold form lines in yellow (AR-16-085c1, 831.8 m). B) Clay-healed axial planar fracture within the limb domain of a sheath fold. Annotations as in Fig. 20A (AR-16-077c2, 617.1 m). C) Crenulated shear foliation defined by fine-grained white mica (sericite), chlorite, and kaolinite (AR-18-200c4, 775.7 m). D) Folded and weakly crenulated shear foliation defined by chlorite, sericite, and kaolinite (AR-18-200c4, 773.9 m).

Figures 4.3 and 4.6 are stereographic projections of true stretching lineations measured from foliation surfaces throughout the Arrow deformation zone. Plotting stretching lineation measurements from the Arrow Deposit reveals a pattern which resembles the resulting 'Type 1', dome and basin, fold geometry produced by the F_3 and F_4 folds (Fig. 4.5, 4.6, and 4.7). Early ductile to brittle-ductile heterogeneous high strain zones (Section 4.2) are interpreted to have subsequently developed along the limb of a regional scale F_3 fold, resulting in multiple NE-SW trending EM anomalies within the southeastern limb domain, including the Patterson Lake corridor

(Fig. 4.8). The interpreted F_3 fold form lines in Figure 4.8 represent a NE dipping synform, with property scale parasitic folding in the SE limb hosting the Arrow Deposit, as illustrated in Figure 4.7.

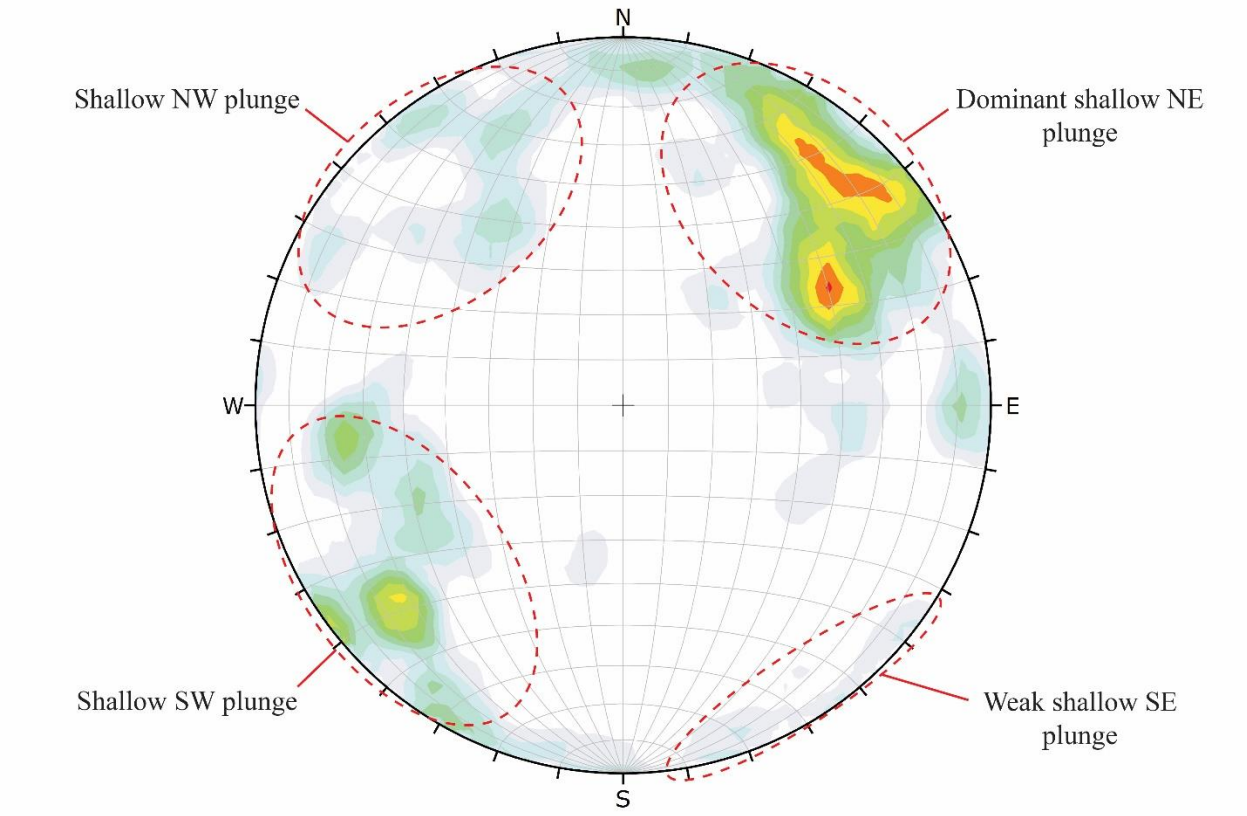

Fig. 4.3. Schmidt equal-area stereographic projection of all ductile stretching/extension lineations measured from oriented Arrow drill core within foliation planes. N = 367.

The opposing clusters of ductile lineations in Figure 4.3 bear a strong resemblance to a shift in lineation plunge expected from Type 1 dome and basin fold geometry produced by the F_3 and F_4 folds. The separation of pole clusters in the stereonet are likely a reflection of the heterogeneous strain within the partitioned, stacked shear system, with lineation plunge and trend being reoriented locally with progressive shearing and strain partitioning during protracted reactivation. Regional 2D tilt magnetic and Z-TEM geophysical surveys also reveal patterns which resemble a Type 1 fold interference pattern (Fig. 4.5), and provide corroborating evidence for the fold model on a property scale (Fig. 4.7). The schematic constructed in Figure 4.7 lies along the southeastern limb of a regional-scale F_3 fold structure, as illustrated in Figure 4.8. The Clearwater Domain is a deep-seated structure, axial planar to the regional fold structure (Fig. 4.8). A variety

of fold structures are observable at drill core scale, reflecting Deposit and regional scale structures, as well as providing information about the formation of the Arrow high strain zones. The high strain zones are discussed in detail in Section 4.2.

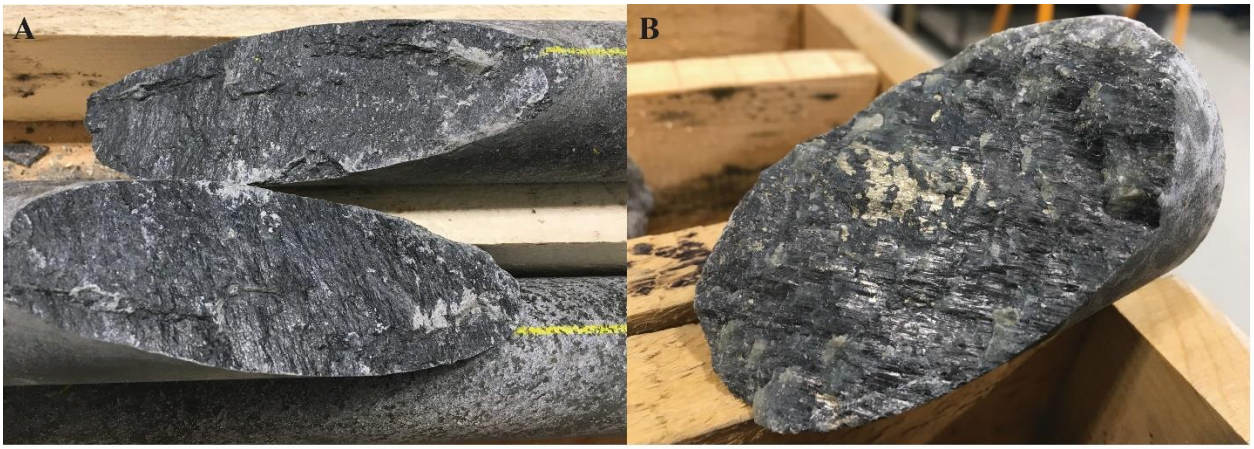

Fig. 4.4. A) Sub-horizontal ductile lineations in chlorite along a foliation plane in Arrow drill core. Drill hole was collared at -70° dip and core diameter is NQ (47.6 mm). Yellow line is bottom-of-hole orientation mark. (AR-18-210c3, 560.0 m). B) Oblique ductile lineations in chlorite along a foliation plane in Arrow drill core. Relatively late, undeformed sulfide mineralization is present along foliation-parallel fracture (GAR-18-007, 489.4 m). Measurements of ductile lineations along foliation surfaces were used to populate the stereographic projections in Figures 4.3 and 4.6.

Fig. 4.5. Well-developed dome and basin interference pattern in minor folds at northeast Turnor Lake, approximately 130 km south-southeast of Patterson Lake. F_3 axial traces are parallel to the long-dashed line and F_4 traces to the short-dashed line. F_3 and F_4 fold generations of the Lloyd fold domain are interpreted to be pervasive through the study area. Figure from Card, 2009.

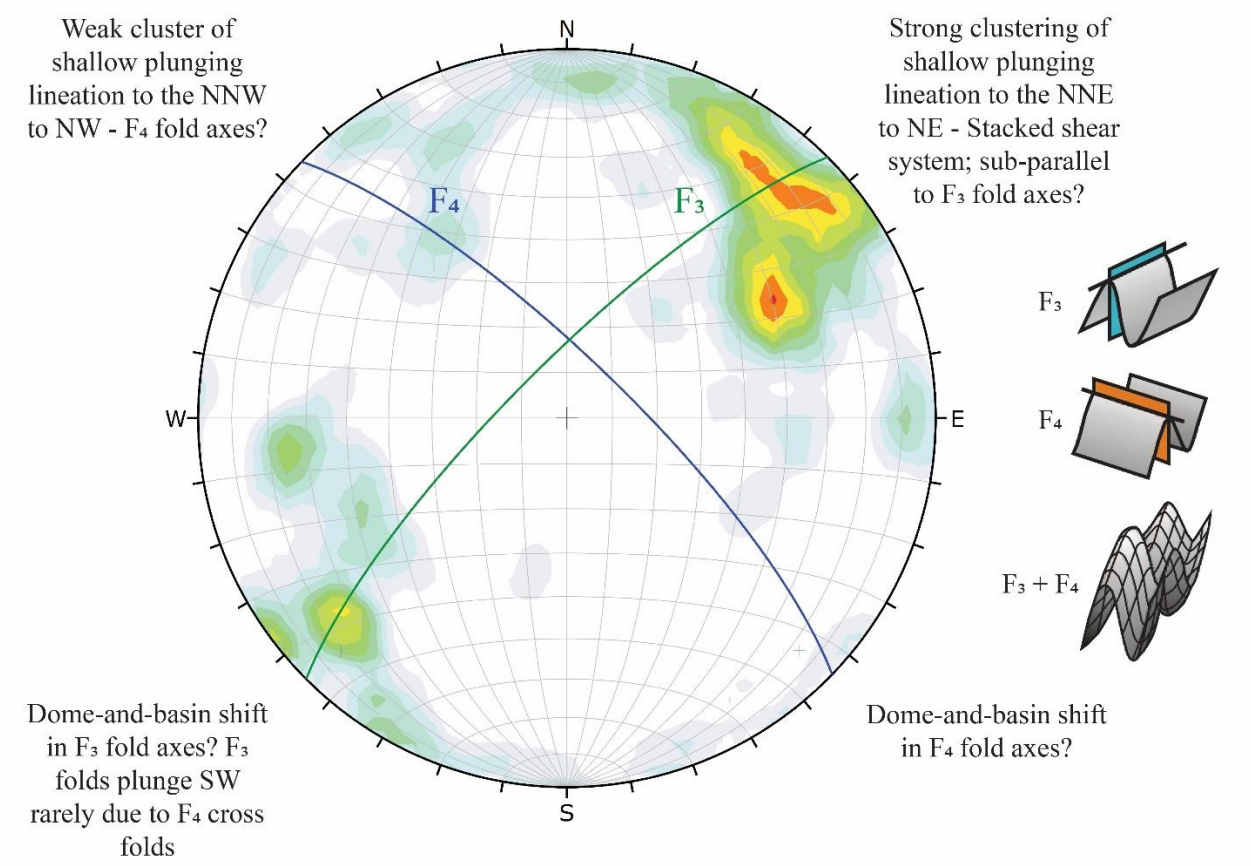

Fig. 4.6. Averaged axial planes constructed from stereographical clustering of Arrow lineations, and three stage schematic of Type 1 dome-and-basin fold geometry. Data of lineations co-linear to axial surfaces display grouping of clusters, resulting in a range of axial plane orientations which correspond to orientations of regional F_3 and F_4 axial planes of the Lloyd fold domain. These orientations also correlate with regional geophysical magnetic fabrics, as well the main foliations observed at Arrow.

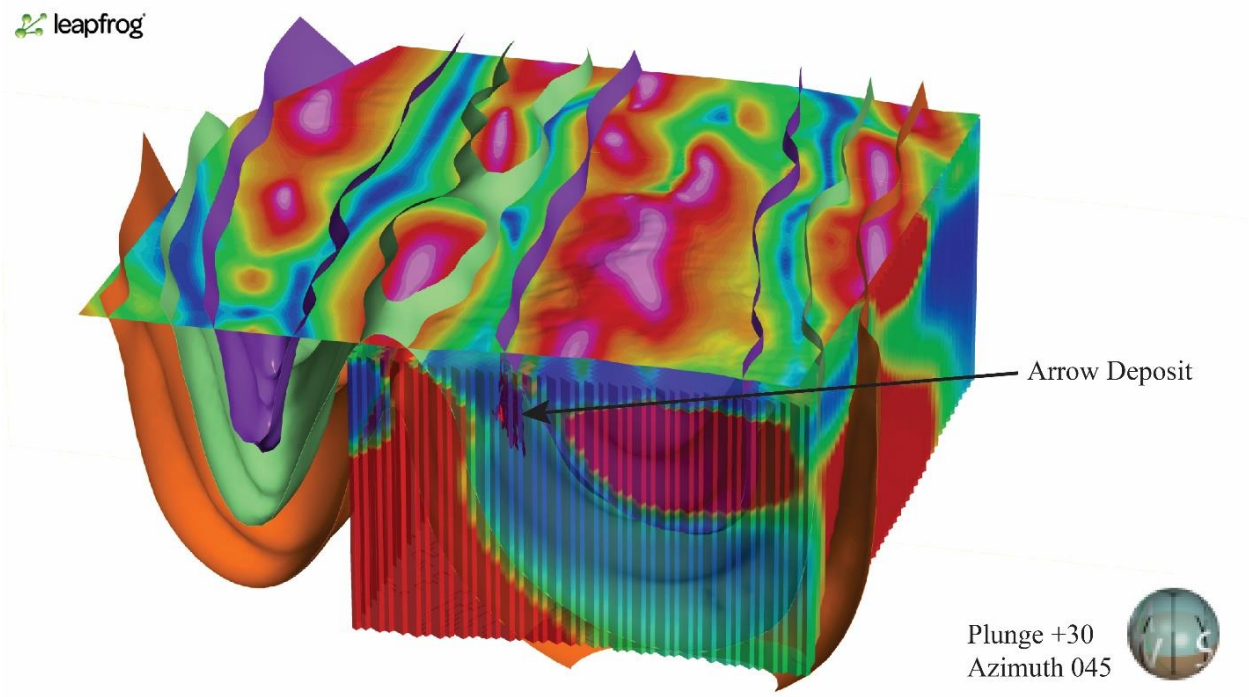

Fig. 4.7. Schematic based on correlation of 2D tilt magnetic and 3D Z-TEM geophysical surveys, showing the Arrow Deposit hosted within the limb of a property-scale F_3 fold, and resulting fold interference patterns within a horizontal slice just above the unconformity surface. Note the scale of the Arrow Deposit resource model.

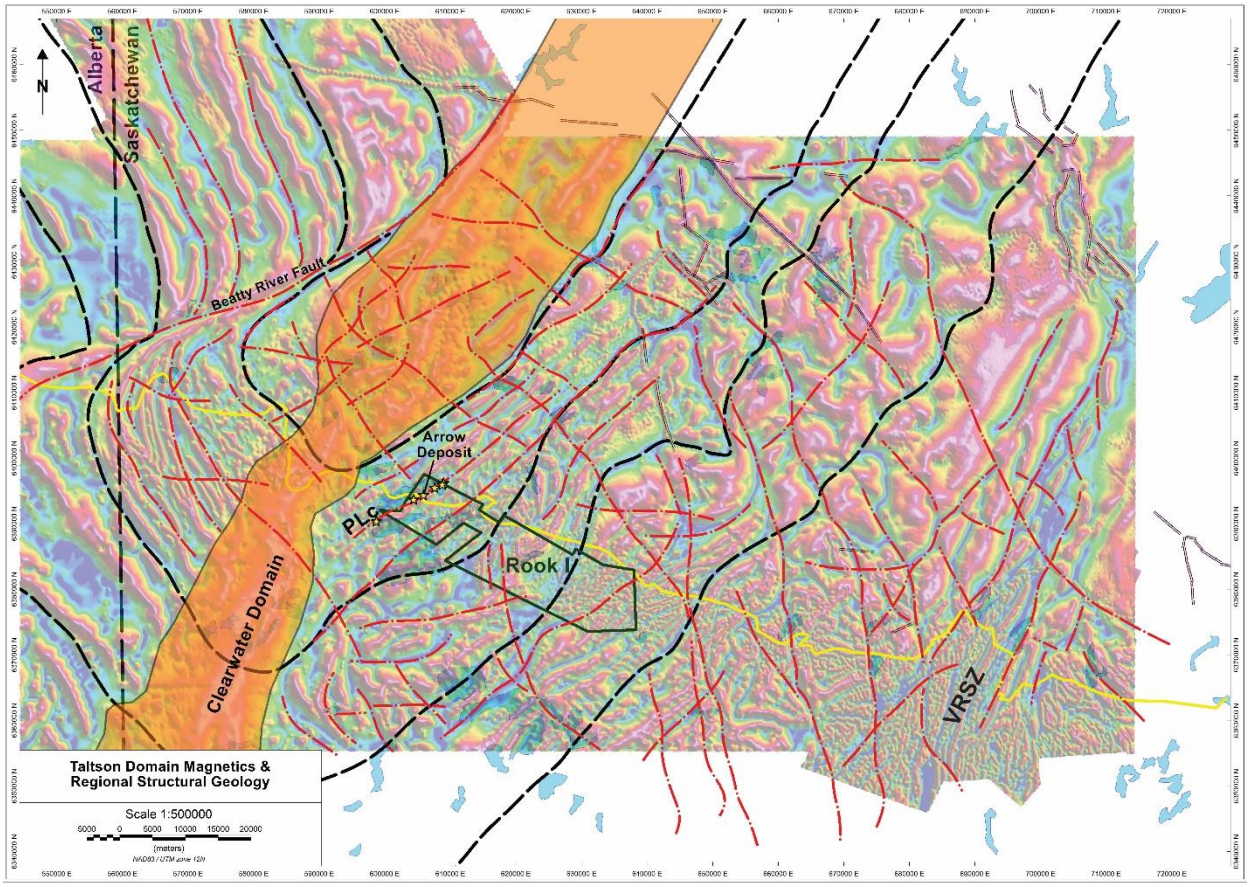

Fig. 4.8. Map illustrating regional structural geology interpretation based on stitched magnetic tilt geophysical surveys (NexGen Energy Ltd., 2018). Note the regional F_3 fold form lines (black dashed lines), interpreted crustal-scale structural corridors (red dashed lines), dykes (purple double lines), Athabasca Basin outline (yellow line), and the Clearwater Domain (orange) following the interpreted F_3 axial plane. Figure 4.7 lies within the SE limb domain of the regional F_3 fold. NexGen's Rook I property is outlined in dark green. Note the aeromagnetic signature of the Virgin River shear zone (VRSZ), and the Arrow and Triple R Deposits, and the South Arrow, Harpoon, Bow, and Spitfire discoveries (yellow stars) along the Patterson Lake corridor (PLc).

4.2 High Strain Zones: A1 to A5 Shears

4.2.1 Structural regime and deformation zone geometry

With depth, strike slip deformation zones become ductile shear zones characterized by sub-vertical foliation and near-horizontal stretching lineations (Fig. 4.1, 4.3, and 4.4), both of which are prominent features proximal to, and within the Arrow high strain zones. Ductile to brittle-ductile shear zones (A1 to A5) developed within the limb domain of a regional-scale F_3 fold (Fig. 4.7 and 4.8) under a partitioned, transpressional strike-slip regime (Fig. 4.9). Transpression is strike-slip deformation that diverges from simple shear due to a component of shortening orthogonal to the deformation zone (Dewey et al., 1998). This type of three-dimensional non-

coaxial strain develops chiefly in response to obliquely convergent (or divergent) relative motions across crustal deformation zones at various scales. Characteristic kinematic partitioning of non-coaxial strike-slip and coaxial strains is prominent in situations where the far-field (plate) displacement direction is sufficiently oblique (< 20°) to the deformation zone boundary (Dewey et al., 1998).

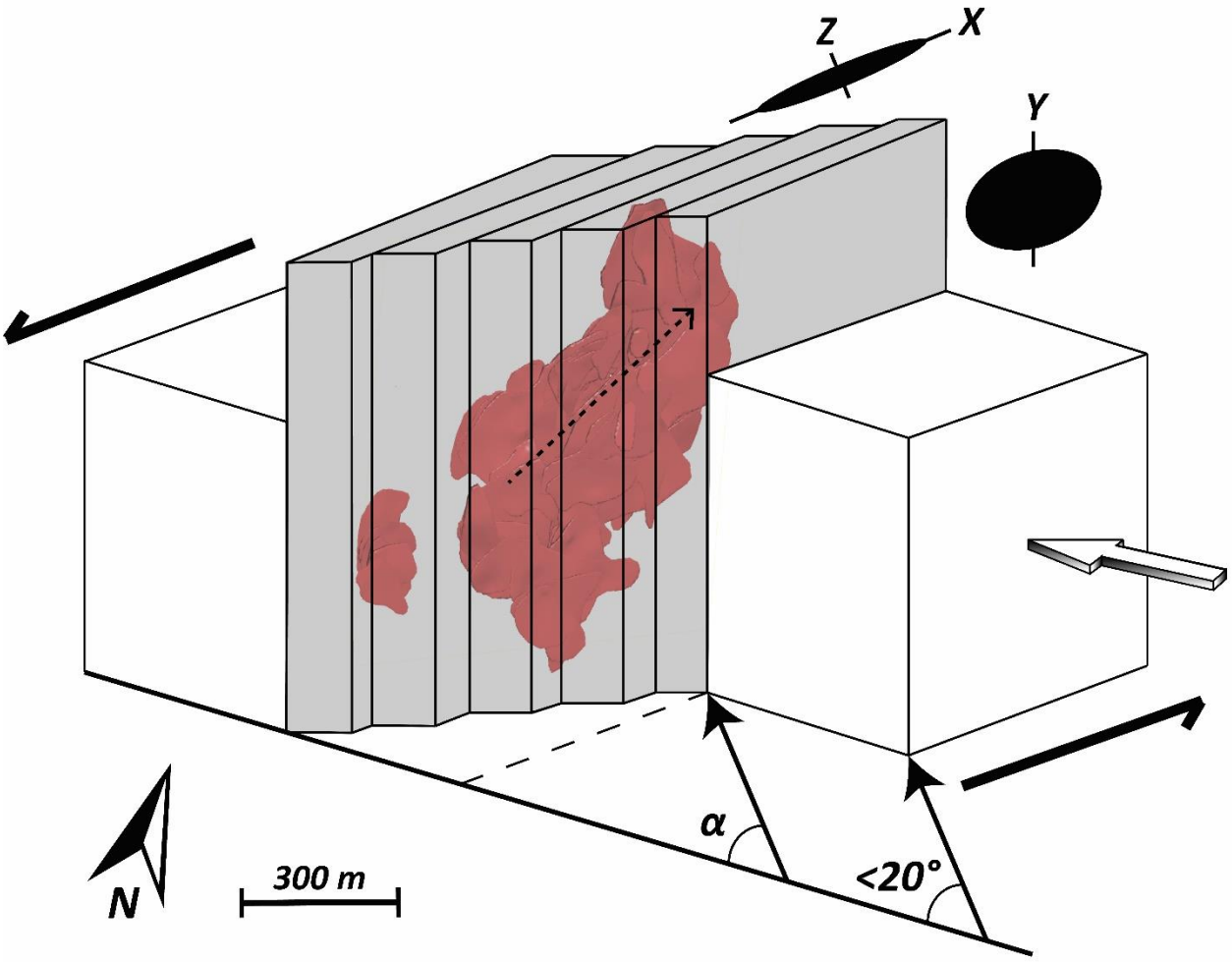

Fig. 4.9. Schematic of a partitioned oblique transpressional strain model overlain on the Arrow Deposit resource model (Mathisen and Ross, 2017). Note the idealized strain ellipses illustrating the principal strain axes (X, Y, and Z) and the shaded arrow indicating direction of bulk shortening (flattening). In nature, relative plate motion vectors, instantaneous strain (or stress) axes and finite strain axes are all oblique to one another in transpression zones (After Dewey et al., 1998). The short-dashed line represents the net slip vector through the Deposit. View azimuth is 355° at 20° plunge.

The angle of obliquity (α, Fig. 4.9), intensity of finite strain, and degree of kinematic partitioning principally control the orientations of fabrics in transpressional and transtensional zones (Dewey et al., 1998). Deformation is localized on steeply dipping faults (> 70°) and

associated structures are typical of a strike-slip regime with Riedel faults when α is small (Section 4.3). As α increases, strain is accommodated by shallow dipping faults that may result in basins or uplift zones. Subsequent reactivation of pre-existing structural weaknesses (shear zones, ductile layers) that are in suitable orientations to minimize work done can facilitate strain partitioning during deformation. Relatively unstrained blocks bound by these shear or fault zones may also help to partition strains into a series of complex displacements, strains, and rotations in response to large-scale tectonic stresses (Dewey et al., 1998). Under transpressional (and transtensional) conditions the deformation zone is commonly steeply dipping or sub-vertical, however the strike of the principal flattening surface (i.e. cleavage, schistosity, foliation/gneissosity) may vary with the non-coaxial component of the strain, as is the case at Arrow (Fig. 4.9 and 4.10).

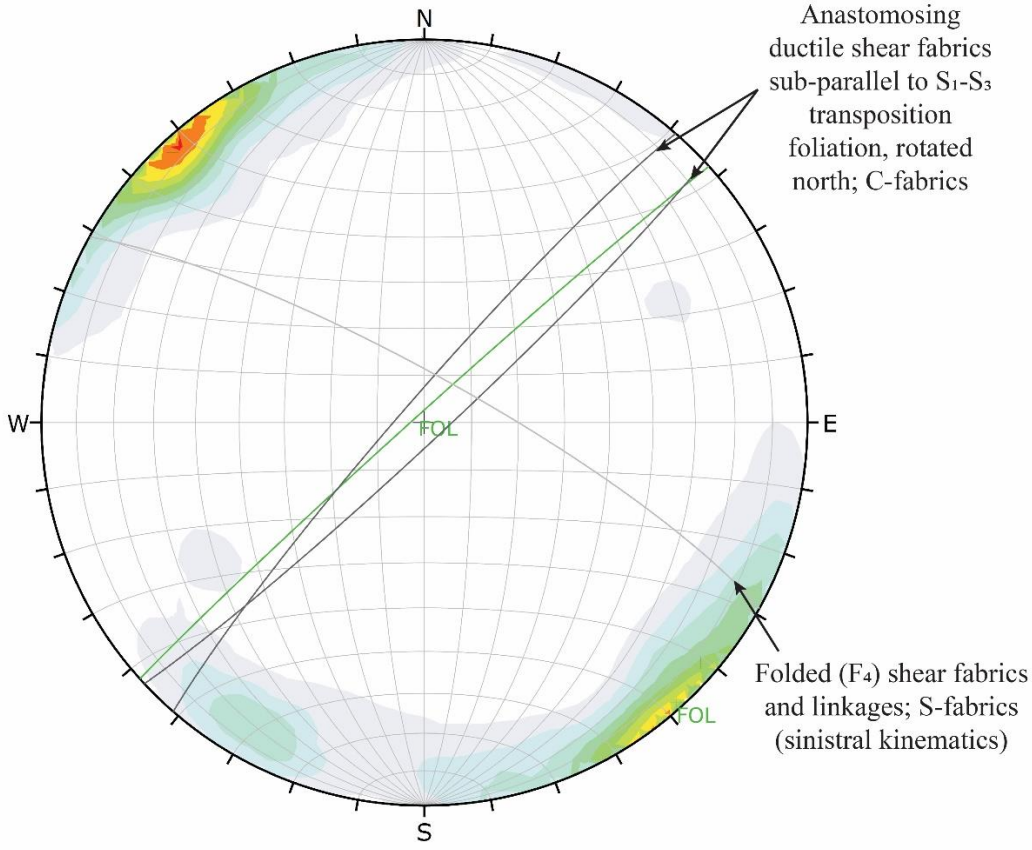

Fig. 4.10. Schmidt equal-area stereographic projection of all high strain zone shear fabric measurements taken from oriented Arrow drill core. Note the shift in strike of the principal 'flattening' surfaces while dip remains sub-vertical. Mean foliation plane (S_1-S_3) is shown in green for reference. N = 555.

In situations where the angle of obliquity (α) is less than 20°, associated stretching and mineral lineations will preferentially form sub-horizontal (Dewey et al., 1998). Such a situation is referred to as 'wrench-dominated transpression' (Dewey et al., 1998). Based on drill core evidence, structural measurements, and deposit-scale structural features (i.e. net plunge/slip), it is suggested that the Arrow deformation zone formed under a partitioned transpressional regime in which a significant component of the wrench component was accommodated by the formation of discrete strike-slip shears/faults (i.e. A1 to A5) within the overall deformation zone (Fig. 4.9). The A1 through A5 shear zones are defined by a series of stacked, near-vertical, NE-striking low- to medium-grade mylonites and phyllonites, extending to at least a kilometer depth below surface. The restraining (transpressional) and releasing (transtensional) bends of the Arrow strike-slip deformation zone are evident in the interpreted structural geometry in Figure 2.8. The staircase-like trajectory of the interpreted graphitic structures in Figure 2.8 made up of alternating long and straight (vertical equivalent to flats) traces connected by oblique bends and jogs (ramps) is a important map-scale geometry resulting from strike slip movement.

4.2.2 Shear zone classification, characteristic fabrics, and shear sense indicators

The heterogeneous strike-slip shear zone hosting the Arrow Deposit contains a spectrum of highly strained rocks. In the literature, authors have classified these rocks in different ways, based on mineralogy (e.g. quartz-feldspar mylonite), on the metamorphic grade at which the structure formed (e.g. high-grade mylonite), or on relative porphyroclasts and matrix percentages (e.g. Schmid and Handy, 1991). Rocks comprising 10-50% matrix are classified as protomylonites, rocks with 50-90% matrix are mylonites, and rocks constituted by >90% matrix are termed ultramylonites (Passchier and Trouw, 2005). Fine-grained mica-rich mylonites are commonly referred to as phyllonites, resembling a phyllite, and being derived from schists (Trouw et al., 2009). Problems with these classifications are attributed to the variety of different mylonitic rocks that can be formed under the same conditions from different parent rocks, and the arbitrary choice of matrix percentages between mylonite classes. For the purposes of this paper, the highly strained rocks within the Arrow deformation zone will be described based on type and completeness of recrystallization, matrix content, and micaceous mineral content. The Arrow A1 through A5 high strain zones are dominantly composed of low- to medium-grade mylonites, with local high-grade mylonites and phyllonites. The terms protomylonite and ultramylonite will be used intermittently

where appropriate, as the same general parent rock is being considered. These strongly deformed rocks are overprinted by abundant brittle fault rocks, described in Section 4.3.

The mylonitized rocks at Arrow are characterized by the presence of a moderate to strong LS fabric, close to isoclinal high-strain and parasitic folding (Fig. 4.11), ribboned and variably recrystallized quartz, a relatively fine-grained matrix with porphyroclasts, and asymmetric structures including C-type and rare C'-type shear bands (Fig. 4.12 and 4.13C and D), mantled porphyroclasts (Fig. 4.13A and B), augen texture (Fig. 4.13A and B), stair-stepping (Fig. 4.13E), and oblique foliations (Fig. 4.13F). Geometries of asymmetric structures and fracture/vein offsets indicate a prevalent oblique, sinistral sense of motion, with a dominant strike-slip component and variable late movement (reverse and normal) along small-scale structures. The high strain zones within the Arrow zone trend NE-SW, with zones of highest strain (i.e. C-fabrics) oriented sub-parallel and oblique to the main S_1-S_3 transposition foliation. Like the main foliation, the shear fabric measurement poles exhibit a distribution across the stereonet due to their sub-vertical, anastomosing nature (Fig. 4.10). A weaker, near orthogonal trend is also present in the data, reflecting local folding of shear fabrics, S-fabrics, and linkages between shear zones as illustrated in drill core (Fig. 4.11 and 4.12). C-type (cisaillement) shear bands observed in drill core are relatively straight and lie parallel to the shear zone boundary, dipping steeply and often sub-parallel or oblique to core axis (Fig. 4.13C). C'-type shear bands are oblique to shear zone boundaries and the older foliation (S fabrics), and commonly form within more micaceous mylonites (Passchier and Trouw, 2005). Shear fabrics may also end up oriented near orthogonal to the shear zone boundary due to changes or distortion of the flow field during deformational events (Fig. 4.13F). Furthermore, a less common dextral sense of motion is also recorded in oriented core data and locally observable in early ductile shear fabrics. However, this is often overprinted by later sinistral motion, indicating changes in stress fields over the deformational history of the Patterson Lake corridor. This is no surprise, as many of the major crustal-scale deformational zones formed during the thermotectonic events affecting the southwestern Rae province, such as the Grease River shear zone, initially formed under dextral kinematics. At Arrow, relatively late brittle-ductile to brittle reactivation appears to have been dominantly under a sinistral deformational regime (Section 4.3).

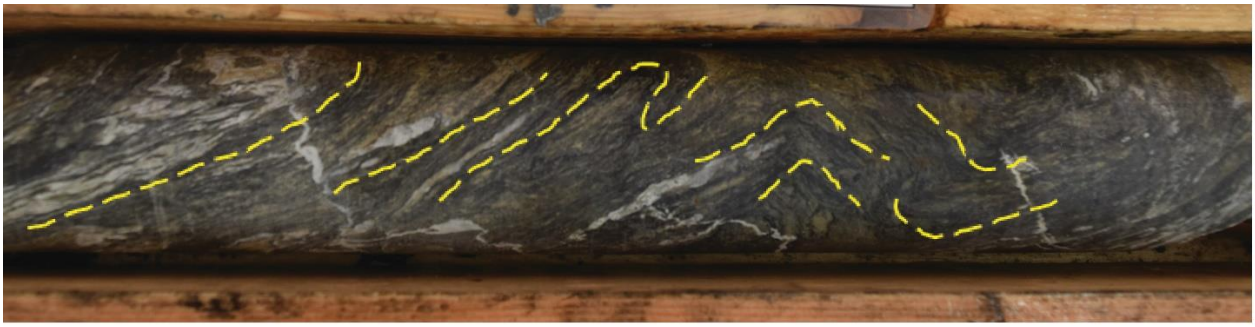

Fig. 4.11. Core photo and fold-trace of a brittle reactivated chloritic-graphitic medium-grade mylonite exhibiting open to isoclinal folding of shear foliations (A1 Shear, AR-16-084c1, 740.6 to 741.0 m, up to 200 cps). Note Brittle reactivation and perpendicular shear fabrics due to F_3 folding and possible F_4 or high strain folding as illustrated in Figure 4.10.

The foliations within in the Arrow high strain zones are locally subject to open to isoclinal folding (Fig. 4.11), interpreted as a result of local distortion in the flow field during their formation. Many of these folds are asymmetric, cylindrical curtain folds, with a straight, sub-horizontal fold axis parallel to the lineation (Fig. 4.14A). Curtain folds are regularly observed to decrease in amplitude and fade out laterally (Passchier and Trouw, 2005).

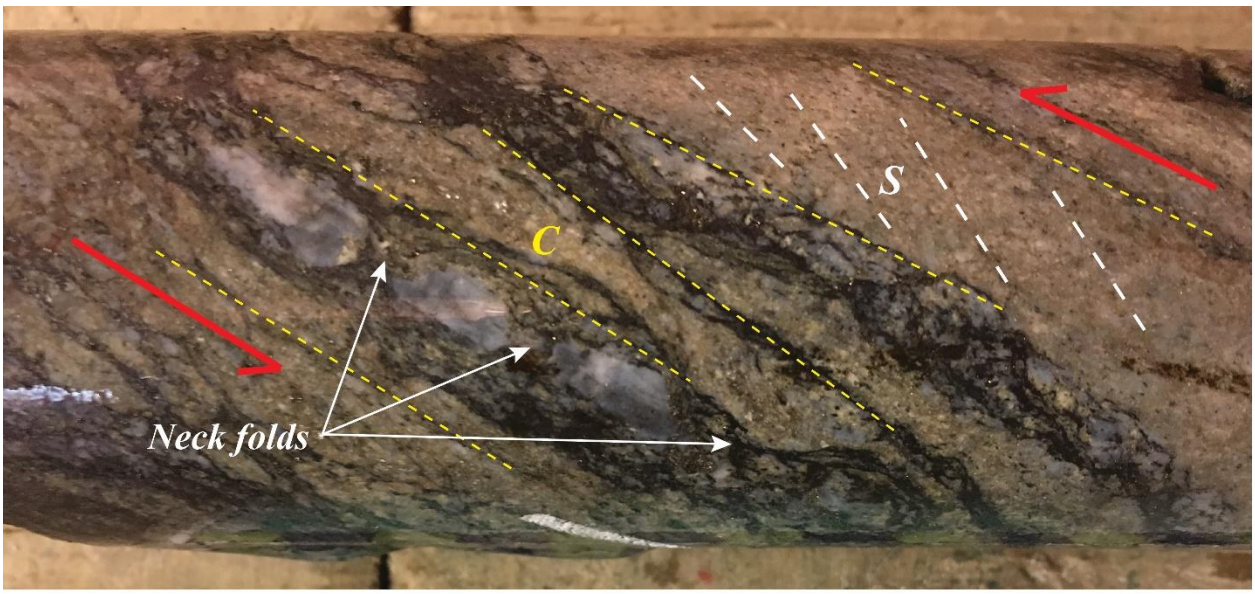

Fig. 4.12. Core photo and kinematic interpretation of a sericitic-chloritic-graphitic low-grade mylonite with graphite- and chlorite-rich C-fabrics, oblique S-fabrics, and slightly asymmetric shearband boudins of quartz with neck folds (A4 Shear, AR-17-147c4, 756.4 m, up to 1,320 cps).

At Arrow, parasitic folds and high strain curtain folds are commonly observed in drill core (Fig. 4.14B through D) and decrease in amplitude vertically due to the steeply dipping geometry of the high strain zones (Fig. 4.14A), while mylonitic foliations decrease in intensity laterally away

from the core of the shear zone. Although sometimes difficult to identify in drill core, fold interference patterns and (limb) foliation angles (Fig. 4.14B through D) indicate curtain and sheath folds are present locally within the Arrow high strain zones. Quartz ribbons very commonly exhibit isoclinal and ptygmatic folding (Fig. 4.13G and H), due to the relative competency contrast between the quartz (high competency) and the chloritic, sericitic, and/or graphitic matrix (low competency) of the shear zone.

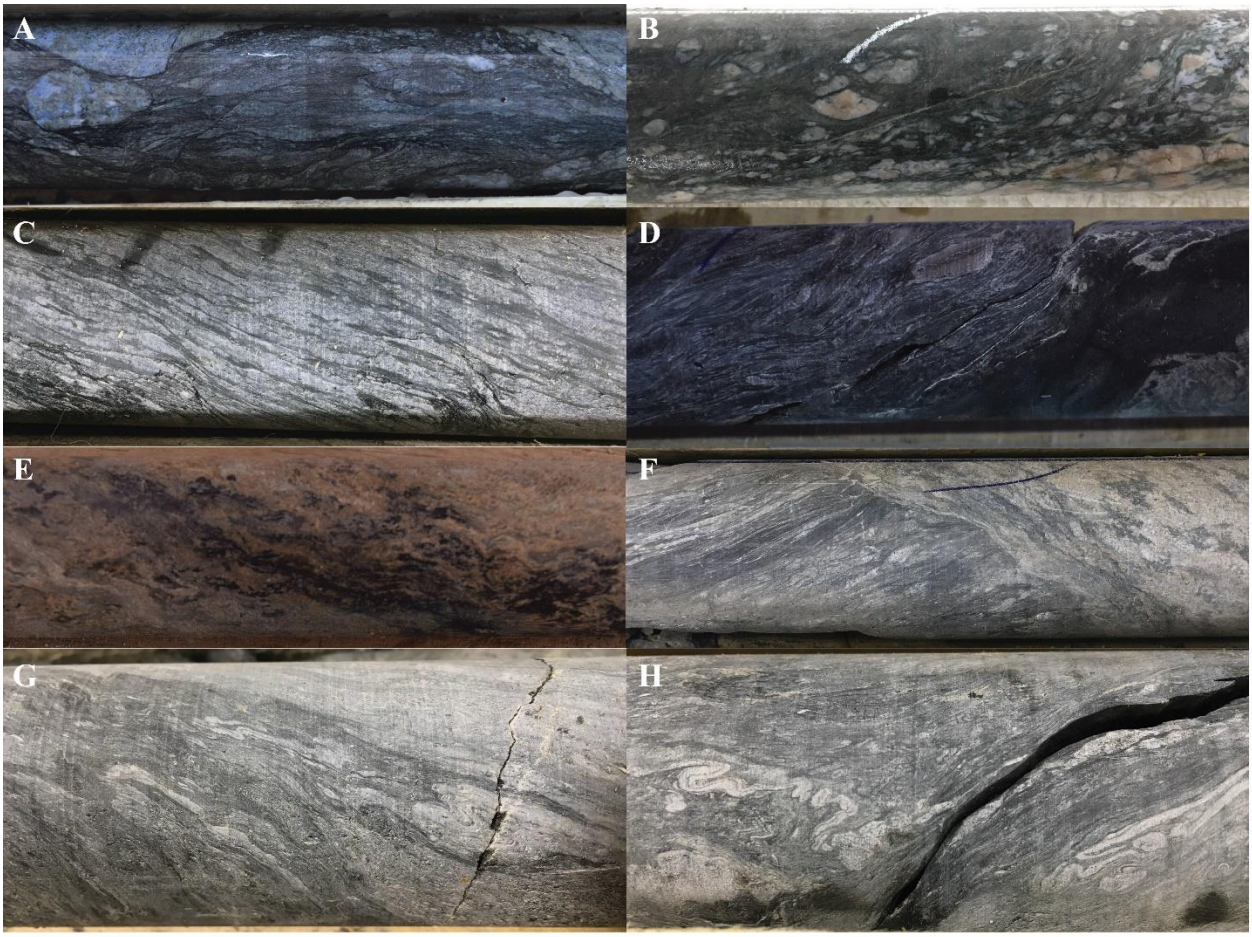

Fig. 4.13. A) Low-grade graphitic mylonite with wall rock porphyroclasts, quartz augen, and local isoclinal folding (AR-15-058c1, 430.1 m). B) Medium-grade mylonite in granitic rock with σ-type porphyroclasts and quartz-feldspar augen (AR-18-210c3, 580.1 m). C) Chloritic-graphitic mylonite exhibiting moderately developed C-S fabrics (AR-18-216c1, 350.4 m). D) Mineralized graphitic mylonite with porphyroclasts, late quartz veining, and sigmoidal curvature of shear bands (AR-17-167c2, 467.1 m, up to 54,500 cps). E) Strongly clay-altered mylonite with uranium mineralization mimicking stair-stepping shear foliation (AR-17-115c1, 604.0 m, up to 9,300 cps). F) Medium-grade graphitic mylonite contact with shear foliations conjugate to wall rock foliation (AR-18-214c1, 254.65 m). G) Graphitic mylonite with isoclinally folded intrafolial quartz ribbons (AR-18-214c1, 255.2 m). H) Graphitic mylonite with intrafolial quartz ribbons exhibiting ptygmatic and isoclinal folding (AR-18-214c1, 255.3 m).

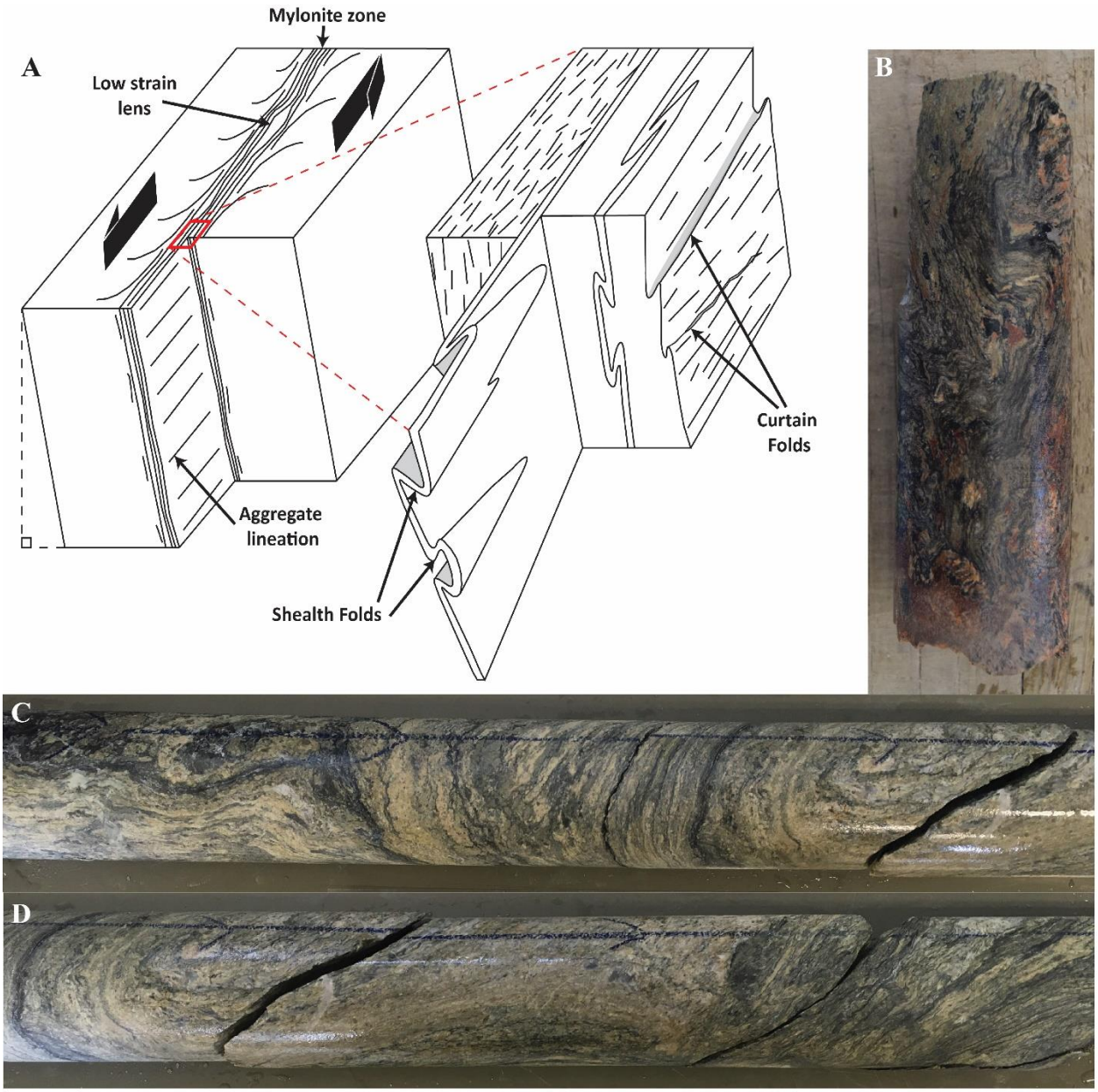

Fig. 4.14. A) Schematic of high strain curtain and sheath folds forming within a sinistral mylonite zone cutting steeply dipping rocks (After Passchier and Trouw, 2005). B) Uranium mineralization precipitated along an asymmetric curtain fold exhibiting smaller-scale parasitic folding (AR-16-093c1, 461.8 to 461.95 m, up to 26,000 cps). C) Sheath fold in chloritic-sericitic phyllonite indicated by "eye-fold" interference pattern (center of photo) in drill core (AR-17-115c1, 678.8 m). D) Asymmetric curtain fold in chloritic-sericitic phyllonite noted by steep foliation core axis angle on the uphole limb (far left of photo) and shallow core axis angle on the downhole limb (left of center in photo; AR-17-115c1, 679.0 m).

4.2.3 Shear zone mineralogy and alteration

The Arrow high strain zones exhibit a range of alteration types, altering or replacing matrix-forming minerals (i.e. phyllonites) and are variable in their mineralogy. Dominant alteration assemblages include sericite (fine-grained white mica; Fig. 4.15A), chlorite (sudoite, clinochlore ± chamosite; Fig. 4.15B), and clay minerals (kaolinite, illite – often associated with mineralization; Fig. 4.15C), forming the sheared groundmass or present within crosscutting structures. Quartz-rich mylonitic rocks are also observed locally within the Arrow zone, indicating pervasive silicification prior to ductile deformation (Fig. 15D). Relatively high finite strain values reached within mylonitized rocks imply that the strain rate in the shear zone exceeded that in the wall rock for a notable period, and that the rock in the zone was 'softer' than the wall rock (Passchier and Trouw, 2005). Chloritization of these structures was among the primary alteration phases during the retrograde metamorphic path, weakening and breaking up the rocks, and thus creating significant rheology contrast between the shears and the quartz-rich wall rock. Following the nucleation of the structures, changes occur in the rheology of material in the ductile shear zone through an effect known as strain-softening, or simply softening, defined simply as decreasing resistance to deformation (Passchier and Trouw, 2005). The A1-A5 shears exhibit many of the important progressions that contribute to softening such as grain boundary migration recrystallization, a decrease in grain size, and development of shear bands or shear band cleavage. Softening through recrystallization and alteration (i.e. chloritization and sericitization) prepped the shear zones for ongoing deformation and fluid movement. Hydrothermal graphite and iron sulphides were introduced into these structures post-chlorite as the fluid evolved through modifications in response to alteration processes and/or during younger fluid flux events, further weakening the rocks and setting up ideal pathways and acting as a reductant for subsequent uraniferous fluids. Based on paragenetic relationships, textural characteristics, and crosscutting relationships in hand specimen and thin section (Section 5.0), the graphite is interpreted to be structurally linked and introduced to the Arrow deformation zone via hydrothermal processes under brittle-ductile conditions (Fig. 4.15E and F). Sulphide minerals were introduced contemporaneously and after graphite, as they are observed to overprint the pre-existing shears, especially those that are graphitic, reusing previous planes of weakness along foliation or fractures, and commonly crosscut earlier fabrics as irregular stringer veins (Fig. 4.15F). The sulphide mineralogy is discussed in more detail in Section 5.0, however iron-rich sulphides (pyrite,

chalcopyrite, pyrrhotite) are the dominant sulphide minerals encountered within the Arrow shear zones.

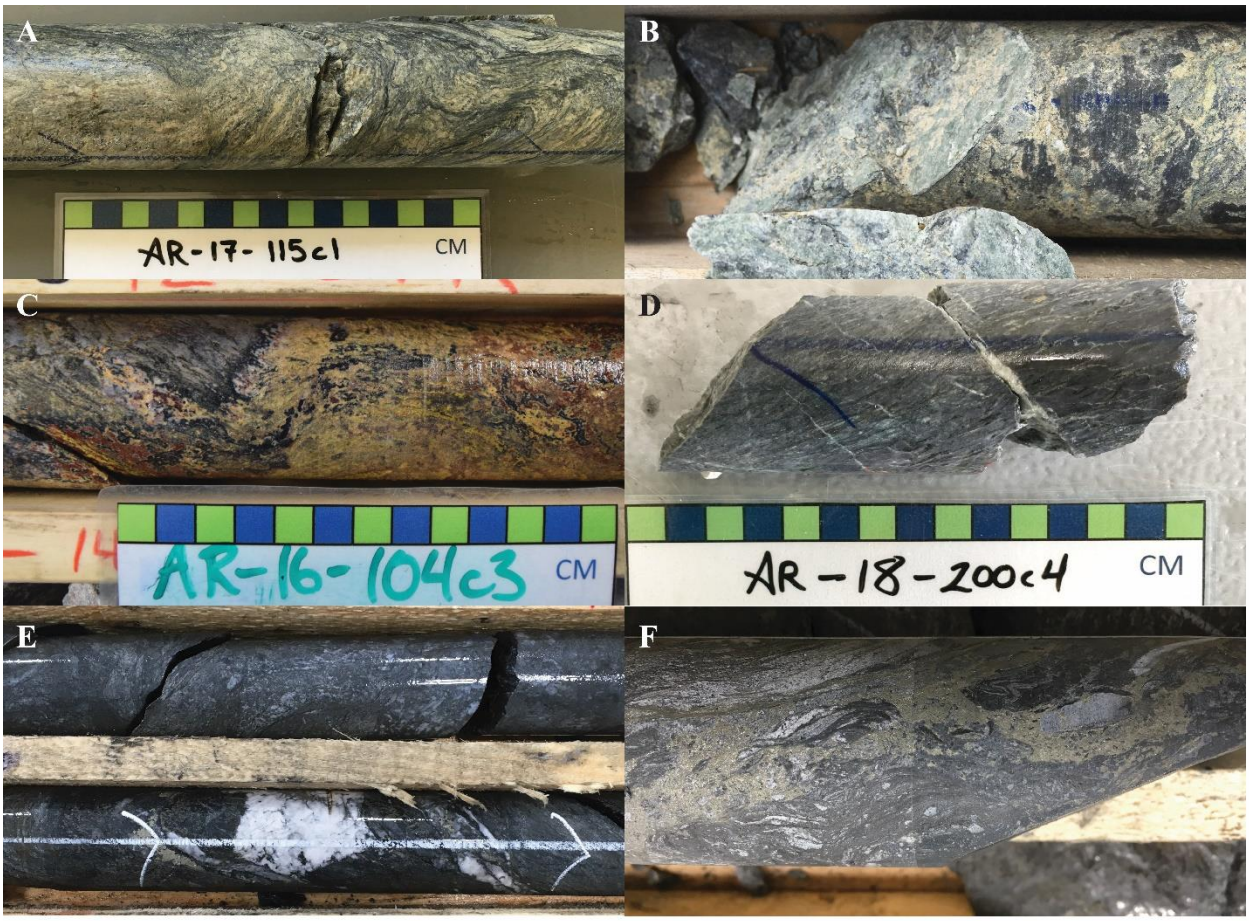

Fig. 4.15. NQ drill core photos illustrating the variable mineralogy of the Arrow high strain zones. A) Pervasively sericite- and chlorite-altered phyllonite with late structurally controlled graphite and sheath folding (AR-17-115c1, 679.4 m). B) Strong pervasive light green sudoite, dark green clinochlore, and yellowish sericite alteration lining fractures and replacing minerals in the A2 high strain zone (AR-17-115c1, 683.0 m). C) Strongly clay- and hematite-altered mylonite hosting black uraninite and yellow secondary uranium mineralization (AR-16-104c3, 708.7 m, up to 27,000 cps). D) Medium-grade mylonite consisting dominantly of smoky blue-grey quartz with late clay- and white quartz-lined fractures crosscutting foliation at high angle (AR-18-200c4, 769.5 m). E) Chloritic-graphitic mylonite with late white quartz veining and sulfide mineralization precipitated during reactivation (AR-18-211c1, 1,083.7 m). F) Brittle-reactivated mylonite with quartz ribbons and clasts hosted in a fine-grained matrix of graphite. Graphite and iron sulfides reuse and crosscut pre-existing shear foliation throughout (AR-18-210c3, 805.4 m).

4.2.4 Shear zone P-T conditions

Preservation of mylonitized rocks at Arrow indicate they likely formed during intense and/or rapid deformation during the retrograde leg of the P-T-t path ca. 1.8 Ga or younger, as their textures have generally not been destroyed or overprinted by recrystallization and grain growth

associated with later higher-grade metamorphism. The temperature range for low-grade mylonites is thought to be approximately 250° to 500°C, with a gradual transition between formation of cataclasites and low-grade mylonites through the brittle-ductile transition zone (Trouw et al., 2009). The temperature range for the formation of medium-grade mylonites is between 500° to 650°C, in which quartz is commonly fully recrystallized and gradual transitions to non-mylonitic country rocks are common (Trouw et al., 2009). These temperature ranges indicate that the Arrow shear zones formed after peak granulite facies metamorphism during the retrograde metamorphic P-T-t path. The quartz grains within the mylonitized rocks at Arrow exhibit a range of characteristics which are associated with the high strain imposed on these rocks during shear zone genesis. Feldspar porphyroclasts within low-grade mylonites commonly exhibit fracturing by cataclasis, however quartz is usually deformed via crystal-plastic processes, evidenced through undulose extinction and change in crystal shape and boundaries (Fig. 4.16A and B). In medium-grade mylonites quartz is dominantly recrystallized through subgrain rotation (SGR; Fig. 4.16B and 4.17A and B), growing to a polygonal crystalloblastic fabric of strain free grains exceeding 50 micrometers (Trouw et al., 2009).

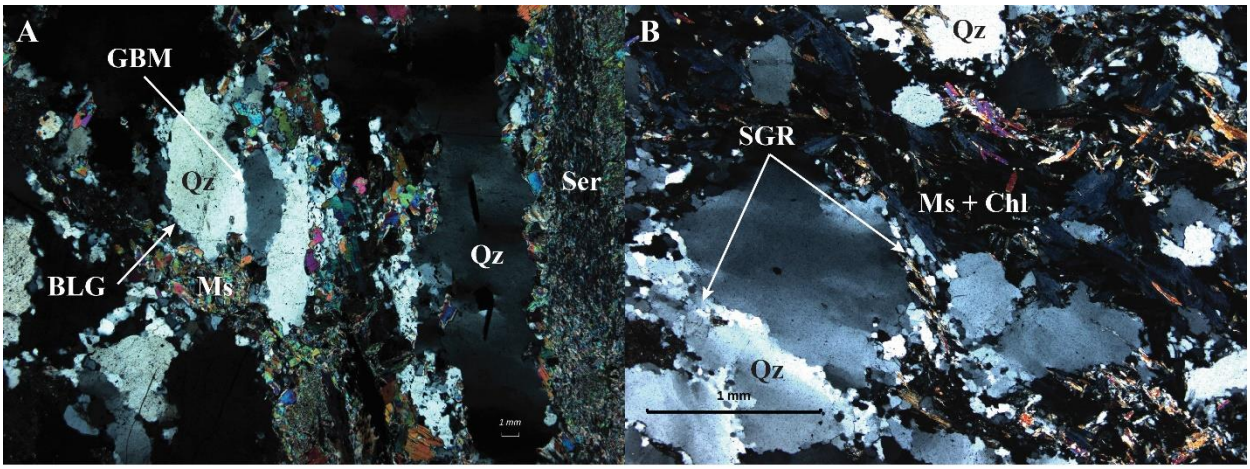

Fig. 4.16. A) Quartz grains within the northeastern portion of the A2 shear zone exhibiting a spectrum of dynamic recrystallization textures including grain boundary migration (GBM) and bulging (BLG) indicative of a transition from high to low temperature and a corresponding decrease in strain rate (A2 Shear, AR-16-078c2, 437.0 m). B) Quartz grains within the A4 shear zone showing evidence for crystal-plastic deformation through well developed undulose extinction and subgrain rotation recrystallization (SGR) (A4 Shear, AR-16-082c2, 717.6 m).

Textural characteristics observable in thin section may be used to approximate temperature ranges of mylonite formation and/or metamorphic grade of the associated deformational event, however earlier deformational stages may be overprinted and no longer recognizable. These include evidence of crystal-plastic deformation in quartz (i.e. undulose extinction and subgrain

rotation recrystallization), size of recrystallized quartz grains (< 50 > micrometers), comminution of refractory minerals (i.e. feldspar) into tiny new grains through cataclasis vs. recrystallization, and asymmetric structures/shear sense indicators (Trouw et al., 2009). Thin section examination of quartz grains within and proximal to the Arrow high strain zones reveals evidence for both crystal-plastic and brittle/frictional deformational processes, indicating these zones underwent continued deformation through the brittle-ductile transition zone (Fig. 4.16A and B, and 4.17B). SGR recrystallization appears to be dominant in the samples examined, however higher temperature grain boundary migration recrystallization (GBM) and lower temperature bulging recrystallization (BLG) have both been observed (Fig. 4.16A).

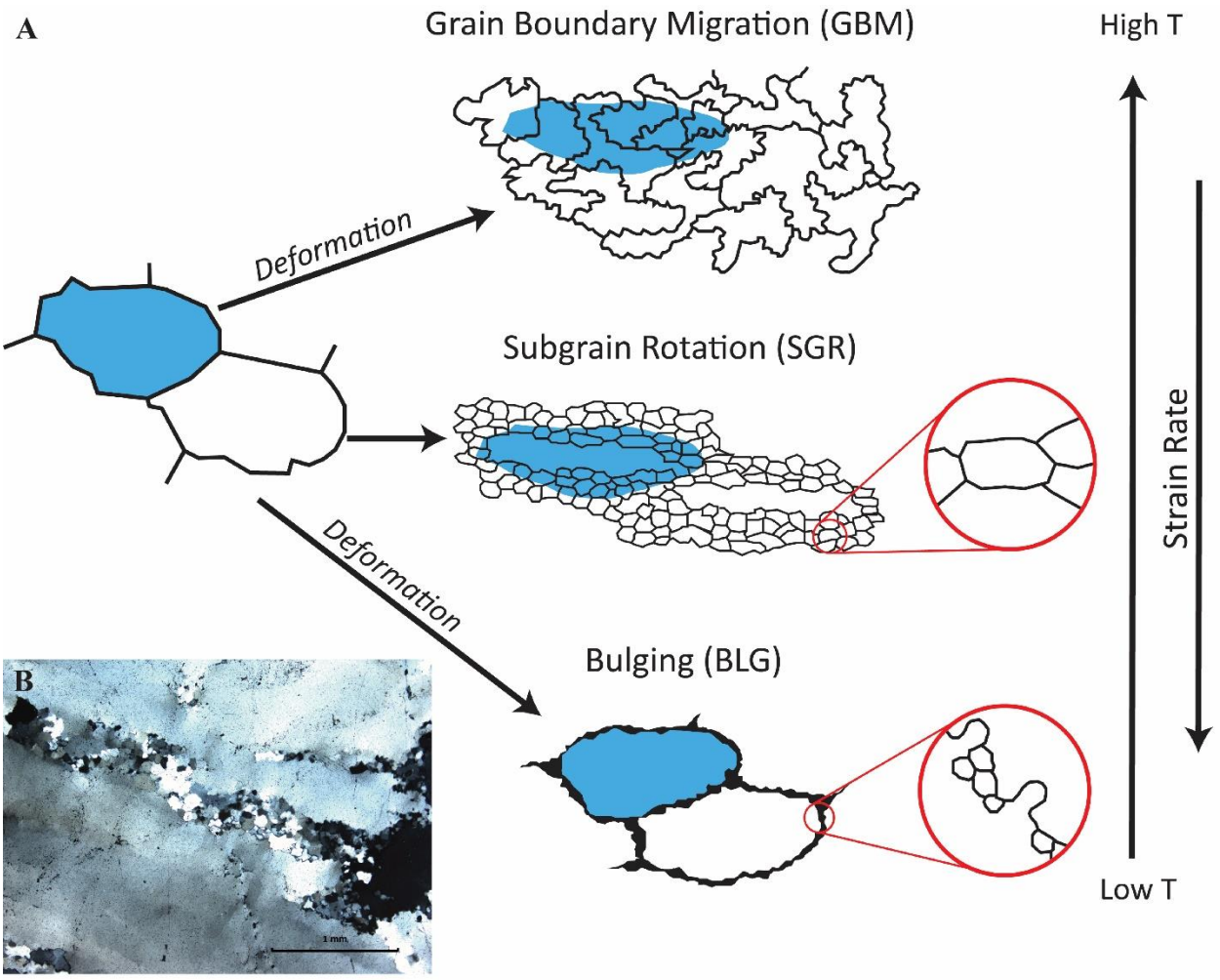

Fig. 4.17. A) Schematic of the three main types of dynamic recrystallization processes in a polycrystalline aggregate with respect to temperature of deformation and strain rate (After Trouw et al., 2009). B) Evidence for subgrain rotation recrystallization in blue quartz proximal to the A3 shear zone in the footwall (AR-16-074c1, 630.3 m).

Based on hand specimen and thin section analysis of mineral textures and grain boundary relationships proximal to and in the core of the Arrow high strain zones, it is suggested that these high strain zones initially formed within a ductile regime at around 20 km crustal depth. These zones then further evolved through the brittle-ductile transition zone forming low-grade mylonites and phyllonites, followed by cohesive cataclasites, and finally incohesive breccias and gouge with prolonged exhumation (Section 4.3; Fig. 4.18). Due to the extensive deformational history and thus recrystallization, it is likely that many of the earlier, higher P-T recrystallization and mineral textures have been overprinted and destroyed.

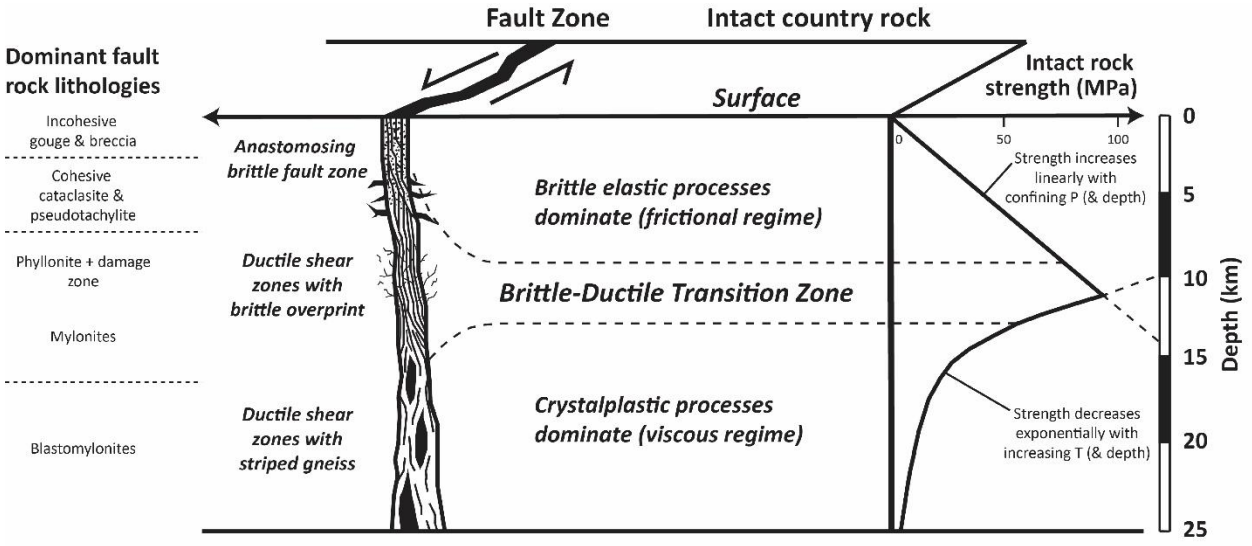

Fig. 4.18. Conceptual model and strength profile for a crustal scale sinistral strike-slip shear zone illustrating the variety of fault rock types and depths of formation, relative to quartz deformation processes and rock strength (After Imber et al., 2008).

4.3 Brittle Fault Rocks

Deformation in rocks is not homogeneously distributed. Ductile shear zones are active at higher metamorphic conditions than brittle shear/fault zones (Passchier and Trouw, 2005). In general, shear zones can be subdivided into brittle zones or faults at higher crustal levels, and ductile shear zones at lower crustal levels, which generate characteristic fabrics and mineral assemblages that reflect the P-T conditions and flow type (Fig. 4.18; Passchier and Trouw, 2005). Thus, major structures that transect the crust have both brittle and ductile segments and may be

active for considerable periods of time resulting in the rocks showing evidence of several overprinting stages of activity at different metamorphic (P-T) conditions (Passchier and Trouw, 2005). A special terminology is used for these rocks that have been deformed within shear zones, commonly referred to as 'fault rocks' or 'deformation zone rocks', which includes mylonites and striped gneiss, as well as brittle fault rocks (Passchier and Trouw, 2005). Brittle fault rocks form via fault propagation through intact rock, frequently along an older plane of weakness, such as a ductile segment of the overall high strain zone (Passchier and Trouw, 2005). The Arrow deformation zone contains abundant brittle fault rocks including incohesive fault breccias, cataclasites, and fault gouge, with rare cohesive cataclasites, typical of low-temperatures within the upper 10 kilometres of the Earth's crust (Imber et al., 2008; Fig. 4.18). Meter-scale extensional 'fault-fill' veins (Section 4.3) also overprint ductile strain and are encompassed by a damage zone of Riedel shear fractures and linkages, tension gashes, and hydraulic (fluid over-pressuring) breccias. These brittle structures overprint the ductile to brittle-ductile high strain zones at Arrow and crosscut relatively unstrained wall rock, often at low angles relative to the near-vertical ductile to brittle-ductile shear zones. Brittle shear fractures and breccias are among the most frequently mineralized structures within the Arrow zone, as described in Section 4.4.

4.3.1 Riedel shear fractures and kinematics

During reactivation of pre-existing structures, strain may be accommodated by a variety of en-échelon structures including Riedel shear fractures, thrusts, normal faults, and folds. In this case, individual fractures may remain active, or become re-activated, after other types have developed, so that simultaneous movement on all fractures accommodate strain within the strike-slip deformation zone. Experiments conducted by Riedel in the early 1900s, and numerous other experiments using 'clay-cake' models (e.g. Tchalenko, 1968; 1970; Naylor et al., 1986; Lazarte and Bray, 1996; Atmaoui 2005), have revealed a consistent timing and faulting sequence of these prominent features in strike-slip fault zones. This led to the discovery that strike-slip faults often do not develop a single, clean fault but a zone of deformation involving an array of small fractures (Fig. 35; e.g. Tchalenko, 1968; Davis et al., 2000; Haakon, 2010). In deep-seated wrench-dominated faulting, synthetic and antithetic Riedel shear fractures are among the primary features to appear in strike-slip zones and evolve as a series of linked displacement surfaces (Davis et al., 2000). Sets of subsidiary shear fractures that propagate a short distance out from the main fault or

shear, but are coeval with it, are termed Riedel shear fractures. Riedel shear structures are common networks of shear bands, commonly developed in zones of simple shear during the early stages of fault formation (Katz et al., 2003). Riedel shear fractures developed along a fault or slip surface show distinct geometric arrangements that carry information about the movement sense on the fault plane (Passchier and Trouw, 2005). Although Riedel shears resemble ductile shear bands, they form by brittle fracturing of rock (Passchier and Trouw, 2005). These small fractures have been given different names based on their orientations and kinematics (Riedel, 1929). In large-scale fault patterns, Riedel fractures may refer to as many as six direction groups (R, R', P, P', Y, T) of associated synthetic or antithetic smaller-scale fractures (Fig. 4.19). Riedel (R) fractures tend to be more common than R' and P-fractures, but they are all broadly coeval. With progressive strain, Riedel structures tend to grow and organize in dense elongated networks through individual shear fractures and extension fractures forming and ultimately linking up. This tendency is related to strain localization during the shear-zone evolution and provides a way in which a strike-slip fault system can form and grow (Katz et al., 2003).

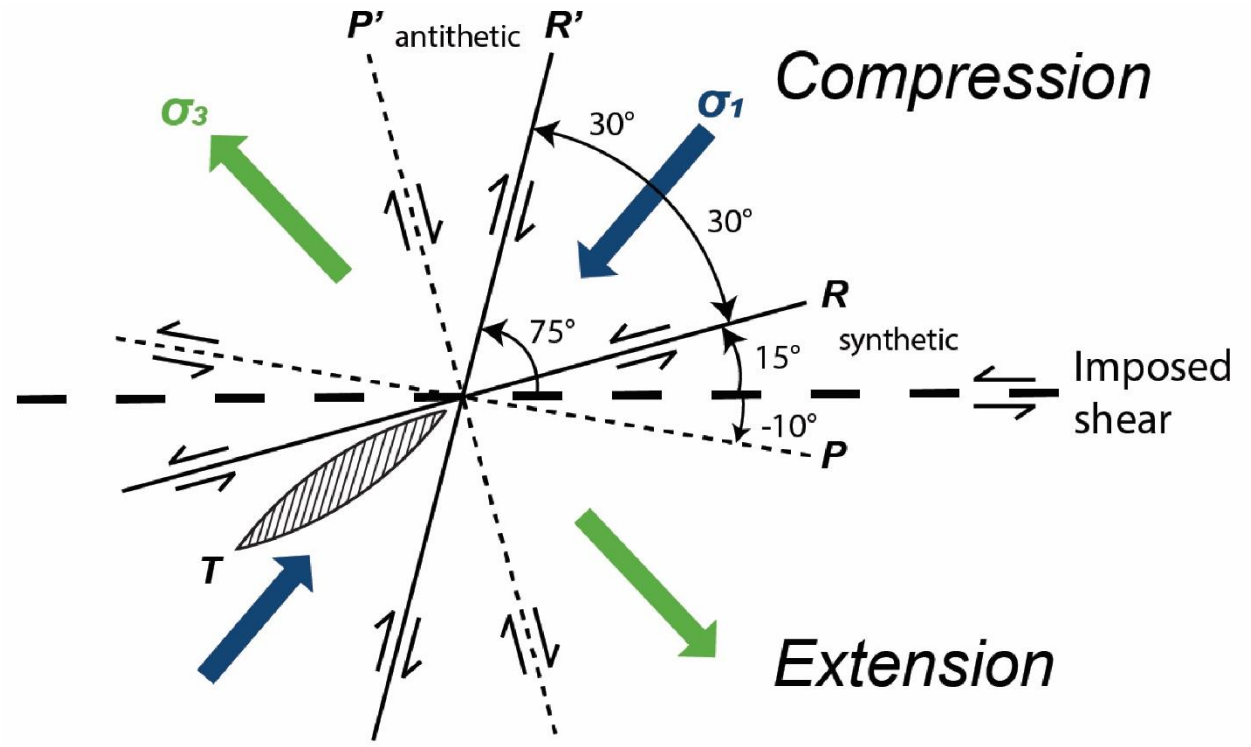

Fig. 4.19. Schematic diagram of the Riedel shear model and the associated synthetic and antithetic subsidiary structures that may develop from a sinistral dominated movement along a strike-slip shear zone (After Twiss and Moores, 1997).

The first subsidiary fractures to develop in strike-slip zones are overstepping, en-échelon arrays of relatively short Riedel (R) shears, forming synthetic to the flattening surface at an acute angle. R-shears are oriented 10-20° clockwise to dextral (right lateral) strike-slip shear zones and counter clockwise to sinistral (left lateral) strike-slip shear zones (Davis et al., 2000; Fig. 35). Propagating and overlapping R-shears may be connected by an en-échelon array of antithetic R'-shears oriented at high angles, approximately 70-80°, counter clockwise to the strike of the deformation zone (Davis et al., 2000). Their orientation is indicative of the sense of displacement along the overall shear zone, forming clockwise to a dextral, and counter clockwise to a sinistral strike-slip shear zone. They are generally less well developed than R-fractures and preferentially occur in the overlap or transfer zone between two parallel R shears, connecting R shears (Haakon, 2010). R'-fractures have shear sense opposite to that of the main fault, and may develop contemporaneously with, or after R-shear fractures while P-shears begin to form with further deformation (Davis et al., 2000; Fig. 4.19).

P-shear fractures are synthetic secondary faults symmetrically oriented to the R shears with respect to the main fault (counter clockwise and clockwise to dextral and sinistral faults, respectively). P-fractures also form an en-échelon array oriented roughly 15° to the shear zone strike, contemporaneous with R-fractures or later as links between R- and R'-shears (Davis et al., 2000). P-fractures are contractional in nature, accommodating fault-parallel shortening as shearing proceeds, and their development is probably related to temporal variations in the local stress field along the shear zone as offset accumulates (Haakon, 2010). Because P-fractures commonly develop later in structural evolution, they are less common than R-fractures and may require a greater degree of displacement to form. P'-shear fractures form correspondingly to R'-fractures, as they develop conjugate to P-fractures and antithetic to the main fault plane. Y-shears form roughly parallel to the trace of the shear zone and act as boundary faults for the brittle fault zone (Davis et al., 2000; Passchier and Trouw, 2005). Finally, an array of extensional T-fractures without displacement may form at 20-50° to Y-shears or the boundaries of the deformation zone (Petit, 1987; Passchier and Trouw, 2005). Linkage of R-, R'-, and P-shear fractures create rhomb-shaped geometry of blocks through the fault zone, which are then commonly overlapped and duplexed, creating an irregular zone of alternating R- and P-shear segments. The geometries of these segments create a result in which P-shears form restraining bends and R-shears form releasing bends (step-over zones) for protracted displacements, influencing where compressional or extensional deformation occurs according to the stepping direction of the fault segments. Drill core-scale examples of these types of shear fractures are common and can provide kinematic information on a local scale (e.g. Fig. 4.20).

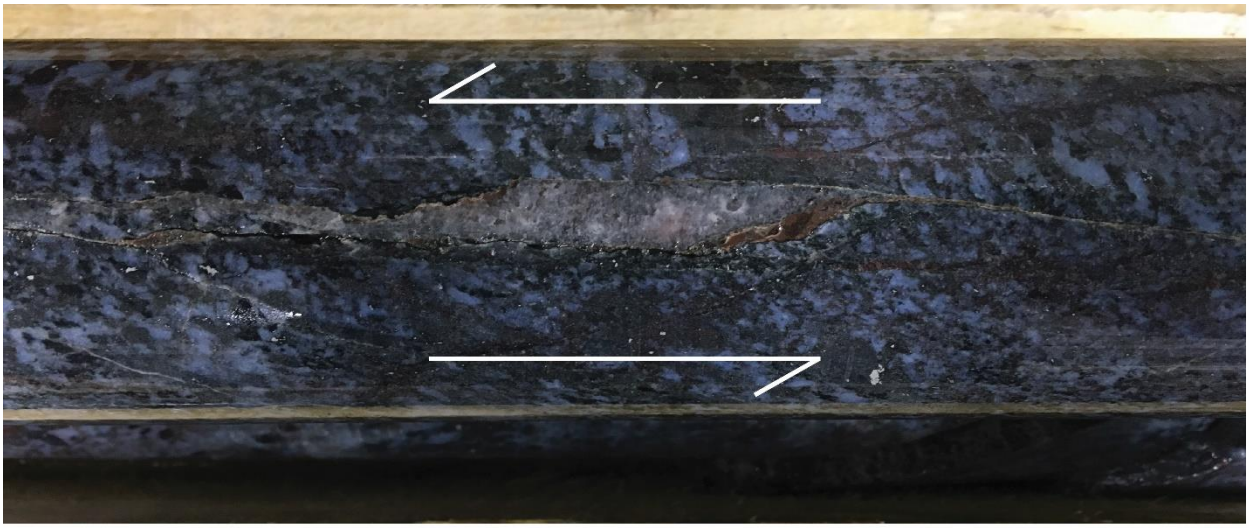

Fig. 4.20. Rhomb-shaped void filled with quartz along a releasing bend of a shear fracture crosscutting foliation. Top-to-the-left movement is indicated.

Riedel shears can be used as shear sense indicators, through observation of deflection of foliation or of older Riedel shears by younger shears (e.g. P by R; Y by R; Passchier and Trouw, 2005). The attitude of the foliation plane is representative of the general strike of the Arrow strike-slip shear zone, shown in green in Figure 4.21, while the most prominent brittle structural orientations represent the development of a Riedel-style geometry. Foliations within the Arrow deformation zone have been deflected and transposed, and resulting anastomosing, transposition foliation (S_1-S_3) accommodated protracted deformation along the zone. Plastic deformation within the major high strain zones (A1 to A5) provides evidence for early shearing under a ductile to brittle-ductile regime, whereas formation of Riedel shears and incohesive fault rocks (Section 4.3.2) indicates ongoing deformation through the brittle-ductile transition into a brittle regime. The most prominent orientation of brittle fractures (bold R-shear plane in Fig. 4.21) represents formation of subsidiary Riedel shear fractures oblique to the shear zone strike at acute angles. A dominantly sinistral displacement is implied by the counter clockwise orientation of R- and R'-shears with respect to the main shear orientation. Through statistical stereographical projection, it is evident that the brittle structural geometry of the Arrow Deposit exhibits a prominent Riedel arrangement (Fig. 4.19 and 4.21). Stereographical interpretation and interpretation of the overall geometry of the brittle structures at Arrow suggests a dominant sinistral, oblique-slip dominated displacement based on the orientation of Riedel directional families about the NE-SW imposed shear angle (Fig. 4.21), kinematic indicators in hand specimen, and fault and fracture off-sets.

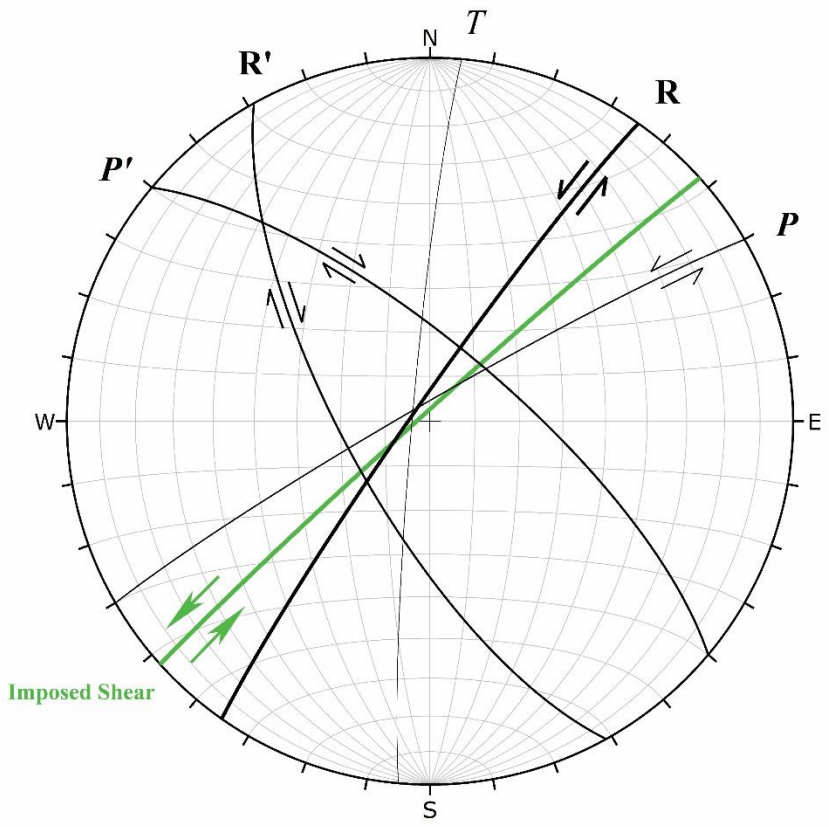

Fig. 4.21. Schematic constructed using statistical mean trends of brittle structures at Arrow illustrating Riedel geometry and interpreted shear sense. The average attitude of the main foliation is representative of the imposed shear, shown in green. Synthetic and antithetic subsidiary structures arranged about the principal flattening surface suggest a dominant sinistral movement. N = 447.

4.3.2 Breccias, cataclasites, and fault gouge

Brittle fault rocks can broadly be subdivided into cohesive and incohesive types. Cohesive fault rocks comprise cohesive breccia, cohesive cataclasite, and pseudotachylyte. These rocks are composed of angular rock fragments hosted within a matrix of quartz, iron oxide, calcite, chlorite, clay minerals, and/or other minerals precipitated from a fluid, or from frictional melt in the case of pseudotachylyte (Trouw et al., 2009). The cohesive nature of the rock is due to the matrix minerals forming via precipitation crystallization, dominantly from a fluid phase (Passchier and Trouw, 2005). In cohesive rocks, the contact between the fault rock and the wall rock is usually gradual, defined by a transition of decreasing brittle deformation intensity (Passchier and Trouw, 2005). Cohesive cataclasites are thought to form under brittle-dominant P-T conditions, with lithostatic pressure up to approximately 3 kbar and temperatures up to 300°C (Trouw et al., 2009).

Incohesive fault rocks are usually found in faults which have been active up to shallow crustal levels, and are subdivided into incohesive breccia, incohesive cataclasite, and fault gouge (Passchier and Trouw, 2005). Breccias of both types are constituted by greater than 30 vol-% angular fragments of wall rock or fractured veins separated by a fine-grained matrix, while cataclasites contain less than 30-vol% fragments (Passchier and Trouw, 2005). In fault gouge, very few isolated fragments are embedded within the matrix (Passchier and Trouw, 2005). Contrary to cohesive breccias and cataclasites, the wall rock contacts and embedded fragments frequently exhibit polished surfaces with slickensides or slickenfibres (Passchier and Trouw, 2005). In some cases, these linear features may be used to determine the direction of movement and shear sense along the fault zone (Section 4.3.3).

The Arrow zone contains abundant fault gouge zones and both cohesive and incohesive cataclasites and breccias, ranging in scale from centimetres in thickness to over 10 meters in thickness (Fig. 4.22, 4.23, and 4.24). Most of these brittle structures within the Arrow deformation zone are cohesive types, as the matrices are most commonly composed of quartz, clay minerals, and chlorite which were precipitated from a fluid (Fig. 4.22, 4.23, and 4.24). Cohesive quartz-healed breccias are extremely prolific at Arrow, often showing evidence for multiple phases of brecciation with quartz matrix becoming clasts along with wall rock in younger, overprinting breccias (e.g. Fig. 4.22B). Fault breccia zones have been logged as deep as one-kilometre in drill hole depth and occur up to the unconformity surface, which averages approximately110 meters in drill hole depth. They exhibit a variety of alteration assemblages and mineralogical composition based on their proximity to surface and wall rock interactions. For example, massive quartz-hematite breccias occur at shallower depths (down to approximately 450 m; Fig. 4.22C) while chlorite, graphite, and sulphide-rich breccias tend to be preserved at greater depths (Fig. 4.22F, G, and I). The matrix forming quartz is commonly euhedral and zoned, and ranges in colour from milky white, smoky black to brown, translucent, and translucent pink. The nature of these quartz matrices and veins is discussed in greater detail in Section 5.1. The prominence of these brittle rocks indicates prolonged reuse and reactivation of the pre-existing A1 to A5 shear zones pre-, post-, and syn-ore, overprinting ductile deformational fabrics and incorporating angular clasts of ductile-deformed wall rock into their structure (Fig. 4.22J). Breccias within the Arrow strike-slip shear zone are frequently observed to be mineralized, hosting clasts of mineralized wall rock, disseminated uraniferous minerals, or even healed with uraninite (Fig. 4.22H). As aforementioned,

many of these structures exhibit polyphase deformation, and several show evidence for brecciation through fluid over-pressuring, or hydraulic brecciation (e.g. Fig. 4.22D).

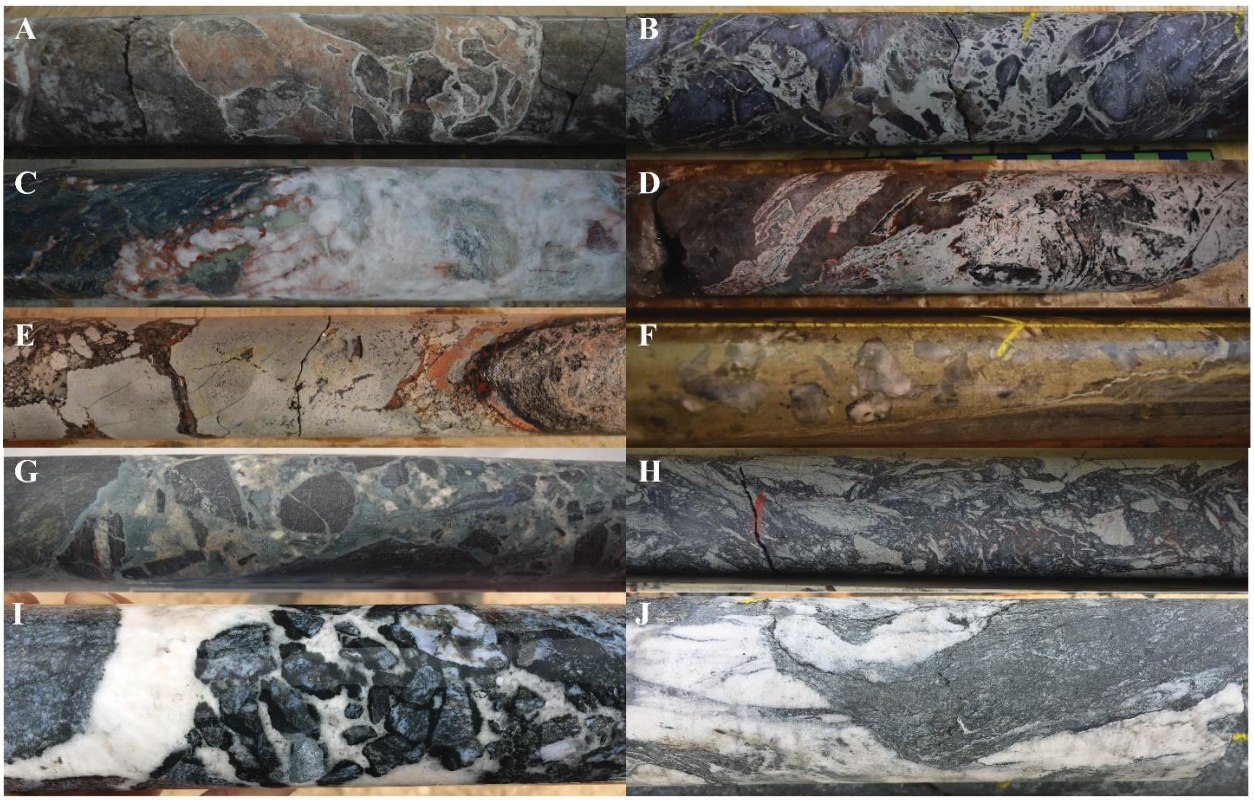

Fig. 4.22. A) Weakly mineralized pink quartz-healed breccia hosting angular clasts of chloritized wall rock rimmed by kaolinite (AR-16-078c3, 404.7 m, up to 720 cps). B) Multi-stage hydraulic breccia previously healed with smoky and pink quartz, re-brecciated and healed with clay minerals and dravite. Paragenetic relationships evidenced by clasts of wall rock and earlier vein quartz in clay-rich matrix (AR-17-136c1, 405.2 m). C) Milky white to translucent quartz-healed breccia with euhedral zoned crystals, hosting chloritized and hematized clasts of wall rock and late light green sudoite alteration filling voids (AR-16-080c2, 422.1 m). D) Mineralized polyphase breccia healed by clay minerals and dravite, with overprint of subsequent druzy smoky quartz veining and mineralization-associated hematite alteration (AR-17-155c3, 500.3 m, up to 3,600 cps). E) Massive clay-sudoite-dravite vein brecciated and healed by clay, uraninite, and hematite. A black uraninite vein is visible on the right of the photo, marking the contact between ductile-deformed wall rock and the overprinting brittle structure (AR-17-176c2, 505.15 m, up to 6,400 cps). F) Massive sulfide mineralization overprinting and hosting sub-angular clasts of a pre-existing milky white-translucent quartz vein (AR-16-095c1, 633.3 m). G) Weakly mineralized sudoite-healed breccia hosting angular and sub-angular clasts of sheared, graphitized, and sericite-altered wall rock and milky-translucent quartz (AR-17-121c2, 661.5 m, up to 980 cps). H) Uraninite-healed breccia hosting angular clasts of sheared, pervasively sericitized and graphitized wall rock, with trace hematite alteration (AR-15-061c2, 780.5 m, up to 55,000 cps). I) Massive milky quartz-healed breccia hosting sub-angular clasts of altered wall rock mantled by chlorite alteration (AR-18-210c3, 865.2 m). J) Massive milky quartz and graphite-healed breccia overprinting heterogeneous ductile strain, hosting angular clasts of sheared, graphitized wall rock (AR-18-210c3, 870.2 m).

Cataclasites are dominantly cohesive-type within the Arrow deformation zone, with matrices most commonly composed of clay minerals, and clasts of quartz (Fig. 4.23A). They range in size from a few centimetres in thickness up to meter-scale structures and represent zones of prolonged movement and fluid flow evidenced through high degrees of comminution of all mineral grains and strong clay alteration. Cohesive cataclasites are prevalent up-dip of the major A1 to A5 shear zones (Fig. 4.23B and C), and commonly host uranium mineralization at greater depths where overprinting mylonitized and/or highly altered rocks within the shears (Fig. 4.23D).

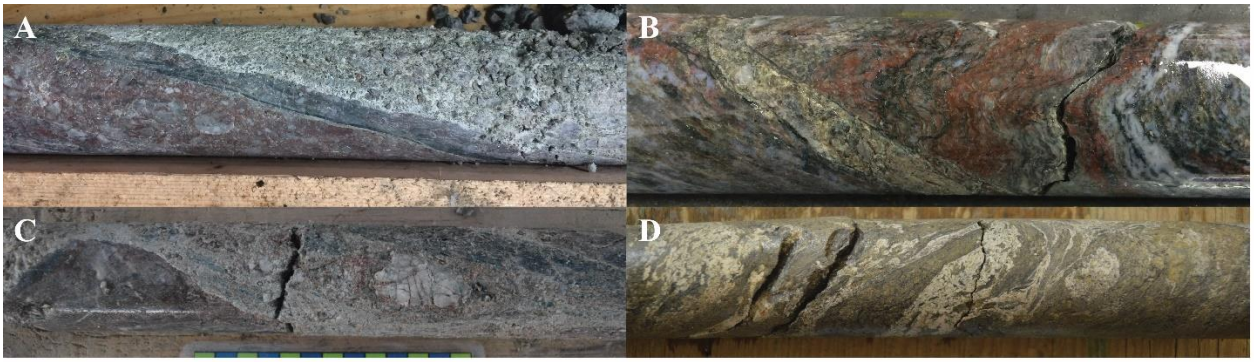

Fig. 4.23. A) Decimetre-scale cohesive cataclasite comprised of rounded wall rock and quartz clasts within a fine to very fine-grained matrix of clay minerals up-dip of the A2 shear zone (AR-16-080c2, 400.6 m). B) Centimetre-scale cohesive quartz-clay-chlorite cataclasite crosscutting sheared and folded wall rock (AR-16-080c2, 416.3 m). C) Cohesive cataclasis overprinting a milky hydrothermal quartz vein up-dip of the A2 shear zone. A 4 cm clast of the relict quartz vein is visible within the fine-grained clay matrix (AR-16-080c2, 401.7 m). D) Mineralized cohesive breccia consisting of sericitized and chloritized wall rock clasts hosted within a clay-chlorite matrix (AR-16-094c1, 862.3 m, up to 1,400 cps).

Fault gouge zones proximal to and overprinting ductile strain are common, ranging from localized centimetre-scale gouge to meter-scale zones of up to or greater than 90 vol-% matrix (Fig. 4.24A). Matrices most commonly consist of clay minerals (kaolinite, illite), chlorite, and muscovite with negligible clasts of wall rock or quartz (Fig. 4.24B and C). These highly altered and evolved structures demonstrate that the portion of the Patterson Lake corridor hosting the Arrow Deposit likely acted as a conduit for the movement of a substantial volume of fluid over a significant period of time.

Fig. 4.24. A) Metre-scale cohesive fault gouge zones comprised of >90% kaolinite-illite matrix with negligible clasts of wall rock or quartz. Gouge contacts are annotated by the yellow dashed lines (AR-15-057c1, 171.0 to 181.7 m). B) Mineralized cohesive fault gouge consisting of millimetre- to centimetre-scale clasts of sheared, chloritized and sericitized wall rock within a kaolinite-illite matrix (AR-17-129c1, 764.7 m, up to 5,400 cps). C) Clay-rich cohesive cataclasite hosting weak uranium mineralization. Yellowish-brown and green-blue clasts are pervasively sericitized and/or chloritized wall rock (AR-17-176c1, 506.4 m, up to 600 cps).

4.3.3 Slickensides and slickenstriae

Slickensides are defined as smoothed or polished fault surfaces, while slickenstriae (or slickenlines) are linear markings or scratches on a slickenside which indicate the slip direction along that surface (Passchier and Trouw, 2005). Slickenstriae are not considered true lineations as they only form on specific planar surfaces within a rock and are not penetrative. Slickensides are abundant throughout the Arrow deformation zone, most well developed along graphite- and chlorite-lined fractures (Fig. 4.25A and B) and along the contacts of incohesive fault rocks. In mineralized zones, slickenstriae are commonly observed on brittle fractures lined with clay, chlorite, and/or hematite, as well as uraninite (Fig. 4.25C and D). Relatively late fractures crosscutting mineralization also exhibit slickenlines, speaking to the prolonged reactivation of major structural zones syn- and post-ore stage. Multiple generations of slickenstriae are observable on the vast majority of slickensides at Arrow, recording polyphase brittle deformation and local

wrench on a local scale (i.e. dip-slip and oblique-slip orientations on conjugate fractures). Orientations of these features range from strike-slip to dip-slip, with near horizontal oblique-slip orientations being most prominent (e.g. Fig. 4.25A). The prevalence of oblique-slip orientations corroborates the deformational model in terms of dominant strike-slip movement with a minor overall dip-slip component. Measurements of these structures in numerous drill holes allow for description of the fault system and to reconstruct the major characteristics of the deformation over a large area (e.g. Angelier, 1984).

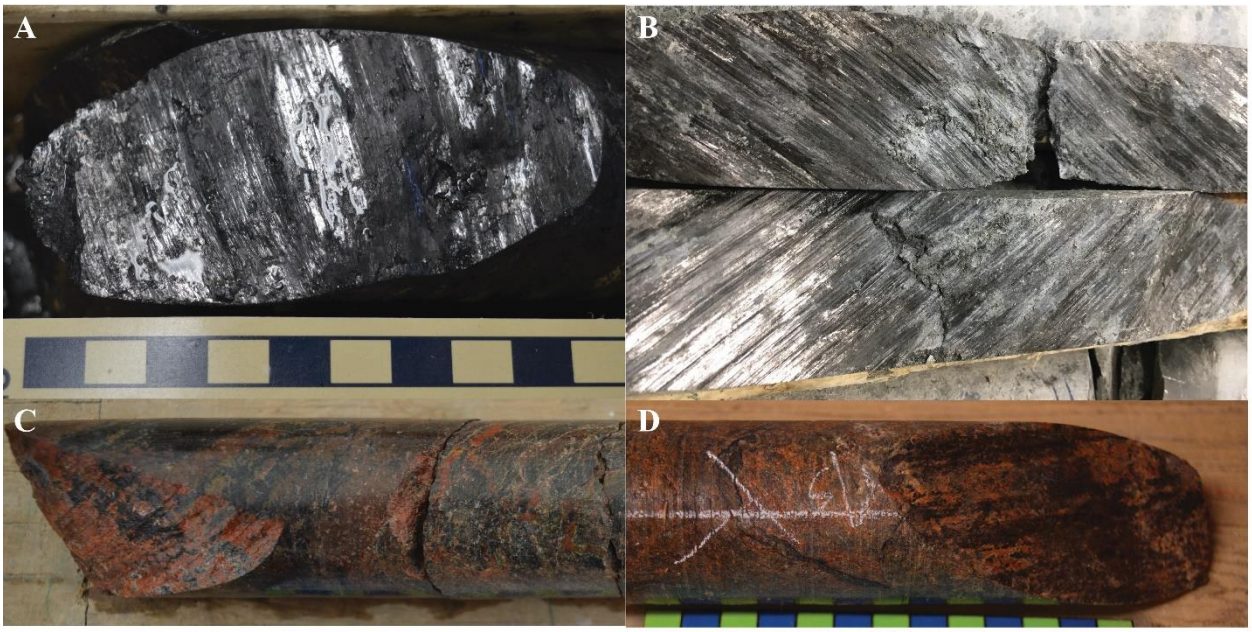

Fig. 4.25. A) Near strike-slip slickenstriae on a graphitic slickenside within the A3 shear zone (AR-16-094c1, 410.1 m). B) Well developed oblique-slip slickenstriae on a graphite- and clay-lined fracture (AR-18-211c3, 902.3 m). C) Oblique-slip slickenlines on a uraninite- and hematite-lined fracture within the A2 shear zone (AR-16-080c2, 500.0 m, up to >61,000 cps). D) Near dip-slip slickenstriae on a mineralized fracture face with associated hematite-limonite alteration (AR-17-171c3, 768.0 m, up to 8,000 cps).

Slickenline data has been compiled and compared with fracture data to give a sense of shear along the Arrow deformation zone. Due to the amount of reactivation along the shear zone, care was taken in interpretation of slickenstriae data as the slickensides often only preserve the most recent reactivation episode. Plotting slickenstriae measurements on a 2D rose diagram reveals patterns which reflect the fracture network geometry (Fig. 4.26). Slip on conjugate polished fracture sets in en-échelon arrays (Fig. 4.27) throughout the Arrow shear zone and wall rocks result in equal and opposite sets of slickenlines, which are apparent in Figure 4.26. Idealized principal

stress directions interpreted based on Figure 4.26 correspond to the orientations of fracture sets and the principal flattening surface at Arrow.

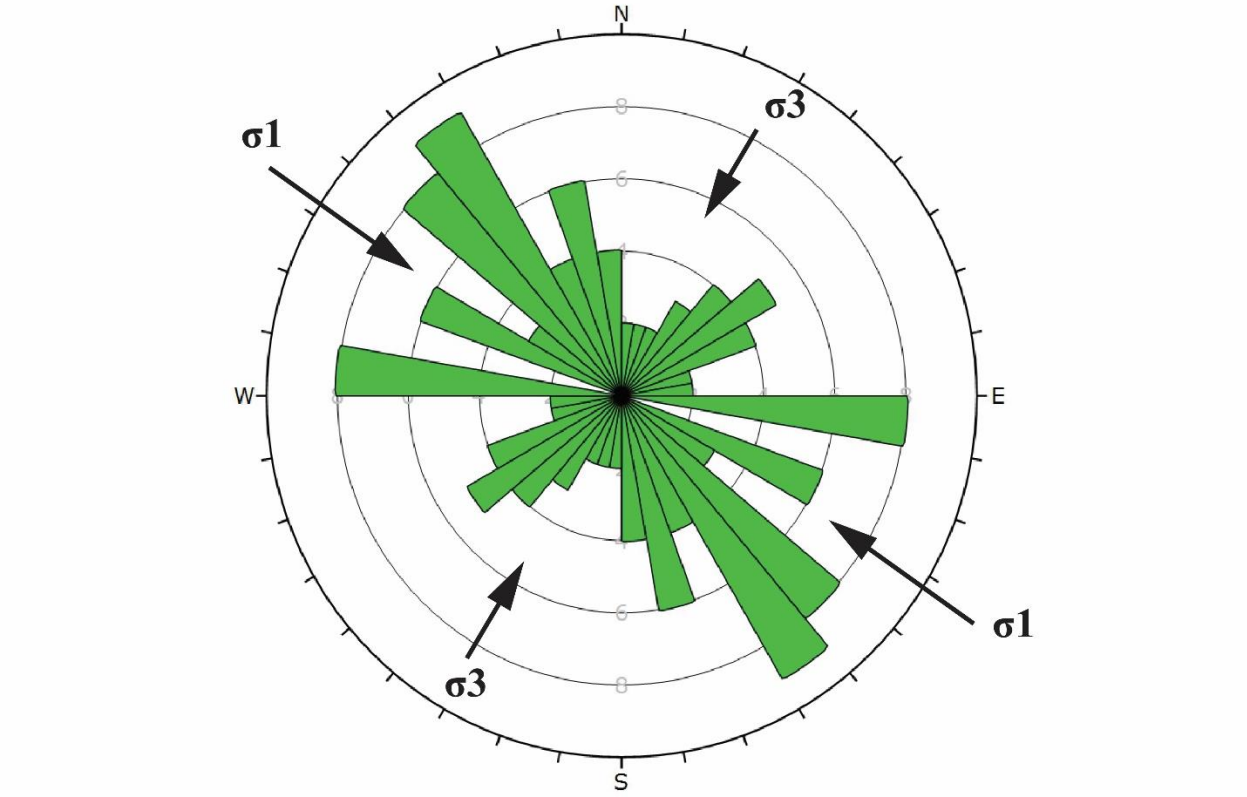

Fig. 4.26. Rosette plot (n=74) of slickenstriae gamma measurements from slickensides in Arrow drill core, including possible corresponding principal stress directions (σ2 is vertical). Slip on conjugate fracture sets can create equal and opposite sets of linear features.

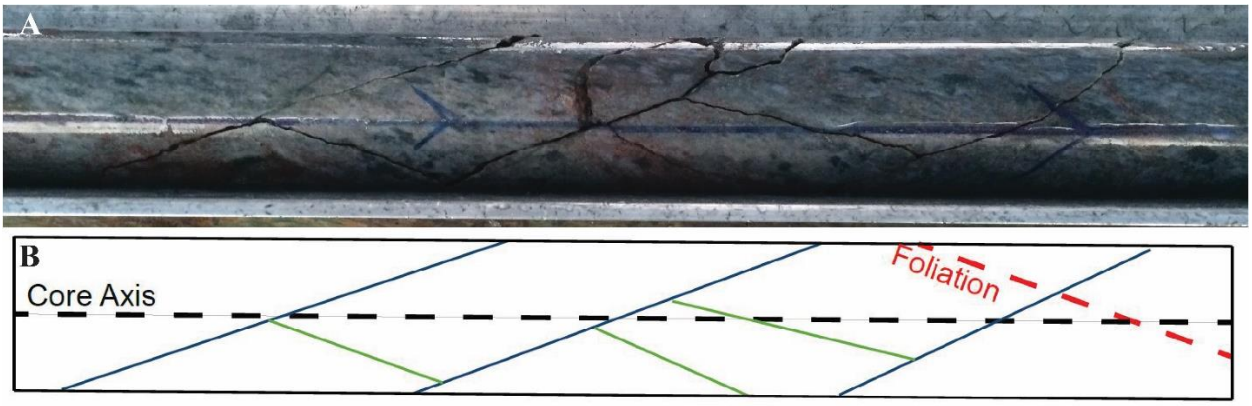

Fig. 4.27. A) En-échelon conjugate fracture sets oblique and sub-parallel to foliation in Arrow drill core. B) Schematic interpretation of late brittle fracture set geometry. The complex array of brittle fracture linkages can make interpretation of measurements across the Deposit difficult, as slip directions can vary greatly within a relatively small volume. This must be considered when making interpretations of bulk slip and principal stress directions.

4.4 Mineralized Structures

The ductile structural framework, shear zone formation, alteration, and subsequent development and linkage through brittle reactivation and reuse of these structures are all integral components in the genesis of the Arrow Deposit. Each factor contributes to the production of favorable chemical conditions (i.e. reducing environment through deposition of graphite and/or sulphides), as well as accommodation space and structural conduits through which hydrothermal fluids were able to deposit and remobilize ore. This has major implications for the models of uranium deposits in the SW Athabasca Basin, suggesting that the largest uranium systems are related to and hosted within deep-seated structural corridors which have been reactivated and reused multiple times, such as the Patterson Lake corridor.

The portion of the Patterson Lake corridor hosting the Arrow Deposit is an area affected by repeated deformations, which have resulted in mylonitization and metasomatic alteration of the rocks and reactivation of major fault systems, therefore structurally controlling the uranium mineralization. Primary formation of the uranium veins at Arrow is related to the reactivation and reuse of pre-existing structures, which formed during the late phases of orogenic events ca. 1.8 Ga and younger. Fluid flow and reactivation of mineralized structures then further concentrated, remobilized, and altered ore within previously established and newly formed subsidiary fractures, cataclasis zones, and shear and mylonite zones. Heterogeneous strain and partitioning during deformational episodes are evident through the stacked nature of the mineral resource outline (Fig. 4.28), indicating a clear structural control on mineralization facilitated by the reactivation of pre-existing structural weaknesses that are in suitable orientations to minimize work done (i.e. structures which may reactivate easier based on their orientations relative to the active stress fields; e.g. oblique to the principal flattening surface).

Mineralized structures at Arrow range from hydrothermal fluid over-pressuring and corrosive replacement-style breccias (Fig. 4.22B), massive “fault-fill” veins or “shoots” (Fig. 4.29), shear fracture and extensional vein fills (Fig. 4.30 and 4.31), and disseminated uraninite through cohesive gouge or breccia fills (Fig. 4.32A and B, respectively). Meter-scale uranium fault-fill veins (Fig. 4.28 and 4.29) hosted within and proximal to the brittle-ductile shears comprise the high-grade domains of semi-massive to massive uraninite mineralization, roughly paralleling the high strain zones with moderate to steep dip. They have great vertical extent (> 100

m; Fig. 4.28) and represent dilational zones during slip, with the densest accumulations of uraninite at Arrow hosted within the A2 wrench zone.

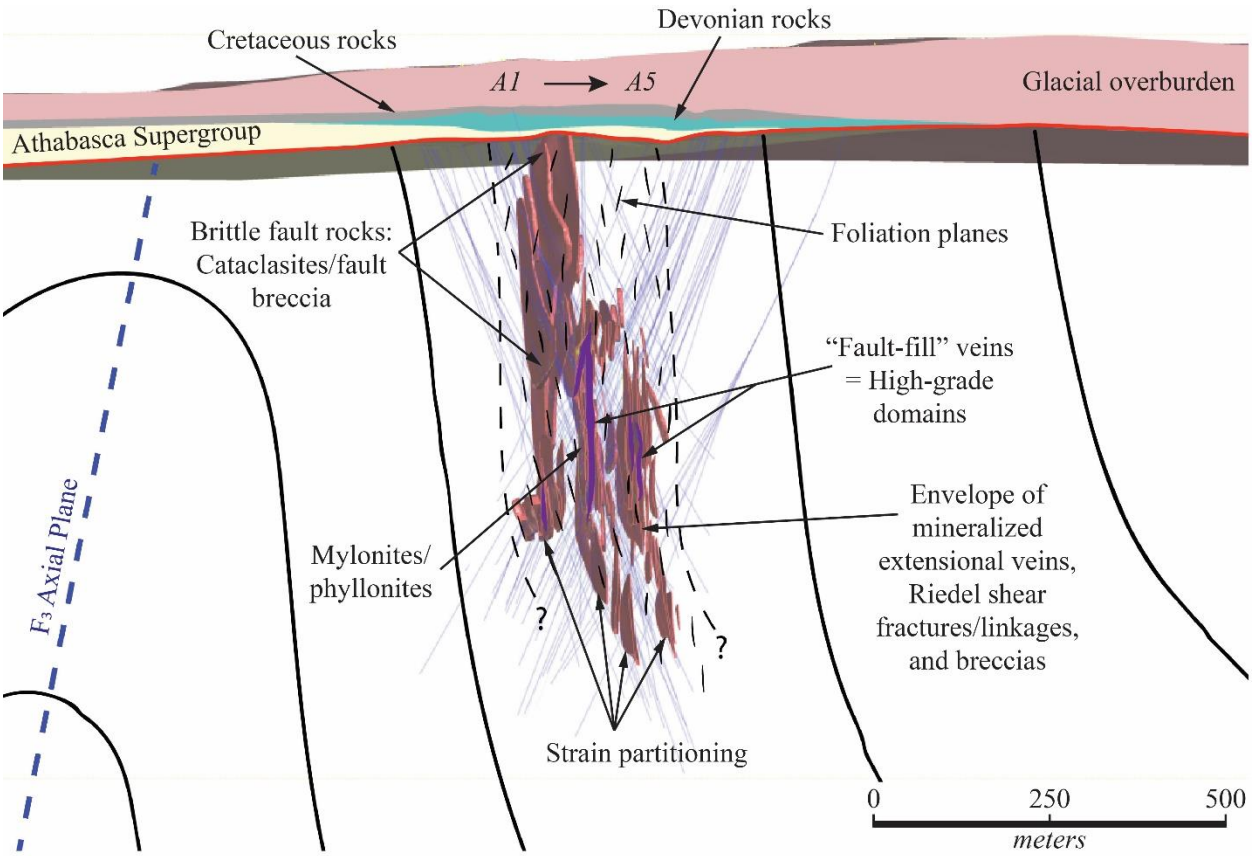

Fig. 4.28. Schematic cross-section looking NE (063°) of the Arrow strike-slip deformation zone showing the stacked A1 to A5 shears (from left to right) hosted within the limb of an F_3 fold and associated fault rocks. Note the stacked nature of the mineral resource outline (Mathison and Ross, 2017) reflecting the partitioned shear system and the overall plunge to the S-SE.

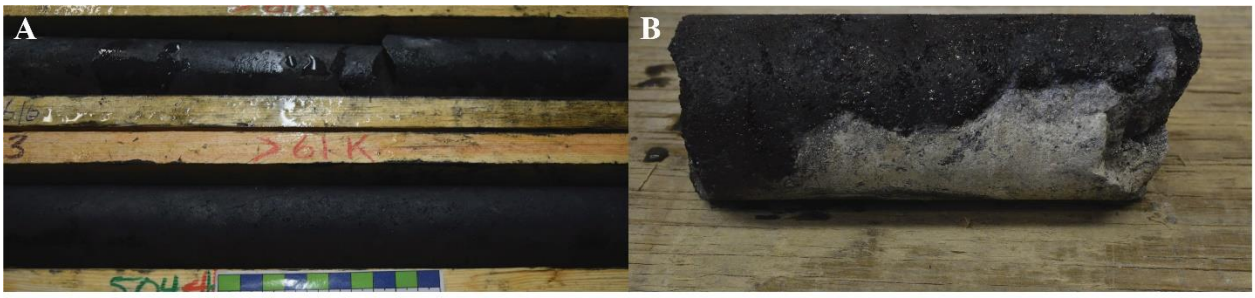

Fig. 4.29. A) Massive uraninite mineralization within a metre-scale extensional fault-fill vein (AR-16-076c1, 502.5 m, up to >61,000 cps). B) Sub-vertical contact of a massive uraninite vein with strongly altered wall rock (AR-16-076c3, 516.2 m, up to >61,000 cps).

Centimetre-scale extensional veins (Fig. 4.30 and 4.31) are broadly coeval with the fault-fill veins in competent rock. They may have steep dip oblique to foliation, similar to the "fault-fill" zones, however they are commonly oriented at much shallower dip and high-angle to foliation. The red resource outline (Mathisen and Ross, 2017) in Figure 4.28 represents an "envelope" of these smaller-scale extensional veins, Riedel shear fractures and linkages (Fig. 4.30 and 4.31), as well as hydraulic breccias and cataclasites healed by kaolinite, illite, chlorite, and/or dravite which host disseminated uranium mineralization (Fig. 4.32A).

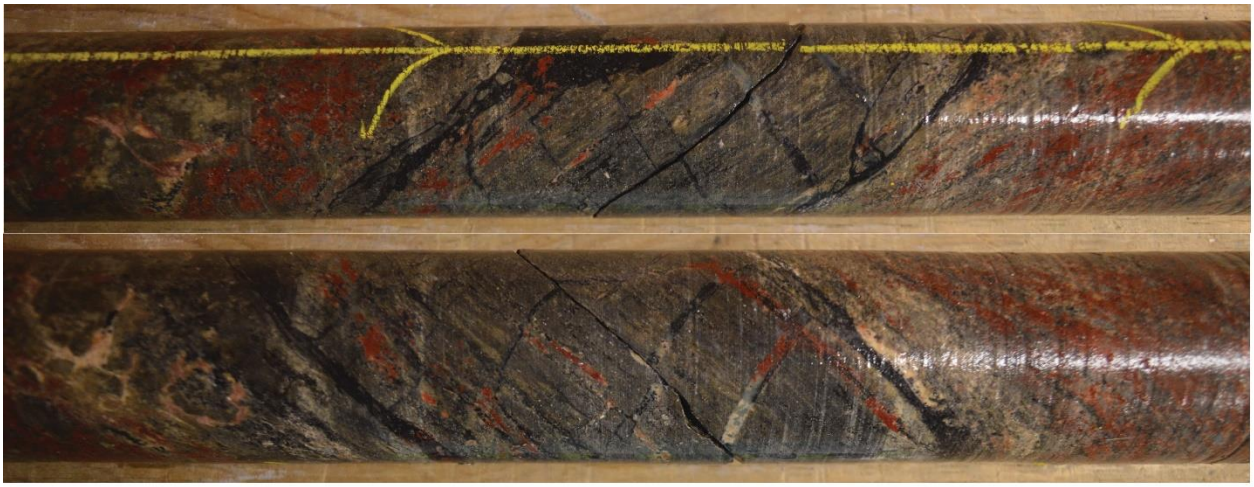

Fig. 4.30. Front and back view of uraninite mineralization healing multi-generational shear fractures oblique to, and at high angles (extensional veins) to ductile shear foliation. Hematite alteration associated with mineralization overprints earlier clay alteration and shows structural and mineral control (AR-17-129c1, 781.15 to 781.5 m, up to 46,000 cps).

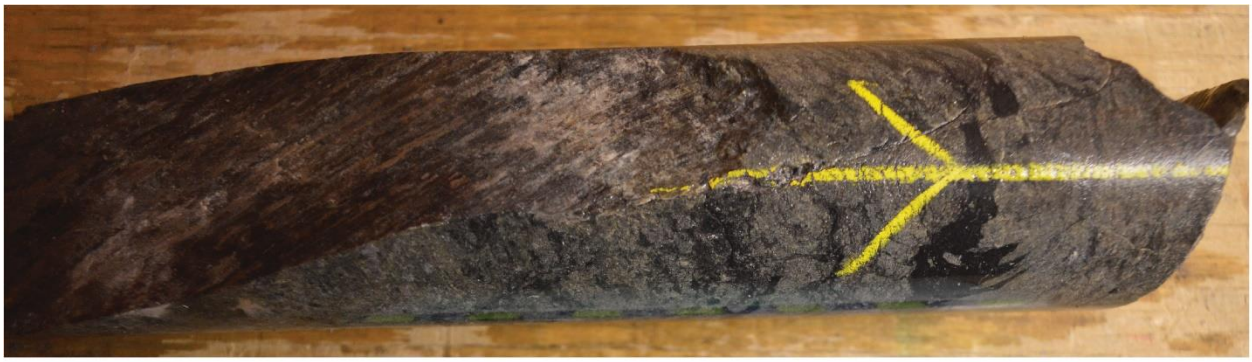

Fig. 4.31. Uraninite mineralization within an extensional shear fracture and precipitating along shear foliation planes. The uraninite-healed tension gash is offset (normal oblique-slip) by a late, striated graphitic fracture, illustrating the protracted brittle reactivation at Arrow. (AR-17-129c1, 913.8 to 914.0 m, up to >61,000 cps).

Conversely, uraninite forms the matrix within some brecciated rocks, hosting angular, altered clasts of wall rock (Fig. 4.32B). Younger and/or remobilized veins of uraninite are also observed to crosscut prior mineralization phases, evidencing polyphase fluid movement through the structures post primary mineralization (Fig. 4.33A and B).

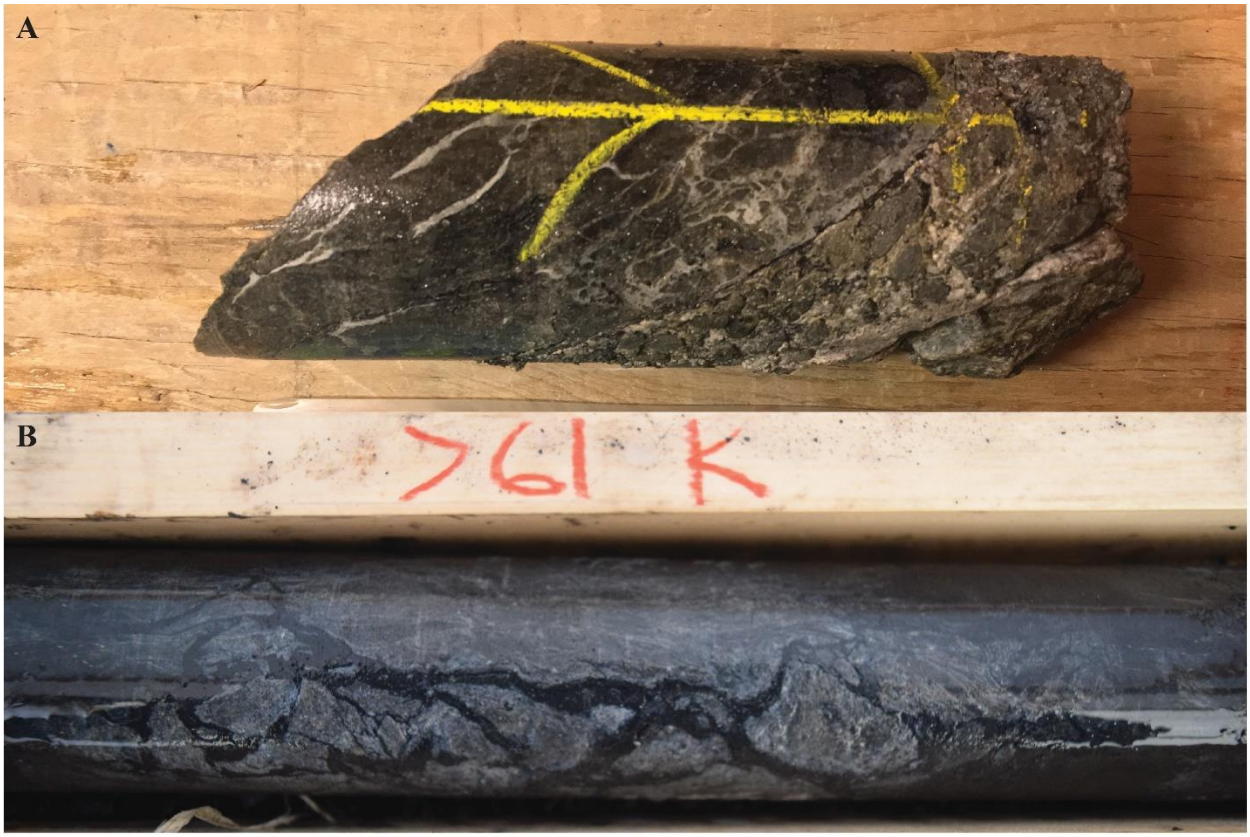

Fig. 4.32. A) Mineralized clay- and chlorite-rich cohesive cataclasite (AR-17-129c1, 782.2 m, up to 10,500 cps). B) Uraninite mineralization forming the matrix of a breccia within the A2 shear zone, hosting angular clasts of altered wall rock (AR-15-059c2, 528.0 to 528.5 m, up to >61,000 cps).

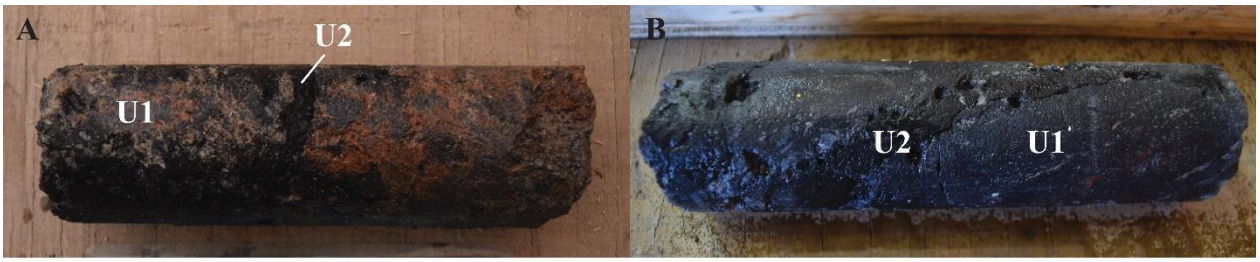

Fig. 4.33. A) Younger generation uraninite vein (U2) crosscutting older uraninite mineralization (U1) in strongly clay-hematite altered rock within the A2 shear zone (AR-16-111c1, 519.0 to 519.15 m, up to >61,000 cps). B) Late uraninite vein (U2) crosscutting massive uraninite mineralization (U1) within the A2 high-grade core (AR-16-098c2, 500.0 m, up to >61,000 cps).

On a millimetre- to micrometre-scale, uraninite is precipitated along grain and vein boundaries (Fig. 4.34A, B and C), foliation (Fig. 4.34D), and mineral cleavage planes, commonly replacing minerals partially or completely such as previously altered garnet or feldspar porphyroblasts (Fig. 4.34E), or muscovite/sericite in the matrix (Fig. 4.34C). Although the uranium mineralization at Arrow post-dates much of the metasomatism of the wall rocks (i.e. pervasive silicification), significant syn- and post-ore alteration of the host rocks is prominent at Arrow. Complete replacement of host rock mineralogy by uraninite and alteration minerals such as clay, chlorite, hematite, and limonite commonly produce spectacular colors and textures such as "worm rock" texture (Fig. 4.34F). Alteration and mineralization phases and textural relationships are discussed in detail in Section 5.0.

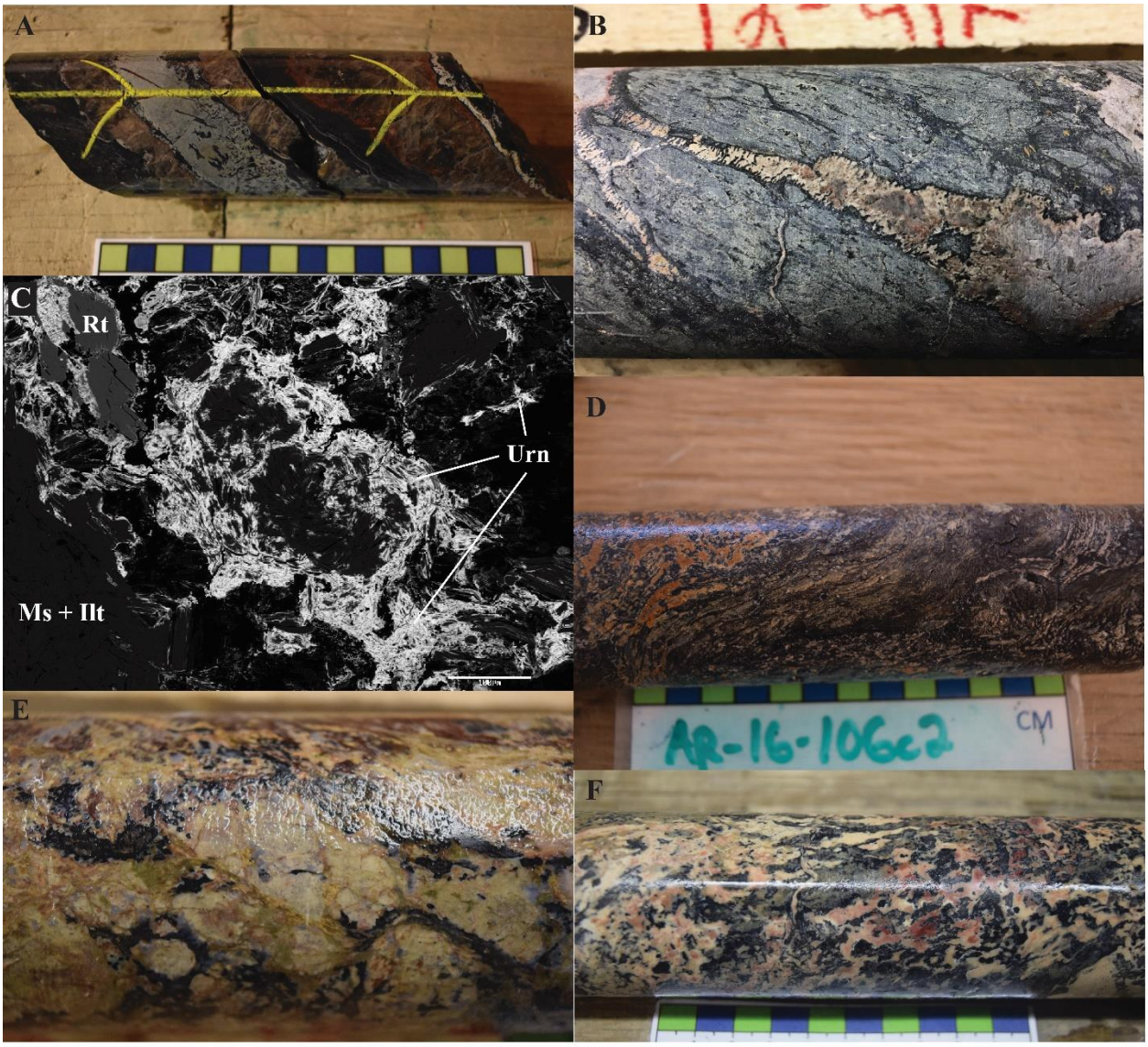

Fig. 4.34. A) 5- to 10-millimetre-thick uraninite veins along the margins of druzy smoky quartz veins with associated hematite alteration (AR-17-129c5, 692.55 m, up to >61,000 cps). B) Uraninite mineralization replacing and precipitated along the margins of smoky-pink quartz veins in sheared graphitized rock (hole and depth not recorded, up to 41,000 cps). C) BSE image of uraninite (Urn) mineralization replacing and precipitating along cleavage planes of muscovite (Ms) and illite (Ilt) in the matrix (AR-16-063c1, 473.3 m, up to 1,300 cps). D) Uraninite mimicking anastomosing foliation planes and replacing white mica in sheared and sericitized rock (AR-16-106c2, 459.0 m, up to 29,000 cps). E) Black uraninite mineralization precipitated along tan-yellow clay-replaced feldspar grain boundaries in syenitic rock (AR-17-116c1, 474.9 m, up to 12,000 cps). F) Worm rock textures created by mineral replacement by uraninite mineralization, chlorite, and clay minerals. Late hematite alteration overprints clay alteration (AR-16-076c1, 710.5 m, up to 34,000 cps).

CHAPTER 5

MINERAL PARAGENESIS

The structural evolution of Arrow can be related to episodes of uranium mineralization and extensive and varied hydrothermal alteration products. The host rocks at the Arrow Deposit have a complex metasomatic history, pre-dating uranium mineralization. They exhibit moderate to intense pervasive silicification, ubiquitous and often pervasive sericitization, and preferential chloritization of quartz-poor mylonitic rocks. Softening of the shear zone and brittle fault rocks through chloritization and sericitization essentially "prepped" the ground for subsequent fluid movement and uranium deposition. The wall rocks immediately adjacent to mineralized structures are affected by syn-ore alteration such as hematization, limonitization, argillization, and chloritization (e.g. Card and Noll, 2016; Section 5.2). Post-ore hydrothermal alteration products overprint both barren and mineralized rocks and comprise phases such as dravite and/or magnesiofoitite, carbonate, quartz, and iron oxides and sulphides (Section 5.2 through 5.4). Numerous generations of quartz veins crosscut wall rocks, structures, and mineralization throughout the Arrow deposit and exhibit a variety of different colors, filling voids and forming druzy veins (Section 5.1). The uranium minerals exhibit post-main ore stage alterations such as the addition of silica to form uranium silicates including coffinite, or formation of late uranium oxides and hydroxides such as uranophane and curite (Section 5.5).

Paragenetic relationships have been determined through examination of more than 40 polished thin sections and hundreds of drill core hand samples. Due to the prolonged reactivation and reuse of the Arrow deformation zone by polyphase fluid fluxes, the relative timing and associations between primary mineralogy, alteration mineralogy, and uranium mineralization defines a synchronous complex relationship. This study attempts to place alteration and mineralization episodes in structural context, integrating structural, petrographical, and geochemical analyses.

5.1 Quartz

The competent, relatively undeformed wall rocks within the Arrow zone exhibit pervasive syn- to post-peak metamorphic silicification, often so intense that it replaces more than 90% of the rock (Fig. 5.1A). The dominant host rock of the Arrow Deposit, termed the "semi-pelitic gneiss" in Figure 2.8, is particularly affected by this immense quartz flooding event.

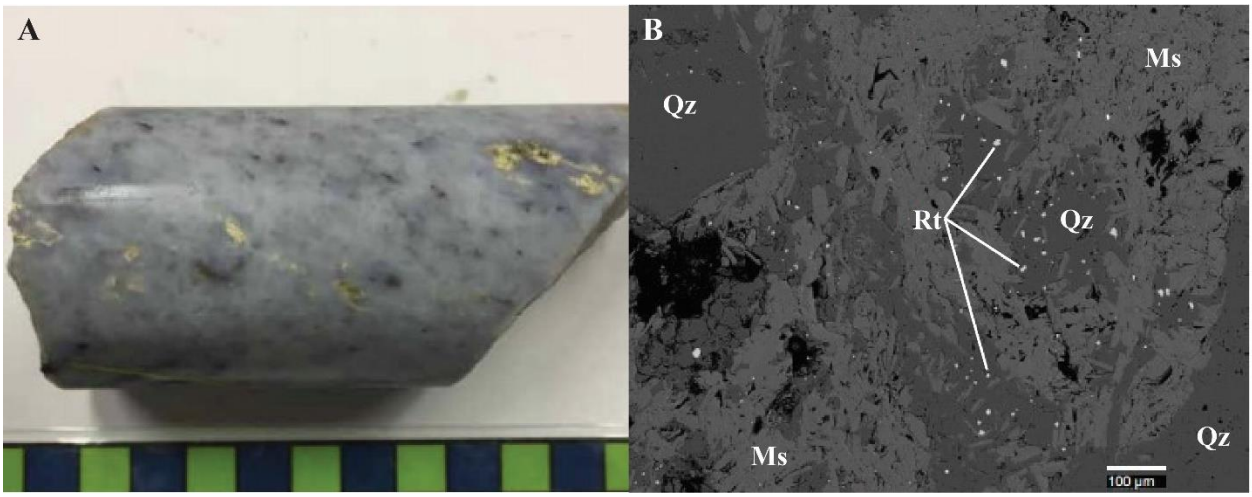

Fig. 5.1. A) Drill core sample of Arrow host rock containing upwards of 80% blue quartz within 5 metres of uranium mineralization. Extremely silicified instances of the Arrow host rock are extremely common through the Arrow zone, with relict foliation still visible. (AR-16-081c3, 657.9 to 658.0 m). B) Electron microprobe BSE image revealing abundant submicrometer rutile (Rt) inclusions in a blue quartz (Qz) sample taken near the southwest margin of the Arrow Deposit. Muscovite (Ms) alteration has replaced feldspars (AR-16-082c2, 717.6 to 717.65 m).

Only trace amounts of altered minerals remain in some instances, with faint relict textures of foliation (Fig. 5.1A). The ensuing quartz is dominantly blue, blue-grey, grey-purple, or milky blue-white in hand specimen (Fig. 5.1A and 5.3A and B). The remarkable blue coloration of the quartz is interpreted to be derived from Rayleigh scattering of light by ubiquitous submicrometer- and nanometer-sized inclusions of titanium-bearing minerals such as rutile/anatase (Fig. 5.1B), ilmenite, and/or mica, fluid inclusions, or deformation/defects within the crystal lattice (e.g. Zolensky et al., 1988; Seifert et al., 2011). Past studies on blue quartz (e.g. Seifert et al., 2011) have shown that it is generally Ti-rich (~100 to 300 ppm) due to these inclusions, and that it forms at high temperatures between approximately 700°C to 900°C, which is consistent with the high grade of the granulite-facies M_1 metamorphic event recorded in the Taltson Domain rocks. ICP-MS analyses on select blue quartz samples within the Arrow zone have returned Ti values from 500 to 800 ppm Ti, and electron microprobe analyses have identified abundant submicrometer

inclusions of rutile (Fig. 5.1B; Johnson, in prep). Titanium oxide concentrations attained from digestion by ICP-MS analysis promote the theory of blue coloration due to the phenomenon of Rayleigh scattering, however, the blue coloration is known to vary, thus prompting a question of blue coloration due to deformation of the crystal lattice or multiple phase fluids in the quartz.

In less altered rocks, the metasomatic quartz is commonly transposed with foliation (Fig. 5.2 and 5.3A and B). Comparative analysis of cathodoluminescence (CL) imaging of the blue quartz and younger quartz veins shows that what appear to be homogeneous blue quartz grains actually exhibit heterogeneity in their structure, likely due to deformation and polyphase fluid interaction (Fig. 5.3D).Texturally, it appears that the established foliation in gneissic rocks helped to focus the silicifying fluid (Fig. 5.2), as did sections of coarser-grained, weakly or unfoliated pegmatitic rocks (Card, 2017). Although most of the host rocks within the Arrow zone exhibit secondary silicification, much of the primary metamorphic quartz in the intermediate rocks also exhibits a blue hue. Therefore, distinguishing between primary metamorphic quartz and secondary silicification through textural and paragenetic relationships is important.

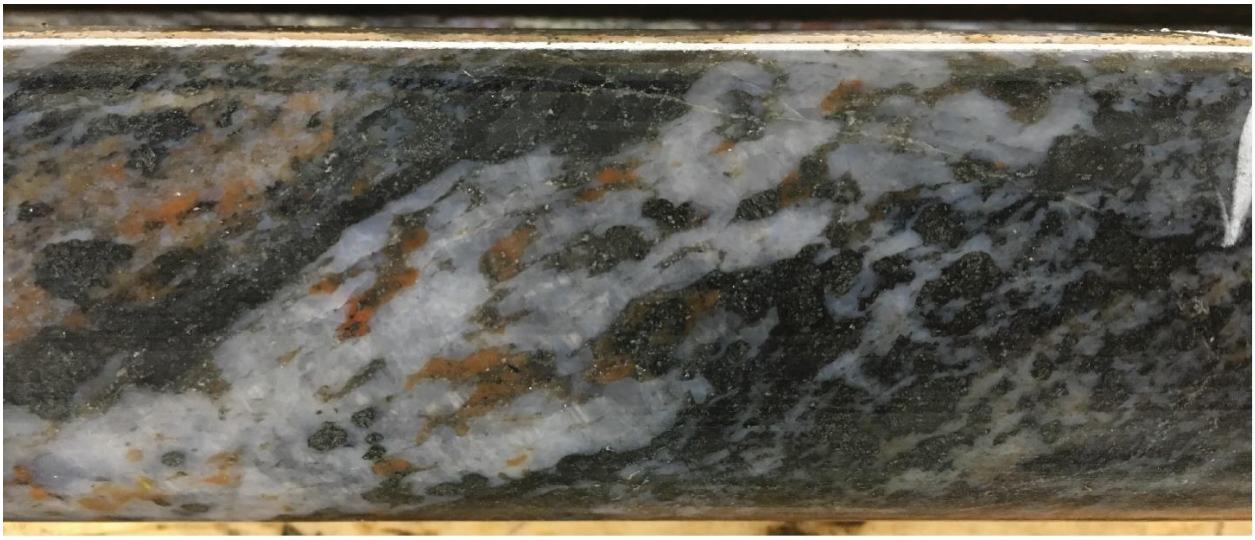

Fig. 5.2. Blue-grey metasomatic quartz transposed and focussed along pre-existing foliation in relatively unaltered Arrow wall rock (AR-18-214c1, 464.5 m).

While the silicification appears to be dominantly post-peak regional deformation, textures indicate that ductile shearing occurred post-silicification, and thus implies that the quartz flooding occurred below the brittle-ductile transition and prior to exhumation and deposition of the overlying Athabasca Supergroup rocks (Card, 2017; Fig. 5.3A through D)). Blue quartz grains

exhibit deformation textures indicative of crystal-plastic processes including undulose extinction and dynamic recrystallization along their boundaries through subgrain rotation (Fig. 4.16 and 5.3C). SGR recrystallization is common within low- and medium-grade mylonites, often fully recrystallizing grains (Trouw et al., 2009).

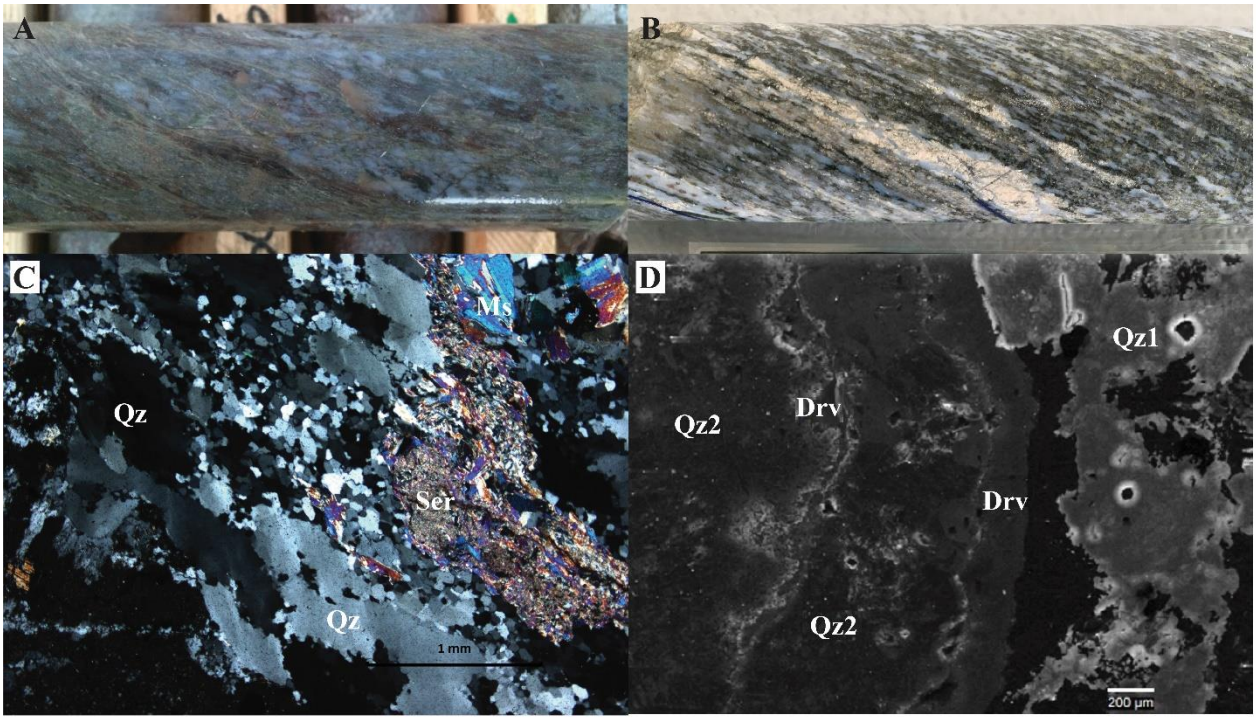

Fig. 5.3. A) Sheared and transposed blue-purple quartz in silicified rock within the A1 shear zone (AR-16-080c2, 251.8 m). B) Blue-white metasomatic quartz transposed along mylonitic foliation (AR-18-199c2, 397.2 m). C) Cross-polarized light (XPL) photomicrograph of deformed blue quartz (Qz) within the A4 shear zone exhibiting well-developed undulose extinction, decussate serrated texture, and dynamic recrystallization via subgrain rotation (SGR), indicating recrystallization caused by high strain (AR-16-082c2, 717.6 m). D) Cathodoluminescence (CL) back-scatter electron (BSE) image of multi-generational smoky vein quartz (Qz2) exhibiting polygonal grain boundaries crosscutting SGR recrystallized blue quartz (Qz1) within the A2-A3 shear transition zone. Highest CL response (white glow) in blue quartz (Qz1), indicative of high-grade metamorphism and deformational textures. Secondary quartz veins (Qz2) are less deformed, emitting a lower CL response. Acicular dravite crystals lining the younger vein post date all other mineral phases, and radiation damage is evident on the boundaries of quartz and opaque minerals (AR-16-082c2, 717.6 m).

Several phases of younger quartz veins are recognized within the Arrow zone. Younger quartz types form druzy veins and cavity fills, breccia matrices, and irregular vein stockworks (Fig. 5.4A through H). These younger veins are commonly overprinted and form clasts within breccias healed by clay minerals or yet another phase of quartz. Massive quartz breccias several meters thick are common features overprinting sheared rocks in the Arrow zone. Late quartz phases exhibit a spectrum of colors ranging from translucent to nearly black, and often display spectacular

zoning (Fig. 5.4G and H). The most common colors include clear to milky white, pink, and smoky grey, brown, or black (Fig. 5.4A through H). Powder electron paramagnetic resonance (EPR) spectroscopy and CL imaging completed by Cerin et al. (2017) have shown that the distinct pink and smoky coloring of the quartz veins is inherited via radiation-induced defects, including characteristic silicon vacancy hole centers formed by bombardment of α particles emitted from radioactive decay of U, Th, and their daughter isotopes. The vein- and breccia-hosted pink quartz is the most damaged, suggesting this phase crystallized from uraniferous fluids contemporaneously with the main ore stage mineralization event (Cerin et al., 2017). This is congruent with the obvious spatial association of pink quartz-bearing structures with uranium mineralization (e.g. Fig. 5.4C through G). Smoky quartz exhibits less homogeneous radiation defects, displaying α particle-induced CL rims which crosscut the growth zoning and thus appear to record late uranium remobilization events (Cerin et al., 2017). The focussing of radiation-induced defects in quartz within approximately 7 meters of mineralization corroborates the structural control on fluid movements through the Arrow deformation zone.

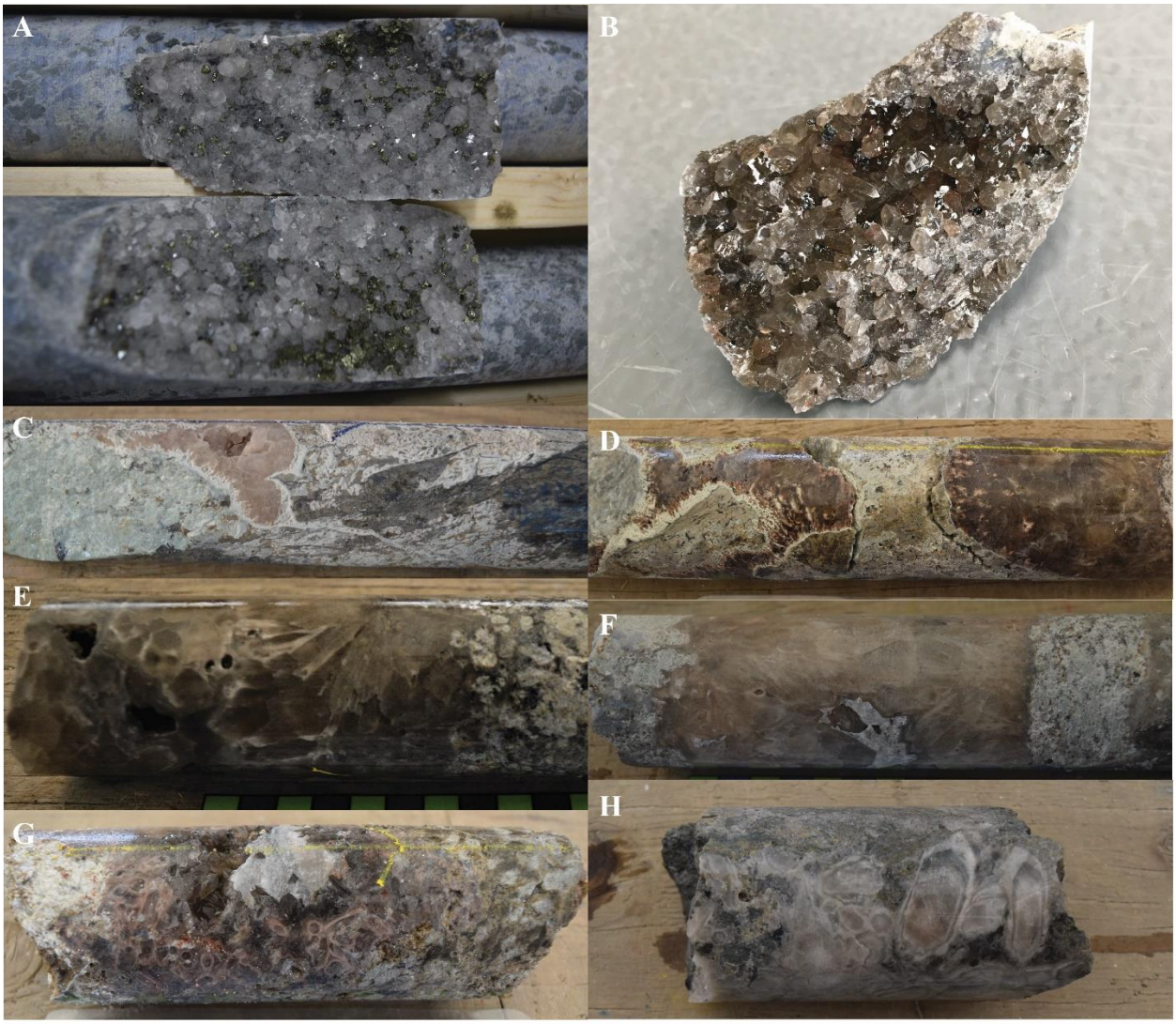

Fig. 5.4. Spectrum of different quartz habits and colors encountered within the Arrow zone as breccia matrices and crosscutting hydrothermal veins or void fill. A) Crosscutting translucent druzy quartz vein with late euhedral pyrite and chalcopyrite mineralization (AR-16-071, 768.0 m). B) Smoky translucent druzy quartz vein proximal to uranium mineralization (AR-18-200c1, 627.1 m). C) Druzy pink quartz within a clay-rich hydrothermal breccia 20 m from A1 shear mineralization, with late robin's egg blue dravite along fractures (AR-16-072c2, 418.3 m). D) Mineralized smoky-pink quartz breccia with late clay-dravite alteration rimming clasts and "eating away" at vein margins (AR-16-085c4, 440.0 m, up to 1,130 cps). E) Smoky brown-black euhedral quartz vein adjacent to A2 shear uranium mineralization (AR-16-080c3, 556.6 m, up to 2,000 cps). F) Smoky brown-pink euhedral quartz vein within the A3 shear zone, adjacent to uranium mineralization (AR-16-086c1, 624.0 m, up to 3,900 cps). G) Vuggy, smoky brown-black druzy quartz void fill with pink-red zoning in crystals proximal to A2 uranium mineralization (AR-16-085c4, 470.0 m, up to 600 cps). H) Spectacular zoning in druzy translucent quartz void fill (AR-16-093c2, 467.4 m).

5.2 Hydrothermal Hydrous Aluminum Silicates

Arrow is a uranium deposit with complex mineral associations, including a variety of ore and gangue minerals. Uranium minerals within the Arrow deformation zone are associated with a variety of hydrous aluminum silicates, including a variety of pre-ore tri-dioctahedral chlorite group minerals and muscovite ($KAl_3Si_3O_{10}(OH,F)_2$). The most prominent alteration type observed, save, the silicification, is early partial to complete sericitization of all pre-existing minerals. The abundance of white mica reflects the abundance of primary K-feldspar in the wall rocks and may suggest the importance of later K-bearing fluids (Alexandre and Kyser, 2014). Sericite (fine-grained white mica; i.e. muscovite or illite) dominantly forms as alteration of feldspars and pyroxene, but in extreme cases may replace all minerals present, including quartz. White mica is extremely common as a metasomatic alteration in rocks exhibiting strong silicification and is likely one of the products of this reaction (Card, 2017). White mica grains range from micrometer- to centimetre-scale, and often obliterate any original mineralogy and texture in the wall rock (Fig. 5.5A through D). A close relationship between uranium mineralization and sericitic white micas is commonly observed throughout the deposit, with uraninite both replacing early white mica grains and precipitating along grain boundaries and cleavage planes (Section 5.3). Sericitization of the wall rock is amongst the earliest metasomatic alteration phases, however phases of broadly syn-ore or post-ore sericite alteration are also evidenced by crosscutting and grain-boundary relationships (e.g. Fig. 5.5B and C). Early sericitization of the wall rocks was likely a large contributor to the softening of the rocks, along with chlorite alteration.

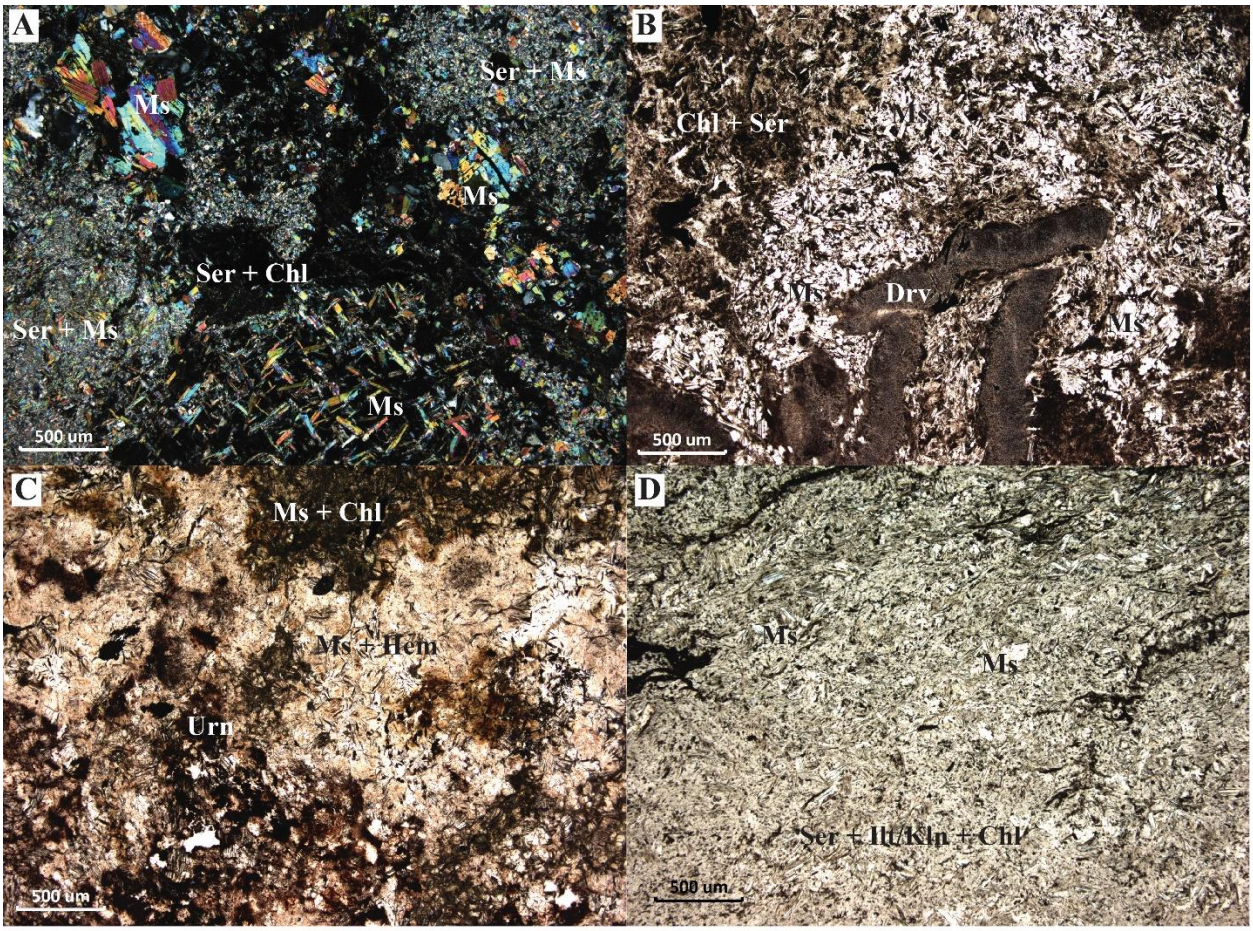

Fig. 5.5. Textural variations and crosscutting relationships in sericitic alteration in Arrow Deposit host rocks. A) Cross-polarized light (XPL) photomicrograph of early pervasive sericite-chlorite (Ser + Chl) alteration overprinted by younger, randomly oriented, coarser-grained muscovite (Ms) (AR-16-084c1, A1 Shear, 665.0 m). B) Plane-polarized light (PPL) photomicrograph of a late dravite (Drv) veinlet rimmed by "clean" muscovite alteration (Ms) crosscutting older "dirty" chlorite-sericite (Chl + Ser) alteration (AR-16-084c1, A1 Shear, 665.0 m). C) PPL image of pervasive muscovite ± chlorite alteration stained with iron-oxide (Ms + Hem) associated with uraninite mineralization (Urn) (AR-16-084c1, A1 Shear, 722.6 m, up to 20,000 cps). D) PPL image of sheared sericite-clay-chlorite (Ser + Ilt/Kln + Chl) matrix within the A2 shear zone, with local coarser-grained muscovite (Ms) (AR-15-059c2, A2 Shear, 506.8 m, up to 45,000 cps).

Chlorite is not as ubiquitous as sericite; however, there is evidence for multiple episodes of chloritization. The most common varieties of chlorite are sudoite ($Mg_2(Al,Fe^{3+})_3Si_3AlO_{10}(OH)_8$) and clinochlore ($(Mg,Fe^{2+})_5Si_3Al_2O_{10}(OH)_8$) based on geochemistry and colour in hand specimen, with sudoite being predominant. Retrograde metamorphic chlorite (clinochlore) commonly rims or completely replaces pre-existing biotite and garnet and commonly defines ductile lineations along foliation planes (e.g. Fig. 4.20). The replacement of garnets by dark green clinochlore is particularly distinctive. Later episodes of hydrothermal chlorite (sudoite) form as cross-cutting fracture linings, small veins, breccia

matrices, or mineral replacements. Chloritic slickensides are abundant along brittle fractures, commonly co-lined with graphite and exhibiting multi-generational slickenstriae. As aforementioned, mylonitic rocks within the Arrow deformation zone are commonly pervasively chloritized, contributing to softening and thus preferential deformation during the formation of the Arrow high strain zones.

Biotitization of feldspars is a common alteration phase within relatively unaltered, coarser-grained feldspar-rich country rocks. Mineral textures and crosscutting relationships indicate that this non-metamorphic biotite grew at the expense of feldspar grains, forming replacement masses and veins of brown, crystalline biotite (Fig. 5.6A). Masses of biotite are locally overprinted by retrograde chloritization and commonly line margins of late quartz veins (Fig. 5.6B), however biotite veins and masses are not commonly observed within more intensely altered Arrow wall rocks proximal to uranium mineralization. This suggests a relatively early timing with respect to the dominant syn- and post-ore alterations.

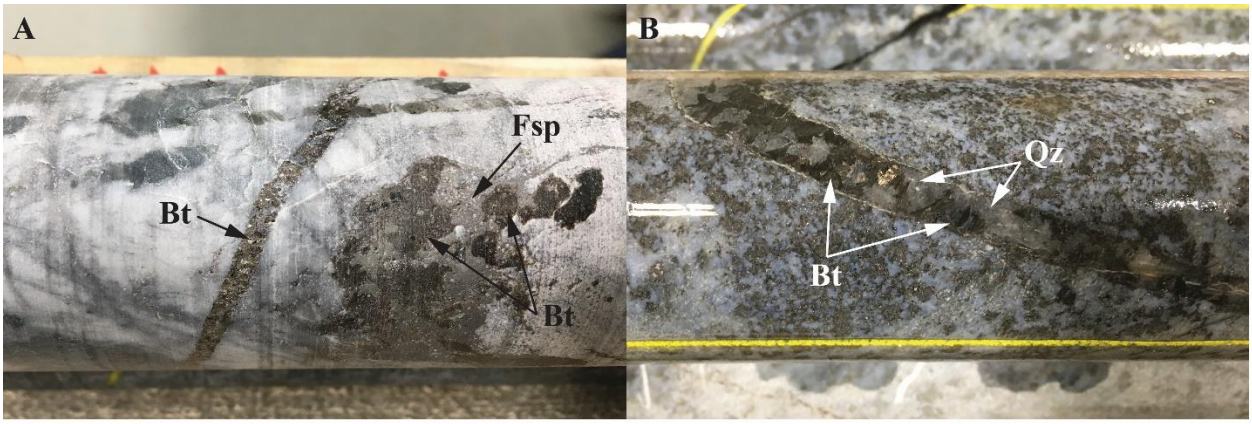

Fig. 5.6. A) Biotitization of feldspar resulting in irregular masses of biotite (Bt) replacing feldspar grains (Fsp) and crosscutting veins (AR-18- 210c3, 769.65 m) B) Crystalline biotite (Bt) lining and growing into a crosscutting quartz (Qz) vein (AR-18-213c1, 512.1 m).

5.3 Graphite and Sulphides

Graphite (and/or graphitic carbon where lacking crystallinity) is interpreted to be relatively early in alteration paragenesis, overprinting previously chloritized mylonitic rocks in the Arrow zone, pre-uranium mineralization, but post-metasomatic alteration (i.e. quartz flooding events) of the host rocks. Studies have shown that graphite may precipitate from carbon-bearing fluids or melts, and often form veins which are structurally controlled within granulites or igneous rocks

(e.g. Luque et al., 2014; Beyssac and Rumble, 2014). Carbon in granulite-hosted graphite veins is derived from sublithospheric sources or from decarbonation reactions of carbonate-bearing lithologies and is transported chiefly in CO_2-rich fluids from which it can precipitate (Luque et al., 2014). Based on mineral textures and crosscutting relationships in thin section and hand specimen (Fig. 5.7A through D), it is suggested that the graphite along the Patterson Lake corridor at Arrow is of secondary origin, precipitated from fluids that were channelled through fracture systems, both conformable to and crosscutting pre-existing ductile structures in brittle fracture networks. Textural relationships also indicate that graphite was subsequently redistributed via relatively late deformation processes at Arrow. Iron sulphide minerals (dominantly pyrite ± pyrrhotite and chalcopyrite) coprecipitated with graphite at Arrow, and quartz veins and breccias are frequently observed to be associated with graphite. Hydrothermal fluids restricted to the C-O-H system are not capable of causing coprecipitation of other minerals with graphite, nor are they effective in dissolving and replacing silicate minerals in the wall rocks (Rumble, 2014). Solutions containing sulphur- and chloride-bearing species would account for the coprecipitation of sulphides and other non-carbonaceous minerals, as well as enhancing the solubility of silicate minerals in the country rock (Rumble, 2014).

Relatively late graphite and sulphides preferentially overprint highly strained and chloritized rocks, which have been subsequently crosscut by quartz veins and/or healed with quartz via hydraulic fracturing and brecciation. The paragenetic relationships are exceedingly complex however, as relatively young quartz veins are commonly brecciated and hosted within a matrix of graphite (Fig. 5.7B) or exhibit graphite-healed fractures (Fig. 5.7A), whereas later quartz phases are observed to host clasts of graphitized wall rock (Fig. 5.7A). The graphitic rocks at Arrow and throughout the Patterson Lake corridor (Card, 2017) demonstrate that high-grade metamorphism was not required accompanying hydrothermal graphite/graphitic carbon precipitation, as the textures and structures hosting the graphite indicate precipitation through or above the brittle-ductile transition.

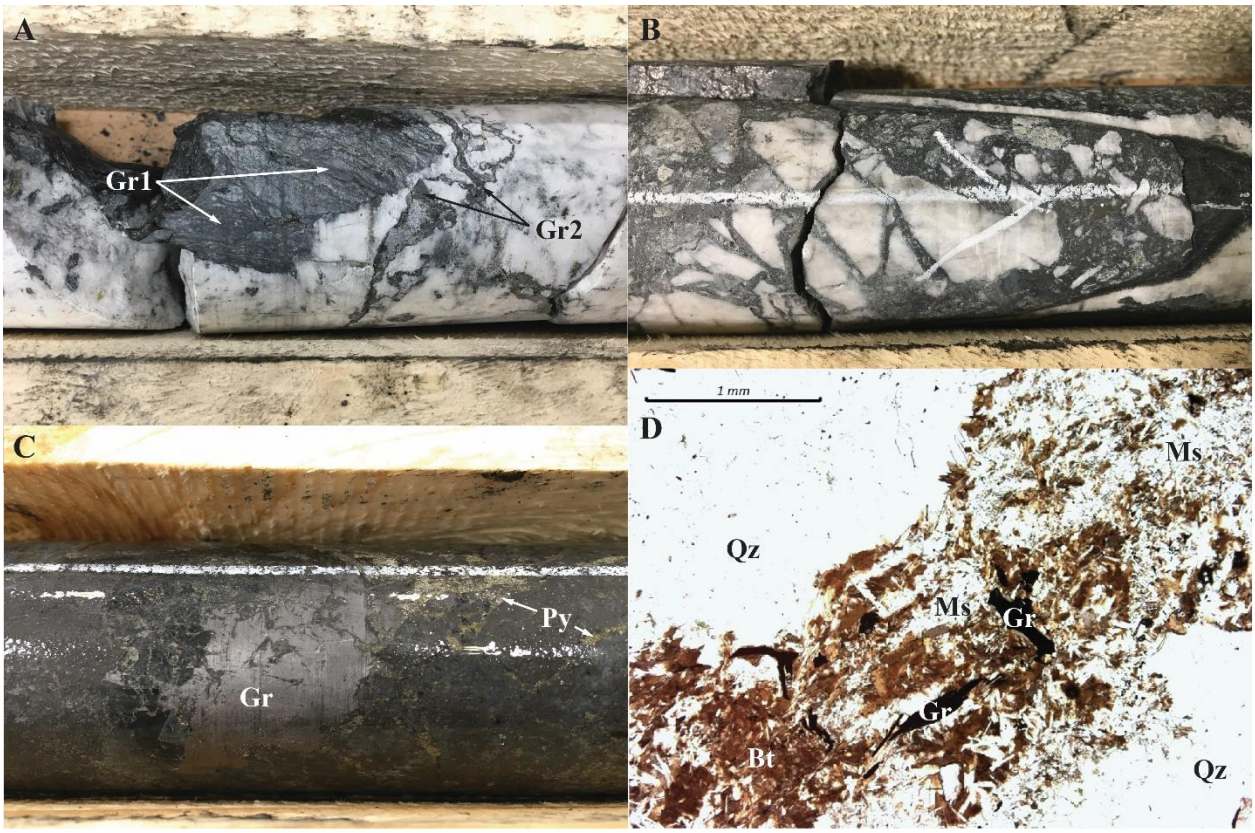

Fig. 5.7. Textural relationships of graphite mineralization within the Arrow zone. A) Angular clast of sheared, graphitized (Gr1) wall rock within a milky quartz breccia. Younger graphite (Gr2) precipitated post-brecciation along fractures in the milky quartz and along clast margins (AR-18-210c3, 869.4 m). B) Late graphite mineralization forming the matrix of a reactivated milky quartz breccia (AR-18-210c3, 871.0 m). C) Late graphite (Gr) and pyrite (Py) mineralization filling voids and precipitated along fractures within a high strain zone (AR-18-211c1, 1,084.85 m). D) Plane-polarized light (PPL) photomicrograph of late graphite (Gr) crosscutting biotite (Bt) and muscovite (Ms) alteration within quartz-rich (Qz) Arrow host rock (AR-16-076c1, 480.1 m).

Sulphide mineralization within the Arrow system consists largely of iron-bearing phases including pyrite and chalcopyrite, with subordinate pyrrhotite, pentlandite, galena, covellite, cobaltite, and arsenopyrite (Fig. 5.8A through D). Sulphides occur typically as disseminated blebs or as stringer veins, commonly with quartz and/or carbonate, which commonly crosscut the dominant foliation and late alteration phases such as dravite. Both pre-ore and post-ore sulphide phases have been identified. Thin section and electron microprobe analyses have revealed pre-ore pyrite, chalcopyrite, pentlandite, pyrrhotite, covellite, cobaltite, and galena (Fig. 5.8D). Syn-ore phases are dominantly composed of pyrite and galena (Fig. 5.8C). Post-ore pyrite and chalcopyrite are common as late veins and disseminations (Fig. 5.8A and B). Pyrite is by far the most common sulphide mineral, forming both contemporaneous with, and subsequently to graphitization of the highly strained rocks comprising the Arrow shear zones.

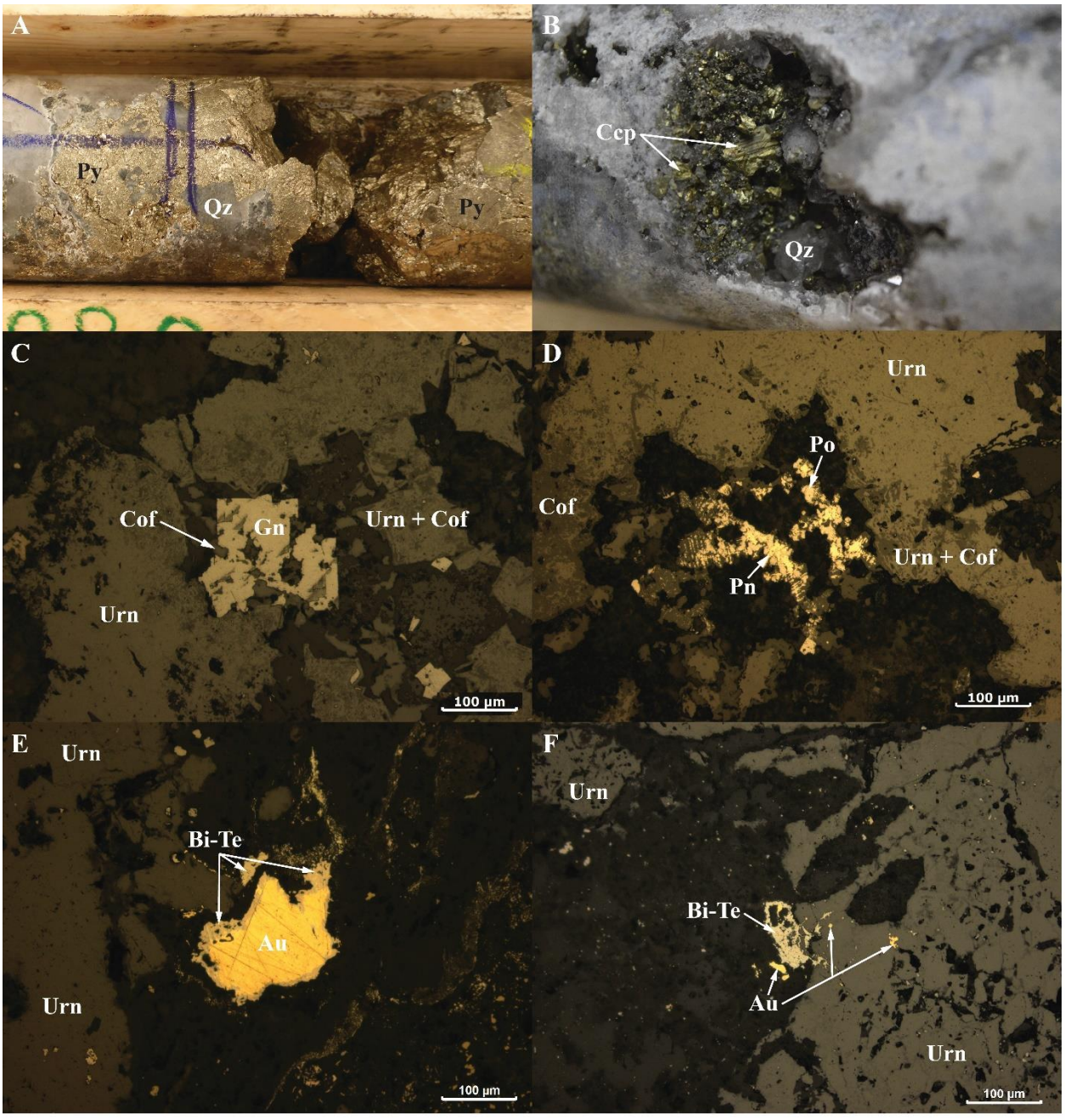

Fig. 5.8. A) Semi-massive pyrite (Py) mineralization associated with late vein quartz (Qz) (AR-15-055, 878.6 m). B) Subhedral chalcopyrite (Ccp) mineralization precipitated within a druzy quartz-filled void (AR-16-071, 768.5 m). C) Reflected light (RL) photomicrograph of syn-ore euhedral galena (Gn) intergrown with uraninite (Urn), with late coffinite (Cof) alteration (AR-16-081c3, 559.5 to 560.0 m). D) RL image of pentlandite (Pn) exsolution lamellae in pyrrhotite (Po), surrounded by coffinite (Cof) altered uraninite (Urn) (AR-15-057c3, 435.05 m). E) RL image of a gold grain (Au) with a bismuth telluride (Bi-Te) mantle surrounded by uraninite (Urn) (AR-16-101c2, 556.95 m). F) Anhedral bismuth telluride mineral (Bi-Te) intergrown with gold (Au) observed infiltrating and filling voids in euhedral uraninite (Urn) (AR-16-081c3, 559.7 m).

5.4 Telluride Minerals and Precious Metals

Trace concentrations of gold and other metals (e.g. bismuth, platinum-group elements) are a common feature of complex, polymetallic unconformity-related uranium deposits, and in some cases may constitute an additional economic resource (e.g. Wilde et al., 1988; Morelli et al., 2012). For example, gold, platinum, and palladium occur in significant amounts in the Jabiluka and Coronation Hill uranium deposits in the Alligator Rivers uranium field in Northern Territory, Australia (Wilde et al., 1988), and economic concentrations of gold (7,970 oz) present as native gold and gold tellurides was extracted from the Cluff Lake D zone leach tailings approximately 75 km north of the Arrow Deposit in Saskatchewan (Morelli et al., 2012). Gold, bismuth, and metal-bearing minerals (e.g. sulphides) within the Cluff Lake D zone are interpreted as relatively late in paragenesis with respect to uranium mineralization, commonly exhibiting intergrowth textures (Morelli et al., 2012). At Cluff Lake, gold is observed to be associated with telluride minerals, specifically altaite, a lead telluride (Morelli et al., 2012).

At Arrow, telluride minerals containing Pb (altaite?), Bi (tellurobismuthite?), and Cu-Se (bambollaite?) have been identified in thin section and are currently interpreted as relatively late in paragenesis based on textural and crosscutting relationships. Native gold (containing silver) and bismuth have also been identified in a suite of samples and are commonly associated with telluride minerals (Fig. 5.8E and F). Gold ± silver mineralization occurs as fine grained (5-250 μm) native gold, which frequently exhibits intergrowth textures with bismuth and telluride minerals (e.g. Fig. 5.8E). Gold does not appear to be intimately related to sulphide mineralization and appears to postdate initial uraninite mineralization (Fig. 5.8F), however textures indicate the gold is older than alteration of uraninite to coffinite in the samples studied. The relationship between Au-Bi-Te-S is has been documented in gold deposits, with bismuth, and to a lesser extent tellurium, being known for their ability to scavenge gold from a hydrothermal fluid (e.g. Tooth, 2008; 2011). Geochemical and textural relationships between gold, bismuth, and telluride minerals indicate that ore refining by liquid bismuth scavenging may have been a key factor in the local gold enrichment at Arrow (Mohrbutter, et al., 2018). Given the appropriate conditions and chemical stimuli, bismuth melt can precipitate in a hydrothermal fluid and affectively scavenge gold from a coexisting hydrothermal fluid, even if the coexisting fluid is undersaturated with respect to gold (Tooth, 2011). Fluid-rock interactions were likely a chief catalyst for precipitation of bismuth

melts from relatively late stage fluids at Arrow, with graphite, pre-ore sulphides, and carbonaceous material (pyrobitumen) available to act as reductants for U-, Bi-, and Au-bearing fluids (Mohrbutter et al., 2018).

5.5 Syn- and Post-Ore Hydrothermal and Metasomatic Alteration Minerals

Although commonly observed proximal to and within mineralized zones, pale bluish-grey to "robin's egg" blue dravite ($NaMg_3Al_6(BO_3)_3Si_6O_{18}(OH)_4$) and/or magnesiofoitite ($Mg_2Al_7Si_6O_{18}(BO_3)_3(OH)_4$) forms either in late vein stockworks or larger hydraulic breccias (Fig. 5.9A and C) that crosscut the wall rock, and in many cases, uranium mineralization. At least two generations of tourmaline have been observed in the matrices of hydrothermal breccias and in veins at Arrow, with the first being relatively coarse-grained and the later being dominantly fibrous or acicular. A study completed by Rosenberg and Foit (2006) showed a similar textural paragenesis at the Rabbit Lake and Key Lake uranium deposits. Quartz veins (especially pink), are very commonly lined with dravite and/or clay minerals (illite, kaolinite, muscovite), clearly illustrating structural control (Fig. 5.9B and C). The tourmalines form a substantial alteration halo around the Arrow Deposit, extending from over 900 meters depth to the unconformity surface (Fig. 5.9A). In thin section, the tourmaline commonly exhibits an acicular habit of radiating crystals from vein boundaries, or as masses with other minerals (Fig. 5.9D). Acicular dravite/magnesiofoitite crystals have been observed to occur with both illite and illite-sudoite mixtures. Based on crosscutting relationships observed in thin section and hand sample, the bluish tourmaline is one of the latest alteration phases, dominantly forming post main ore stage at Arrow. However, some tourmaline may be locally synchronous with the main ore forming event, such is the suggested case at McArthur River (Adlakha and Hattori, 2016), with a younger stage of magnesiofoitite forming coeval with, or after, late ore remobilization or alteration stages. Although there are variations in the timing of dravite/magnesiofoitite across the Basin, the temporal relationship between tourmalines and uranium mineralization at many unconformity-related uranium deposits in the Athabasca Basin (e.g. Shea Creek; Kister et al., 2005; Sheahan et al., 2016, and McArthur River; Adlakha and Hattori, 2016) appears to be broadly syn- to post-uranium mineralization.

The most common clay minerals encountered within the Arrow zone are kaolinite and illite. Kaolinite is the most common clay mineral proximal to the unconformity, whereas mixtures of illite and muscovite (i.e. sericitic and coarser-grained white mica) appear to be more commonly

associated with mineralization over kaolinite. Textural and crosscutting relationships evidence multiple phases of clay alteration, replacing minerals or exhibiting a clear structural control through fracture linings and overprinting of previously sericitized or chloritized structures.

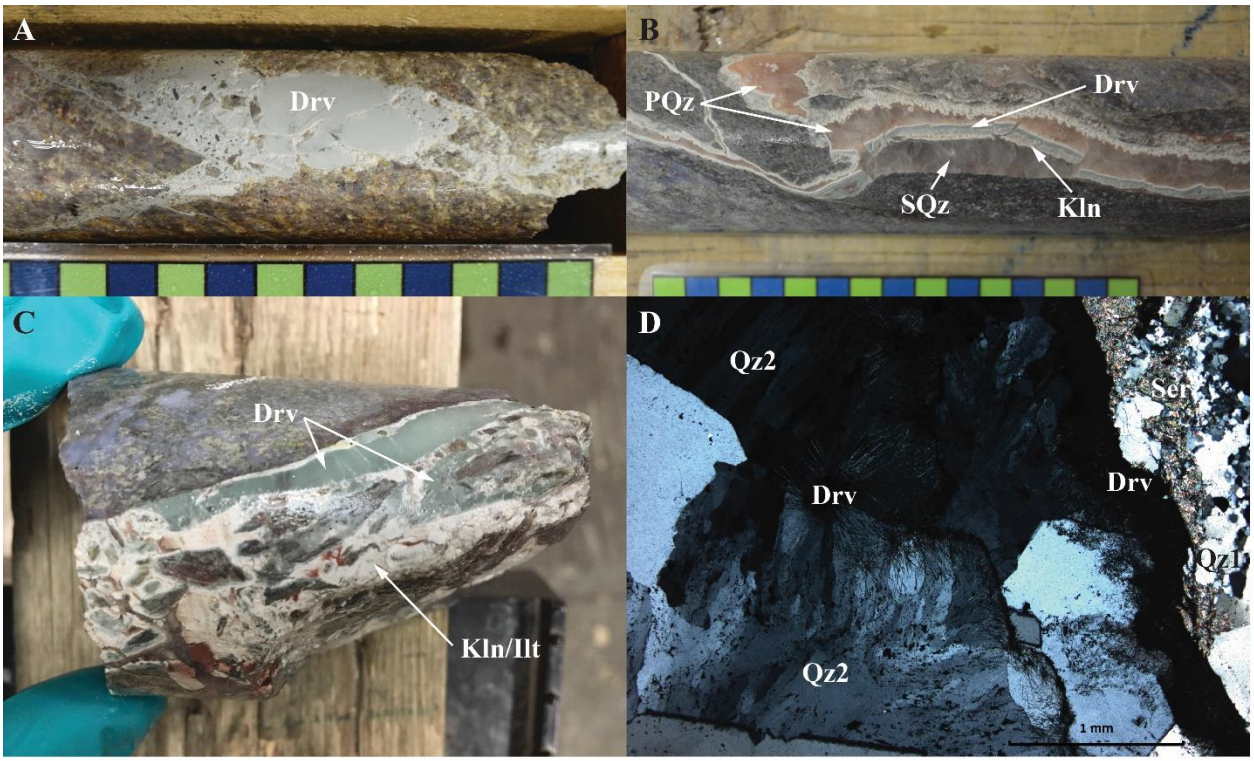

Fig. 5.9. A) Dravite (Drv) healed breccia 15.8 m below the unconformity at 97.7 m (AR-18-212c1, 113.5 m). B) Fracture network lined with dravite (Drv) and white kaolinite (Kln), with subsequent pink (PQz) and smoky quartz (SQz) fill hosting clasts of older dravite-clay lining (AR-17-129c1, 590.7 m). C) Kaolinite/Illite-healed (Kln/Ilt) breccia hosting clasts of dravite (Drv) and dravite-rimmed wall rock (AR-17-129c1, 600.1 m). D) Acicular dravite crystals (Drv) radiating from the margins of a quartz vein (Qz2) crosscutting blue quartz (Qz1) and sericite (Ser) alteration (AR-16-078c4, 621.25 m).

Carbonate minerals form relatively late phases throughout the Arrow zone, associated with fenitic alteration or comprising late stage veins cutting wall rock and uranium mineralization (Fig. 5.10A through F). Black or white calcite ($CaCO_3$) veins are observed crosscutting barren wall rock as well as high-grade uranium mineralization as micro stockworks or druzy veins (e.g. Fig. 5.10E and B, respectively). Druzy calcite veins are commonly associated with relatively late sulphide mineralization (Fig. 5.10E). Late siderite ($Fe^{2+}CO_3$) veins and druzy void fills are common within the upper 50 to 100 meters of basement rock below the unconformity (Fig. 5.10F), and locally extend into the overlying Athabasca Supergroup sandstones.

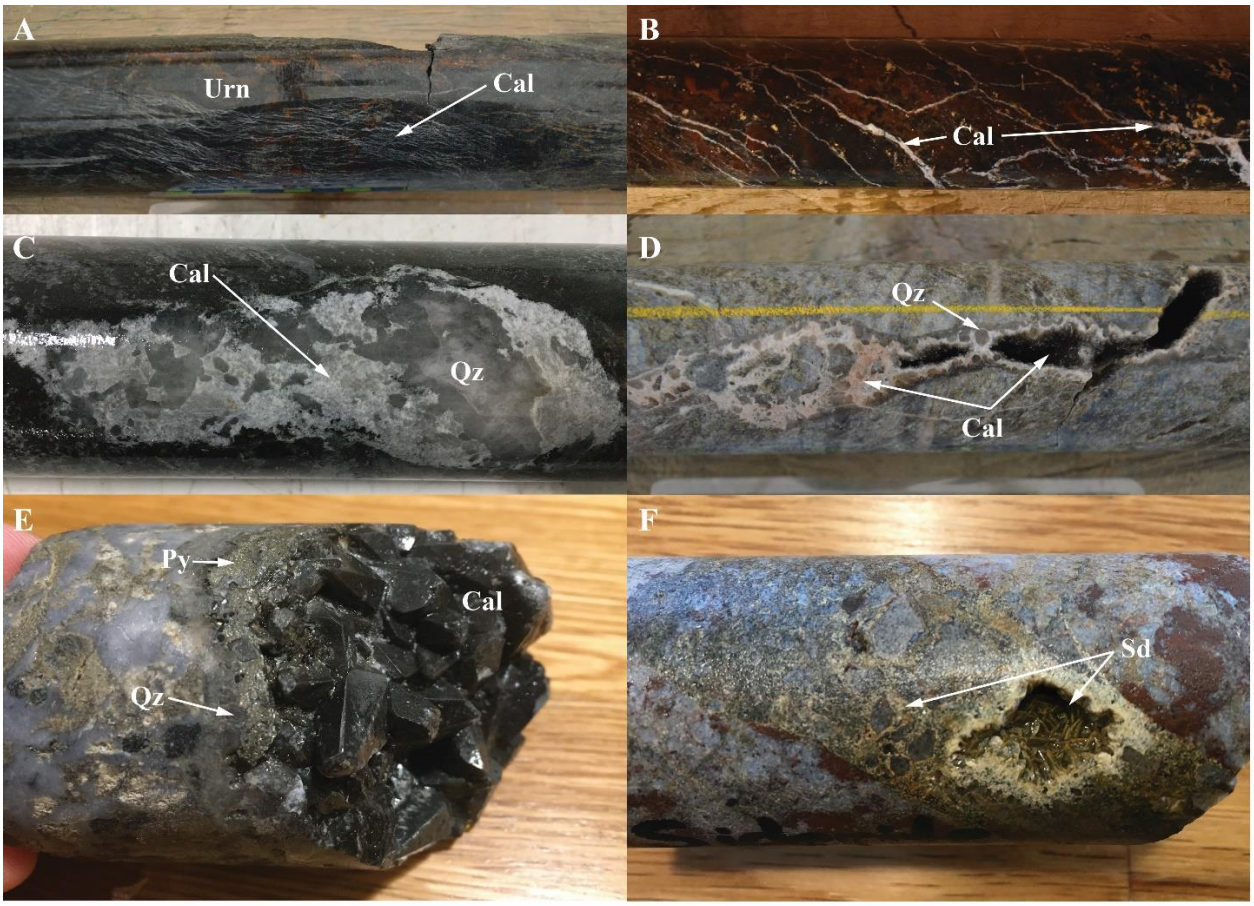

Fig. 5.10. A) Crackle stockwork of calcite (Cal) veins crosscutting semi-massive uraninite (Urn) mineralization within the A2 shear zone (AR-16-080c2, 466.5 to 467.0 m, up to 60,000 cps). B) Calcite vein network crosscutting uraninite mineralization and associated hematite-limonite alteration (AR-17-155c2, 562.4 to 562.8 m, up to >61,000 cps). C) Crystalline calcite vein enveloping euhedral quartz (Qz) crystals (Hole and depth not recorded). D) Translucent quartz-lined fracture infilled with white and smoky calcite (AR-16-080c1, 541.5 to 542.0 m). E) Druzy black calcite and smoky quartz vein with late pyrite (Py) mineralization (AR-16-096c1, 350.4 m). F) Tabular brown-yellow siderite (Sd) crystals in a cohesive breccia hosting clasts of hematized wall rock (AR-16-078c1, 215.0 m).

Hematite and limonite alteration are variable, occurring as discrete stains intimately associated with uranium mineralization and overprinting earlier sericite alteration (e.g. Fig. 4.4.7), or contemporaneous with sericitization, and as groundmass alteration of quartz-clastic breccias. Moderate to strong hematization is also well-developed in the upper portion of the crystalline basement rock, interpreted to be part of the paleoweathering profile. Figure 5.11 illustrates the compiled Arrow paragenesis integrated with detailed structural analysis, further refining the genetic model and evolutionary timeline of the deposit. The chemistry, textural characteristics, and geochronology of uranium-bearing minerals at Arrow are discussed in Section 6.0.

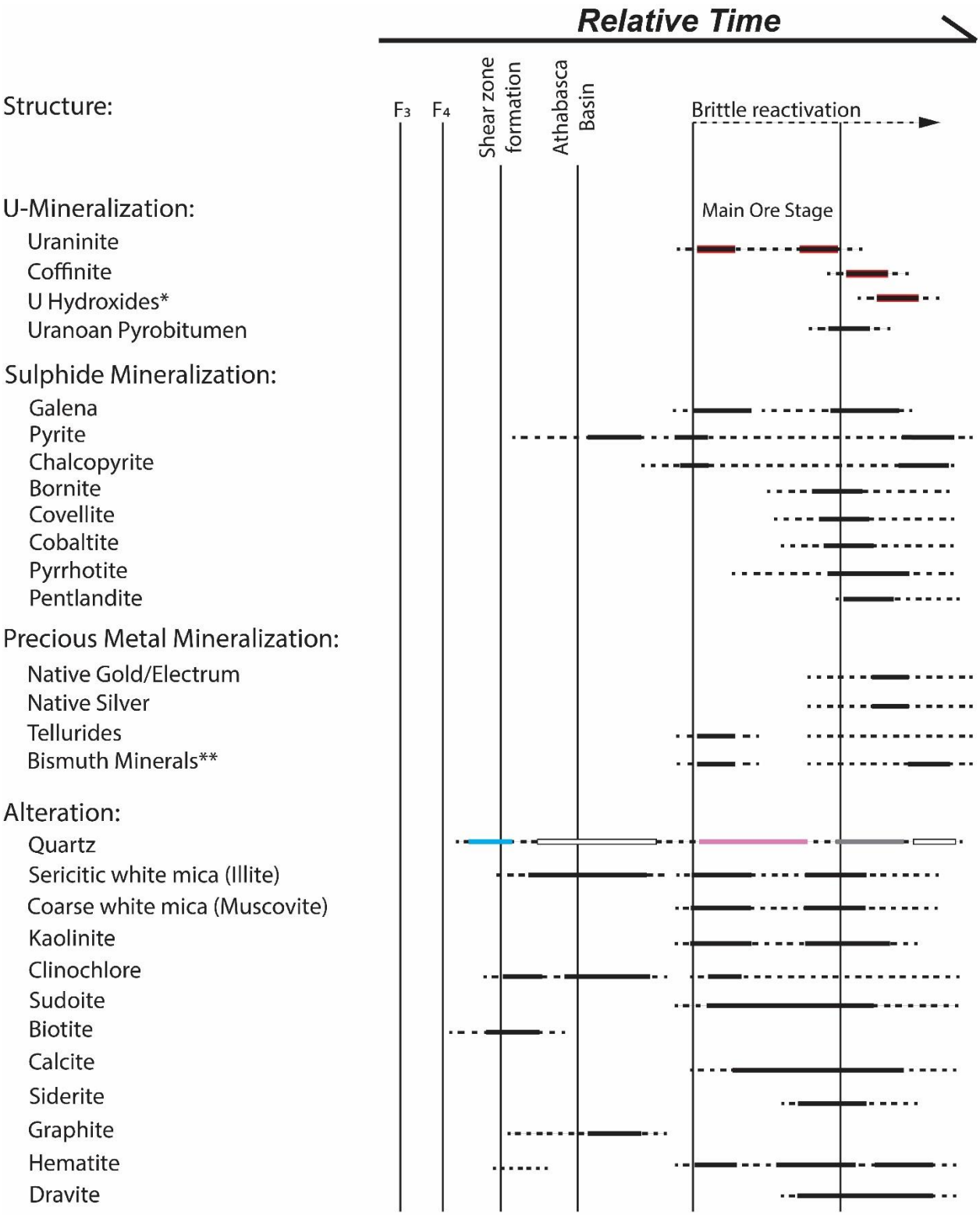

Fig. 5.11. Paragenetic chart for the Arrow Deposit integrating structural evolution, U-mineral phases, precious metals, and hydrothermal alteration products. Quartz episodes are colorized to represent different phases. *Minor U silicates and hydroxides/oxyhydroxides. **Native bismuth, bismuthinite, and Bi-Te-Se minerals.

CHAPTER 6

TEXTURAL RELATIONSHIPS, CHEMISTRY, STABLE O ISOTOPES, AND U-PB GEOCHRONOLOGY OF URANIFEROUS PHASES

6.1 Geochemical and Textural Characteristics of Uranium Minerals

Uraninite, UO_2, is the most common uranium-bearing ore mineral in unconformity-related uranium deposits in the Athabasca Basin, containing up to 90 wt% U (Alexandre and Kyser, 2005). This is a markedly higher uranium content relative to other primary uranium minerals such as coffinite (~70 wt% U; found in Colorado Plateau-type U-V deposits or as an alteration of uraninite), brannerite (~30-35 wt% U; found in Witwatersrand paleoplacers), or davidite (~3-4 wt% U; found in U-rich pegmatites). Elements including Th, REE, Ca, and radiogenic elements including Pb, Ra, and Po may also be contained in natural uraninite, making its formula $(U^{4+}_{1-x-y-z}U^{6+}_{x}REE^{3+}_{y}M^{2+}_{z})O_{2+x-y-z}$ (Alexandre and Kyser, 2005). In the literature, uraninite and pitchblende are often treated as synonymous, whereas some mineralogists have attempted to distinguish between the two. Some workers (e.g. Ellsworth, 1932; Rogers, 1947) have made the distinction based on crystallinity and specific gravity and advise that they should be considered separately. They propose that the name uraninite used for the isometric, crystalline uranium dioxide mineral with specific gravity ranging from 8.0 to 10.5 and low water content, and pitchblende for its amorphous, massive or colloform (mineraloid) equivalent with specific gravity varying from 6.8 to 8.5 and higher water content (Rogers, 1947).

Due to the exceptional crystal habit of much of the uranium minerals at Arrow and to avoid ambiguity, UO_2 will be referred to as uraninite for the purposes of this paper. The main uraniferous mineral present at Arrow is uraninite (UO_2), whereas coffinite (uranium-silicate) may partially or wholly replace uraninite (Fig. 6.1A through D). Cubic uraninite and massive void-fill or replacement pitchblende (Fig. 6.2) are the main styles of uranium mineralization in the Arrow Deposit, along with local fracture-filling veins, colloform or botryoidal “crusts”, relatively fine-grained aggregates (locally dendritic; Fig. 6.3) and disseminated grains. Many of the uraninite samples from Arrow display largely homogeneous reflectance, however the majority of samples analyzed show uraninite crystals having zones or mantles of different reflectivity due to alteration or recrystallization (Fig. 6.1). Subsequent alteration of uraninite may form secondary uranium

minerals containing variable amounts of Pb, rare-earth elements (REE), Si, Ca, and K, such as compreignacite ($K_2(UO_2)_6O_4(OH)_6•8(H_2O)$), becquerelite ($Ca(UO_2)_6O_4(OH)_6•8(H_2O)$), sayrite ($Pb_2(UO_2)_5O_6(OH)_2•4(H_2O)$), and curite ($Pb_{3.5}(H_2O)_22(UO_2)_42(OH)_{2.5}$), or Si-bearing alteration phases including coffinite ($U(SiO_4)_{0.9}(OH)_{0.4}$), soddyite ((UO2)2(SiO4)•2(H2O)), and uranophane ($CaH_2(SiO_4)_2(UO_2)•5(H_2O)$) which may partially or wholly replace uraninite (Fig. 6.4). These altered rims or zones display a lower reflectivity, and often a pitted or porous appearance in BSE images (e.g. Fig. 6.1D).

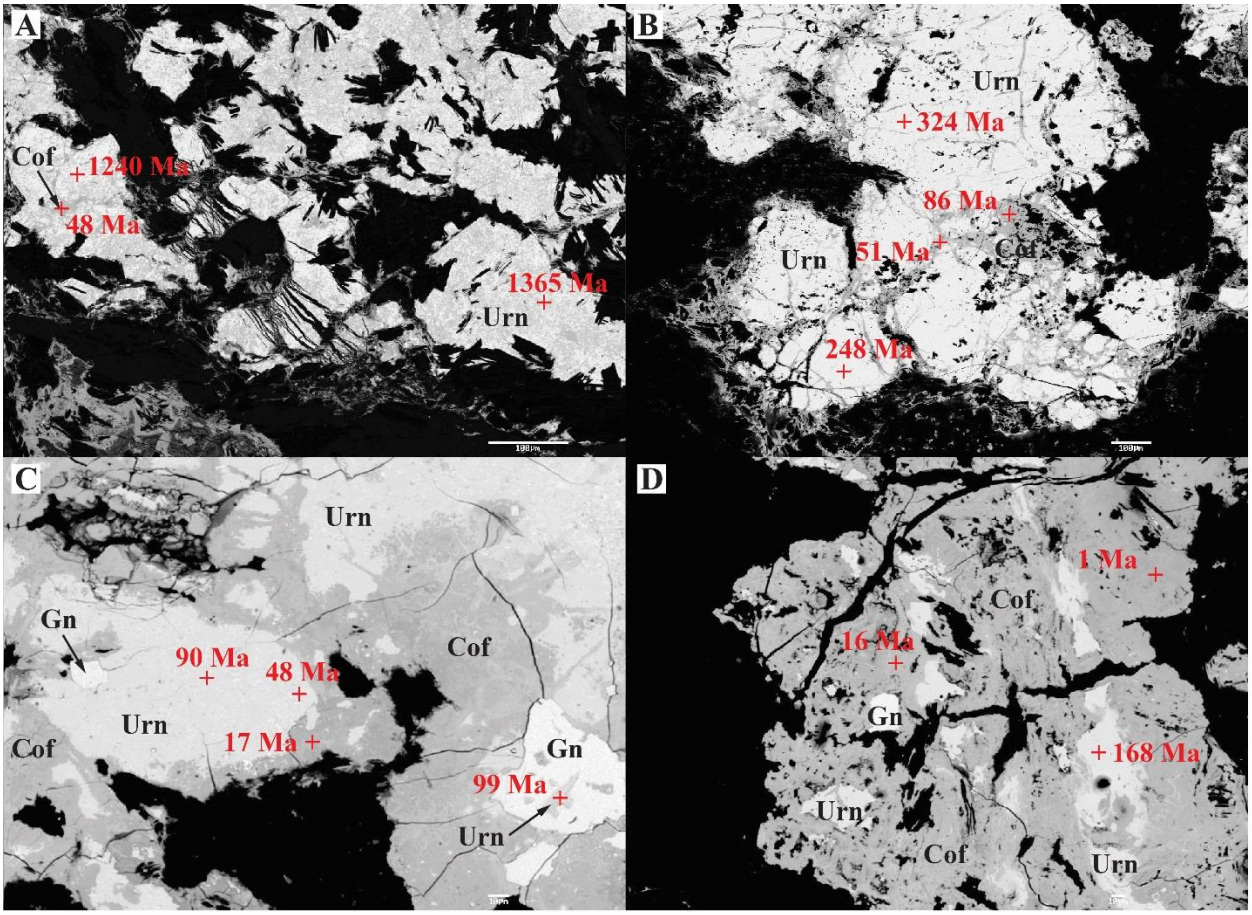

Fig. 6.1. Backscattered electron (BSE) images of Arrow U mineralization with average chemical ages calculated from EMPA analyses. Chemical ages correspond to crosscutting and textural relationships between U phases. A) BSE image of altered primary uraninite (Urn) from the A2 Shear (AR-15-059c2, A2 Shear, 531.15 m). B) BSE image of remobilized, brecciated uraninite with coffinite (Cof) alteration mantling and penetrating fractures (AR-15-059c2, A2 Shear, 531.1 m). C) BSE image of heavily altered uraninite with mantles of darker grey coffinite with relatively late galena (Gn) enveloping uraninite within the A2 shear wrench zone (AR-16-076c3, A2 Shear, 518.85 m). D) Extremely altered uraninite with late coffinite mineralization replacing uraninite and overgrowing galena (AR-16-076c3, A2 Shear, 518.9 m).

Fig. 6.2. Semi-massive uraninite (group 1) mineralization and associated hematite alteration within the A2 high-grade core (AR-16-093c2, 485.7 to 485.85 m, up to >61,000 cps).

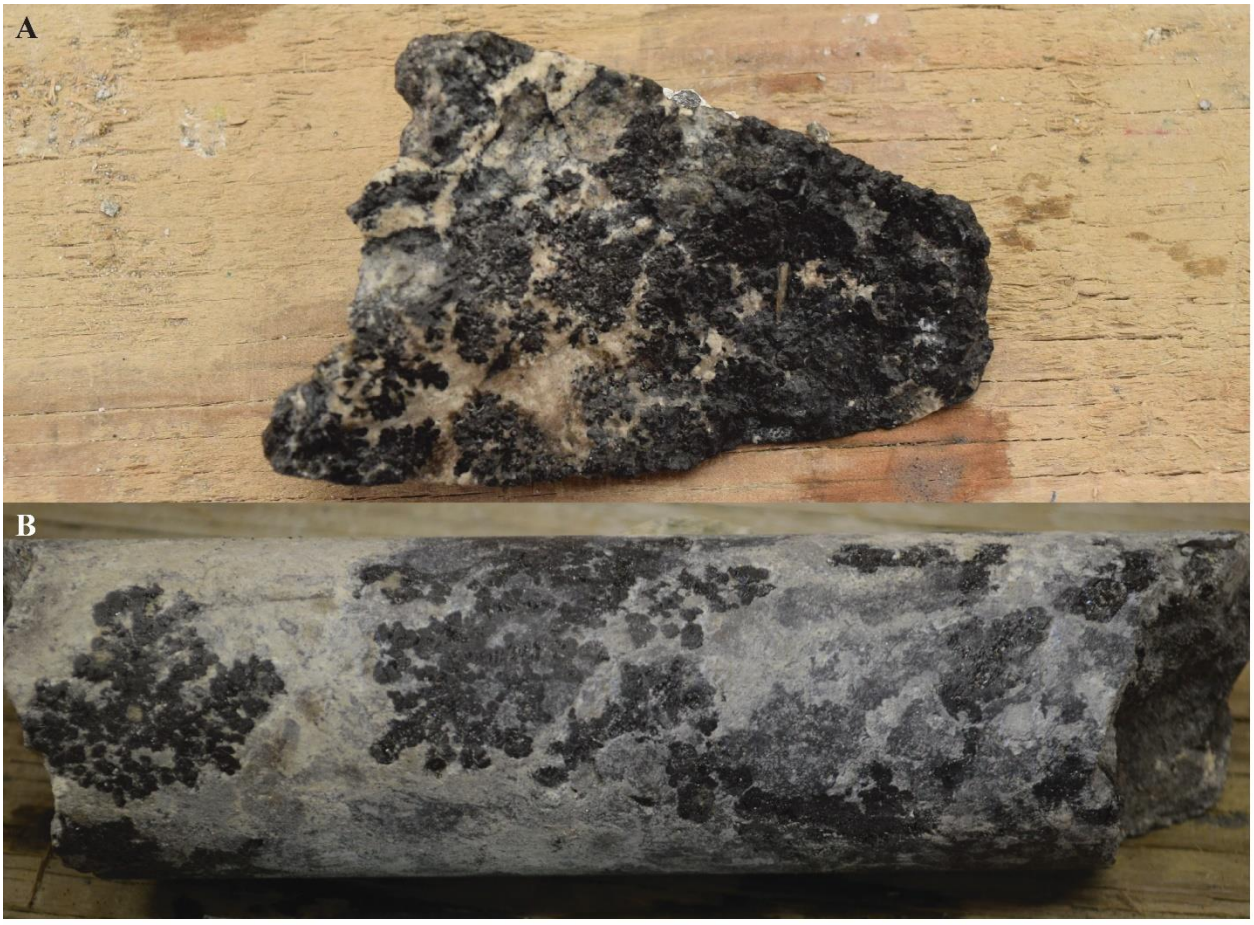

Fig. 6.3. A) Dendritic uraninite (group 1) mineralization along a fracture (AR-16-086c1, 822.2 m, up to 34,000 cps). B) Dendritic patches of uraninite (group 1) mineralization within moderately to strongly clay-altered wall rock (AR-16-076c3, 518.4 m, up to >61,000 cps).

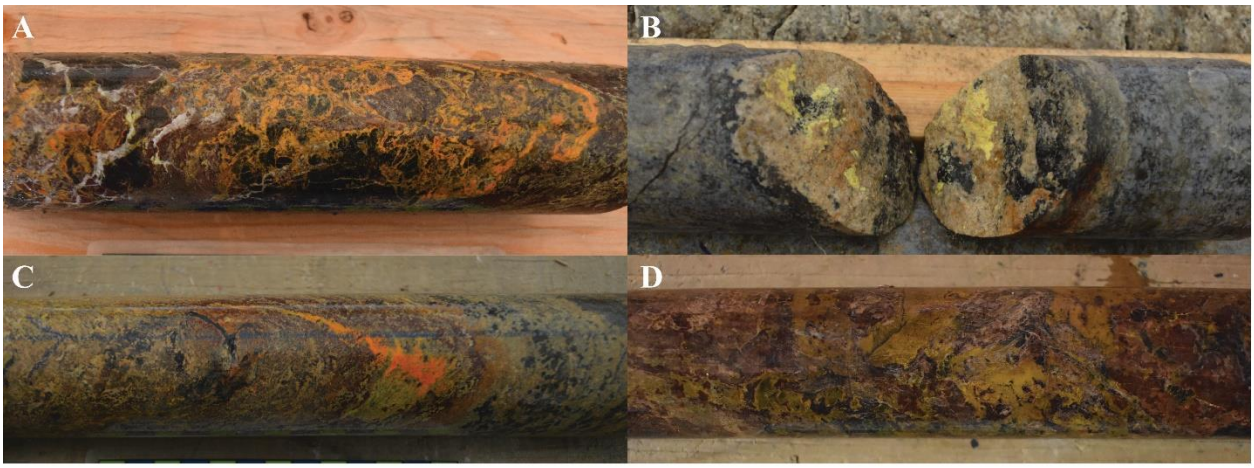

Fig. 6.4. Examples of various uraniferous phases comprising group 2 uranium silicates, hydroxides, and oxyhydroxides. A) Bright orange (curite?) and yellow (soddyite?) secondary uranium minerals altering black uraninite and precipitated along fractures and grain boundaries. Note late white calcite veins (AR-16-096c3, 579.5 m, up to >61,000 cps). B) Canary yellow uranophane altering black uraninite along a mineralized fracture (AR-16-081c1, 731.3 m, up to 17,500 cps). C) Bright orange (sayrite?) and yellow (uranophane?) secondary uranium minerals altering uraninite (AR-16-076c4, 599.7 m, up to 40,000 cps). D) Golden yellow (compreignacite?) secondary uranium mineral replacing black uraninite within a hydrothermal breccia zone (AR-17-147c4, 638.3 m, up to >61,000 cps).

Uraninite mineralization at Arrow is locally accompanied by uranoan pyrobitumen ("thucholite"; Fig. 6.5A and B), however instances of pyrobitumen in barren rock proximal to mineralization has also been logged (Fig. 6.5C). Thucholite is an unusual mineral, composed of approximately 50% carbon, 25% volatile gases, and 25% ash (Barthauer et al., 1953). The ash commonly contains proportions of thorium oxide, rare earth oxides, and uranium oxide with subordinate amounts of lead, calcium, and magnesium oxides (Barthauer et al., 1953). Hoekstra and Fuchs (1960) suggest that thucholite at the Besner mine (Ontario)formed by the action of aqueous solutions containing organic material, possibly as an oil-in-water emulsion, wherein U, Pb, and other relatively soluble oxides were leached from uraninite while Al, Fe, Mg, and silica were deposited in the thucholite (Hoekstra and Fuchs, 1960). Another sample from Ontario, analyzed by Barthauer et al. (1953) revealed a thoria component in the ash of less than 1%, which is in sharp contrast with the higher percentages reported in previous samples (Barthauer et al., 1953). Furthermore, the rare earth fraction of the sample contained anomalous yttrium oxide, comprising more than 50% of the total REE oxide proportion (Barthauer et al., 1953). The pyrobitumen at Arrow has not been studied in detail, however one sample containing mainly pyrobitumen analyzed by ICP-MS (Fig. 6.5D) returned 1.23% U, 0.294% TiO_2, 0.0235% Th, 925 ppm Pb, 850 ppm Cu, 671 ppm Zr, and 371 ppm Ni. The rare earth component is dominated by

yttrium and cerium, returning 214 ppm Y and 155 ppm Ce, while all other REE values were well below 100 ppm with the exception of neodymium and dysprosium at 76.9 and 73.5 ppm, respectively. Pyrobitumen is interpreted to be relatively late in the Arrow paragenetic sequence as it is most commonly observed along clay-lined fractures (Fig. 6.5C), within crosscutting druzy quartz veins, or within voids or vugs.

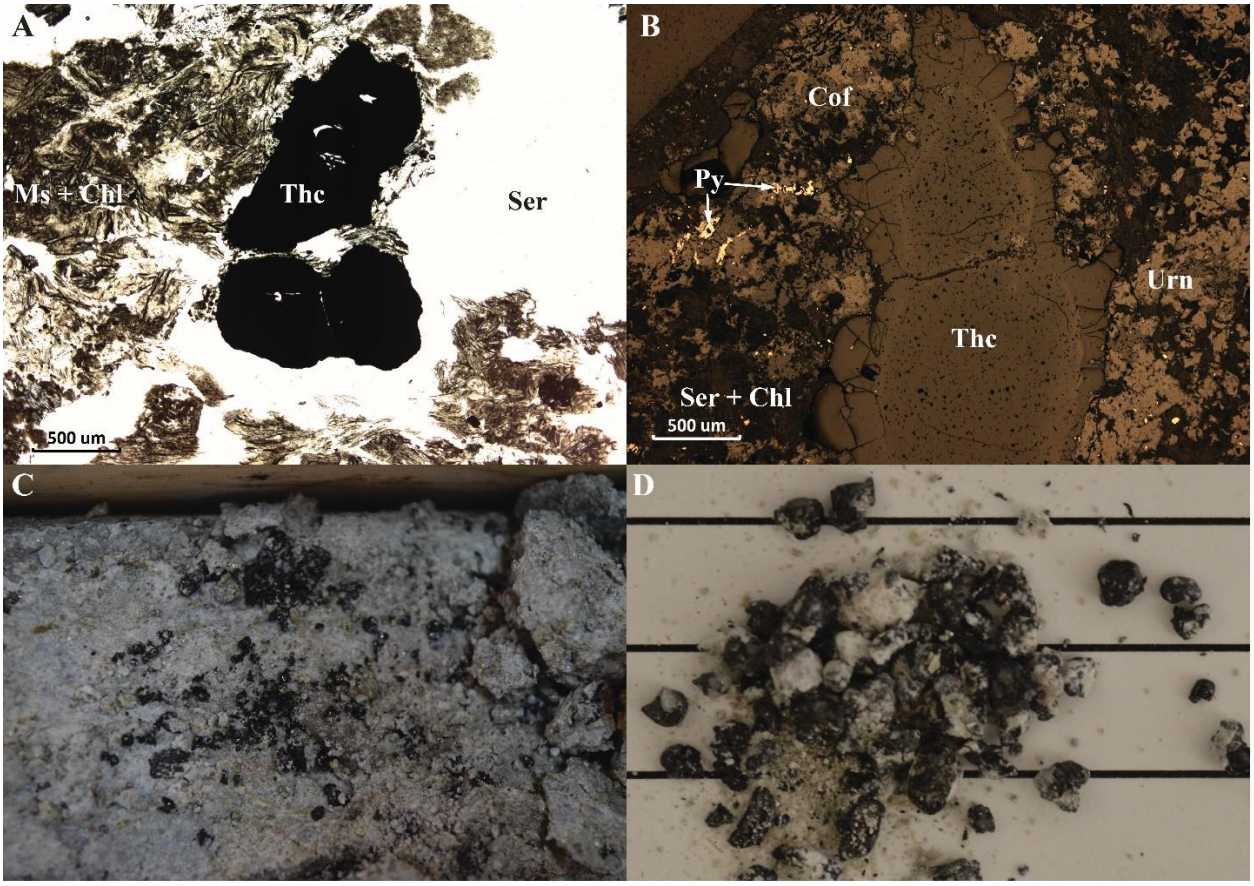

Fig. 6.5 A) PPL image of amorphous thucholite grains (Thc) within a matrix of sericite (Ser), chlorite (Chl), and muscovite (Ms) (AR-16-063c1, 473.25 m). B) RL photomicrograph of a thucholite grain exhibiting a pitted texture with a visible rim, surrounded by uraninite (Urn) mineralization locally altered to coffinite (Cof), within a matrix of sericite and chlorite. Local pyrite (Py) mineralization is visible to the left of the grain (AR-16-076c3, A2 wrench zone, 518.85 m). C) Jet black, amorphous thucholite along a strongly clay-altered fracture surface, proximal to uranium mineralization (AR-16-082c3, 703.25 m). D) Individual thucholite grains extracted for ICP-MS analysis (AR-15-058c1).

Uranium mineralization occurs proximal to the margins of the major graphite-bearing mylonitic structures (A1 to A5; Section 4.1) in both footwall and hanging wall blocks, as well as locally within the structures themselves. Based on current EMPA and BSE image analysis,

uraniferous phases have been characterized in to two broad groups based on their chemical composition and textural relationships (Fig. 6.6; Table 1 and 2).

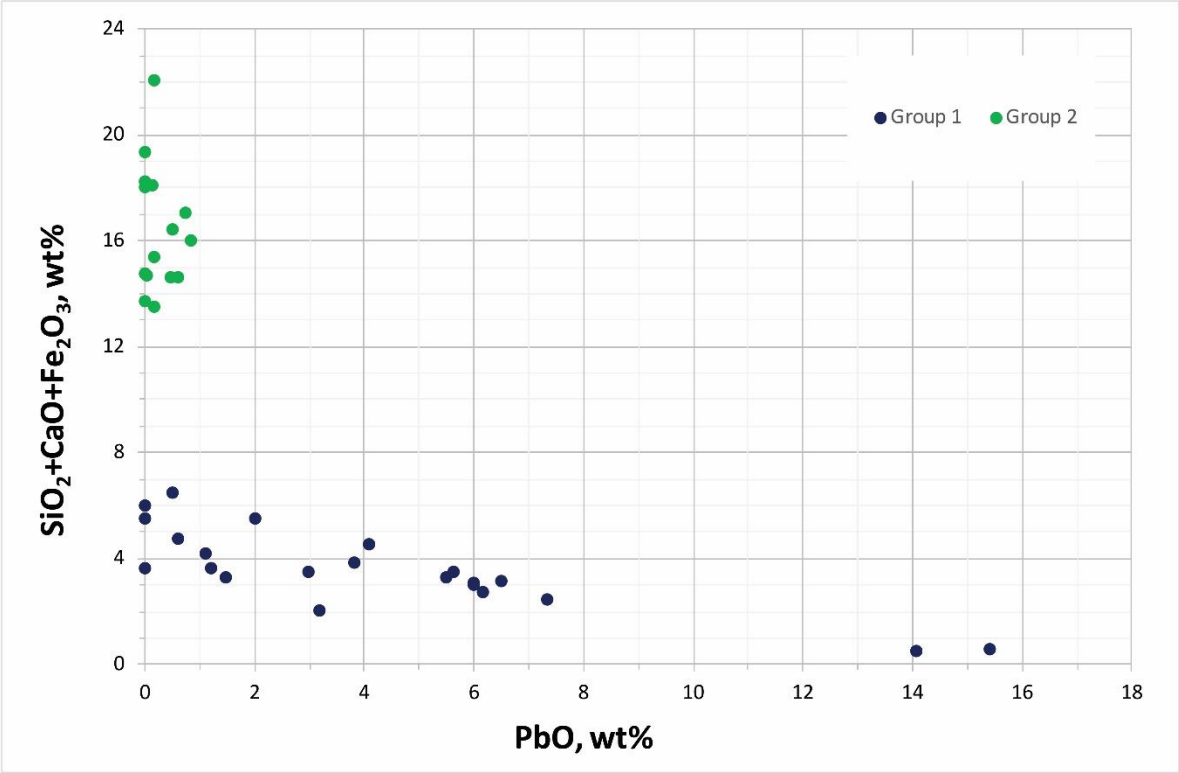

Fig. 6.6. Plot of lead oxide versus major substituting element oxides from EMPA chemical analyses completed on uranium minerals from the Arrow Deposit. Note group 1 and 2 minerals plot in two distinct populations.

The concentration of uranium in group 1 uraninites from the Arrow Deposit is variable, with UO_2 values ranging from 52.77 to 93.08 wt% (Table 1). All other components analyzed also vary significantly. Pb content varies from 0.00 to 15.42 wt% PbO, Si, from 0.20 to 5.74 wt% SiO_2, Ca, from 0.00 to 2.91 wt% CaO, and Ti, from 0.00 to 32.43 wt% TiO_2. The two analyses with the highest Ti content of 23.17 and 32.43 wt% TiO_2 (Table 1) result from uraninite replacement of pre-existing rutile crystals. These two analyses also correspond to the highest V_2O_5 and the lowest UO_2 components. Fe content is the only component that remains relatively constant, ranging from 0.12 to 0.86 wt% Fe_2O_3 (Table 1). Group 1 minerals contain the highest uranium and lead oxide contents, and the lowest silica, calcium, and iron proportions (Table 1). The lack of these common substituting elements indicates that group 1 minerals are primary uraninite/pitchblende that have not been subject to as much alteration (i.e. preserved cores) and/or remobilization. Group 1 minerals comprise dominantly subhedral to euhedral isometric crystals and semi-massive

occurrences of variably altered uraninite. Group 1 minerals exhibit a bright white color and relatively "clean" appearance in BSE images and correspond to the oldest phases of mineralization based on textures (Fig. 6.1) and chemical ages (Section 6.2). Group 1 minerals contain the highest uranium and lead oxide contents, and thus yield the oldest chemical ages (Section 6.2), however the spectrum of PbO content in group 1 minerals from 15.42 wt% to 0.00 wt% indicates many of the primary uraninite grains have undergone significant lead loss over geological time.

The EMPA data also define a second group of uraniferous minerals, with lower lead and uranium, and higher silicon, calcium, iron, aluminum, and REE + Y contents (Table 2). Elevated concentrations of SiO_2, CaO, and Fe_2O_3 are often indicative of uraninite alteration products, which in many cases may reset the ages of the primary uraninite grains during alteration (Alexandre and Kyser, 2005). The concentration of uranium in the U-minerals comprising group 2 ranges from 55.77 to 83.57 wt% UO_2, with low lead values ranging from 0.00 to 0.85 wt % PbO (Table 2). Substituting element concentrations are higher, with Si ranging from 7.15 to 18.02 wt% SiO_2, Ca, from 0.51 to 7.19 wt% CaO, Fe, from 0.05 to 1.35 wt% Fe_2O_3, and Ti, from 0.00 to 3.29 wt% TiO_2. Analyzed REE + Y values are high relative to group 1 minerals, with Tb values up to 0.16 wt% Tb_2O_3, and Y, from 0.14 to 2.35 wt% Y_2O_3. Group 2 minerals are constituted by dominantly anhedral, "dirty" looking grains, alteration rims, or mantles on uraninite or rutile/anatase. They are far less reflective in the BSE images, exhibiting a distinct grey color (Fig. 6.1). Group 2 minerals correspond to younger uranium silicates and hydroxides/oxyhydroxides (Fig. 6.4) such as coffinite, uranophane, soddyite, rameauite, or becquerelite, as indicated by the relatively high proportions of substituting elements (e.g. Fe, Si, and Ca; Fig. 6.6), relatively low totals, and relatively young chemical ages (Fig. 6.7 and 6.8; Section 6.2). The low totals in Table 2 may reflect the presence of structural H_2O within the secondary uranium silicates and hydroxides comprising this group. The different mineral groups are clearly visible in BSE images (e.g. white uraninite vs. grey coffinite; Fig. 6.1), and crystal chemistry (Fig. 6.6) obtained via electron microprobe EDS spectra correspond to the paragenetic sequences evidenced by textural relationships and calculated chemical ages (Section 6.2). The element substitutions and effects of alteration and recrystallization in natural uraninite have been analyzed to date on the basis of electron-microprobe data and BSE images. The results obtained offer an example of how post-mineralization fluid circulation events can affect and change the composition of the primary uranium orebody over geological time.

Table 1. Results of electron microprobe analyses for uraninite (Group 1) from the basement-hosted Arrow uranium deposit, and calculated chemical ages.

SiO_2	TiO_2	ThO_2	UO_2	Al_2O_3	Cr_2O_3	Fe_2O_3	Y_2O_3	Tb_2O_3	MnO	CuO	PbO	CaO	V_2O_5	P_2O_5
3.3800	0.8937	0.0000	93.0800	0.2676	0.0422	0.6378	0.5688	0.0026	0.0373	0.0000	1.0912	0.1588	0.0000	0.0000
3.5600	0.6491	0.0000	92.4600	0.3263	0.0230	0.6908	0.8438	0.0000	0.0501	0.0000	0.5841	0.5110	0.0000	0.0000
3.2500	2.5432	0.0340	91.5900	0.2626	0.0000	0.3797	0.8214	0.0000	0.0851	0.0000	1.1928	0.0000	0.0000	0.0000
3.6500	0.0413	0.0000	90.9300	0.3630	0.0000	0.7331	0.2642	0.0000	0.1019	0.0000	2.0011	1.1223	0.0163	0.0000
0.7014	2.9406	0.1638	90.7000	0.0369	0.0000	0.5939	0.4799	0.0756	0.0388	0.0000	3.1900	0.7548	0.0000	0.0442
2.0851	3.1400	0.1563	87.7300	0.2096	0.0000	0.7563	0.3430	0.0078	0.0469	0.0150	1.4657	0.4282	0.0000	0.5003
5.0100	2.9764	0.1250	79.8500	0.5309	0.0000	0.1328	0.4235	0.0000	0.1025	0.0000	0.0000	0.3955	0.2253	1.1940
5.7400	3.4700	0.0400	78.1000	0.8192	0.0281	0.2404	0.0273	0.0000	0.0735	0.0125	0.0000	0.0168	0.2338	1.3140
3.3400	23.1700	0.0000	60.0300	0.4474	0.0670	0.3134	0.5497	0.0000	0.0046	0.0000	0.0000	0.0000	0.7599	0.8822
0.7524	0.5535	0.0000	88.9900	0.0498	0.0064	0.8592	0.6210	0.0000	0.1886	0.0000	4.0800	2.9058	0.0000	0.3356
0.7973	0.6379	0.1243	89.5500	0.0673	0.0000	0.8454	0.8160	0.0000	0.0614	0.0000	3.8300	2.1746	0.0000	0.3312
0.8021	0.6009	0.1365	91.1900	0.0539	0.0000	0.6955	0.9784	0.0000	0.0160	0.1268	2.9817	1.9727	0.0000	0.1971
1.0039	2.0811	0.0000	87.7300	0.0220	0.0000	0.3823	0.1615	0.0000	0.0948	0.0000	6.1600	1.3338	0.0000	0.0775
3.7600	32.4300	0.0053	52.7700	0.4539	0.0306	0.6885	0.0000	0.0000	0.0475	0.0000	0.4846	2.0169	0.5724	0.2875
0.2505	0.0694	0.0000	83.1000	0.0000	0.0000	0.2405	0.0395	0.0000	0.0418	0.0280	15.4200	0.0610	0.0000	0.0000
0.2006	0.1245	0.0000	83.6300	0.0188	0.0000	0.1235	0.1769	0.0000	0.0722	0.0615	14.0600	0.1777	0.0000	0.0000
0.7299	0.0372	0.0000	90.1400	0.0456	0.0000	0.5064	1.2421	0.0723	0.0784	0.0000	5.9900	1.8609	0.0000	0.0000
0.6350	0.0539	0.0000	90.3300	0.0000	0.0000	0.5378	0.8848	0.0000	0.0609	0.0000	5.4900	2.0910	0.0000	0.1667
0.4284	0.0860	0.0000	89.2300	0.0211	0.0000	0.4360	0.5657	0.0000	0.1106	0.0007	7.3500	1.6037	0.0000	0.1640
0.6322	0.0918	0.0000	90.1400	0.0342	0.0000	0.5344	0.5698	0.0000	0.0550	0.0146	5.9800	1.8281	0.0000	0.0000
0.7643	0.1626	0.0000	88.9800	0.0178	0.0000	0.5539	1.5869	0.0521	0.0904	0.0286	5.6300	2.1782	0.0000	0.1315
0.5517	0.0000	0.0000	90.2700	0.0027	0.0000	0.5568	0.5412	0.0000	0.0267	0.0535	6.4800	2.0347	0.0000	0.0000

Compositions are reported in wt%, and the age in Ma.

Table 1. Continued.

K_2O	Sample #	Total	Age (Ranchin, 1968)	Age (Cameron-Schiman, 1978)	Age (Bowles 1990; 2015)	Average Age
0.1344	B00093	100.3000	93	88	87	90
0.2184	B00093	99.9100	50	47	47	48
0.1626	B00093	100.3200	104	98	97	99
0.2475	B00093	99.4700	175	165	163	168
0.2528	B00228	99.9700	279	262	257	266
0.2761	B00228	97.1600	133	125	124	127
0.4062	B00228	91.3700	0	0	0	0
0.4951	B00228	90.6200	0	0	0	0
0.3833	B00228	89.9400	0	0	0	0
0.2183	B00036	99.5600	365	344	334	348
0.1721	B00036	99.4100	340	319	311	324
0.1510	B00036	99.9100	260	244	240	248
0.2019	B00036	99.2500	558	527	502	529
0.4457	B00036	94.0000	73	68	68	70
0.2906	B00036	99.5400	1476	1393	1225	1365
0.1940	B00036	98.8400	1337	1262	1123	1240
0.1649	B00066	100.8700	528	493	471	497
0.1021	B00066	100.3500	483	456	437	459
0.2067	B00066	100.2100	655	618	583	619
0.2217	B00066	100.1100	527	498	476	501
0.1699	B00066	100.3400	502	469	449	474
0.1528	B00066	100.6700	570	539	512	540

Compositions are reported in wt%, and the age in Ma.

Table 2. Results of electron microprobe analyses for uranium silicates and uranyl hydroxide/oxyhydroxide minerals (Group 2) from the basement-hosted Arrow uranium deposit, and calculated chemical ages.

SiO_2	TiO_2	ThO_2	UO_2	Al_2O_3	Cr_2O_3	Fe_2O_3	Y_2O_3	Tb_2O_3	MnO	CuO	PbO	CaO	V_2O_5	P_2O_5
15.8900	0.7399	0.0000	77.5900	1.1685	0.0000	0.3019	1.3119	0.0000	0.0000	0.0000	0.7384	0.8831	0.0000	0.0000
17.6400	0.7440	0.0000	78.6500	1.6608	0.0000	0.0970	0.3936	0.0525	0.0000	0.0000	0.0000	0.5107	0.0000	0.0616
14.0100	0.4422	0.0000	82.1300	1.1407	0.0000	0.0649	0.9806	0.0000	0.0044	0.0000	0.0289	0.5855	0.0000	0.0539
14.8000	3.2900	0.0004	78.1400	0.9072	0.0000	0.0844	0.6956	0.0486	0.0125	0.0000	0.1722	0.5338	0.0000	0.0000
12.4000	0.0000	0.0707	83.5700	0.9394	0.0000	0.2077	0.3498	0.1605	0.0071	0.0000	0.1714	0.8917	0.0000	0.0000
17.6400	0.2511	0.0000	79.4200	1.2110	0.0144	0.0631	0.6928	0.0000	0.0000	0.0000	0.0072	0.5243	0.0000	0.0000
11.6100	1.7741	0.0000	66.7500	4.3100	0.0000	1.3478	0.1416	0.0102	0.0488	0.0000	0.0000	0.7278	0.4154	0.7839
18.0200	0.8041	0.1700	56.3400	2.9376	0.0000	0.3580	0.5969	0.0000	0.0599	0.0000	0.0000	0.9886	0.0000	1.4378
13.6800	0.8993	0.2139	62.2800	1.1967	0.0038	0.1298	0.3069	0.0000	0.0000	0.0613	0.0000	0.9733	0.0000	1.7474
16.8700	0.8644	0.3199	55.7700	1.6247	0.0000	0.1160	0.6140	0.0000	0.0000	0.0383	0.0000	1.0576	0.0000	1.6045
14.6600	0.0580	0.7975	72.7400	1.2620	0.0000	0.0646	2.0531	0.0092	0.0116	0.0000	0.4880	1.7226	0.0000	0.6687
14.0200	0.6220	1.0056	73.6300	1.0799	0.0150	0.0515	1.6144	0.0000	0.0294	0.0000	0.8498	1.9765	0.0000	0.1748
9.1100	0.0000	0.0000	79.9300	0.3812	0.0000	0.1454	0.2537	0.0000	0.2426	0.0000	0.6033	5.3900	0.0000	0.4675
16.2700	0.0595	0.0000	73.4700	1.1623	0.0000	0.1063	0.2991	0.0000	0.0816	0.2734	0.1283	1.6942	0.0000	0.0250
7.1500	0.0010	0.0057	76.6700	0.5465	0.0000	0.3002	1.6574	0.0000	0.1933	0.0030	0.4831	7.1900	0.0000	0.2070
17.2500	0.3538	0.1674	67.2600	0.1130	0.0000	0.4940	2.3476	0.0000	0.0000	0.0000	0.1791	4.3200	0.0491	0.6554

Compositions are reported in wt%, and the age in Ma.

Table 2. Continued.

K_2O	Sample #	Total	Age (Ranchin, 1968)	Age (Cameron-Schiman, 1978)	Age (Bowles 1990; 2015)	Average Age
0.3417	B00093	98.9700	76	72	71	73
0.2172	B00093	100.0200	0	0	0	0
0.1962	B00093	99.6400	3	2	3	3
0.1499	B00093	98.8300	18	17	17	17
0.1628	B00093	98.9300	16	16	15	16
0.1752	B00093	100.0000	1	1	1	1
1.1219	B00228	89.0400	0	0	0	0
0.3405	B00228	82.0500	0	0	0	0
0.3053	B00228	81.8100	0	0	0	0
0.2026	B00228	79.0900	0	0	0	0
0.3060	B00036	94.8400	53	49	50	51
0.1823	B00036	95.2400	91	82	85	86
0.2272	B00036	96.7400	60	56	56	58
0.2473	B00036	93.8200	14	13	13	13
0.3121	B00036	94.7200	50	48	47	48
0.4282	B00036	93.6200	21	20	20	20

Compositions are reported in wt%, and the age in Ma.

6.2 Chemical U-Pb Geochronology of Uranium Minerals

Chemical ages have been calculated from a variety of unconformity-related uranium deposits in the Athabasca Basin (e.g. Kotzer & Kyser 1993; Alexandre & Kyser 2005; Cloutier et al 2010; Dieng et al. 2013) with positive results since Bowles first published his work focusing on chemical age dating of uraninites in 1990. Chemical ages of uranium minerals at Arrow have been calculated from EMPA analyses on a selection of four polished thin sections (Table 1 and 2; Fig. 6.7 and 6.8). Chemical ages for Arrow uraninites are calculated based on the assumption that all Pb contained in the analyzed mineral is radiogenic and that U has not been re-introduced into the system (Section 3.3).

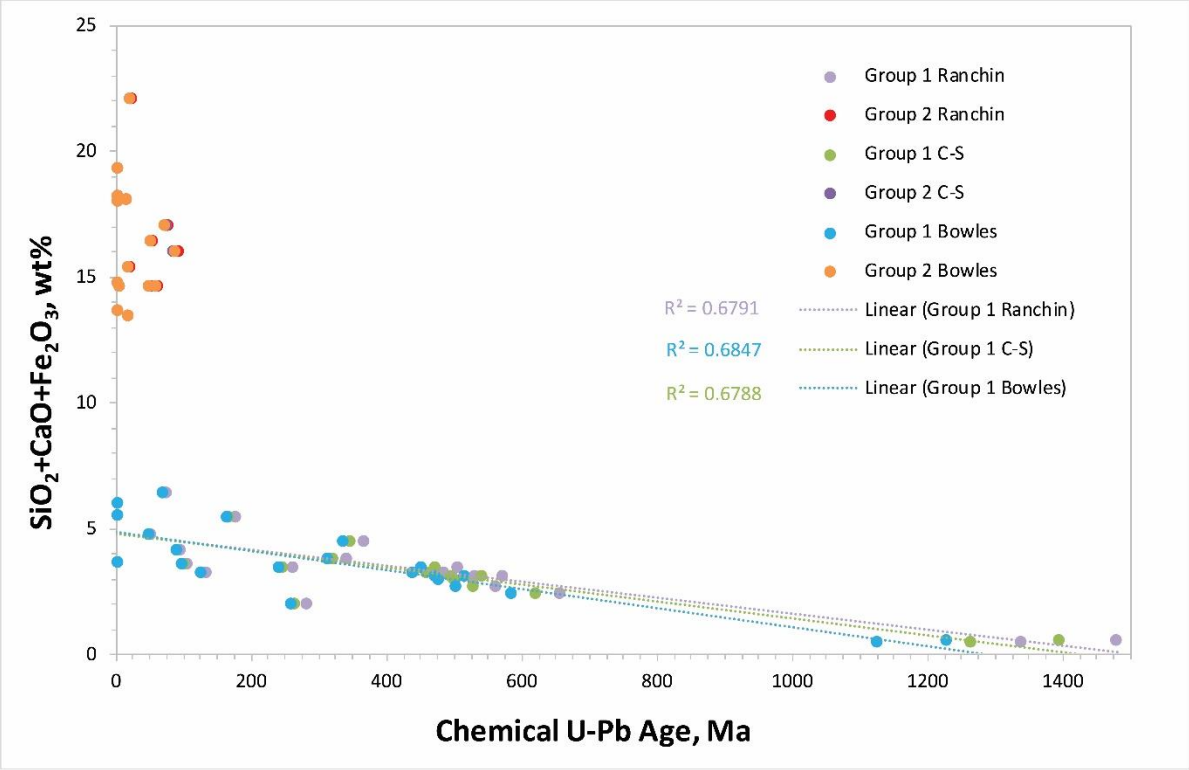

Fig. 6.7. Variation diagram of wt% SiO_2, CaO, and Fe_2O_3 contents of group 1 and 2 U-minerals from the Arrow Deposit as function of chemical U–Pb ages calculated through Ranchin (1968), Cameron-Schiman (1978), and Bowles (1990; 2015) methods. The group 1 Linear regression lines intercept the age axis at ca. 1,480 Ma, 1,425 Ma, and 1,290 Ma, respectively, indicating possible initial uraninite crystallization ages.

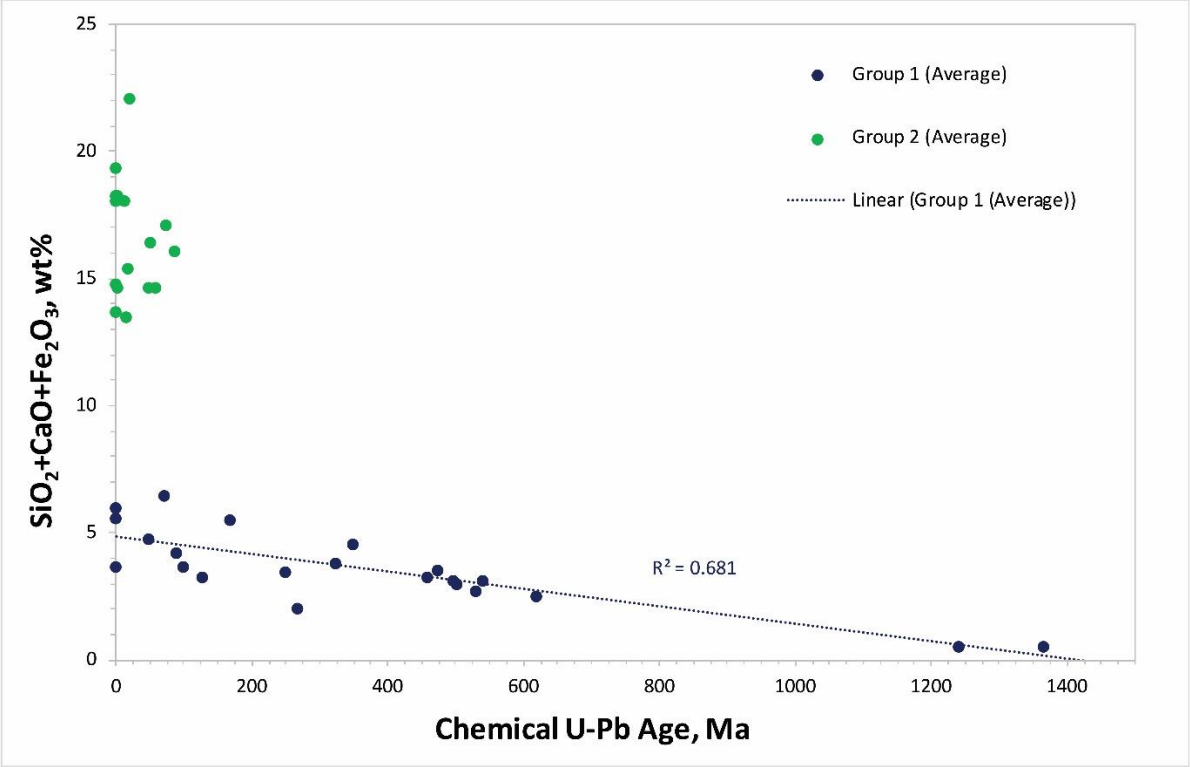

Fig. 6.8. Variation diagram of wt% SiO_2, CaO, and Fe_2O_3 contents of group 1 and 2 U-minerals from the Arrow Deposit as function of averaged chemical U–Pb age. The group 1 Linear regression lines intercept the age axis at ca. 1,425 Ma, indicating the average minimum initial crystallization age for the analyzed Arrow uraninites.

The EMPA analyses on Arrow uraninites completed during this study indicate that the uraninites have exchanged elements with later fluids, and that radiogenic Pb was locally replaced by Ca, Fe, and Si via discrete alteration processes by both oxidizing and reducing fluid fluxes (e.g. Janeczek and Ewing, 1992b). The nature of the cationic elemental substitutions in the uraninite depends on the composition and volume of the alteration fluids, principally their capacity for oxidation (i.e. U-silicates form in reducing environments whereas uranyl minerals tend to form in oxidizing environments). Evidence for interaction with both late oxidizing and reducing fluids is apparent at Arrow, as both U-silicate minerals and uranyl hydroxide and oxyhydroxide minerals have been observed replacing primary uraninite (e.g. Fig. 6.1 and 6.4). Fluid-rock interactions with wall rocks may also play a role in the alteration processes, as the composition of host-rock minerals can control the redox state of the fluids (Alexandre and Kyser, 2005; Fayek et al. 2002a). Regression of the concentrations of substituting elements through the chemical age axis in a variation diagram of chemical age vs. substituting element oxides (e.g. CaO, SiO_2) can give a clue as to the initial ages of uraninite crystallization (Alexandre and Kyser, 2005; Fig. 6.7 and 6.8). The

linear regression line of group 1 U-minerals from the Arrow Deposit has an age-axis intercept at ca. 1,290 Ma for the Bowles (1990; 2015) method, ca. 1,425 Ma for the Cameron-Schiman (1978) method, and ca. 1,480 Ma for the Ranchin (1968) method (Fig. 6.7). These three methods give an average age-axis intercept of ca. 1,425 Ma for Group 1 uraninites from Arrow (Fig. 6.8). This age therefore represents an average minimum initial crystallization age of the uraninite within the Arrow Deposit. In general, calculated chemical U–Pb ages are usually younger than those obtained by isotopic dating, as Pb escapes the uraninite over time (Fig. 6.9). The chemical U–Pb ages should thus be used with caution as the age is commonly underestimated, and in all cases, ages should be used in conjunction with the chemical composition of the U-minerals (e.g. Fig. 6.7).

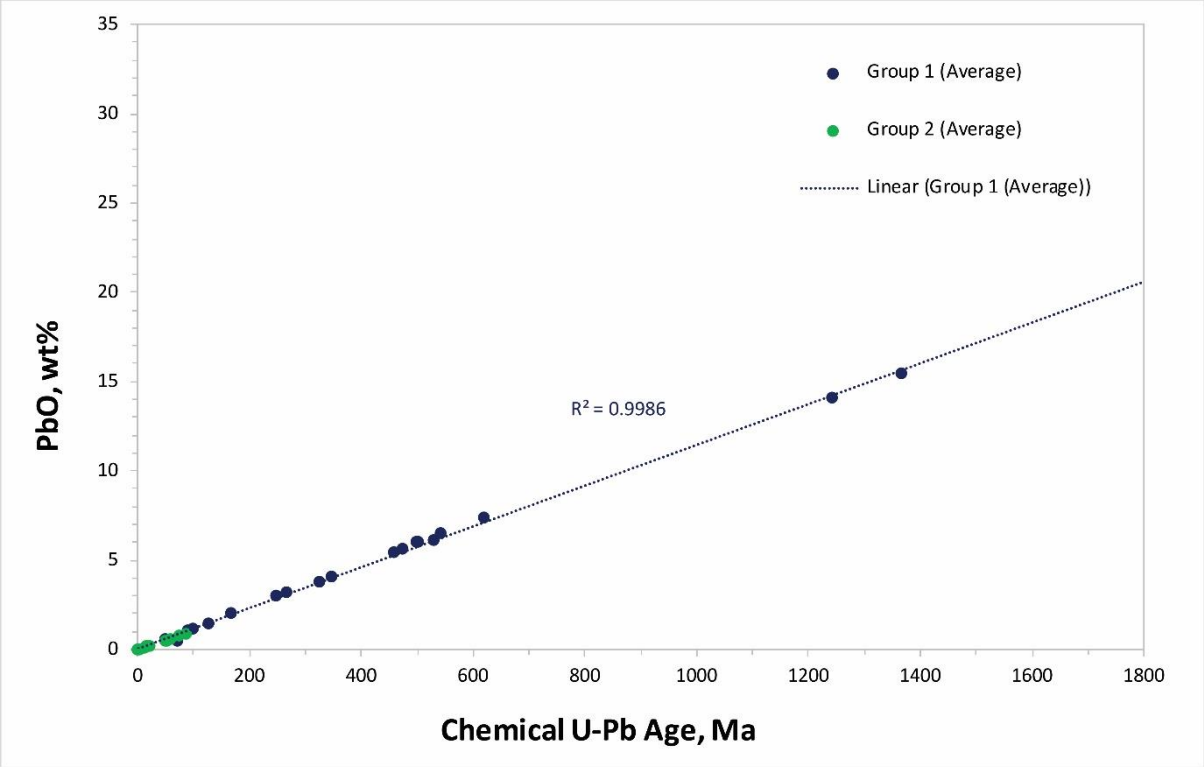

Fig. 6.9. Plot of wt% PbO as a function of average chemical age. Group 2 minerals are young and plot near the origin, whereas group 1 minerals comprise a spectrum along a linear trend as Pb is lost as uraninite crystals are altered, recrystallized, and/or remobilized over geological time.

6.3 Secondary Ionization Mass Spectrometry (SIMS) U-Pb Geochronology of Uraninite

In-situ U-Pb isotope analyses of Arrow uraninites were obtained via SIMS and plotted on Concordia diagrams (Fig. 6.10, 6.11, and 6.12). Isotopic U-Pb and Pb/Pb ratios on uraninite from the massive ore zones at the basement-hosted Arrow Deposit (Table 3 and 4) are discordant and

indicate a spectrum of different ages. The oldest upper intercept U-Pb age obtained is 1,309 ± 44 Ma (Fig. 6.10; MSWD=0.62; $^{207}Pb/^{206}Pb$ age of 1,330 Ma), interpreted as the minimum age for initial crystallization of the Arrow uraninite. Two younger age groups are defined by the discordia upper intercept ages of 1,225 ± 23 Ma (Fig. 6.11; MSWD=0.71) and 680 ± 19 Ma (Fig. 6.12; MSWD=2.4). The lower intercept ages of 47 ± 18 Ma, 96 ± 94 Ma, and 148 ± 38 Ma correspond to recrystallizations and alteration of the uraninite, given the tendency of the U-Pb isotopic system to be reset in uraninite through interaction with subsequent fluid-flow events (Fayek and Kyser, 2000; Fayek et al., 2002a; 2002b; Alexandre and Kyser, 2005). The age groups defined in the discordia in Figures 6.3.1 and 6.3.2 (~1,300 and ~1,200 Ma) nearly overlap within analytical uncertainty, and thus probably indicate a spectrum of alteration and remobilization of the primary uraninite mineralization at Arrow, rather than distinct mineralizing stages. The highest age is therefore interpreted as a minimum estimate of the initial crystallization age of the uranium mineralization at the Arrow Deposit, whereas the younger age groups are a result of alteration, recrystallization and/or remobilization of the uraninites and perturbation of the isotopic system with loss of radiogenic Pb during subsequent events.

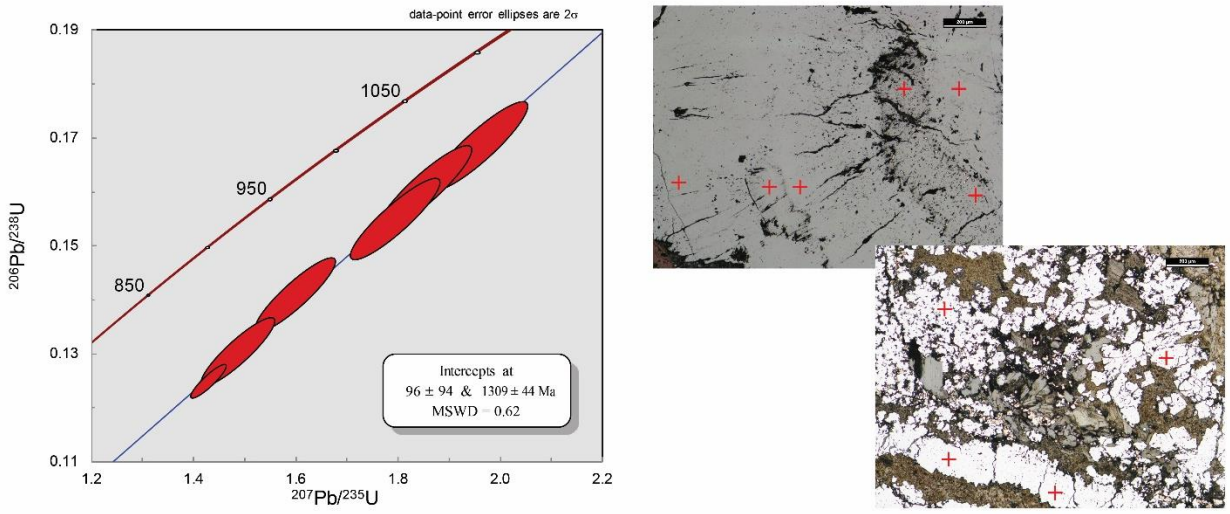

Fig. 6.10. U-Pb Concordia diagram constructed from SIMS data (Table 3) and reflected light photomicrographs of mineralization styles with SIMS analysis points (red crosses). The upper intercept represents the minimum age of uraninite crystallization. Texturally oldest uraninites (~1300 Ma) are botryoidal, cubic, vein, and semi-massive occurrences commonly replacing clay minerals and micas (kaolinite, illite, muscovite, sericite).

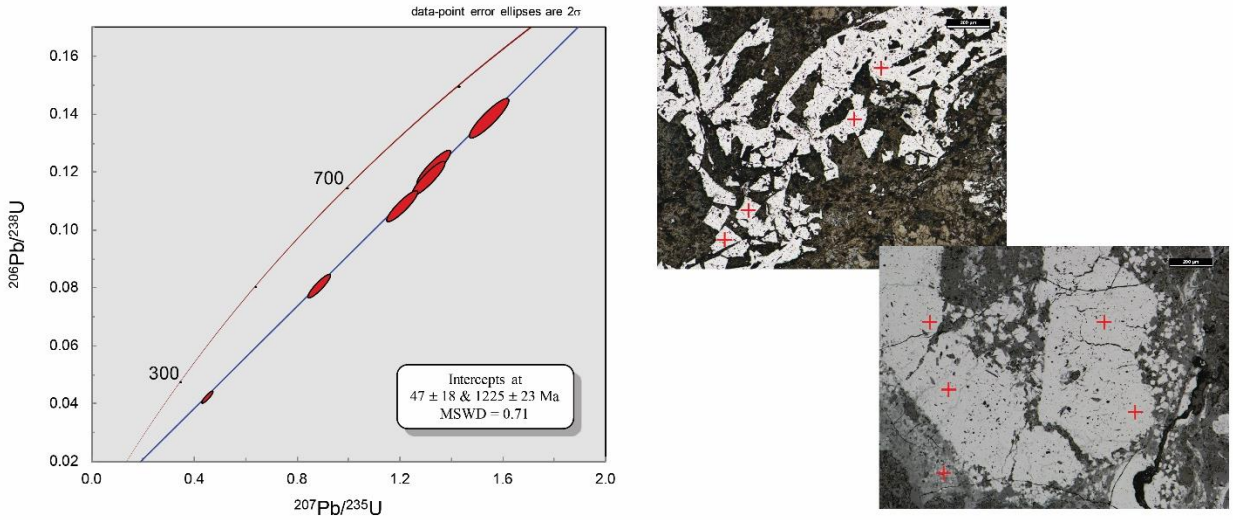

Fig. 6.11. U-Pb Concordia diagram constructed from SIMS data (Table 3) and reflected light photomicrographs of mineralization styles with SIMS analysis points (red crosses). The upper intercept represents the minimum age of uraninite crystallization. Texturally younger and/or remobilized/altered (~1200 Ma) uraninites occur as cubic crystals, semi-massive and massive lenses, and form the matrix of breccias.

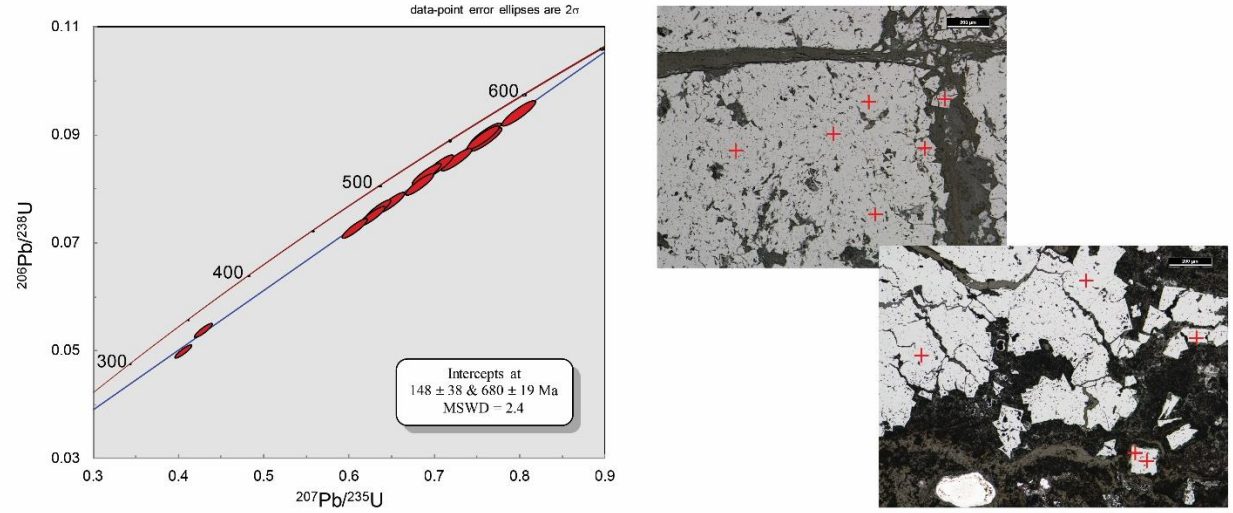

Fig. 6.12. U-Pb Concordia diagram constructed from SIMS data (Table 3) and reflected light photomicrographs of mineralization styles with SIMS analysis points (red crosses). The upper intercept represents the minimum age of uraninite crystallization. The most altered/remobilized uraninites (~700 Ma) are present as euhedral cubic crystals and semi-massive occurrences.

Table 3. Analytical data of the U-Pb SIMS analyses of uraninite from the basement-hosted Arrow uranium deposit.

Sample-Analytical point	Zone	207Pb/235U	Error	206Pb/238U	Error	207Pb/206Pb	Error	Sample analytical point
B00032-1-1	A2 - south	1.943861	2.0	0.166683	2.0	0.084690	2.0	86
B00032-1-2	A2 - south	1.789322	2.0	0.155149	2.0	0.084872	2.0	87
B00032-1-3	A2 - south	1.488956	2.0	0.128930	2.0	0.085006	2.0	88
B00032-2-4	A2 - south	1.517857	2.0	0.131534	2.0	0.085311	2.0	89
B00032-2-5	A2 - south	1.322351	2.0	0.114463	2.0	0.085346	2.0	90
B00032-2-6	A2 - south	1.857463	2.0	0.161705	2.0	0.084375	2.0	91
B00032-2-7	A2 - south	1.971785	2.0	0.170668	2.0	0.084540	2.0	92
B00036-1-1	A2 - south	1.339567	2.0	0.121440	2.0	0.081685	2.0	12
B00036-1-2	A2 - south	1.347541	2.0	0.121897	2.0	0.082207	2.0	13
B00036-1-3	A2 - south	1.329042	2.0	0.122489	2.0	0.080819	2.0	14
B00036-1-4	A2 - south	1.312965	2.0	0.120279	2.0	0.080925	2.0	15
B00036-1-5	A2 - south	0.526880	2.0	0.051919	2.0	0.077236	2.0	16
B00036-2-6	A2 - south	1.207266	2.0	0.108670	2.0	0.083540	2.0	17
B00036-2-7	A2 - south	1.302769	2.0	0.116066	2.0	0.083329	2.0	18
B00036-2-8	A2 - south	0.978878	2.0	0.089118	2.0	0.083153	2.0	19
B00036-2-9	A2 - south	0.785185	2.0	0.072601	2.0	0.081244	2.0	20
B00036-3-10	A2 - south	0.392497	2.0	0.054489	2.0	0.053762	2.0	21
B00036-3-11	A2 - south	0.285646	2.0	0.039320	2.0	0.053926	2.0	22
B00036-3-12	A2 - south	0.368931	2.0	0.050523	2.0	0.053927	2.0	23
B00093-1-1	A2 - wrench	0.468548	2.0	0.049531	2.0	0.070831	2.0	38
B00093-1-2	A2 - wrench	0.784275	2.0	0.089916	2.0	0.064880	2.0	39
B00093-1-3	A2 - wrench	0.792741	2.0	0.091011	2.0	0.064529	2.0	40
B00093-1-4	A2 - wrench	0.590308	2.0	0.069161	2.0	0.063641	2.0	41
B00093-2-5	A2 - wrench	0.251958	2.0	0.024421	2.0	0.077899	2.0	42
B00093-2-6	A2 - wrench	0.374824	2.0	0.035524	2.0	0.079805	2.0	43
B00093-2-7	A2 - wrench	0.389298	2.0	0.036806	2.0	0.080429	2.0	44
B00093-2-8	A2 - wrench	0.232029	2.0	0.023606	2.0	0.073436	2.0	45
B00094-1-1	A2 - wrench	1.035796	2.0	0.105411	2.0	0.072887	2.0	46
B00094-1-2	A2 - wrench	0.688487	2.0	0.072908	2.0	0.071310	2.0	47

B00094-1-3	A2 - wrench	1.205654	2.0	0.108523	2.0	0.083112	2.0	48
B00094-1-4	A2 - wrench	1.309215	2.0	0.118513	2.0	0.081894	2.0	49
B00094-2-5	A2 - wrench	0.378121	2.0	0.035002	2.0	0.081751	2.0	50
B00094-2-6	A2 - wrench	0.436050	2.0	0.041665	2.0	0.085172	2.0	51
B00094-2-7	A2 - wrench	1.613273	2.0	0.141548	2.0	0.084407	2.0	52
B00094-2-8	A2 - wrench	1.086905	2.0	0.095462	2.0	0.085116	2.0	53
B00135-1-1	A2 - north	1.660080	2.0	0.146818	2.0	0.083240	2.0	54
B00135-1-2	A2 - north	1.610687	2.0	0.142140	2.0	0.083502	2.0	55
B00135-1-3	A2 - north	1.523458	2.0	0.135724	2.0	0.083097	2.0	56
B00135-1-4	A2 - north	1.335336	2.0	0.118115	2.0	0.084696	2.0	57
B00135-2-5	A2 - north	1.363605	2.0	0.126879	2.0	0.079951	2.0	58
B00135-2-6	A2 - north	1.321972	2.0	0.122681	2.0	0.079783	2.0	59
B00135-2-7	A2 - north	0.726972	2.0	0.079564	2.0	0.068440	2.0	60
B00135-2-8	A2 - north	1.517096	2.0	0.136913	2.0	0.081558	2.0	61
B00135-2-9	A2 - north	0.449630	2.0	0.041670	2.0	0.081753	2.0	62
B00138-1-1	A2 - north	1.492531	2.0	0.137459	2.0	0.080195	2.0	63
B00138-1-2	A2 - north	1.356067	2.0	0.120808	2.0	0.082688	2.0	64
B00138-1-3	A2 - north	0.769013	2.0	0.072701	2.0	0.079080	2.0	65
B00138-1-4	A2 - north	1.232481	2.0	0.124161	2.0	0.073263	2.0	66
B00138-1-5	A2 - north	0.890361	2.0	0.093565	2.0	0.070475	2.0	67
B00138-2-10	A2 - north	1.854009	2.0	0.160121	2.0	0.084452	2.0	71
B00138-2-7	A2 - north	1.481065	2.0	0.130727	2.0	0.083826	2.0	68
B00138-2-8	A2 - north	1.771033	2.0	0.153287	2.0	0.084903	2.0	69
B00138-2-9	A2 - north	1.774237	2.0	0.155180	2.0	0.084374	2.0	70
B00160-1-1	A2 - north	1.136319	2.0	0.108660	2.0	0.077261	2.0	72
B00160-1-2	A2 - north	1.121800	2.0	0.108240	2.0	0.076488	2.0	73
B00160-1-3	A2 - north	1.004801	2.0	0.106341	2.0	0.070399	2.0	74
B00160-2-4	A2 - north	1.289477	2.0	0.119319	2.0	0.079860	2.0	75
B00160-2-5	A2 - north	1.427359	2.0	0.133005	2.0	0.079391	2.0	76
B00160-2-6	A2 - north	1.463548	2.0	0.135645	2.0	0.079841	2.0	77
B00203-1-1	A3 - south	1.475286	2.0	0.131033	2.0	0.083755	2.0	78
B00203-1-2	A3 - south	1.843831	2.0	0.160819	2.0	0.083840	2.0	79

B00203-1-3	A3 - south	1.462172	2.0	0.130160	2.0	0.083437	2.0	80
B00203-1-4	A3 - south	1.836175	2.0	0.156739	2.0	0.085557	2.0	81
B00203-2-5	A3 - south	1.427026	2.0	0.125005	2.0	0.084692	2.0	82
B00203-2-6	A3 - south	1.672603	2.0	0.143835	2.0	0.085420	2.0	83
B00203-2-7	A3 - south	1.579988	2.0	0.138438	2.0	0.084266	2.0	84
B00203-2-8	A3 - south	1.646818	2.0	0.144617	2.0	0.083412	2.0	85
B00225-2-1	A2- wrench	0.629714	2.0	0.075257	2.0	0.062554	2.0	27
B00225-2-2	A2- wrench	0.719395	2.0	0.085545	2.0	0.062715	2.0	28
B00225-2-3	A2- wrench	0.748234	2.0	0.088025	2.0	0.063151	2.0	29
B00225-2-4	A2- wrench	0.530982	2.0	0.064243	2.0	0.061889	2.0	30
B00225-2-5	A2- wrench	0.653589	2.0	0.079536	2.0	0.061218	2.0	31
B00225-2-6	A2- wrench	0.553498	2.0	0.069072	2.0	0.059758	2.0	32
B00225-3-10	A2- wrench	0.665680	2.0	0.079219	2.0	0.062914	2.0	36
B00225-3-11	A2- wrench	0.749216	2.0	0.086763	2.0	0.064203	2.0	37
B00225-3-7	A2- wrench	0.743569	2.0	0.087234	2.0	0.063734	2.0	33
B00225-3-8	A2- wrench	0.669985	2.0	0.080163	2.0	0.062425	2.0	34
B00225-3-9	A2- wrench	0.651218	2.0	0.078564	2.0	0.061804	2.0	35

All isotope ratios are corrected.

Table 4. Analytical data of the Pb/Pb SIMS analyses of uraninite from the basement-hosted Arrow uranium deposit, and calculated Pb/Pb isotopic ages.

Sample-Analytical point	$^{207}Pb/^{206}Pb$	Age (Ma)	Sample-Analytical point	$^{207}Pb/^{206}Pb$	Age (Ma)
B00032-1-1	0.0847	1308	B00094-2-6	0.0852	1320
B00032-1-2	0.0849	1314	B00094-2-7	0.0844	1302
B00032-1-3	0.0850	1315	B00094-2-8	0.0851	1318
B00032-2-4	0.0853	1322	B00135-1-1	0.0832	1275
B00032-2-5	0.0853	1322	B00135-1-2	0.0835	1280
B00032-2-6	0.0844	1302	B00135-1-3	0.0831	1272
B00032-2-7	0.0845	1305	B00135-1-4	0.0847	1308
B00036-1-1	0.0817	1235	B00135-2-5	0.0800	1198
B00036-1-2	0.0822	1250	B00135-2-6	0.0798	1192
B00036-1-3	0.0808	1216	B00135-2-7	0.0684	880
B00036-1-4	0.0809	1220	B00135-2-8	0.0816	1235
B00036-1-5	0.0772	1126	B00135-2-9	0.0818	1240
B00036-2-6	0.0835	1280	B00138-1-1	0.0802	1202
B00036-2-7	0.0833	1276	B00138-1-2	0.0827	1262
B00036-2-8	0.0832	1275	B00138-1-3	0.0791	1175
B00036-2-9	0.0812	1226	B00138-1-4	0.0733	1022
B00036-3-10	0.0538	358	B00138-1-5	0.0705	942
B00036-3-11	0.0539	365	B00138-2-10	0.0845	1305
B00036-3-12	0.0539	365	B00138-2-7	0.0838	1288
B00066-1-1	0.0633	720	B00138-2-8	0.0849	1314
B00066-1-12	0.0618	668	B00138-2-9	0.0844	1302
B00066-1-13	0.0623	685	B00160-1-1	0.0773	1130
B00066-1-14	0.0622	680	B00160-1-2	0.0765	1108
B00066-1-2	0.0628	698	B00160-1-3	0.0704	940
B00066-1-3	0.0626	695	B00160-2-4	0.0799	1195
B00066-1-4	0.0633	715	B00160-2-5	0.0794	1182
B00066-2-5	0.0623	685	B00160-2-6	0.0798	1192
B00066-2-6	0.0635	725	B00203-1-1	0.0838	1288
B00066-2-7	0.0635	725	B00203-1-2	0.0838	1288
B00066-3-10	0.0623	685	B00203-1-3	0.0834	1278

B00066-3-11	0.0601	608	B00203-1-4	0.0856	1330
B00066-3-8	0.0594	578	B00203-2-5	0.0847	1308
B00066-3-9	0.0630	708	B00203-2-6	0.0854	1325
B00093-1-1	0.0708	952	B00203-2-7	0.0843	1300
B00093-1-2	0.0649	770	B00203-2-8	0.0834	1278
B00093-1-3	0.0645	758	B00225-2-1	0.0626	695
B00093-1-4	0.0636	730	B00225-2-2	0.0627	698
B00093-2-5	0.0779	1145	B00225-2-3	0.0632	715
B00093-2-6	0.0798	1192	B00225-2-4	0.0619	670
B00093-2-7	0.0804	1208	B00225-2-5	0.0612	645
B00093-2-8	0.0734	1025	B00225-2-6	0.0598	595
B00094-1-1	0.0729	1010	B00225-3-10	0.0629	705
B00094-1-2	0.0713	965	B00225-3-11	0.0642	748
B00094-1-3	0.0831	1272	B00225-3-7	0.0637	733
B00094-1-4	0.0819	1242	B00225-3-8	0.0624	688
B00094-2-5	0.0818	1240	B00225-3-9	0.0618	668

All isotope ratios are corrected.

Significant perturbation and remobilization of the primary uraninite mineralization at the Arrow Deposit evidenced by the spread of isotopic ages is also corroborated by deposit-scale spatial distribution and structural context. Plotting calculated Pb/Pb ages obtained within the A2 shear high-grade domain of massive mineralization in three dimensions reveals a distinct uraninite remobilization pattern within the wrench zone in the A2 core (Fig. 6.13). Figure 6.13 shows a longitudinal view of the A2 high-grade domain looking northwest, with isotopic Pb/Pb ages calculated from nine polished thin sections.

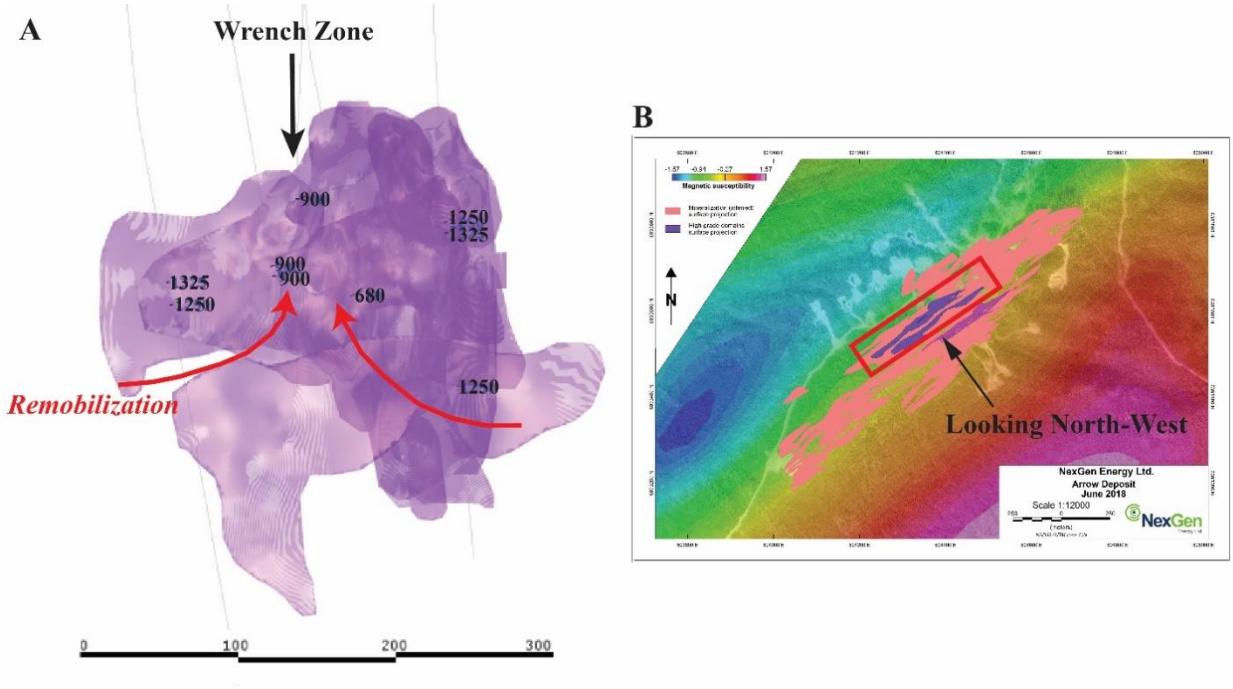

Fig. 6.13. A) Pb-Pb Ages plotted in 3D, revealing a distinct uraninite remobilization pattern within the wrench-zone of the A2 high-grade core. B) Plan map of the Arrow Deposit mineral resource outline (Mathisen and Ross, 2017), showing the location and orientation of the long-section shown in Fig. 6.13A.

The oldest ages (1,325 to 1,250 Ma) are all situated along the margins of the high-grade core, with the youngest ages (900 to 680 Ma) concentrated within dilational zones proximal to the wrench zone of the A2 shear. This suggests that as wrench-dominated transpressional deformation advanced along the corridor, subsequent fluid fluxes were focussed into this zone, remobilizing and recrystallizing pre-existing uraninite. The high-grade cores within the A1 and A3 shears likely experienced a similar evolution, with extensive zones of dilation forming with protracted deformation, thus allowing for the re-concentration of the surrounding pre-existing, lower-grade ore into extremely high-grade “fault-fill” veins. Further geochronological work and subsequent

plotting in three dimensions could therefore help to model fluid flow pathways on a deposit and corridor scale, which could serve as a proxy for delineation of undiscovered high-grade domains. Figure 6.13 illustrates the palpable structural control on uranium mineralization at the Arrow Deposit; specifically, where the highest grades of ore are likely to be discovered.

6.4 Ion Microprobe Oxygen Isotopic Analyses of Uraninite

Oxygen isotope measurements on uraninite were obtained via SIMS. The $\delta^{18}O$ values for all generations of uraninite from the Arrow Deposit are relatively consistent and range from -34.5 to -15.2‰ (Table 5). The resultant values are consistent with the oxygen isotope compositions of uraninites obtained from U deposits across the Athabasca Basin (e.g., Kotzer and Kyser, 1993; Fayek et al., 2002a; 2010; Sheahan et al., 2016). Figure 6.14 illustrates the similarity of $\delta^{18}O$ values for uraninites obtained from Arrow (this study), Cigar Lake (Fayek et al., 2002a), and Kianna (Shea Creek; Sheahan et al., 2016) uranium deposits and corresponding isotopic $^{207}Pb/^{206}Pb$ ages. Upper intercept $^{206}Pb/^{238}U$ ages were used in the case of Shea Creek as no Pb/Pb ages were available for the published $\delta^{18}O$ values. The approximate temperature of uraninite deposition in uranium deposits across the Athabasca Basin has been suggested to be in the range of 150 to 200°C (e.g. Kotzer and Kyser, 1993, 1995; Fayek and Kyser, 2000; Fayek et al., 2002a). Furthermore, isotopic and microthermometric studies on clay and silicate minerals in textural equilibrium with uraninite in unconformity-related U deposits in the Basin (e.g. Kotzer and Kyser, 1995) have indicated that the dominant fluids responsible for the formation of the uraninite were saline with $\delta^{18}O$ values of approximately 4 ± 4‰ (Fayek et al., 2002a). Taking this into account and utilizing theoretical and experimental uraninite-water fractionation factors, uraninite that precipitated from such a brine should have a $\delta^{18}O$ value of approximately –10‰ (Fayek and Kyser, 2000; Fayek et al., 2002a). The low $\delta^{18}O$ values obtained from the Arrow uraninite, however, indicate that the mineralization should have been in equilibrium with fluids with $\delta^{18}O$ values of at least -20‰ at 200°C. Therefore, the low $\delta^{18}O$ values of uraninite from the Arrow Deposit, and Athabasca Basin U deposits in general, are likely the result of late meteoric water interaction with uraninite previously deposited under reduced conditions (Fayek et al., 2002a), as meteoric waters are substantially ^{18}O-depleted (i.e. $\delta^{18}O$ = -20 to -16‰) relative to those of the ore-forming fluids (i.e. $\delta^{18}O$ = ~4‰). Although the $\delta^{18}O$ values of the Arrow uraninite have been altered significantly by subsequent fluid movement, their overall chemical composition and textural characteristics appear

to be largely unaffected by the recrystallization process in this case. This suggests that the late fluids interacting with the uraninite were relatively reducing due to uranium solubility being generally a function of fO_2, and uraninite is only stable under very reducing conditions (Fayek et al., 2002a).

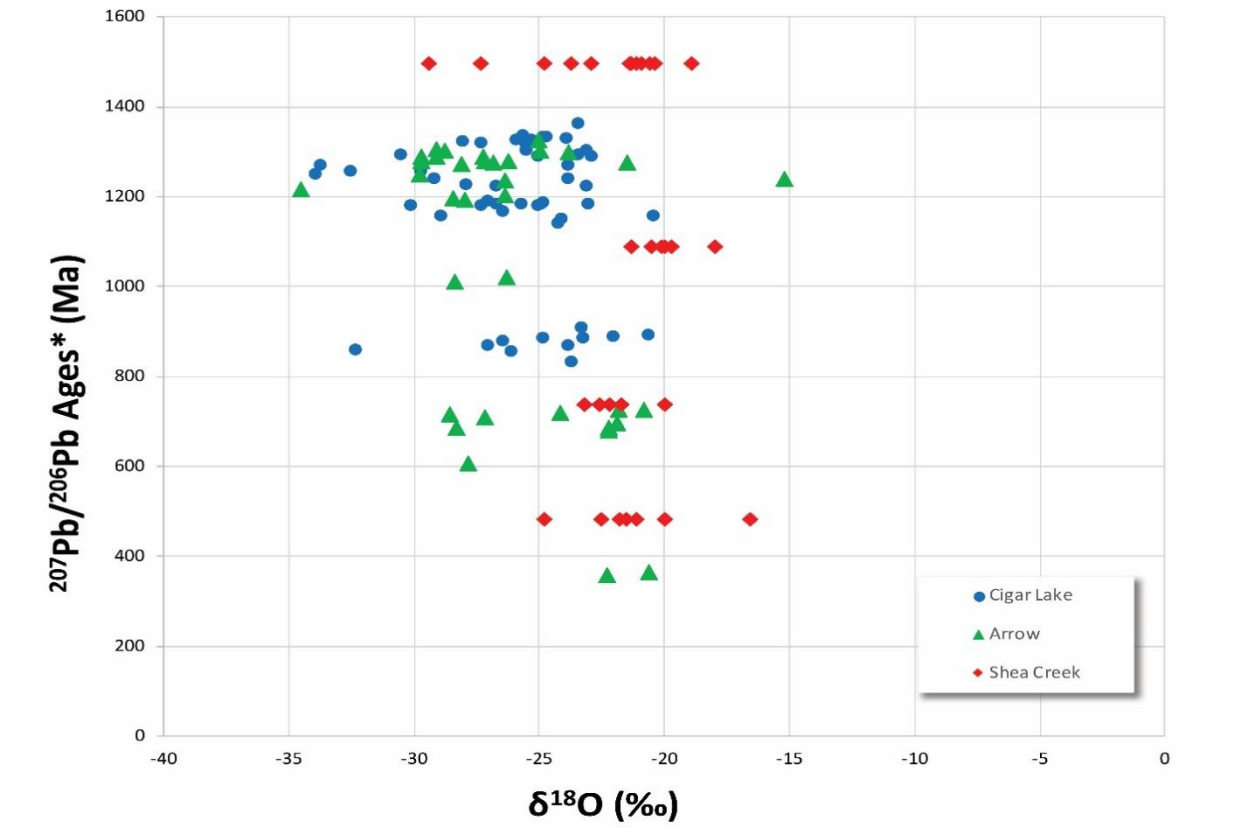

Fig. 6.14. Graphical comparison of $\delta^{18}O$ values for uraninites obtained from Arrow (this study), Cigar Lake (Fayek et al., 2002a), and Kianna (Shea Creek; Sheahan et al., 2016) uranium deposits and corresponding isotopic $^{207}Pb/^{206}Pb$ ages. *Upper intercept $^{206}Pb/^{238}U$ ages were used for Shea Creek $\delta^{18}O$ analyses based on U generation.

Table 5. Analytical data on the SIMS $\delta^{18}O_{V\text{-}SMOW}$ (‰) analyses on uraninites from the Arrow basement-hosted uranium deposit.

Sample	Mineral	$\delta^{18}O_{V\text{-}SMOW}$ (‰)	1σ
B00066-1-1	Uraninite	-24.2	1.2
B00066-1-2	Uraninite	-28.5	1.2
B00066-1-3	Uraninite	-22.2	1.2
B00066-1-4	Uraninite	-21.9	1.2
B00066-2-1	Uraninite	-28.3	1.2
B00066-2-2	Uraninite	-21.8	1.2
B00066-2-3	Uraninite	-20.8	1.2
B00066-3-1	Uraninite	-27.2	1.2
B00066-3-2	Uraninite	-22.2	1.2
B00066-3-3	Uraninite	-27.8	1.2
B00036-1-1	Uraninite	-26.4	1.2
B00036-1-2	Uraninite	-29.7	1.2
B00036-1-3	Uraninite	-34.5	1.2
B00036-2-1	Uraninite	-26.2	1.2
B00036-2-2	Uraninite	-26.8	1.2
B00036-3-1	Uraninite	-22.3	1.2
B00036-3-2	Uraninite	-20.6	1.2
B00094-1-1	Uraninite	-28.1	1.2
B00094-1-2	Uraninite	-28.4	1.2
B00094-2-1	Uraninite	-15.2	1.2
B00094-2-2	Uraninite	-25.0	1.2
B00135-1-1	Uraninite	-21.5	1.2
B00135-1-2	Uraninite	-29.7	1.2
B00135-2-1	Uraninite	-28.0	1.2
B00135-2-2	Uraninite	-28.4	1.2
B00138-1-1	Uraninite	-26.3	1.2
B00138-1-2	Uraninite	-26.3	1.2
B00138-2-1	Uraninite	-29.1	1.2
B00138-2-2	Uraninite	-28.8	1.2
B00138-2-3	Uraninite	-29.1	1.2
B00203-1-1	Uraninite	-27.2	1.2
B00203-1-2	Uraninite	-29.7	1.2
B00203-2-1	Uraninite	-23.8	1.2
B00203-2-2	Uraninite	-27.2	1.2
B00203-2-3	Uraninite	-25.0	1.2

CHAPTER 7

DISCUSSION AND CONCLUSIONS

The overall objective of this research is to integrate structural, mineralogical, geochemical, and paragenetic characteristics of the high-grade Arrow uranium deposit in order to provide better understanding of basement-hosted uranium deposits in the SW Athabasca Basin, which in turn may provide a template to aid exploration in this region. Furthermore, the characterization of the uranium-bearing phases present within the Arrow Deposit through EMPA and SIMS analyses adds geochronological and isotopic context for the mineralization episodes and perturbation events which affected the deposit over time. This thesis is the first comprehensive study of a uranium deposit along the Patterson Lake corridor in the SW Athabasca Basin and provides regional implications for uranium exploration along this corridor. This manuscript addresses the genetic and evolutionary model for the Arrow uranium deposit, providing and integrating structural and paragenetic observations. Overall, structure is the critical component to the formation of the Arrow uranium deposit.

The Patterson Lake corridor displays evidence of episodic structural reactivation and exhumation at progressively shallower crustal levels, related to the protracted tectonic evolution of the North American shield, and accompanied by various episodes of hydrothermal fluid-flow and alteration, and uranium mineralization, recrystallization, and remobilization. The present research suggests the processes active within the portion of the PLc hosting Arrow, such as softening of shear zones and silicification of host rocks through metasomatism and/or hydrothermal alteration, are a critical factor in forming world-class, high-grade uranium deposits such as Arrow. Structural analysis along the ore-hosting portion of the Patterson Lake corridor at Arrow indicate a sequential development of early ductile and brittle-ductile, to late brittle episodes of movement along the SE limb of a NE-SW trending fold. Structural and metamorphic relationships suggest that mylonitization was initiated in the ductile environment, followed by overprinting by brittle-ductile and brittle faulting involving widespread cataclasis and brecciation, reflecting the progressive unroofing of the high strain zones to shallower lithospheric levels. Through this study, the structural system at Arrow has been interpreted to have originally developed along near vertical dipping, partitioned, NE-SW-trending brittle-ductile high strain zones (A1 to A5 shears) formed under a dominantly transpressional regime along the strained limb

of a km-scale F_3 generation fold of the Lloyd fold domain. The Lloyd fold domain architecture has been mapped throughout the Taltson Domain (e.g. Card et al., 2008), and structural analysis completed at Arrow suggests that dome-and-basin-style folding is present along the Patterson Lake corridor, creating the early ductile framework with limb domains being ideal nucleation sites for the formation of high strain zones. Strain partitioning was likely facilitated by the reactivation of these pre-existing structural weaknesses, which where in orientations suitable to facilitate transpressional strike-slip movement through the development of a stacked shear system. The stacked high strain zones at Arrow are nearly parallel and are grouped into a fault zone approximately 200 m wide, with ore shoots defining an overall plunge to the S-SW. As these structures evolved through the brittle-ductile transition and became sites for focussed fluid flow, they were overprinted with abundant graphite, followed by, and contemporaneous with, Fe-sulphide mineralization and quartz veins. The A1 through A5 high strain zones at Arrow are broadly similar in orientation and geometry to type IV fault structures in the southern Shea Creek area, as described by Lorilleux et al. (2002).

The heterogeneous high strain zones hosting the Arrow Deposit further evolved through episodic reactivation events creating various small-scale brittle fault linkages oblique to and connecting the main fault zone. Influenced by early regional framework, brittle reactivation and linkage between these deep-seated, pre-existing ductile to brittle-ductile high strain zones through repeated deformation was extremely important in the formation of the Arrow Deposit. Geological mapping completed by Card et al. (2008) revealed a prominent set of dextral shear zones striking ENE within the Lloyd fold domain, which, based on their strike and displacement sense, are interpreted to have formed as distinct Riedel shear zones related to one of the dextral reactivation episodes on the larger-scale VRSZ. A similar brittle to brittle-ductile deformational evolution is postulated for the A1 to A5 shears within the Arrow zone, as the geometry of the brittle structures overprinting the ductile structures exhibit a prominent Riedel-style orientation. It is therefore likely that many deep-seated high strain corridors, such as the PLc, were reactivated in this manner during orogenic events affecting the southern part of the Rae province (i.e. Taltson-Thelon orogenesis). Interpretation of the major structural trends suggests a predominantly oblique-reverse, wrench-dominated transpressional, sinistral strike-slip fault system of complex Riedel-style geometry, where primary and subsidiary R-, R'-, P-, P'-, and T-shear fractures experienced multiple episodes of brittle structural reactivation, and fluid migration, during which the primary

uranium mineralization was emplaced and subsequently remobilized and/or recrystallized. The dilatant areas and extensional fault bends created through wrench-dominated movement and Riedel brittle reactivation are favorable structural sites for fluid flow, and a remobilization pattern within the wrench zone of the A2 high grade core has been identified through integration of structural analysis and uraninite geochronology (see Fig. 6.13).

Multiple phases of uranium mineralization have been identified and classified based on mineral chemistry and textural relationships and related to absolute ages and stable isotope data. Two groups of uraniferous phases have been identified; the first comprising early euhedral, brecciated, and remobilized uraninite, and the second composed of late uranium silicates and hydroxides/oxyhydroxides such as coffinite and uranophane. Electron-microprobe analyses indicate that uraninite at Arrow has exchanged elements with the later fluid events, resulting in the replacement of radiogenic Pb by Ca, Si, and Fe via discrete alteration. The character of these substitutions brought on by alteration fluids depends on the amount and composition of the fluids, and whether they are reducing or oxidizing in nature.

Calculated chemical U–Pb ages are in general younger than those obtained by isotopic dating as Pb leaves the uraninite, however a minimum initial crystallization age of ca. 1,425 Ma is indicated by regression of the concentrations of substituting elements through the age-axis. It is unclear to what perturbation event this age corresponds to, and although it is older than the obtained isotopic ages in this study, it is relatively young when compared to other unconformity-related U deposits in the Basin such as McArthur River or Rabbit Lake, with ages of initial uranium mineralization in the range of ca. 1,550 to 1,600 Ma (e.g. Alexandre and Kyser, 2003). The application of in situ ion microprobe analyses via SIMS has provided precise isotopic measurements on individual uraninite grains to further understand the genesis of the Arrow uranium deposit, as well as characterize mineralizing and alteration fluids. Concordia plots constructed using U-Pb data obtained by SIMS analyses on uraninite from the Arrow Deposit are discordant with upper intercepts of 1,309 ± 44, 1,225 ± 23, and 680 ± 19 Ma. The two oldest age groups defined by the Concordia diagrams in Figures 6.10 and 6.11 broadly overlap within analytical uncertainty, and as there are no major textural differences between these phases (i.e. Fig. 6.10 and 6.11 BSE images), it is likely that these ages represent a spectrum of alteration and/or remobilization of the primary uranium mineralization at Arrow, rather than distinct mineralization

stages. The oldest age is therefore interpreted as a minimum estimate of the initial crystallization age of the uranium mineralization at the Arrow Deposit, whereas the younger age groups are a result of alteration, recrystallization and/or remobilization of the uraninites and perturbation of the isotopic system with loss of radiogenic Pb during subsequent events.

The ages calculated for the Arrow Deposit overlap with ages obtained in other Athabasca Basin U deposits, such as Shea Creek and McArthur River, however the oldest Arrow ages obtained thus far are still younger than the oldest ages at McArthur which indicate initial crystallization of ca. 1,540 Ma. The U-Pb and Pb/Pb ages obtained in this study may correspond to significant far-field tectonic events that are interpreted to have reactivated the deep-seated basement structures associated with the Arrow Deposit and initiated subsequent fluid fluxes along structural conduits. Events that may have influenced these perturbations include the Mackenzie dike swarm event ca. 1,275 Ma (LeCheminant and Heaman, 1989) and the accretion and breakup of Rodinia as indicated by ages obtained from Arrow uraninites in the range of 1,000 to 850 Ma (Mayers et al., 1996; Condie, 2001). These isotopic system resetting events provoked the recrystallization and/or remobilization of the primary uraninite at Arrow, and thus mask the true primary crystallization age. Consequently, the minimum initial crystallization age of ca. 1,300 Ma obtained from the Arrow uraninite is interpreted as a resetting age.

Chemical and isotopic ages determined through this study correspond closely to textural and paragenetic relationships of mineralization phases, which are in turn related to the structural evolution of the deposit. The broad age groups defined through the geochronological study of uranium mineralization at the Arrow Deposit has been integrated with the Arrow paragenesis chart in Figure 7.1. Note that the ages and position of the lines in Figure 7.1 aren't meant to be read as precise ages (i.e. the sulphide and gold mineralization at Arrow isn't necessarily 700 Ma or younger), but rather as guidelines or minimum ages. Age determinations on alteration minerals or sulphides would corroborate their timing relative to mineralization, and thus would yield a more accurate picture of the age relationships between structure, alteration, and mineralization. Ongoing work to examine the Ar-Ar systematics of the white micas at Arrow is currently being undertaken (Appendix D: Cross et al., 2018).

In situ oxygen isotopic analyses of uraninite from the Arrow Deposit that appear to be largely free of alteration have among the lowest $\delta^{18}O$ values reported for an Athabasca Basin U deposit, ranging from -34.5 to -15.2‰. These highly negative values suggest that the uraninite at Arrow interacted with fluids with $\delta^{18}O$ values in the range of approximately -16 to -20‰, (i.e. composition akin to that of recent meteoric waters) resulting in only minor disturbances to their general chemical composition and mineral textures.

Integration of mineral paragenesis, geochronology, geochemical data, and subsequent structural interpretations in three dimensions (i.e. Fig. 6.13) provides corroborating evidence for the Arrow Deposit model in terms of timing, and spatial association between fault linkages/concentrations, fluid flow/remobilization patterns, and structural controls on mineralization. The Arrow high strain zones and uranium mineralization are hosted within strongly metasomatized basement rocks of the Taltson Domain, which record an extended and complex history of fluid-rock interaction and structural disturbance. Understanding the relative and absolute ages of mineralization stages, alteration episodes, and structural events/re-activations and their effects is critical to understanding this mineralized system. Uranium mineralization is associated with large- and small-scale primary and subsidiary structures formed through the prolonged evolution and re-activation of the major A1 through A5 shear zones during continent-scale protracted tectonic evolution. Uranium minerals, precious metals, and hydrothermal metasomatic alteration phases have been related to the structural history of the Arrow Deposit, yielding a genetic model encompassing structural and paragenetic relationships. The present research at the Arrow Deposit provides implications for the understanding of the overall structure and other uranium occurrences along the Patterson Lake corridor. The PLc is characterized by heterogeneous strain evidenced by fault rocks exhibiting characteristics reflecting multiple perturbation events. Due to the heterogeneity in rheology related to alteration/metasomatism, the style and intensity of deformation, and formation of suitable zones of dilation (i.e. releasing bends, Riedel fractures and pull-apart basins, etc.) is not consistent along the corridor. Extrapolating the structural analysis completed at Arrow and along the portion of the PLc contained within NexGen's Rook I property (e.g. Fig. 4.1) suggests that the highest concentrations of uranium are associated with these zones of higher structural disturbance, indicated by increased transposition of regional foliation due to shearing (i.e. steeper dip at Arrow and SW towards the Triple R deposit; Fig. 4.1) and increased brittle reactivation of ductile structures and formation of Riedel shear fracture arrays (i.e.

brecciation, cataclasis, and extensional fracture overprint; Section 4.3). As a result, the location of the Triple R deposit and Spitfire discovery, south and north of Arrow along strike, respectively, are likely a direct result of the heterogeneity (i.e. extent of brittle overprint and thus permeability) and periodicity of the deformation style (i.e. extensional vs. compressional, fault bends) along the PLc. Overall, the fault/shear architecture appears to play a large role in the distribution of uranium accumulations along the Patterson Lake structural corridor, with fluid flux (and thus uranium mineralization) potential being highest in zones of composite deformation, consisting of widespread, permeable damage zones around well-developed core zones where mass amounts of fluid may precipitate ore (i.e. the A2 and A3 "fault-fill" high-grade cores). The highly prospective Patterson Lake corridor represents only one of many sub-parallel corridors of heterogeneous strain in the SW Athabasca region (e.g. Fig. 1.3), with others such as the Derkson corridor (Fig. 1.3) remaining largely untested to date. The overall NE-SW orientation of the Patterson Lake corridor and others in the area also provides implications for the prospectivity of the corridors in the region, as a large majority of fault orientations hosting known uranium mineralization in the Athabasca Basin strike NE-SW (Thomas et al., 2018).

This study also provides the framework for future analytical studies in the Patterson Lake area, as the geological, structural, and paragenetic background is vital for such studies. The discovery of the Arrow and Triple R deposits, and this research, has sparked other work in the area, including structural studies of some of the other deposits along the PLc (Johnstone et al., 2018) and regional age and fluid inclusion studies (Potter et al., 2018), which rely heavily on paragenetic control for sample selection and determination of corridor-scale relationships. Other future research objectives that could refine the current paragenetic and structural information outlined by this research include further isotopic studies on pre-, syn-, and post-mineralization metamorphic and/or alteration phases such as illite/muscovite and chlorite. Isotopic dating (e.g. Ar-Ar) on these mineral species could perhaps overcome the difficulties in dating uraninite (e.g. susceptibility to lead loss, alteration, etc.), and provide more accurate ages which may help refine the mineral and structural paragenesis outlined by this study. Furthermore, temperatures and fluid composition information could also be obtained via isotopic analyses on these mineral phases.

The intimate relationship between brittle reactivated faults and unconformity-related uranium deposits has been recognized since the classic reports on the Rabbit Lake deposits by Hoeve and Sibbald (1978) and Hoeve et al. (1980) and are the starting point for nearly all exploration targeting in the Athabasca Basin (Jefferson et al., 2007). A number of structural studies have been completed on various uranium deposits in the Athabasca Basin (e.g. Lorilleux et al., 2002, Dieng et al., 2013), and have illustrated the importance of the developmen1.3t of subsidiary structures and other complexities (e.g. cross structures, splays, bifurcations, extensional and compressional flexures, and breccia/cataclasite zones) within basement fault complexes for the focussing fluid flow and ore deposition. For example, the various polyphase hydrothermal breccias associated with uranium mineralization in the southern part of the Shea Creek area mapped and described by Lorilleux et al. (2002) are similar to those encountered within the basement rock at the Arrow Deposit and exemplify the importance of basement fault reactivations and ensuing development of permeable damage zones. The structural connections created through subsequent seismic events affecting pre-existing basement and sandstone faults help induce fluid circulation and interaction, and thus uranium mineralization. Several originally ductile deformation zones in various arrays, including the strike-slip dominated PLc, have undergone repeated brittle reactivation with various offsets, and were critical for the focussing of mineralizing fluids. In summation, Arrow is undoubtedly a structurally controlled uranium deposit, and continued studies such as this one on these controls may allow for more precise vectoring templates in exploration of new areas in the SW and the Athabasca Basin as a whole.

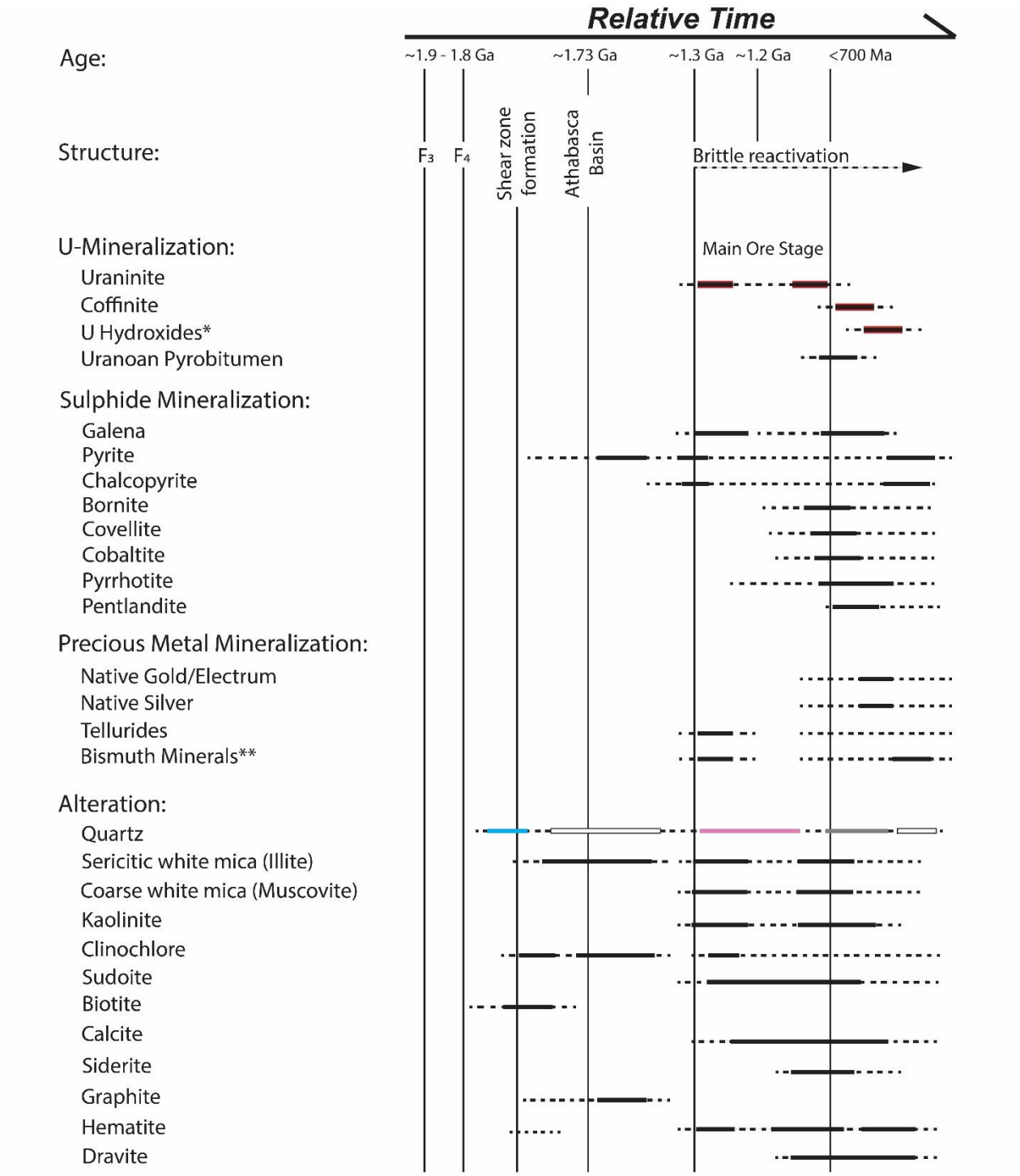

Fig. 7.1. Paragenetic chart for the Arrow Deposit integrating absolute U-Pb ages with structural evolution, U-mineral phases, precious metals, and hydrothermal alteration products. Quartz episodes are colorized to represent different phases. *Minor U silicates and hydroxides/oxyhydroxides. **Native bismuth, bismuthinite, and Bi-Te-Se minerals. The ages shown for uranium mineralization and alteration (1.3 Ga, 1.2 Ga, 700 Ma) are considered to represent minimum ages, and should not be treated as the actual age of the Main Ore Stage or subsequent alteration and mineralization (see Chapter 6, and p. 127-128 for discussion).

REFERENCES

Adlakha, E.E., Hattori, K., Zaluksi, G., Kotzer, T., and Potter, E.G., 2014, Alteration within the basement rocks associated with the P2 fault and the McArthur River uranium deposit, Athabasca Basin: Geological Survey of Canada, Open File 7462, p. 35.

Adlakha, E.E., and Hattori, K, 2016, Paragenesis and composition of tourmaline types along the P2 fault and McArthur River uranium deposit, Athabasca Basin, Canada: The Canadian Mineralogist, v. 54(3), p. 661.

Alexandre, P., and Kyser, T.K., 2003, Geochronology of the Paleoproterozoic basement-hosted unconformity-type uranium deposits in northern Saskatchewan, Canada: Conference paper: Uranium geochemistry conference, 4 p.

Alexandre, P., and Kyser, T.K., 2005, Effects of cationic substitutions and alteration in uraninite, and implications for the dating of uranium deposits: The Canadian Mineralogist, v. 43, p. 1005-1017.

Alexandre, P., and Kyser, T.K., 2014, Report: On the Petrography, Mineralogy, Uranium Mineralization and Associated Alterations, and the Age of Uranium Mineralization; Queen's University: Internal Report.

Alexandre, P., Kyser, T.K., Polito, P., and Thomas, D., 2005, Alteration mineralogy and stable isotope geochemistry of Paleoproterozoic basement-hosted unconformity-type uranium deposits in the Athabasca Basin, Canada: Economic Geology, v. 100, p. 1547-1563.

Alexandre, P., Kyser, T.K., Thomas, D., Polito, P., and Marlat, J., 2007, Geochronology of unconformity-related uranium deposits in the Athabasca Basin, Saskatchewan, Canada and their integration in the evolution of the basin: Miner Deposita, DOI 10.1007/s00126-007-0153-3.

Alexandre, P., Kyser, K., Jiricka, D., 2009, Critical geochemical and mineralogical factors for the formation of unconformity-related uranium deposits: Comparison between barren and mineralized systems in the Athabasca Basin, Canada: Economic Geology, v. 104, p. 413 – 435.

Angelier, J., 1984, Tectonic Analysis of Fault Slip Data Sets: Journal of Geophysical Research, v. 89, no. B7, p. 5835-5848.

Ashton, K.E., Hartlaub, R.P., Heaman, L.M., Morelli, R.M., Card, C.D., Bethune, K., Hunter, R.C., 2009, Post-Taltson sedimentary and intrusive history of the southern Rae province, along the northern margin of the Athabasca Basin, Western Canadian Shield: Precambrian Research, v. 175, p. 16 – 34.

Atmaoui, N., 2005, Development of pull-apart basins and associated structures by the Riedel shear mechanism: insight from scaled clay analogue models: Ruhr-University of Bochum, Institute of Geology, Mineralogy and Geophysics, Germany.

Azer, M.K., Stern, R.J., and Kimura, J., 2008, Origin of a late Neoproterozoic (605–13 Ma) intrusive carbonate–albitite complex in Southern Sinai, Egypt: International Journal of Earth Sciences, v. 99: p. 245–267.

Barthauer, G.L., Rulfs, C.L., and Pearce, D.W., 1953, Investigation of thucholite: American Mineralogist, v. 38 (9-10), p. 802-814.

Beyssac, O., and Rumble, D., 2014, Graphitic carbon: a ubiquitous, diverse, and useful geomaterial: Elements, v. 10, p. 415-420.

Bickford, M.E., Collerson, K.D., and Lewry, J.F., 1994, Crustal history of the Rae and Hearne provinces, southwestern Canadian Shield, Saskatchewan: constraints from geochronologic and isotopic data: Precambrian Research, v. 68, p. 1-21.

Bosman, S.A., Card, C.D., Brewster, Z., Fehr, C., 2011, The Athabasca Basin Ore-systems Project: A New Generation of Geoscience in the Athabasca Basin: Summary of Investigations 2011, v. 2, Saskatchewan Geological Survey, Saskatchewan Ministry of Energy and Resources, Miscellaneous Report 2011-4.2, p. 9.

Bosman, S.A., and Ramaekers, P., 2015, Athabasca Group + Martin Group = Athabasca Supergroup? Athabasca Basin multiparameter drill log compilation and Interpretation, with updated geological map: Saskatchewan Geological Survey, Miscellaneous Report 2015-4.2, Paper A-5, p. 13.

Bosman, S.A., 2017, Uranium potential of Phanerozoic rocks: Stratigraphy and potential traps in the Patterson Lake region. [abs.]: SGS Open House 2017 abstract volume, Technical session 1: Uranium – Global distribution, ore systems and exploration.

Bosman, S.A., Card, C.D., and Delaney, G., 2018, Phanerozoic stratigraphy of the Patterson Lake area, southwest margin of the Athabasca Basin Saskatchewan: Implications for uranium exploration. [abs.]: Resources for Future Generations, Technical Session EN14: Unconformity-Related Uranium Deposits, with a Focus on the Southwest Athabasca Basin (Canada) – III #1807, 2018.

Bowles, J.F.W., 1990, Age dating of individual grains of uraninite in rocks from electron microprobe analyses: Chemical Geology, v. 83, p. 47-53.

Bowles, J.F.W., 2015, Age dating from electron microprobe analyses of U, Th, and Pb: Geological advantages and analytical difficulties: Microscopy and Microanalysis, v. 21, p. 1114-1122.

Bucher, K., and Frey, M., 1994, Petrogenesis of Metamorphic Rocks, Springer-Verlag, Berlin, 318 p.

Cameron-Schiman, M., 1978, Electron microprobe study of uranium minerals and its application to some Canadian deposits: Ph.D. Thesis, University of Alberta, Edmonton, Alberta. (Unpublished).

Campbell, J.E., 2007, Quaternary geology of the Eastern Athabasca Basin, Saskatchewan: EXTECH IV: geology and uranium EXploration TECHnology of the Proterozoic Athabasca Basin, Saskatchewan and Alberta, Jefferson, C.W. and Delaney, G. (eds.), Geological Survey of Canada Bulletin 588, 2007. p. 211-228.

Card, C.D., 2002, New investigations of basement to the western Athabasca Basin: Summary of Investigations 2002, v. 2; Saskatchewan Geological Survey, Saskatchewan Energy and Mines, Miscellaneous Report 2002-4-2, p. 17.

Card, C.D., 2009, Cree South Project 2009: reconnaissance bedrock mapping in the Lloyd Domain and Virgin River Shear Zone: Summary of Investigations 2009, v. 2, Saskatchewan Geological Survey, Saskatchewan Ministry of Energy and Resources, Miscellaneous Report 2009-4.2, Paper A-7, p. 21.

Card, C.D., 2012, A proposed domainal reclassification for Saskatchewan's Hearne and Rae provinces: Summary of Investigations 2012, v. 2, Saskatchewan Geological Survey, Saskatchewan Ministry of the Economy, Miscellaneous Report 2012-4.2, Paper A-11, p. 9.

Card, C.D., 2017, Distribution and significance of crystalline rocks in the Patterson Lake uranium exploration corridor of northwest Saskatchewan: Summary of Investigations 2017, v. 2, Saskatchewan Geological Survey, Saskatchewan Ministry of the Economy, Miscellaneous Report 2017-4.2, Paper A-11, p. 18.

Card, C.D., and Bosman, S.A., 2007, The Cree Lake South Project: reconnaissance bedrock mapping in the Mudjatik and Virgin River domains, and the Virgin River Shear Zone near the southwest margin of the Athabasca Basin: Summary of Investigations 2007, v. 2, Saskatchewan Geological Survey, Saskatchewan Ministry of Energy and Resources, Miscellaneous Report 2007-4-2, Paper A-7, p. 22.

Card, C.D., and Noll, J., 2016, Host-rock protoliths, pre-ore metasomatic mineral assemblages and textures, and exotic rocks in the western Athabasca Basin: ore-system controls and implications for the unconformity-related uranium model: Summary of Investigations 2016, v. 2, Saskatchewan Geological Survey, Miscellaneous Report 2016-4.2, Paper A-8, p. 19.

Card, C.D., Campbell, J.E., and Slimmon, W.L., 2003, Basement lithologic framework and structural features of the western Athabasca Basin: Summary of Investigations 2003; Saskatchewan Geological Survey, Saskatchewan Industry and Resources, Miscellaneous Report 2003-4.2, p. 17.

Card, C.D., Pana, D., Stern, R.A., and Rayner, N., 2007, New insights into the geological history of the basement rocks to the southwestern Athabasca Basin, Saskatchewan and Alberta: EXTECH IV: Geological Survey of Canada, Bulletin 588, p. 119-133.

Card, C.D., McEwan, B., and Bosman, S.A., 2008, The Cree Lake South Project 2008: Regional Implications of Bedrock Mapping Along the Virgin River Transect: Saskatchewan Geological Survey, Miscellaneous Report 2008-4-2, p. 23.

Card, C.D., Bethune, K.M., Davis, W.J., Rayner, N., and Ashton, K.E., 2014, The case for a distinct Taltson orogeny: Evidence from northwest Saskatchewan, Canada: Precambrian Research, v. 255, p. 245-265.

Card, C.D., Bosman, S.A., and Delaney, G., 2018, KEYNOTE: Are uranium deposits of the Athabasca Basin more closely related to unconformities or to deep-seated structural control? [abs.]: Resources for Future Generations, Technical Session EN14: Unconformity-Related Uranium Deposits, with a Focus on the Southwest Athabasca Basin (Canada) – III #1793, 2018.

Cerin, D., Götze, J., and Pan, Y., 2017, Radiation-induced damage in quartz at the Arrow uranium deposit, southwestern Athabasca Basin, Saskatchewan: The Canadian Mineralogist, v. 55, p. 457-472.

Chi, G., Li, Z., Chu, H., Bethune, K.M., Quirt, D.H., Ledru, P., Normand, C., Card, C.D., Bosman, S., Davis, W.J., and Potter, E.G., 2018, A shallow-burial mineralization model for the unconformity-related uranium deposits in the Athabasca Basin: Economic Geology, v. 113, no. 5, p. 1209-1217.

Cloutier, J., Kyser, K., Olivo, G.R., Alexandre, P., and Halaburda, J., 2009, The Millenium Uranium Deposit, Athabasca Basin, Saskatchewan, Canada: An atypical basement-hosted unconformity-related uranium deposit: Economic Geology, v. 104, p. 815 – 840.

Cloutier, J., Kyser, T.K., Olivo, G.R., and Brisbin, D., 2010, Geochemical, isotopic, and geochronologic constraints on the formation of the Eagle Point basement-hosted uranium deposit, Athabasca Basin, Saskatchewan, Canada and recent remobilization of primary uraninite in secondary structures: Mineralium Deposita, v. 46, issue 1, p. 35-56.

Cobbold, P.R., and Quinquis, H., 1980, Development of sheath folds in shear regimes: Journal of Structural Geology, v. 2, p. 119–126.

Condie, K.C., 2001, Rodinia and continental growth: Divi RS, Yoshida M (eds) Tectonics and mineralization in the Arabian Shield and its extensions, Gondwana Research, v. 4(2), p. 154–155.

Crocker, C.H., Collerson, K.D., Lewry, J.F., Bickford, M.E., 1993, Sm–Nd, U–Pb, and Rb–Sr geochronology and lithostructural relationships in the southwestern Raeprovince: constraints on crustal assembly in the western Canadian shield: Precambrian Research, v. 61, p. 27–50.

Cross, S., Hillacre, S.E., Ansdell, K.M., and McEwan, B., 2018, Preliminary study of white micas at the Arrow unconformity-related uranium deposit, Saskatchewan, and their relationship to uranium mineralization: SGS Geological Open House, 2018, Saskatoon, Saskatchewan, Technical poster session, December 3-5, 2018.

Cumming, G.L., and Kristic, D., 1992, The age of unconformity uranium mineralization in the Athabasca Basin, northern Saskatchewan: Canadian Journal of Earth Sciences, v. 29, p. 1623–1639.

Currie, K.L., and Ferguson, J., 1971, A study of fenitization around the alkaline carbonatite complex at Callander Bay, Ontario, Canada: Canadian Journal of Earth Sciences, v. 8, p. 498-517.

Davis, G.H., Bump, A.P., Garcia, P.E., and Ahlgren, G., 2000, Conjugate Riedel deformation band shear zones: Journal of Structural Geology, v. 22, p. 169-190.

Derome, D., Cathelineau, M., Cuney M., and Fabre. C., 2003, Reconstitution of the P, T, X properties of paleo-fluids in the McArthur River unconformity-type uranium deposit (Saskatchewan, Canada): Uranium Geochemistry 2003, International Conference, Nancy, France, April 13-16 2003, Proceedings, p. 141-144.

Derome, D., Cathelineau, M., Cuney, M., Fabre, C., Lhomme, T., 2005, Mixing of sodic and calcic brines and uranium deposition at McArthur River, Saskatchewan, Canada: A Raman and Laser-Induced Breakdown Spectroscopic study of fluid inclusions: Economic Geology, v. 100, p. 1529 – 1545.

Dewey, J.E., Holdsworth, R.E., and Strachan, R.A., 1998, Transpression and transtension zones: Continental Transpressional and Transtensional Tectonics: Geological Society, London, Special Publications, v. 135, p. 1-14.

Dieng, S., Kyser, T.K., and Godin, L., 2013, Tectonic history of the North American shield recorded in uranium deposits in the Beaverlodge area, northern Saskatchewan, Canada: Precambrian Research, v. 224, p. 316-340.

Ellsworth, H.V., 1932, Rare-element minerals of Canada (No. 11-12): FA Acland, printer to the king.

Fayek M., and Kyser, T.K., 1993, Petrography, chemical ages, stable isotopic compositions, and REE contents of three stages of uranium mineralization from the Athabasca Basin in Summary of Investigations 1993, Saskatchewan Geological Survey, Saskatchewan Energy and Mines, Miscellaneous Report 93-4, p. 166 – 173.

Fayek, M., and Kyser, T.K., 1997, Characterization of multiple fluid-flow events and rare-earth-element mobility associated with formation of unconformity-type uranium deposits in the Athabasca Basin, Saskatchewan: Canadian Mineralogist, v. 35, p. 627–658.

Fayek, M., and Kyser, T.K., 2000, Low temperature oxygen isotopic fractionation in the uraninite–UO2–CO2–H2O system: Geochim. Cosmochim. Acta, v. 64, p. 2185– 2197.

Fayek, M., Harrison, T.M., Grove, M., and Coath, C.D., 2000a, A rapid in situ method for determining the ages of uranium oxide minerals: Int. Geol. Rev. 42, p. 163–171.

Fayek, M., Harrison, T.M., Ewing, R.C., Grove, M., and Coath, C.D., 2002a, O and Pb isotopic analyses of uranium minerals by ion microprobe and U-Pb ages from the Cigar Lake deposit: Chemical Geology, v. 185, p. 205-225.

Fayek, M., Kyser, T.K., and Riciputi, L.R., 2002b, U and Pb isotope analysis of uranium minerals by ion microprobe and the geochronology of the McArthur River and Sue Zone uranium deposits, Saskatchewan, Canada: The Canadian Mineralogist, v. 40, p. 1553-1569.

Fission Uranium Corporation, 2018, Press release: Fission increases indicated resource; Doubles inferred resource, February 20, 2018: https://www.fissionuranium.com/project/triple-r-deposit/news/index.php?content_id=629.

Haakon, F., 2010, Structural Geology: New York, Cambridge University Press, 463 p.

Hanmer, S., and Passchier, C.W., 1991, Shear-sense Indicators: A Review: Geological Survey of Canada, p. 90-17.

Hoekstra, H.R., and Fuchs, L.H., 1960, The origin of thucholite: Economic Geology, v. 55 (8), p. 1716-1738.

Hoeve, J., and Sibbald, T., 1978, On the Genesis of Rabbit Lake and other unconformity-type uranium deposits in Northern Saskatchewan, Canada: Economic Geology, v. 73, p. 1450 – 1473.

Hoeve, J., Sibbald, T., Ramaekers, P., and Lewry, J., 1980, Athabasca unconformity-type uranium deposits: A special class of sandstone-type deposits?: Uranium in the Pine Creek Geosyncline, (eds.) S. Ferguson and A. Goleby, IAEA, Vienna, p. 575 – 594.

Hoffman, P.F., 1988, United Plates of America, The Birth of a Craton: Early Proterozoic Assembly and Growth of Laurentia: Ann. Rev. Earth Planet. Sci., v. 16, p. 543 – 603.

Holcombe Coughlin and Associates (HCA), 2007, Oriented core manual: http://www.holcombecoughlin.com/HCA_downloads.

Holland, H.D., and Gottfried, D., 1955, The effect of nuclear radiation on the structure of zircon: Acta Crystallographica, v. 8, p. 291-300.

Holliger, P., 1988, Ages U–Pb définis in-situ sur les oxydes d'uranium à l'analyseur ionique: méthodologie et consequences géochimiques. C.R. Acad. Sci. Paris, Sér. 2, v. 307, p. 367-373.

Holliger, P., 1991, SIMS isotope analyses of U and Pb in uranium oxides: geological and nuclear applications. 8th Int. SIMS Conf., Proc., p. 719-722.

Hulbert, L., 1988, Investigation of mafic and ultramafic rocks for nickel–copper and platinum group elements in northern Saskatchewan: preliminary findings: Summary of Investigations 1988, Saskatchewan Geological Survey, Saskatchewan Energy and Mines, Miscellaneous Report 88-4, p. 152–154.

Imber, J., Holdsworth, R., Smith, S.A.F., Jefferies, S.P., and Collettini, C., 2008, Frictional-viscous flow, seismicity and the geology of weak faults: A review and future directions: Geological Society, London, Special Publications, v. 299, p. 151-173.

Jaffey, A.H., Flynn, K.F., Glendenin, L.E., Bentley, W.C., and Essling, A.M., 1971, Precision measurement of half-lives and specific activities of 235U and 238U: Phys Rev C Nuclear Physics, v. 4, p. 1889–1906.

Janeczek, J., and Ewing, R.C., 1992a, Structural formula of uraninite: Journal of Nuclear Materials, v. 190, p. 128-132.

Janeczek, J., and Ewing, R.C., 1992b, Dissolution and alteration of uraninite under reducing conditions: Journal of Nuclear Materials, v. 190, p. 157-173.

Jeanneret, P., Goncalves, P., Durand, C., Poujol, M., Trap, P., Marquer, D., Quirt, D., and Ledru, P., 2017, Geochronological constraints on the trans-Hudsonian tectono-metamorphic evolution of the pre-Athabasca basement within the Wollaston-Mudjatik Transition Zone, Saskatchewan: Precambrian Research, v. 301, p. 152-178.

Jefferson, C.W., Thomas, D.J., Gandhi, S.S., Ramaekers, P., Delaney, G., Brisbin, D., Cutts, C., Portella, P., and Olson, R.A., 2007, Unconformity-associated uranium deposits of the Athabasca Basin, Saskatchewan and Alberta: EXTECH-IV: Geology of uranium EXploration TECHnology of the Proterozoic Athabasca Basin, Saskatchewan and Alberta, Jefferson, C.W. and Delaney, G. (eds.), Geological Survey of Canada Bulletin 588, Saskatchewan Geological Society Special Publication 18, Mineral Deposits Division (GAC) Special Publication 4, p. 23-68.

Jercinovic, M.J., and Williams, M.L., 2005, Analytical perils (and progress) in electron microprobe trace element analysis applied to geochronology: Background acquisition, interferences, and beam irradiation effects: American Mineralogist, v. 90, p. 526–546.

Johnstone, D., Bethune, K., Tschirhart, V., 2018, The structural and lithological evolution of the Patterson Lake corridor, southwestern Athabasca Basin [abs.]: SGS Geological Open House, 2018, Technical Session 2: Structural Geology and Ore Deposits, December 4, 2018.

Johnson, J., in prep, Origin of the ubiquitous blue quartz at the Arrow Uranium Deposit, Saskatchewan through textural and chemical analysis: Primary quartz or secondary silicification?: Unpublished B.Sc. Hons thesis, Saskatoon, Canada, The University of Saskatchewan.

Katz, Y., Weinbergerb, R., and Aydinc, A., 2004, Geometry and kinematic evolution of Riedel shear structures, Capitol Reef National Park, Utah: Journal of Structural Geology, v. 26, p. 491-501.

Kister, P., Vieillard, P., Cuney, M., Quirt, D., and Laverret, R., 2005, Thermodynamic constraints on the mineralogical and fluid composition in a Proterozoic clastic sedimentary basin: The Athabasca Basin (Saskatchewan, Canada): European Journal of Mineralogy, v. 17, p. 325–342.

Kotzer, T.G., and Kyser, T.K., 1993, O, U, and Pb isotopic and chemical variations in uraninite: implications for determining the temporal and fluid history of ancient terrains: American Mineralogist, v. 78, p. 1262–1274.

Kotzer T., and Kyser, T.K., 1995, Petrogenesis of the Proterozoic Athabasca Basin, northern Saskatchewan, Canada, and its relation to diagenesis, hydrothermal uranium mineralization and paleohydrogeology: Chemical Geology, v. 120, p. 45 – 89.

Kresten, P., 1988, The chemistry of fenitization: Examples from Fen, Norway: Chemical Geology, v. 68, p. 329-349.

Kyser, T.K., 2000, Controls on fluids and basins: Fluids and Basin Evolution, Mineralogical Association of Canada, short course 28, p. 1-18.

Kyser, T.K., Hiatt, E., Renac, C., Durocher, K., Holk, G., and Deckart, K., 2000. Diagenetic fluids in paleo- and meso-Proterozoic sedimentary basins and their implications for long protracted fluid histories: Kyser, K. (Ed) Fluids and basin evolution, Mineralogical Association of Canada Short Course, 28, p. 225-262.

Kyser, T.K., Cuney, M., 2008, Unconformity-related uranium deposits; in Unconformity-related uranium deposits rocks, (eds.) T.K. Kyser and M. Cuney, Geological Association of Canada, Mineral Association of Canada Short Course, Québec City, May 2008, p. 161 – 219.

Lang, A.H., Griffith, J.W., and Steacy, H.R., 1962, Canadian deposits of uranium and thorium: Geological Survey of Canada, Economic Geology Ser. No. 16, p. 324.

Lazarte, C.A., and Bray, J.D., 1996, A study of strike-slip faulting using small-scale models: Geotech Testing Journal, v. 19, p. 118-129.

LeCheminant, A.N., and Heaman, L.M., 1989, Mackenzie igneous events, Canada: middle Proterozoic hotspot magmatism associated with ocean opening: Earth Planet Sci Lett 96, p. 38–48.

Lewry, J.F., and Sibbald, T.I.I., 1977, Variation in lithology and tectonometamorphic relationships in the Precambrian basement of northern Saskatchewan: Canadian Journal of Earth Sciences, v. 14, p. 1453–1467.

Lorilleux, G., Jebrak, M., Cuney, M., and Baudemont, D., 2002, Polyphase hydrothermal breccias associated with unconformity-related uranium mineralization (Canada): from fractal analysis to structural significance: Journal of Structural Geology, v. 24, p. 323-338.

Ludwig, K.R., 1993, ISOPLOT. A plotting and regression program for radiogenic-isotope data. U.S. Geol. Surv., Open File Rep., p. 91-445.

Luque, F.J., Huizenga, J-M., Crespo-Feo, E., Wada, H., Ortega, L., and Barrenechea, J.F., 2014, Vein graphite deposits: geological settings, origin, and economic significance: Mineralium Deposita, v. 49: p. 261-277.

Lyon, I.C., Saxton, J.M., Turner, G., 1994, Isotopic fractionation in secondary ionization mass spectrometry. Rapid Commun. Mass Spectrom. 8, 837– 843. Mallard, L.D., Rogers, J.J., 1997.

MacDonald, C., 1980, Mineralogy and Geochemistry of a Precambrian Regolith in the Athabasca Basin: M.Sc. Thesis, Saskatoon, Canada, The University of Saskatchewan, 151 p.

Mathisen, M., and Ross, D., 2017, Technical Report on the Rook I Property, Saskatchewan, Canada, NI 43-101 Report, RPA Canada.

Mayers, J.S., Shaw, R.D., and Tyler, I.M., 1996, Tectonic evolution of Proterozoic Australia: Tectonics, v. 15(6), p. 1431–1446.

McNutt, J.A., 2014, Technical Report on the Rook I Property, Saskatchewan, Canada. NI 43-101 Report.

Mercadier, J., Richard, A., Bioron, M-C., Cathelineau, M., Cuney, M., 2010, Migration of brines in the basement rocks of the Athabasca Basin through microfracture networks (P-Patch U deposit, Canada): Lithos, v. 115, p. 121 – 136.

Mercadier, J., Cuney, M., Cathelineau, M., and Lacorde, M., 2011, U redox fronts and kaolinisation in basement-hosted unconformity-related U ores of the Athabasca Basin (Canada): Late U remobilisation by meteoric fluids: Mineralium Deposita, v. 46, p. 105–135.

Mohrbutter, R., Hillacre, S.E., Ansdell, K.M., and Batty, M., 2018, Precious metals in the Arrow uranium deposit, Patterson Lake corridor, southwestern Athabasca Basin, Saskatchewan, Canada [abs.]: SEG Conference 2018: Metals, Minerals, and Society, Keystone, Colorado, Poster session – Technology and energy metals and minerals: Co, Li, U, REE #P.197, September 23, 2018. http://www.segabstracts.org/abstract_summary.php?mode=public&abs_id=1429.

Moores, E.M., and Twiss, R.J., 1997, Tectonics: Long Grove, IL, Waveland Press, Inc., p. 403.

Morelli, R.M., and MacLachlan, K., 2012, Saskatchewan gold: Mineralizing styles and mining history: Saskatchewan Ministry of Energy and Resources, Report 262, 171 p.

Naylor, M.A., Mandl, G., Sijpesteijn, C.H.K., 1986, Fault geometries in basement-induced wrench faulting under different initial stress states: Journal of Structural Geology, v. 8, p. 737–752.

Norris, A.W., 1963, Devonian stratigraphy of northeastern Alberta and northwestern Saskatchewan: Geological Survey of Canada, Memoir 313, p. 168.

Onstad, C., Hillacre, S.E., Ansdell, K.M., McEwan, B., and McNamara, G., 2017, Geochemical analysis of host rock lithologies at the Arrow uranium deposit, Athabasca Basin, Saskatchewan: Interpretation of protolith and alteration [abs]: PDAC-SEG Student Minerals Colloquium 2017 poster, Toronto, Ontario, March 6, 2017.

Passchier, C.W., 1984, The generation of ductile and brittle shear bands in a low-angle mylonite zone: Journal of Structural Geology, v. 6, p. 273–281.

Passchier, C.W., 1998, Monoclinic model shear zones: Journal of Structural Geology, v. 20, p. 1121–1137.

Passchier, C.W., and Trouw, R.A.J., 2005, Microtectonics, 2nd edition: Heidelberg, Springer Verlag, 366 p.

Peterson, T.D., Van Breemen, O., Sandeman, H., and Cousens, B., 2002, Proterozoic (1.85-1.75 Ga) igneous suites of the Western Churchill Province: granitoid and ultrapotassic magmatism in a reworked Archean hinterland: Precambrian Research, v. 119, p. 73-100.

Petit, J.P., 1987, Criteria for the sense of movement on fault surfaces in brittle rocks: Journal of Structural Geology, v. 9, p. 597–608.

Potter, E., Tschirhart, V., Powell, J., Card, C.D., Pana, D., McEwan, B., Ashley, R., MacKay, C., and Wheatley, K., 2018, Integrated geochronological, geophysical, and isotopic investigation into the Patterson Lake corridor of the southwestern Athabasca Basin [abs.]: SGS Geological Open House, 2018, Technical Session 1: Uranium – Global distribution, ore systems, and exploration, December 4, 2018.

Quirt, D., 1986, Host rock alteration in the Spring Point Area, Northern Saskatchewan: Saskatchewan Research Council, SRC Pub. No. R-855-9-C-86, p. 66.

Quirt, D., 1989, Host rock alteration at Eagle Point South: Saskatchewan Research Council, SRC Pub. No. R-855-1-E-89, p. 95.

Quirt, D., 1999, The significance of green sandstones and illite-chlorite mixed-layer clay-bearing sandstones of the Athabasca Group in the Close Lake-McArthur River area (NTS 74H): Summary of Investigations 1999, v. 2, Saskatchewan Geological Survey, Saskatchewan Energy and Mines, Miscellaneous Report 99-4.2, p. 121 – 131.

Ramaekers, P., 1979d, Stratigraphy of the Athabasca Basin: Summary of Investigations 1979, Saskatchewan Geological Survey, Miscellaneous Report 79-10, p. 154-160.

Ramaekers, P., 1980, Stratigraphy and tectonic history of the Athabasca Group (Helikian) of Northern Saskatchewan: Summary of Investigations 1980, Saskatchewan Geological Survey, Miscellaneous Report 80-4.

Ramaekers, P., Jefferson, C.W., Yeo, G.M., Collier, B., Long, D.G.F., Catuneanu, O., Bernier, S., Kupsch, B., Post, R., Drever, G., McHardy, S., Jiricka, D., Cutts, C., and Wheatley, K., 2007, Revised Geological Map and Stratigraphy of the Athabasca Group, Saskatchewan and Alberta: EXTECH IV: Geology and Uranium Exploration TECHnology of the Proterozoic Athabasca Basin, Saskatchewan and Alberta, C.W. Jefferson and G. Delaney (eds.), Geological Survey of Canada, Bulletin 588, p. 155-191.

Ramsay, J.G., 1980, Shear zone geometry: a review: Journal of Structural Geology, v. 2, p. 83–101.

Ranchin, G., 1968. Contribution a l'etude de la repartition de l'uranium a l'etat de traces dans les roches granitiques saines les uranites a teneur elevee du Massif de Saint-Sylvestre (Limousin - Massif Central Francais). Sci. Terre, v. 13, p. 161-205.

Reid, K.D., Ansdell, K., Jiricka, D., Witt, G., and Card, C.D., 2014, Regional setting, geology, and paragenesis of the Centennial unconformity-related uranium deposit, Athabasca Basin, Saskatchewan, Canada: Economic Geology, v. 109, p. 539-566.

Riciputi, L.R., Paterson, B.A., and Ripperdan, R.L., 1998, Measurement of light stable isotope ratios by SIMS: matrix effects for oxygen, carbon, and sulfur isotopes in minerals: International Journal of Mass Spectrometry, v. 178, p. 81-112.

Riedel, W., 1929, Zur mechanik geologischer Brucherscheinungen. Zentralblatt Mineral Geol Paläont B, p. 354-368.

Rogers, A.F., 1947, Uraninite and pitchblende: American Mineralogist, v. 32, num. 1-2, p. 90-91.

Rosenberg, P.E., and Foit, F.F., 2006, Magnesiofoitite from the uranium deposits of the Athabasca Basin, Saskatchewan, Canada: The Canadian Mineralogist, v. 44(4), p. 959-965.

Rumble, D., 2014, Hydrothermal Graphitic Carbon: Elements, v. 10, p. 427-433.

Ruzicka, V., 1993, Vein uranium deposits: Ore Geology Reviews, v. 8, p. 247-276.

Saskatchewan Mining Association, 2017, Uranium in Saskatchewan Facts on the Industry for 2017. Regina, Saskatchewan, http://saskmining.ca/ckfinder/userfiles/files/2017%20Uranium%20Fact%20Sheet.pdf, accessed November 1, 2018, p. 22.

Schmid, S.M., and Handy, M.R., 1991, Towards a genetic classification of fault rocks: geological usage and tectonophysical implications: Controversies in modern geology, evolution of geological theories in sedimentology, earth history and tectonics, Müller, D.W., McKenzie, J.A., Weissert, H, (eds.), Academic Press, London, p. 339–361.

Scott, B.P., 1985, Geology of the Upper Clearwater River area, Saskatchewan Energy and Mines, Open File Report 85-2, p. 26.

Seifert, W., Rhede, D., Thomas, R., Forster, H.J., Lucassen, F., Dulski, P., and Wirth, R., 2011, Distinctive properties of rock-forming blue quartz: Interferences from a multi-analytical study of submicron mineral inclusions: Mineralogical Magazine, v. 75(4), p. 2519-2534.

Sheahan, C., Fayek, M., Quirt, D., and Jefferson, C.W., 2016, A combined ingress-egress model for the Kianna unconformity-related uranium deposit, Shea Creek project, Athabasca Basin, Canada: Economic Geology, v. 111, p. 225-257.

Shimizu, N., and Hart, S.R., 1982, Applications of the ion microprobe to geochemistry and cosmochemistry: Annual Review Earth Planetary Science, v. 10, p. 483–526.

Shroeer, J.M., Rhodin, T.N., and Bradley, R.C., 1973, A quantum-mechanical model for the ionization and excitation of atoms during sputtering: Surf. Sci., v. 34, p. 571– 580.

Sibbald, T., 1974, La Loche (north) area: reconnaissance geological survey of 74C-NW and 74C-NE: Summary Report of Field Investigations by the Saskatchewan Geological Survey, Saskatchewan Department of Mineral Resources, p. 38-45.

Sibbald, T., 1985, Geology and genesis of Athabasca Basin uranium deposits: Summary of Investigations 1985, Saskatchewan Geological Survey, Saskatchewan Energy and Mines, Miscellaneous Report 85-4.

Sigmund, P., 1969, Theory of sputtering: I. Sputtering yield of amorphous and polycrystalline targets: Physics Review, v. 184, p. 383– 416.

Stern, R.A., Card, C.D., Pana, D., and Rayner, N., 2003, SHRIMP U–Pb ages of granitoid basement rocks of the southwestern part of the Athabasca Basin, Saskatchewan and Alberta: Radiogenic Age and Isotopic Studies, Report 16, Geological Survey of Canada, Current Research 2003-F, p. 20.

Sykes, J., and Schwab, M., 2014a, 2013 Fall Diamond Drilling Report, Rook I Property, Northern Saskatchewan, Canada, NexGen Energy Limited: Saskatchewan Mineral Resources Assessment File # pending (report currently not publicly available).

Sykes, J., and Schwab, M. 2014b, 2014 Winter Diamond Drilling Report, Rook I Property, Northern Saskatchewan, Canada, NexGen Energy Limited: Saskatchewan Mineral Resources Assessment File # pending (report currently not publicly available).

Sykes, J., Rozdilsky, S., Kocay, J., Browne, A., and Ainsworth, G., 2014, Arrow: A New High-Grade Uranium Discovery in an Emerging District [abs.]: Saskatchewan Geological Survey Open House: Technical Session 4: Emerging Projects, Exploration Techniques and Economics. Saskatoon, Saskatchewan.

Tchalenko, J.S., 1968, The evolution of kink-bands and the development of compression textures in sheared clays: Tectonophysics, v. 6, p. 159–174.

Tchalenko, J.S., 1970, Similarities between shear-zones of different magnitudes: Geological Society of America, Bulletin 81, p. 1625–1640.

Terzaghi, R.D., 1965, Sources of Error in Joint Surveys: Geotechnique, v. 15, p. 287-304.

Thomas, D., Aubin, A., and Zaluski, G., 2018, KEYNOTE: What does an Athabasca Basin uranium deposit footprint look like? [abs.]: Resources for Future Generations, Technical Session EN14: Unconformity-Related Uranium Deposits, with a Focus on the Southwest Athabasca Basin (Canada) – III #2203, 2018.

Tooth, B., Brugger, J., Ciobanu, C.L., and Liu, W., 2008, Modeling of gold scavenging by bismuth melts coexisting with hydrothermal fluids: Geology, v. 36, p. 815-818.

Tooth, B., Ciobanu, C.L., Green, L., O'Neill, B., and Brugger, J., 2011, Bi-melt formation and gold scavenging from hydrothermal fluids: An experimental study: Geochimica et Cosmochimica Acta, v. 75, p. 5423-5443.

Tremblay, L.P., 1982, Geology of the Uranium Deposits Related to the Sub-Athabasca Unconformity, Saskatchewan: Geological Survey of Canada Paper 81-20, p. 56.

Trouw, R.A.J., Passchier, C.W., and Wiersma, D.J., 2009, Atlas of Mylonites and related microstructures: Heidelberg, Springer Verlag, 322 p.

Twiss, R. J., and Moores, E. M., 1992, Structural geology: San Francisco, W.H. Freeman and Company, 532 p.

Whitney, D.L., and Evans, B.W., 2010, Abbreviations for names of rock-forming minerals: American Mineralogist, v. 95, p. 185-187.

Wilde, A.R., Bloom, M.S., and Wall, V.J., 1988, Transport and deposition of gold, uranium, and platinum-group elements in unconformity-related uranium deposits: The Geology of Gold Deposits - The Perspective in 1988, Monograph 6, p. 637-665.

Woodhead, J.A., Rossman, G.R., and Silver, L.T., 1991, The metamictization of zircon: Radiation dose-dependent structural characteristics: American Mineralogist, v. 76, p., 74-82.

World Nuclear Association, 2018, Nuclear Power in Canada. http://www.world-nuclear.org/information-library/country-profiles/countries-a-f/canada-nuclear-power.aspx, updated August 2018, accessed November 18, 2018.

World Nuclear Association, 2018, Uranium in Canada. http://www.world-nuclear.org/information-library/country-profiles/countries-a-f/canada-uranium.aspx, updated November 2018, accessed November 18, 2018.

Yu, M.L., and Lang, N., 1986, Mechanisms of atomic ion emission during sputtering. Nucl. Instrum. Methods B14, p. 403– 413.

Zolensky, M.E., Sylvester, P.J., Paces, J.B., 1988, Origin and significance of blue coloration in quartz from Llano rhyolite (llanite), north-central Llano County, Texas: American Mineralogist, v. 73, p. 313-323.

Appendix A: List of applicable mineral abbreviations adapted from Whitney and Evans (2010).

Symbol	Mineral Name	Symbol	Mineral Name
Ab	Albite	Pn	Pentlandite
Afs	Alkali feldspar	Pl	Plagioclase
Amp	Amphibole	Py	Pyrite
Ap	Apatite	Po	Pyrrhotite
Apy	Arsenopyrite		
		Qz	Quartz
Bt	Biotite		
		Rt	Rutile
Cal	Calcite		
Cb	Carbonate mineral	Ser	Sericite
Ccp	Chalcopyrite	Sd	Siderite
Chl	Chlorite	Sil	Sillimanite
Clc	Clinochlore	Sud	Sudoite
Cpx	Clinopyroxene		
Cv	Covellite	Thc	Thucholite
		Ttn	Titanite (sphene)
Drv	Dravite	Tur	Tourmaline
Ep	Epidote	Urn	Uraninite
Fsp	Feldspar	Zrn	Zircon
Gn	Galena		
Grt	Garnet		
Gr	Graphite		
Hem	Hematite		
Hbl	Hornblende		
Ilt	Illite		
Ilm	Ilmenite		
Kln	Kaolinite		
Kfs	K-feldspar		
Lm	Limonite		
Mnz	Monazite		
Ms	Muscovite		

Appendix B: Calibration standards and count times used for each element in EMPA analysis. (SPI indicates standards developed by Structure Probe Inc.; yag is an yttrium aluminum garnet; $TbPO_4$ was synthesized at the Smithsonian Institute, its composition corrected for Pb).

Element	Standard	Measurement Time (peak)	Measurement Time (high and low background)
Si	SPI quartz	30 seconds	15 seconds
Ti	SPI rutile	30 seconds	15 seconds
U	SPI U metal	40 seconds	20 seconds
Th	SPI Th metal	40 seconds	20 seconds
Pb	SPI crocoite	40 seconds	20 seconds
Y	SPI yag	40 seconds	20 seconds
Al	SPI yag	30 seconds	15 seconds
Cr	SPI chromite	30 seconds	15 seconds
V	SPI vanadium metal	40 seconds	20 seconds
Mn	SPI bustamite	30 seconds	15 seconds
Fe	SPI magnetite	30 seconds	15 seconds
Cu	SPI cuprite	30 seconds	15seconds
Tb	Smithsonian $TbPO_4$	40 seconds	20 seconds
Ca	SPI diopside	30 seconds	15 seconds
K	SPI sanidine	30 seconds	15 seconds
P	SPI apatite	30 seconds	15 seconds

Raw data was corrected for atomic number, adsorption and fluorescence (ZAF correction) using Noran φρζ (phi rho zeta), modeled after Bastin.

Appendix C: List of conference abstracts for presentations based on this research.

Hillacre, S.E., Ansdell, K.M., McEwan, B., and McNamara, G., 2017, Structural analysis and preliminary alteration-mineral paragenesis of the Arrow uranium Deposit, Athabasca Basin, Saskatchewan [abs.]: PDAC-SEG Student Minerals Colloquium 2017 poster, Toronto, Ontario, March 6, 2017.

Hillacre, S.E.*, Ansdell, K.M., McEwan, B., and McNamara, G., 2017, Structural analysis and paragenesis of the Arrow uranium Deposit, Athabasca Basin, Saskatchewan [abs.]: GAC-MAC 2017, Kingston, Ontario, Technical session GS2: Drivers and effects of ancient and modern hydrothermal processes, May 17, 2017.

Hillacre, S.E.*, Ansdell, K.M., McEwan, B., and McNamara, G., 2017, Structural analysis, paragenesis, and preliminary geochronology of the Arrow uranium Deposit, Athabasca Basin, northern Saskatchewan, Canada: Implications for controls on mineralization [abs.]: SGA Biennial Meeting 2017, Quebec City, Quebec, Technical session S04: Uranium deposits: from source to ore, August 21, 2017.

Hillacre, S.E.*, Ansdell, K.M., McEwan, B., McNamara, G., and Ainsworth, G., 2017, Structural analysis, paragenesis, and preliminary geochronology of the Arrow uranium Deposit, Athabasca Basin, Saskatchewan [abs.]: SGS Geological Open House, 2017, Saskatoon, Saskatchewan, Technical session 1: Uranium – Global distribution, ore systems and exploration, November 27, 2017.

Hillacre, S.E.*, Ansdell, K.M., McNamara, G., and Fayek, M., 2018, Uraninite geochronology of the Arrow uranium Deposit, Patterson Lake corridor, Athabasca Basin, Saskatchewan [abs.]: Resources for Future Generations 2018, Vancouver, British Columbia, Technical Session EN14: Unconformity-Related Uranium Deposits, with a Focus on the Southwest Athabasca Basin (Canada) – #2095, June 20, 2018.

Hillacre, S.E., Ansdell, K.M., McEwan, B., and McNamara, G., 2018, Structural analysis and mineral paragenesis of the Arrow uranium Deposit, Athabasca Basin, Saskatchewan: Implications for controls on mineralization in the Patterson Lake corridor [abs.]: Resources for Future Generations 2018, Vancouver, British Columbia, Poster session – Energy #1590, June, 2018.

Hillacre, S.E., Ansdell, K.M., McEwan, B., and McNamara, G., 2018, Structural analysis and mineral paragenesis of the Arrow uranium Deposit, Athabasca Basin, Saskatchewan: Controls on mineralization in the Patterson Lake corridor [abs.]: SEG Conference 2018: Metals, Minerals, and Society, Keystone, Colorado, Poster session – Technology and energy metals and minerals: Co, Li, U, REE #P.233, September 23, 2018.

*Denotes speaker

Appendix D: List of coauthored abstracts for presentations related to this research.

Cross, S., Hillacre, S.E., Ansdell, K.M., and McEwan, B., 2018, Preliminary study of white micas at the Arrow unconformity-related uranium deposit, Saskatchewan, and their relationship to uranium mineralization: SGS Geological Open House, 2018, Saskatoon, Saskatchewan, Technical poster session, December 3-5, 2018.

Johnson, J., Hillacre, S.E., Ansdell, K.M., McEwan, B., and McNamara, G., 2016, Textural relationships of the ubiquitous blue quartz within rocks hosting the Arrow Zone, Athabasca Basin, Saskatchewan: Can primary and secondary quartz be identified?: SGS Geological Open House, 2016, Saskatoon, Saskatchewan, Technical poster session, November 28-30, 2016.

Mohrbutter, R., Hillacre, S.E., Ansdell, K.M., Batty, M., McEwan, B., McNamara, G., and Ainsworth, G., 2017, Distribution and petrographic relationships of precious metals in the Arrow uranium deposit, northern Saskatchewan: Initial observations: SGS Geological Open House, 2017, Saskatoon, Saskatchewan, Technical poster session, November 27-29, 2017.

Mohrbutter, R., Hillacre, S.E., Ansdell, K.M., Batty, M., and McNamara, G., 2017, Distribution and petrographic relationships of precious metals in the Arrow uranium deposit, northern Saskatchewan: Initial observations [abs.]: PDAC-SEG Student Minerals Colloquium 2017 poster, Toronto, Ontario, March 6, 2017.

Mohrbutter, R., Hillacre, S.E., Ansdell, K.M., and Batty, M., 2018, Precious metals in the Arrow uranium deposit, Patterson Lake corridor, southwestern Athabasca Basin, Saskatchewan, Canada [abs.]: SEG Conference 2018: Metals, Minerals, and Society, Keystone, Colorado, Poster session – Technology and energy metals and minerals: Co, Li, U, REE #P.197, September 23, 2018.

Onstad, C., Hillacre, S.E., Ansdell, K.M., McEwan, B., and McNamara, G., 2016, Preliminary geochemical analysis of host rock lithologies at the Arrow uranium deposit, Athabasca Basin, Saskatchewan: Interpretation of protolith and alteration: SGS Geological Open House, 2016, Saskatoon, Saskatchewan, Technical poster session, November 28-30, 2016.

Onstad, C., Hillacre, S.E., Ansdell, K.M., McEwan, B., and McNamara, G., 2017, Geochemical analysis of host rock lithologies at the Arrow uranium deposit, Athabasca Basin, Saskatchewan: Interpretation of protolith and alteration [abs]: PDAC-SEG Student Minerals Colloquium 2017 poster, Toronto, Ontario, March 6, 2017.